Opportunities and Challenges for FDM 3D Printed Oral Dosage Forms for Personalized Medicine

Inaugural-Dissertation

zur Erlangung des Doktorgrades der Mathematisch-Naturwissenschaftlichen Fakultät der Heinrich-Heine-Universität Düsseldorf

vorgelegt von

Hellen Mazur, geb. Windolf

aus Hamburg

Düsseldorf, Februar 2023

Aus dem Institut für Pharmazeutische Technologie und Biopharmazie

der Heinrich-Heine-Universität Düsseldorf

Gedruckt mit der Genehmigung der
Mathematisch-Naturwissenschaftlichen Fakultät der

Heinrich-Heine-Universität Düsseldorf

Berichterstatter:

1. Prof. Dr. Jörg Breitkreutz

2. Prof. Dr. Anne Seidlitz

Tag der mündlichen Prüfung: 23. Mai 2023

Für meine Familie

Table of contents

List of abbreviations

Abbreviation	
3D	Three-dimensional
3DFbD	3D Printing Formulation by Design
3DP	3D Printing
ANN	Artificial Neural Network
API	Active Pharmaceutical Ingredient
ASD	Amorphous Solid Dispersion
ASTM	American Society of Testing Materials
ATP	Adenosine Triphosphate
BCRP	Breast Cancer Resistance Protein
BCS	Biopharmaceutics Classification System
BMBF	Bundesministerium für Bildung und Forschung (engl. Federal Ministry for Education and Research)
BZ	Benserazide
CAD	Computer-aided Design
CMC	Chemistry, Manufacturing and Control
CQA	Critical Quality Attributes
DA	Dopamine Agonist
DDF	Drug Dosage Form
DDI	Dopamin-Decarboxylase Inhibitor
DDS	Drug Delivery Systems
DiHeSys	Digital Health Systems
DM	Distributed Manufacturing
DPE	Direct Powder Extrusion
DRP	Drug-related Problems
EMA	European Medicines Agency
ETP	Emerging Technology Program
FDA	United States Food and Drug Administration
FDM	Fused Deposition Modeling
FFF	Fused Filament Fabrication
GMP	Good Manufacturing Practice
GRAS	Generally Recognized as Safe
HER-2	Human Epidermal Growth Factor Receptor 2
HIV	Human Immunodeficiency Virus
HLA	Human Leukocyte Antigen

HME	Hot-melt extrusion
IND	Investigational New Drug
IPC	In-process Control
IR	Immediate-release
LD	Levodopa
MDT	Mean Dissolution Time
MEC	Minimal Effective Concentration
MED	Melt Extrusion Deposition
MRP2	Multidrug Resistance-associated Protein 2
MTC	Minimal Toxicologic Concentration
NIR	Near-infrared Spectroscopy
ODF	Orodispersible Film
ODMT	Orodispersible Mini Tablets
ODT	Orodispersible Tablet
OROS	Osmotic Release Oral System
P-gp	P-glycoprotein
PAM	Pressure Assisted Micro Syringe Printing
PAT	Process Analytical Technologies
PD	Parkinson`s Disease
PDM	Pramipexole Dihydrochloride Monohydrate
Ph. Eur.	European Pharmacopoeia
PLA	Polylactic Acid
PMI	Precision Medicine Initiative
POC	Point-of-Care
PVA	Polyvinyl Alcohol
QbD	Quality by Design
QC	Quality Control
SA	Surface Area
SA/V	Surface Area to Volume ratio
SLA	Stereolithography
SLS	Selective Laser Sintering
SMEDD	Self-microemulsifying Drug Delivery System
SR	Sustained Release
UCL	University College London
V	Volume
VCM	Vacuum Compression Molding
WHO	World Health Organization

List of publications and contributions

Published manuscripts:

1) <u>Hellen Windolf</u>, Rebecca Chamberlain, and Julian Quodbach. *"Predicting Drug Release from 3D Printed Oral Medicines Based on the Surface Area to Volume Ratio of Tablet Geometry"*. Pharmaceutics (2021), 13(9): 1453.

   - Own contribution: 80%

   - HW planned the experiments in agreement with JQ. HW conducted the experiments and evaluated the data. HW wrote the manuscript. RC and JQ reviewed the manuscript.

2) Julian Quodbach, Malte Bogdahn, Jörg Breitkreutz, Rebecca Chamberlain, Karin Eggenreich, Alessandro Giuseppe Elia, Nadine Gottschalk, Gesine Gunkel-Grabole, Lena Hoffmann, Dnyaneshwar Kapote, Thomas Kipping, Stefan Klinken, Fabian Loose, Tristan Marquetant, <u>Hellen Windolf</u>, Simon Geißler, Tilmann Spitz. "*Quality of FDM 3D Printed Medicines for Pediatrics: Considerations for Formulation Development, Filament Extrusion, Printing Process and Printer Design*". Therapeutic Innovation & Regulatory Science (2021), 56(6): 910-928.

   - Own contribution: 5%

   - HW helped to plan the structure of the review and study design. The chapters *3D Printed Dosage Forms for Pediatric Use* and *Characterization of 3D Printed Structures* especially were co-written by HW. HW helped with the revision of the text and references.

3) Rebecca Chamberlain, <u>Hellen Windolf</u>, Julian Quodbach, and Jörg Breitkreutz. *"Precise Dosing of Pramipexole for Low-Dosed Filament Production by Hot Melt Extrusion Applying Various Feeding Methods"*. Pharmaceutics (2022), 14(1): 216.

   - Own contribution: 20%

   - HW assisted in the design of the experiments. RC conducted the experiments and evaluated the data. RC wrote the manuscript. HW, JB, and JQ reviewed the manuscript.

4) <u>Hellen Windolf</u>, Rebecca Chamberlain, and Julian Quodbach. "*Dose-independent Drug Release from 3D Printed Oral Medicines for Patient-specific Dosing to Improve Therapy Safety*". International Journal of Pharmaceutics (2022), 616(9): 121555.

- Own contribution: 70%

- HW planned the experiments in agreement with JQ. HW conducted the experiments and evaluated the data. HW wrote the manuscript. RC and JQ reviewed the manuscript.

5) <u>Hellen Windolf</u>, Rebecca Chamberlain, Arnaud Delmotte, and Julian Quodbach. "*Blind-Watermarking—Proof-of-Concept of a Novel Approach to Ensure Batch Traceability for 3D Printed Tablets*". Pharmaceutics (2022), 14(2): 432.

- Own contribution: 75%

- HW planned the experiments in agreement with JQ. HW conducted the experiments and evaluated the data with help of AD. HW wrote the manuscript. RC, AD, and JQ reviewed the manuscript.

6) Rebecca Chamberlain, <u>Hellen Windolf</u>, Björn Burckhardt, Jörg Breitkreutz, and Björn Fischer. "*Embedding a Sensitive Liquid-Core Waveguide UV Detector into an HPLC-UV System for Simultaneous Quantification of Differently Dosed Active Ingredients during Drug Release*". Pharmaceutics (2022), 14(3): 639.

- Own contribution: 35%

- HW assisted in the design of the experiments. RC conducted the experiments and evaluated the data in agreement with BB and BF. RC wrote the manuscript. HW, BB, JB, and BF reviewed the manuscript.

7) <u>Hellen Windolf</u>, Rebecca Chamberlain, Jörg Breitkreutz, and Julian Quodbach. "*3D Printed Mini-Floating-Polypill for Parkinson's Disease: Combination of Levodopa, Benserazide, and Pramipexole in Various Dosing for Personalized Therapy*" Pharmaceutics (2022), 14(5): 931.

- Own contribution: 50%

  - HW planned the experiments in agreement with JQ, JB, and RC. HW conducted the experiments and evaluated the data with help of RC. HW wrote the manuscript. RC, JB, and JQ reviewed the manuscript.

8) Rebecca Chamberlain, <u>Hellen Windolf</u>, and Jörg Breitkreutz. *„Arzneizubereitungen für die Therapie des idiopathischen Parkinson-Syndroms"* Pharmakon (2022), 10(3), pp. 216-226(11).

- Own contribution: 45%

  - RC and HW conducted the literature research. RC, HW, and JB together determined the structure of the article. RC and HW wrote the manuscript. JB reviewed the manuscript.

9) <u>Hellen Mazur</u>, Leon Erbrich, and Julian Quodbach. *„Investigations into the Use of Machine Learning to Predict Drug Dosage Form Design to Obtain Desired Release Profiles for 3D Printed Oral Medicines"* Pharmaceutical Development and Technology (2023), 28(2): 219-231.

- Own contribution: 75%

  - HM planned the experiments in agreement with JQ. HM conducted the experiments and evaluated the data. LE created the neural networks. HM and LE wrote the manuscript. JQ reviewed the manuscript.

Poster presentations:

- <u>H. Windolf,</u> R. Chamberlain, J. Breitkreutz, J. Quodbach.
  Vergleich der Druckpräzision von zwei 3D Druckern
  1. Doktoranden und Post-Doc Konferenz des Programms „ProMatLeben",
  September 3 - 4, 2019, Berlin, Germany

- R. Chamberlain, <u>H. Windolf,</u> L. Hoffmann, A. Michel, S. Klinken, J. Breitkreutz, J. Quodbach.
  Prozessoptimierung der Filamentherstellung mittels Schmelzextrusion mit einem niedrigdosierten Arzneistoff
  1. Doktoranden und Post-Doc Konferenz des Programms „ProMatLeben",
  September 3 - 4, 2019, Berlin, Germany

- <u>H. Windolf</u>, R. Chamberlain, J. Quodbach.
  3D gedruckte orale Darreichungsformen mit dosisunabhängiger Freisetzung
  Midterm Konferenz des Programms „ProMatLeben", May 18 - 19, 2021, online,
  (2. Platz Posterpreis)

- <u>H. Windolf</u>, R. Chamberlain, J. Quodbach.
  Dose-independent Drug Release from 3D Printed Oral Dosage Forms
  12th World Meeting on Pharmaceutics, Biopharmaceutics and Pharmaceutical Technology (PBP), May 11 - 14, 2021, online

- R. Chamberlain, <u>H. Windolf</u>, B. Fischer, J. Breitkreutz J. Quodbach.
  Raman Microscopy of Low-dose Filaments for 3D Printing
  12th World Meeting on Pharmaceutics, Biopharmaceutics and Pharmaceutical Technology (PBP), May 11 - 14, 2021, online

Oral presentations:

- R.Chamberlain*, <u>H. Windolf</u>, L.Hoffmann, N.Gottschalk.
  Polyprint - vom Polymer zur 3D gedruckten Arzneiform
  1. Doktoranden und Post-Doc Konferenz des Programms „ProMatLeben",
  September 3 - 4, 2019, Berlin, Germany

  *presenter

A. Introduction

A.1 Personalized Medicine

The world hosts about eight billion people [1], so there should be equal variations of every drug substance, drug dosage form (DDF), dosage strength, or drug product in general to meet individual needs and make medical therapy maximally effective. After all, every human being has a different genome (even identical twins can have slight genetic differences despite having the same genetic code, due to genetic mosaicism or epigenetic changes), metabolism, and fundamental biological phenotype and processes [2–8]. If a disease is to be treated in one out of these eight billion people, the factors that play a role are not only individual characteristics like age, gender, body weight, comorbidities, and ethnicity, but also more complex functions such as kidney function, metabolism, lifestyle, and the genetic code of the individual, as these can impact the production of enzymes and other bodily processes. Owing to variations in people's genetic constitutions, an active pharmaceutical ingredient (API) has different effects on different people [5,9–11]. However, by studying the genome, predictions can be made regarding the case-specific effects of a drug, allowing dosing to be more tailored to a patient's individual needs and avoiding relative overdoses. With personalized medicine (or precision medicine), responding to an individual patient's needs is possible. This is based on knowledge of the genetic variability of drug effects and the application of this understanding in drug development and individualized pharmacotherapy [7,12,13]. In the past years, the "one-size-fits-all" approach to medicine was evaluated as less beneficial, as it was observed that people responded to medical therapy differently from each other. This is expressed by adverse effects or a complete lack of therapeutic effect of the administered drug preparations. From 2012 to 2017, approximately 15% of patients were admitted to the emergency department for drug-related problems (DRPs) [14]. On average, 2.7% of the patients died due to a DRP within these years. A high lethal risk from DRPs was observed in the elderly and in those who had to take multiple medications every day. In precision medicine, drug therapy is tailored to every patient, increasing compliance with the applied drug treatment, while reducing the incidence of DRPs [15]. Diagnostic tests based on the analysis of an individual's unique enzymatic and genetic profiles can be used to design individual therapies.

A.1.1 The Evolution of Personalized Medicine

In the early 19th century, the scientists Cuénot and Garrod made some important discoveries in the field of pharmacogenetics. At the time, Lucien Cuénot had been studying the different coat colors of mice and Archibald E. Garrod had been studying alcaptonuria in humans [16–20]. Both scientists discovered a link between enzymes and genes. Garrod developed the idea that genetically determined differences in biochemical processes could be the cause of DRPs. He established the theory that enzymes are part of the metabolism of substances, and that problems can occur when such a mechanism is damaged or when the required enzyme is even missing [21]. In 1931 and 1932, Laurence Snyder demonstrated the inherited disease of "taste blindness" for phenylthiocarbamide [22]. He proved that the disease is inherited as an autosomal recessive disorder according to the Mendelian traits. This is among the first known examples of genetic polymorphisms and has been the first pharmacogenetic study. During World War II, the antimalarial drug primaquine was found to cause "primaquine hemolysis" in African American soldiers [23,24]. Later studies showed that this disease was caused by a genetic defect, a deficiency of glucose-6-phosphate dehydrogenase. In 1950, the first observation of a genetically based difference in the effect of a drug was made concerning suxamethonium, a muscle relaxant used for anesthesia [21,25]. It was noticed that in rare cases (1:3500 in people of white skin color), the duration of muscle paralysis was prolonged. The cause was found to be a reduced presence of pseudo-cholinesterase, an enzyme required to metabolize drugs, in these patients [26]. In October 1990, the Human Genome Project was launched in the USA. The purpose of this project was to decode the human genome and gain knowledge about gene-related diseases [27]. In 1992, the project published genetic maps for the chromosomes 21 and Y [28,29]. By 1999, chromosome 22 had been completely sequenced, and chromosome 21 was fully sequenced in 2000, increasing the opportunities to study the effects of trisomia 21 [30,31]. In the following years, further projects were initiated based on this project. As of May 2021, the human genome is considered to have been completely decoded with 19,969 genes [32,33]. Individual diagnosis and therapy of diseases are built on this knowledge. The expression of different DNA sequences influences how a patient reacts to a drug, how the drug is metabolized, and which dose ultimately affects the patient [34]. Pharmacogenetic diagnostics offer the possibility of identifying individual characteristics of a patient's metabolism and based on this, determining the type and dosage of the drug that the patient needs. However, genotyping currently is of great interest for drug therapies that have a narrow therapeutic

range or a risk of serious adverse drug reactions. One example of pharmacogenetic therapy is trastuzumab, a specific monoclonal antibody against human epidermal growth factor receptor 2 (HER-2) on mammary carcinoma cells [35,36]. This drug is used for the treatment of breast carcinoma in only a third of the patients in whom overexpression of HER-2 receptors is detected in the tumor tissue. This overexpression leads to a more aggressive course of breast carcinoma. With the personalization of the treatment, patient survival could increase significantly while the risk of DRPs could decrease [37]. However, tumor growth remains a major concern in cancer therapy due to the heterogeneity within a tumor. This may hinder personalized medicine based on the results of individual tumor biopsy samples. In previous studies by Gerlinger et al., exome sequencing, chromosomal aberration analysis, and ploidy profiling have been performed on renal carcinomas and associated metastases [38]. Strong heterogeneity has been observed within the tumors, with 26 out of 30 tumor samples (86.67%) from four tumors had variant allelic-imbalance profiles, with ploidy heterogeneity in two of four tumors [38]. Therefore, biopsies from a tumor can lead to the underestimation of the genomic landscape and represent a major challenge for personalized medicine and biomarker development [38]. However, precision medicine has already proven useful in other disease patterns and therapies. For example, in Human Immunodeficiency Virus (HIV) therapy, a combination of drugs is prescribed to prevent the virus from replicating inside patients. In most cases, abacavir, an API, is part of the combination. However, studies have found that about 3% of the patients do not tolerate this substance (mostly hypersensitivity reaction with e.g., fever, rash, vomiting) [39–41]. Further research has revealed that these patients have a particular variant of a specific gene (human leukocyte antigen, HLA-B), referred to as HLA-B*5701. The HLA-B gene is crucial in the immune system's ability to identify and respond to pathogens and to transmit hypersensitivity reactions [42]. As a result, a genetic test was developed to detect this variant in patients' blood and since 2008, doctors are obliged to carry out this test before drawing up a medication plan. If a patient has this gene variant, abacavir must not be used for the treatment of HIV but a different virustatic must be chosen for pharmacotherapy.

Especially in the Netherlands, pharmacogenetics is already well established. The Dutch Pharmacogenetics Working Group has issued recommendations for more than 100 medicines to adjust the dose based on genotype [43,44]. This approach has already been integrated into the clinical routine in this country and is regularly applied in everyday practice. Since 2005, the multidisciplinary team, consisting of clinical pharmacists, physicians,

clinical pharmacologists, clinical chemists, epidemiologists, and toxicologists, has been working on the goals of developing pharmacogenetic-based therapeutic (dose) recommendations and, concomitantly, supporting prescribing physicians and pharmacists by integrating the recommendations into computerized drug prescribing and automated drug monitoring systems. To build the database, systematic research was performed for each drug, literature was screened, and information on gene-drug interactions was collected. For each article found, two parameters were specified: the level of evidence of gene-drug interaction (0: lowest to 4: highest evidence) and the clinical relevance (AA: lowest impact to F: highest impact) of the potential side effects, reduced therapeutic response, or other clinical impact resulting from the gene-drug interaction [43,45–47]. The interactions found, references to publications, and recommended dosages were published by the group and made available worldwide.

In 2015, the then- U.S. president Barack Obama announced the Precision Medicine Initiative (PMI) [48]. The initiative was intended to improve health, cure diseases such as cancer and diabetes, and accelerate progress toward personalized therapy [4]. The focus was on cancer research, building a cancer- knowledge- network, and performing more clinical trials with novel designs. In addition, the initiative supported a better understanding of disease risk and mechanisms and furthermore the prediction of optimal therapy.

Most recently in 2023, an open-label, multicentre, controlled, cluster-randomised crossover implementation study (seven European countries, about 7000 patients) was published by the Leiden University Medical Centre, in which patients were prescribed drugs based on their genetic information with the "DNA Medication Passport" [49,50]. This card contains information about the patient's genetic constitution and links it to medications, the metabolization of which could be altered depending on the genetic code. These data were used by trained doctors for tailored therapies and individual drug dosages. This resulted in high patient acceptance and a 30% lower rate of adverse effects. Such an approach to personalized medicine could reduce hospitalizations based on DRPs. With effective disease prevention, fast and accurate diagnosis, and efficient therapies through personalized medicine and tailored individual medical care, the healthcare system could be relieved and costs saved, which would otherwise achieve suboptimal results with only "general" prescriptions. Reducing the number of patients admitted with DRPs will also reduce the burden on hospital personnel, who are understaffed anyway.

Retrospectively, the foundation for personalized therapy was laid at the beginning of the 19th century. Many discoveries have already made it feasible to cure some diseases and optimize therapies for individual patients. The decoding of the genome is another major step toward precision medicine. Cancer therapy is making great strides through selective drug targeting, which can significantly reduce side effects and improve the course of the therapy. As a result of the PMI and other breakthroughs in drug therapy, personalized medicine is becoming increasingly important, and more institutes and research groups, as well as industries, are taking an interest in this field and working and investing in it. So, the next few years will see many new findings, substances, APIs, drug preparations, and dosage forms that will improve the health of the individual.

A.2 Oral Dosage Forms

A.2.1 General

The route of administration and DDF is often chosen based on the indication, convenience, absorption of the API (pharmacokinetic and pharmacodynamic profile), toxicity, and stability [51,52]. If a very rapid onset and long-lasting, consistent effect are desired, an aqueous infusion should be administered intravenously. However, this procedure can be only performed in hospitals under medical supervision. By introducing the API directly into the bloodstream, the absorption through the mucous membrane and metabolization process in the liver are bypassed, and the pharmacological effect can be induced immediately. The most convenient administration route is the oral route; approximately 80% of all
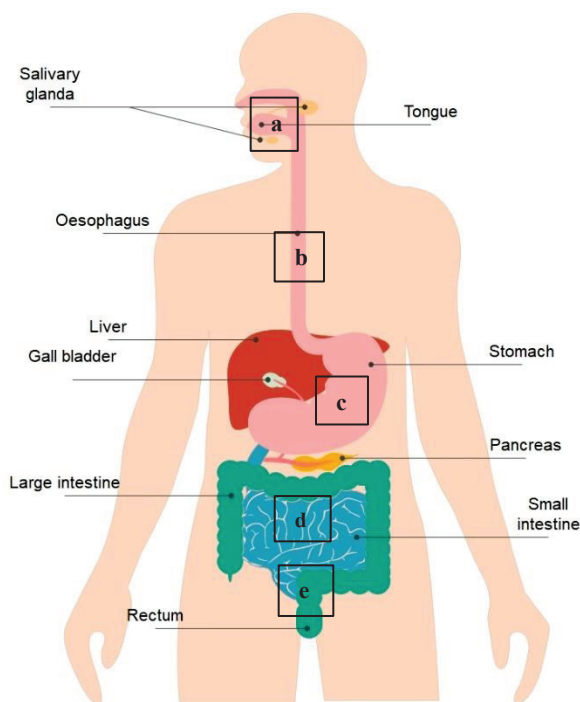

Figure 1: Schematic illustration of the transport path of an oral dosage form in the human body. [a]: mouth; [b]: oesophagus; [c]: stomach; [d]: small intestine; [e]: large intestine. (Created with EdrawMax Version 12.0.2).

drugs are applied perorally [53]. The most popular DDF is a tablet [52]. For peroral dosage forms, the onset of action cannot be generalized. Depending on the drug substance, dosage form, and physiological conditions, the intestinal absorption of the API is affected [54]. Solid (e.g., powders, granules, tablets, capsules), semi-solid (e.g., gels, pastes) and liquid dosage forms (e.g., emulsions, suspensions, solutions, syrups) can be taken by mouth (Figure 1a). Subsequently, the dosage form is transported together or dissolved within the saliva and an often-added liquid via the oesophagus (Figure 1b) into the stomach (Figure 1c). During the passage through the oesophagus, no absorption of the API occurs. The stomach is unsuitable for drug absorption due to its small specific surface area and a fasting volume of only 25 to 50 mL at pH 1.2, which limits drug dissolution capacities [53,55]. Nevertheless, the bioavailability of the API in the stomach is influenced, for example, by the ingested food, or the fasting state, the present pH value, the volume of fluid (taken with the DDF or already present in the stomach) or the intake of other drugs [56]. The API, the complete dosage form, or even particles of the dosage form are transferred from the stomach to the

small intestine (Figure 1d) via electrically stimulated muscle contractions. Due to the large specific surface area (provided by the intestinal microvilli), most dissolved drugs are absorbed from the (upper) small intestine, so that the duration of the small intestinal passage significantly impacts bioavailability. This is influenced by various parameters, for example, diet (especially food intake frequency), the age of the patient, and the impact of a disease. The residence time for solid dosage forms can vary widely, from two to more than ten hours in stomach [57,58]. Peristaltic waves force the contents of the small intestine toward the large intestine (Figure 1e), where hardly any drug absorption occurs. Here, the residence time can range from a few hours to several days [55,59]. After the API has been released from the DDF (liberation) and is dissolved, it can be absorbed by permeating the intestinal barrier. After absorption of the API via the intestinal cells (enterocytes), the drug substance is directed towards the liver where it may be biotransformed (hepatic first-pass-effect). Through metabolism, the API is either activated, or a certain proportion is inactivated. From the liver, the drug enters the bloodstream and thus, is supposed to be transported to the target site (distribution). Subsequently, the excretion from the body (elimination) takes place via the kidneys (urine), bile, and or intestines (faeces). In addition, the waste products of metabolism are also removed from the body by other organs such as the lungs (exhaled air), salivary, sweat, and mammary glands.

A.2.2 Basics of Drug Dissolution

The dissolution of the drug from the solid DDF results from a series of simultaneous and successive processes. First, the API is liberated from the DDF e.g., via erosion, diffusion, or disintegration and afterwards the released drug particles solubilize in the surrounding medium [60,61]. The disintegration is affected by various attributes like components of the DDF, capillary penetration of the medium, swelling, and wettability properties of the DDF. Mainly, the drug release and its absorption profile is determined by its solubility and intrinsic dissolution rate [51]. In addition, there are influencing properties such as particle size, wettability of the API, and physico-chemical properties like the dissociation constant (pKa value), salt form, and solid-state properties [60]. For substances to act systemically in the body, they must be absorbed via the intestine. The absorption rate and extent are determined by the solubility and permeability of the API. Easily soluble drugs that pass well through the mucosa can be used for an immediate drug effect. APIs that are difficult to dissolve in gastrointestinal fluids, on the other hand, require more time before becoming available to the body. APIs are categorized via the Biopharmaceutics Classification System (BCS) into

four groups, which differentiate according to solubility and permeability properties (Table 1) [54,62]. In 1995, Amidon et al. related the amount of drug absorbed to the surface area available, residence time in the intestine, apparent luminal drug concentration, and membrane permeability based on Fick's first law [63].

Table 1: BCS classification of APIs [62,63].

Class	Solubility	Permeability	Rate limiting step
I	High*	High**	Gastric emptying rate
II	Low	High	Dissolution rate
III	High	Low	Absorption rate
IV	Low	Low	Dissolution and/or absorption rate

*Highest dose strength is soluble in $\leq$ 250 mL media

**Extent of absorption $\geq$ 85%

Over 70% of the APIs on the market belong to BCS II and IV [64]. Due to this fact, formulation development of DDFs is becoming increasingly important and various techniques are being used to make these drug substances accessible to the body, for example by crystallization, solubilization, amorphous solid dispersions (ASD), and micronization [65]. Uptake of the substance across the intestinal membrane occurs via transcellular pathways, such as passive diffusion, endocytosis, or carrier-mediated transport, or by paracellular transport (Figure 2). Mostly, API uptake follows passive diffusion, which is influenced by the lipophilicity, polarity, and molecular size of the API [66,67]. On the other hand, efflux pumps, e.g., adenosine triphosphate (ATP)-binding cassette transporters like P-glycoprotein (P- gp), breast cancer resistance protein (BCRP), and multidrug resistance-associated protein 2 (MRP2), located in the apical membrane of enterocytes, eject a variety of substances out of the cell, thereby reducing API absorption into the bloodstream. Especially by P-gp and BCRP the bioavailability of drugs is limited [68,69].
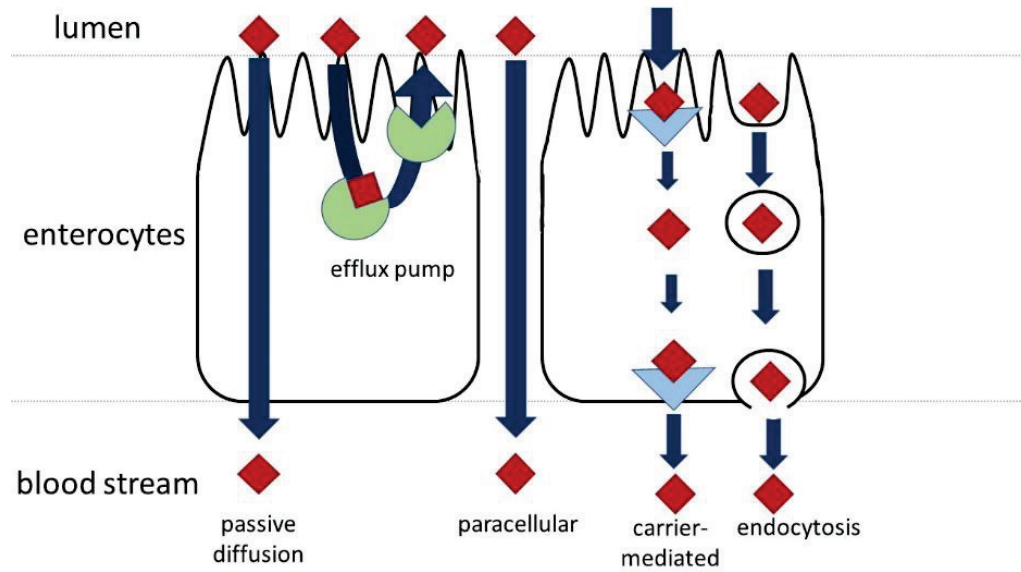
Figure 2: Transport mechanisms from lumen across the intestinal membrane to blood. Red cube: API.

Generally, the API must be dissolved for the permeation from lumen to bloodstream. The kinetics of the dissolution process can be described with the Noyes-Whitney equation. This formula presents the diffusion-related dissolution rate of drug particles from the dosage form, when the surface area is constant.

$$\frac{dC}{dt} = k \times (c_s - c_t) \tag{1}$$

The term $\frac{dC}{dt}$ describes the dissolution rate, k the constant, c_s specifies the thermodynamic saturation solubility of the API and c_t is the dissolved concentration of the API at time t. With this equation, Noyes and Whitney proved in 1897 that the rate at which a solid drug dissolves in its own solution is proportional to the difference between the saturation solubility and the bulk solution concentration [61,70,71]. In 1904, Nernst and Brunner published the diffusion layer model in which they assume a constant, unstirred layer with stagnant diffusion around the particle across which a concentration gradient exists [61,72,73]. Equation 2 represents the amount of API which dissolves over time ($\frac{dM}{dt}$).

$$\frac{dM}{dt} = \frac{S \times D}{\delta} \times (c_s - c_t) \tag{2}$$

At the surface of the particle, the highest concentration of API is present, a saturated solution (c_s). This concentration decreases outward within the layer until the concentration of the surrounding bulk fluid is reached (c_t). The thickness of the unstirred layer is defined

by δ. The surface area of the particle is described with S and the diffusion coefficient of the drug with D.

Based on this equation, it is apparent that different approaches can be used to modify the dissolution rate of a drug [61]. The larger the surface area in contact with the medium, the more API can dissolve per time interval (before approaching the thermodynamical solubility). The API concentration in the surrounding fluid should be kept as small as possible to keep the gradient as large as possible and to maintain the diffusion rate. This can be ensured, for example, using a circulating medium with an appropriate volume. By reducing the thickness of the diffuse layer, the drug could dissolve more quickly. In vitro, this can be adjusted with the stirring speed in a dissolution apparatus, but in vivo it cannot be influenced. The diffusion coefficient can be impacted by the viscosity of the medium. If the viscosity is reduced, the diffusion coefficient changes in favor of the solubility of the API. Again, this can only be influenced in vitro [61,74].

As previously mentioned, these formulas assume a constant surface area. However, in eroding systems, the surface area changes over time. Therefore, in 1931, Hixson and Crowell developed the descriptive "cube root law", which considers a constant change in surface area over time (Equation 3) [61,75].

$$\sqrt[3]{M_t} = \sqrt[3]{M_0} - k_{HC} \times t \tag{3}$$

M_0 and M_t characterize the masses of the particle at time t and time $t = 0$. k_{HC} describes the Hixson-Crowell constant, including the surface-volume relation. The equation is only applicable to spherical geometries under perfect sink conditions (i.e., volume of the dissolution medium that is at least three times the volume required for the saturation concentration of the API [76]). The particles remain spherical over time and must not disintegrate into smaller parts.

These formulas can be used to calculate the dissolution of the API and describe all actions that can intervene in this process and directly influence the dissolution rate.

A.2.3 Basics of Drug Release from Oral Dosage Forms

Besides the dose strength and BCS classification of the API, the release of the API from a DDF is also of high importance in personalized medicine. DDF formulation development can be used to dictate when and how much of the API is released from the dosage form. A drug can be released immediately from the DDF, or drug release can also be delayed, pulsatile, or prolonged (Figure 3). In the European Pharmacopoeia (Ph. Eur.), the immediate- (unmodified) release is specified as 80% API release within 45 min (Figure 3a) [77]. This release profile is achieved with highly soluble APIs (BCS Class I + III) formulated in rapidly disintegrating dosage forms. To accelerate the onset of action even more, a drug can be chemically modified, or its solid-state properties can be adjusted by e.g., co-crystals, salts, or amorphization, for example by preparing an ASD. Modified API release includes delayed, prolonged, and pulsatile release profiles. Delayed-release of an API is mostly used when the API is unstable in an acidic environment and would thus degrade in the stomach, or for taste-masking, for example, when the API has a bitter taste and may prevent successful medical therapy, especially in children. (Figure 3b). Often, for these cases, the oral dosage form is coated with a non-acidic soluble coating material that will not dissolve until a certain pH value is present (in the intestine) and the API can then be released from the DDF. However, the patient's diet as well as further medical treatment must be taken into account, as this can change the pH value in the stomach and thus cause an early release of the API from the DDF. A prolonged-release (sustained-release, or retarded DDF) can shorten the interval between multiple drug administrations and built up a constant drug level in the blood plasma, preventing fluctuations and reducing side effects (Figure 3c). The prolonged-release relies on the slow, constant release of the API from a depot (drug reservoir). Often, poorly soluble APIs result in prolonged-release (BCS II + IV), due to low solubility and dissolution rate. Also, a functional coating, a hydrocolloid matrix, or an insoluble matrix with small pores, as well as binding to an ion exchanger can produce a prolonged-release. In addition, osmotic systems (such as OROS®) as well as gastro-retentive dosage forms (e.g., floating DDF) have been developed, which help to achieve a constant release of the API. Often a retarded oral dosage form is provided with an initial dose that can act immediately and also a depot reservoir that maintains the plasma drug concentration level. In pulsatile-release (Figure 3d), or repeated-release, the API is released in several phases, often each with different release characteristics. Usually, an initial dose is released first, followed by a lag-time (period of no release), resulting in a plateau. Then, after a certain time,

another portion of the single dose is released, which can be followed by others at the given time. Pulsatile systems can be divided into two categories; Site-controlled systems, in which the API is released at the desired location in the intestine (e.g., colon-targeting systems), and time-controlled systems, in which the API is released after a defined period of time [78]. Site-specific release can be regulated by environmental factors such as pH or enzymes present in the gastrointestinal tract [78]. Drug release in time-controlled systems can be controlled primarily by the formulation of the DDF. For example, different coatings with varying dissolution properties, or press-coated tablets with various excipients matrices, can lead to this type of release in eroding or even inert systems.
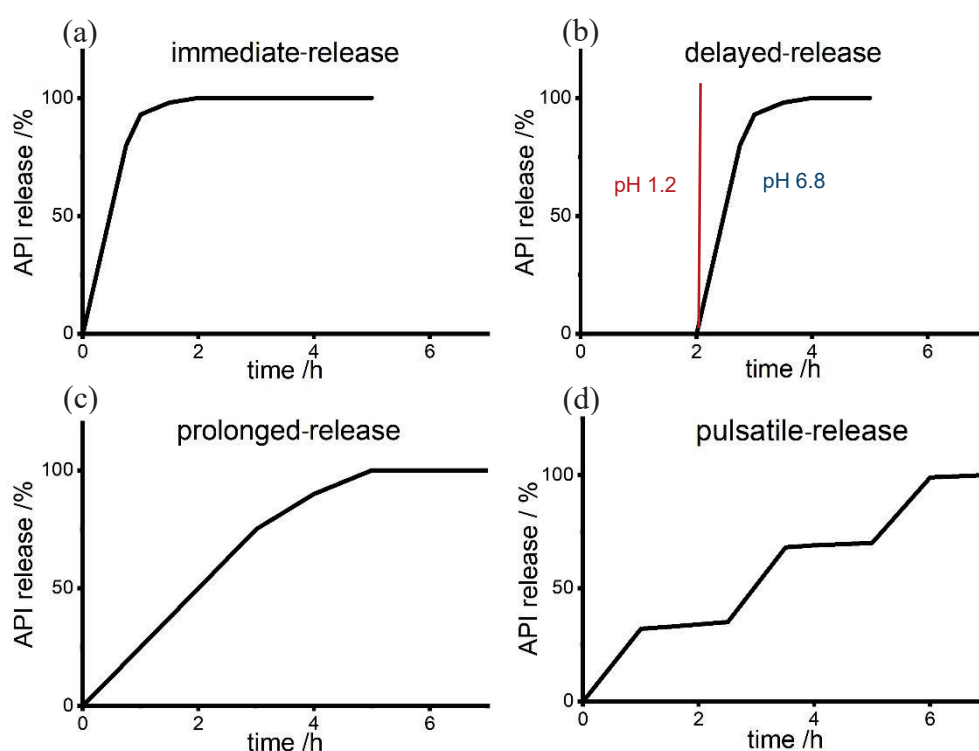

Figure 3: Examples of release curves with a) immediate-release profile; b) delayed-release profile; c) prolonged-release profile; d) pulsatile-release profile.

These release profiles were described using various mathematical models (Table 2) [79]. The mathematical equations try to describe the diffusion and erosion based activities so that it is possible to make predictions about the processes. An unmodified release mostly follows 1st order kinetics (Table 2a), i.e., that there is a linear relationship between concentration and release rate. The release rate is directly proportional to the amount of undissolved API. With increasing duration of release, the API is released more slowly, based on the decreasing difference between the saturation concentration and the API concentration

at time t. This can be both immediate and delayed release. For prolonged release, zero order kinetics is targeted (Table 2b). This means that a constant amount of drug is released from the DDF over a certain period of time. The release rate is independent of its concentration in solution. Often, however, in inert systems a longer diffusion path develops over time, so that less API is released over time and the slope of the straight-line decreases. This release profile was described by Higuchi with square-root-of time kinetics (Table 2c) [80–83]. The Weibull equation (Table 2d) is also used to describe dissolution curves mathematically but does not describe the physical API release process from the DDF that takes place. In 1983, Korsmeyer and Peppas developed an equation (Table 2e) to characterize the underlying release process, whether diffusion (Fick's law), erosion (Case-II transport, zero order kinetics), or anomalous transport dominates [79,84]. The Peppas Sahlin equation (Table 2f) can be used to describe the anomalous transport. The first part of the formula describes the Fickian diffusion, the second part the Case-II relaxational contribution [79].

Table 2: Mathematical equations for release description.

a)	First order kinetics	$c_t = c_0 \times (1 - e^{-kt})$
b)	Zero order kinetics	$c_t = k \times t$
c)	Higuchi square-root-t model	$c_t = k \times \sqrt{t}$
d)	Weibull function	$c_t = 1 - e^{(\frac{-(t-T_i)^b}{a})}$
e)	Korsmeyer-Peppas	$c_t = k \times t^n$
f)	Peppas Sahlin	$c_t = k_1 \times t^n + k_2 \times t^{2n}$

c_t= API concentration at time t; c_0 = initial API concentration; t= time; k= constant; T_i= lag-time before start of API release; b= shape of the curve; a= time scale of release; n= diffusional constant.

These mathematical approaches, as well as other formulas not mentioned here, are used to better understand and predict the API release process. Additionally, these descriptions can help in formulation development of the DDF and provide insights into possible modifiable attributes to influence release behavior. To meet the individual needs of patients in personalized medicine, controlled release techniques are often used to make therapy as effective as possible and to increase compliance.

A.2.4 Pharmacokinetics of Oral Dosage Forms

The aims of pharmacokinetics are to describe the time course of plasma drug concentrations and to develop dosage and administration suggestions based on the profile. Pharmacokinetics includes the processes of absorption, distribution, metabolization, and elimination (section A.1.2.1). Assuming an oral dosage form, several processes must occur before the API is available to the body:

DDF → Disintegration/Erosion/Diffusion → Dissolution → Absorption

Each of these steps is influenced by different processes and substances in the gastrointestinal tract, like the pH value of the digestive fluids, motility of the gastrointestinal tract, passage time, gastric emptying time, enzymes, blood circulation [55]. The oral absorption of the drug can be described pharmacokinetically in the single-compartment model with the Bateman function (schematic curve of a plasma concentration time course described by the Bateman function is shown in Figure 4). Initially, absorption of the drug predominates (1st order kinetics), until after a certain time the API depot is exhausted and elimination predominates (1st order kinetics) [85]. If the API is already dissolved (solution) at the time of administration, invasion from the gastrointestinal tract can be equated with absorption. However, if the API must first be released from the dosage form, invasion involves both release and absorption of the API. The effective period begins when the minimum effective concentration (MEC) is exceeded at the target site. The blood plasma level begins to decline until it falls below the MEC and the patient no longer perceives any drug effect. If the dose is too high, the minimum toxic concentration (MTC) will be crossed, and adverse effects up to a fatal outcome may occur. Between the MEC and MTC is the effective range of the API, also known as the therapeutic index. Depending on the efficacy and toxicity of the API, this range may be larger or smaller.
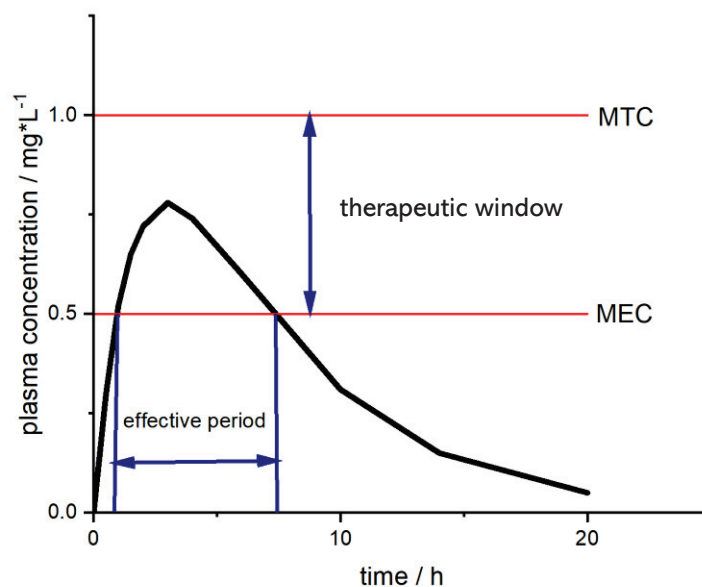
Figure 4: Schematic time course of a single dose after oral administration. MTC= minimum toxic concentration, MEC= minimum effective concentration.

A cumulation of the plasma concentration can be achieved by the repeated application of an oral dosage form (Figure 5). The narrower the therapeutic index of a drug, the more difficult it becomes to precisely target this range and to maintain the drug concentration in this optimal field without the dosage becoming too high and exceeding the MTC, or too low and falling below the MEC. The curve in grey represents a hypothetical ideally pro-longed course of API plasma concentration. In the steady-state, the absorption of the API as well as the biotransformation and elimination are balanced.
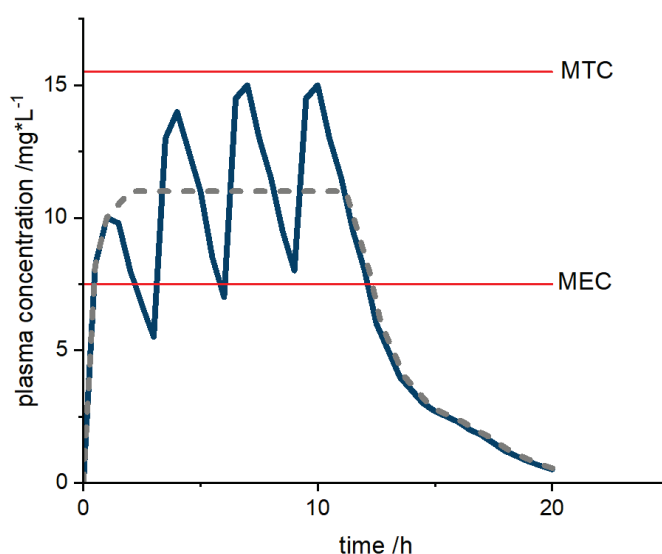

Figure 5: Schematic representation of the time course of plasma level concentration after repeated oral intake of a single dose (blue) and the course of an ideally prolonged DDF (grey).

The increase in API plasma concentration and the shape of the curve are determined by the dissolution and permeation properties of the API, as well as the release properties of the dosage form (Figure 6), but if the ingested dose remains the same, the area under the curve remains constant. Depending on the formulation, an immediate, a delayed, or a prolonged effect can be achieved.
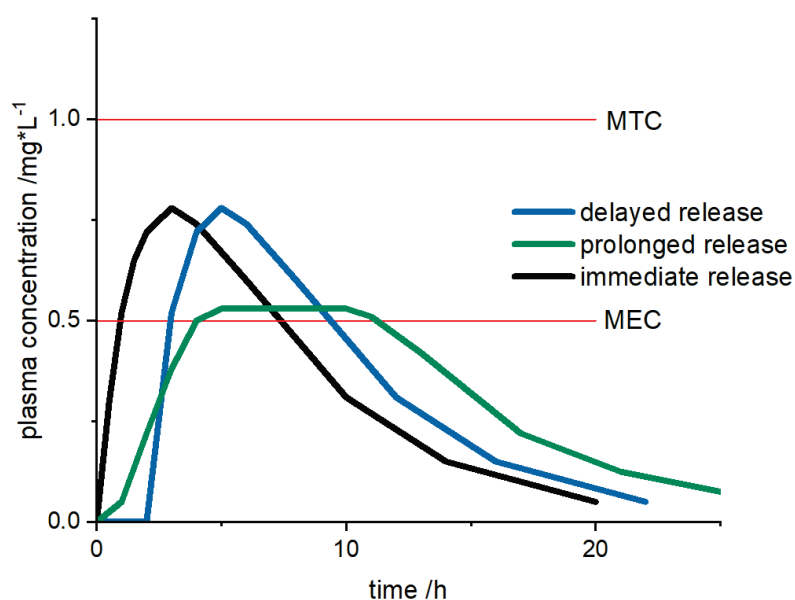

Figure 6: Schematic plasma concentration profiles of immediate (black), delayed (blue), and prolonged (green) drug formulations. Example of three equal doses of the same API only various formulations releasing the API differently.

DDF with a prolonged effect (retarded DDF) can prevent fluctuations and dose spikes, thus improving therapy and patient's compliance. Moreover, it reduces the risk of overdosing and the occurrence of adverse effects. In addition, the dosing intervals are increased, which relieves patients and caregivers, due to fewer drug administrations. With the help of these modifications, the individual needs of the patient can be addressed, as well as the properties of the APIs can be taken into account. For personalized medicine, the pharmacokinetics of the DDF is of great importance and requires consideration.

A.2.5 Oral Dosage Forms for Personalized Medicines

To meet the individual requirements of therapy, the dosage form must also be as flexible as possible and cover a wide range of dosages and release profiles. Moreover, children and elderly patients often have difficulty swallowing, which means they should preferably not be prescribed tablets [6,86–91]. Industrially, only the average required dosages can be produced on a large scale. Thus, a maximum of four to six different dosages are available for most drugs. If tablets are provided with a score line, the range of the dosage can be increased even further, but several studies have shown that dividing a tablet results in large fluctuations in the dosage [92–94]. In support of the notch, various dividing devices can be used, which ensure a more precise division of the tablets than what is achieved with dividing by hand. However, this can also lead to overdosing or underdosing [6,92,95]. In addition, tablets with a functional coating (e.g., enteric-coating, sustained release, colon-targeting, saliva-resistant, and taste masking) cannot be divided without losing the desired function. The World Health Organization (WHO) states in a report that about 50% of the prescribed medications are not taken as advised and that around one-tenth of the medicines prescribed for children are off-label or unlicensed [96]. However, children cannot be treated as "small adults". Not only are their bodies smaller, but their body composition, enzyme equipment, skin permeability, and the size and pH of their stomach, as well as the length of the intestine and the number of circular folds, differ from those of adults. For these reasons, drugs developed for adults cannot simply be given to children in smaller doses. The rate of absorption in a child must also be considered, as well as their metabolism [96]. The same is valid for elderly patients. They often face health issues such as metabolism slowing down, reduction of kidney or liver function, the gastrointestinal peristalsis being limited, and swallowing becoming difficult. They also usually suffer from several diseases, which means multiple-drug treatment [97–99].

In the case of APIs with a narrow therapeutic index, where individual dosing is often necessary, even a small variation in the dosage can be dangerous or devastating. To address individual requirements in terms of dosage, drug release, API combination, and compliance with therapy, various dosage forms have been developed or are still under development, as described below:

- **Liquids and semi-solids**: Individual dosage is of huge importance, especially for children, as here the dosage is based on body weight. Furthermore, children under the age of six cannot swallow large tablets, or do not want to due to unpleasant taste and swallowing problems [6,100]. Therefore, a liquid or semi-solid preparation such as a juice, drop, suspension, or syrup is often suitable as the dosage form of choice. The formulation is usually dosed and administered to patients using syringes, cups, or measuring spoons. However, the different mediums also show large variations in dosing accuracy [101,102]. Liquid and semi-solid formulations can be refined with sugar or different flavors, so that children accept them more readily and the sometimes bitter tastes of the APIs can be masked. However, not all APIs can be incorporated into a liquid or semi-solid preparation due to limiting stability properties or incompatibilities. In addition, the liquid base provides a good culture medium for bacteria and other microorganisms and can severely impair the quality of the dosage. Often, the preparations are also not stable over a longer period, and the medicine must be used up quickly after the preparation and opening of the container. Solutions and most emulsions only allow immediate, unmodified release of APIs. Suspensions, on the other hand, also allow modified release.

- **Mini-tablets:** A mini-tablet is a dosage form that enables both fast and slow or delayed release. Mini-tablets can also be dosed individually, as single or multiparticulate dosage forms [103]. In the literature, they are described as spherical tablets with diameters of 1-5 mm [104–107]. Due to their small geometry, mini-tablets are particularly suitable for patients who have swallowing difficulties [86,89,103]. A randomized, open-label, cross-over study of 306 children (6 months to 5 years) compared the acceptability of mini-tablets and syrup. It was found that the acceptance of mini-tablets was greater than that of syrup. These are important findings, which will determine the development of dosage forms suitable for children and thus improve the therapy of this patient group [103]. Dispensers for mini-tablets are ideal for easy and accurate dosing, but still not widely commercialized [6,95,108]. Due to their composition, mini-tablets can be used both as unmodified and modified release versions, but also as orally dispersing dosage forms (e.g., OD-MTs) [107,109]. In addition, these dosage forms can be provided with a functional film coating after their production. However, due to their small shapes, the tablets are limited in terms of API loading. If a high dosage of an API is required, the mini-

tablets must be ingested in many small intervals, or a larger quantity of mini-tablets must be taken at one time. This could also be provided in the form of capsules or sachets whose contents consist of mini-tablets (e.g., Orfiril® long Retardtablette, Orfiril® long, Desitin Arzneimittel GmbH; Rhythmol SR, Glaxo Smith Kline) [110]. However, placing mini-tablets into a capsule eliminates this dosage form's advantages for patients with swallowing difficulties, unless taking the contents separately without the capsule shell is possible. Regarding this topic, there are studies dealing with Parkinson's disease (PD), a neuronal disorder. These patients often suffer swallowing difficulties, so a mini-tablet dosage form would be beneficial for them. Moreover, a fine-tuned dosing regimen with continuous API release could increase the effectiveness of Parkinson's therapy. Due to a predefined combination of levodopa and carbidopa in a ratio of 4:1, this API combination can be compressed into one formulation, reducing the number of tablets the patients must swallow. The desired mini-tablet quantity can be calculated and dispensed via the associated electronic dose dispenser (MyFID; CE-classified as medical device) [111–114].

- **Orodispersible and mucoadhesive buccal films**: Another dosage form suitable for personalized medicine are orodispersible films (ODFs). Since films dissolve in the oral cavity or can be removed after an appropriate period and the APIs (even poorly-soluble) can be swallowed with the saliva, this dosage form is suitable for pediatric and geriatric patients with swallowing difficulties. In the case of buccal films, the APIs can be released in the oral cavity and excreted; they also act locally or are absorbed into the bloodstream via the oral mucosa. An advantage of this dosage form is the fast onset of action due to the circumvention of the gastrointestinal tract and the first-pass effect. Both types of films are frequently produced from a polymer dispersion or a solution and solvent casting process, which can even run as a continuous manufacturing process [115–117]. Another production technique can be the hot-melt extrusion process (HME) [118]. The respective dosage of the film can be ensured via cutting different film sizes, and thus also varied, so that different dosages can be realized with one formulation [92,119]. By dividing an ODF into multiple compartments (tandem-films), combining two or more APIs in one film is possible, without affecting the stability, incompatibility, and safety. In addition, it is possible to use different polymers for each compartment and thus differ the release profile and physical properties of both types of films [120]. Despite these

advantages, the number of ODFs on the market is low (e.g., migraine, PD, pain, nausea). Due to the moderate size, volume, and required physical properties of ODF, a limited drug-load is given (mostly < 25 mg/ 6 cm^2) [121,122]. Therefore, this dosage form is commonly used for high-potency, low-dose APIs. Moreover, the larger surface area (SA) in this dosage form, when compared to tablets, makes it more sensitive to temperature and humidity. Since this dosage form is still relatively new, its pharmacopoeia requirements are limited. In the monograph for ODFs as well as mucoadhesive preparations [123], only a suitable mechanical strength is required, without more precise definitions. As a specific test, only the release of the API is tested according to *Ph. Eur. 2.9.3 Dissolution of solid dosage forms*. There are no given limitations such as disintegration time, mucoadhesion testings, or a specific dissolution test for films.

- **Imprinted DDF (Inkjet printing)**: For further personalization of medicine, some approaches have been made toward individualized dosing with inkjet printing of APIs onto ODFs [124]. Inkjet printing offers a precise, flexible, and contactless technique. Since this method produces reliable small amounts of drops, precisely printing expensive and high potent APIs is possible [125,126]. In addition, due to the heatless process, even thermosensitive drugs can be processed in this dosage form, in contrast to the solvent- casting or HME processes. A challenge of inkjet printing are recrystallization issues at the nozzle. This results in clogging problems that affect the dose uniformity and homogeneity of the drops on the film surface. Furthermore, similar to ODFs, this technique still has limitations in terms of drug loading. Researchers and pharmaceutical companies are continuously working on the optimization of imprinted DDFs to achieve higher drug loading rates [125, 126].

All these processes aim at making the dosage as personalized as possible and responsive to a patient's needs. However, besides the ability to produce patient-tailored dosage forms, all these processes have their limitations. For example, dosage forms are often limited in terms of drug loading, as well as in the design of the release behavior of the API. Therefore, studies are continuously developing and investigating new processes to provide the broadest possible range of customization for a patient.

A.3 3D Printing – A New Way for Personalized Medicine

In recent years, 3D printing (3DP) has been intensively investigated as a revolutionary technology process for individual drug therapy [127–135]. Due to the different processes (mentioned in Section A.3.1), a wide range of various pharmaceutical forms, such as implants, inserts, oral dosage forms, patches, or micro needle systems can be manufactured [127,136–144]. The ease of production of different dosages, drug combinations, and release profiles also makes 3DP suitable for producing clinical samples for efficacy studies. Furthermore, the low-cost and compact equipment involved in 3DP makes this technology an attractive choice for producing dosage forms in developing countries.

Due to the flexibility regarding the printed geometry and complex structures, 3DP is especially interesting for individual therapy, as it can influence both dosage and release via not only the formulation but also the DDF design [128,130,131,136,145]. Unlike pressed tablets, printed tablets have no limits in this respect, as they do not require punches or dies to dictate the shape. Furthermore, as no compression of the formulation takes place, it is possible to insert pores and other fragile structures [131,136]. A potential on-demand production in community pharmacies or hospitals makes this technology very interesting for tailored medicines. In contrast to the mass production of tablets and other industrially manufactured DDF, 3DP could be used to produce only small batches, which usually requires more time, as the printed DDF is built up layer by layer. Since the dose is to be adjusted specifically for patients, fewer errors should occur in dosing, resulting in fewer adverse effects [146]. In addition, less waste will be produced because the complete batch is produced for one patient. The 3DP technology also allows flavors to be incorporated in dosage forms for taste masking without adding a film coating. The on-demand batches can be produced in pharmacies, hospitals, clinics, and remote locations. The small batch sizes are suitable for individual therapies as well as clinical samples in dose-finding studies. The potential to readily adapt dosages is a great advantage, especially for early phase drug development (pre-clinical, Phase I + II clinical trials). With dose-flexibility, production on-demand, easily changeable SA/V ratio, and thus the release profile, 3DP offers a level of flexibility, that cannot be implemented with tablets or capsules [135].

A.3.1 3D Printing Technologies

Over the past years, various 3DP technologies have been developed. These processes can be categorized into seven groups which cover a total of 18 different processes according to American Society of Testing Materials (ASTM) Standard F2792 [135,147,148]. The groups are: binder jetting, VAT polymerization, powder bed fusion, material jetting, material extrusion, direct energy deposition and sheet lamination (Figure 7).
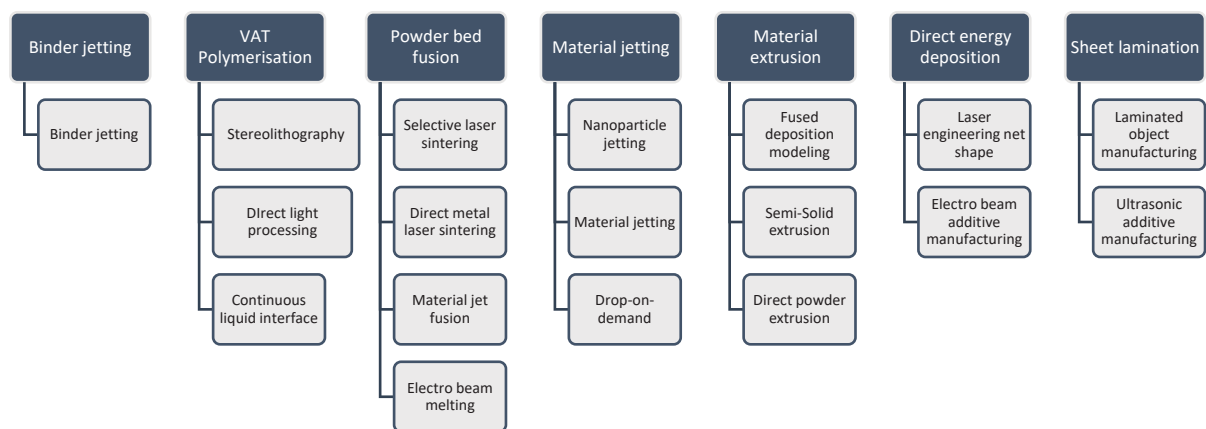

Figure 7: Categorization of the different 3D printing technologies according to ASTM Standard F2792 [148].

The following sections elaborate on the 3DP technologies used for 3D printed pharmaceuticals.

A.3.1.1 General Process

Generally, 3DP is referred to as an additive process that builds an object layer by layer. The desired object is first designed in a computer-aided design (CAD) program (Figure 8a). With this program, the object's geometry can be designed precisely and the volume and surface area can be calculated in advance. If the designed shape meets the requirements (e.g., dose, SA/V ratio, swallowable form), the file is saved in an stl. (stereolithography) format. Afterward, the stl. file is loaded into a slicer program (Figure 8b). Then, it is divided into horizontal cross-sectional layers. Various settings now allow choosing temperature, speed, and accuracy (layer height and extrusion width), as well as the print sequence to be

used for printing. This information is rewritten into a G-code, a computer numerical control programming language, so that the commands tell the printer to which position the nozzle should move and how much material should be fed out of the nozzle to print the desired object (Figure 8c). This sequence of steps is independent of the printing technique. The different types of 3DP processes mainly differ in the material processing, the state of aggregation (excipients and 3DP object), the temperature used, and the printing process.

(a)   (b)   (c)
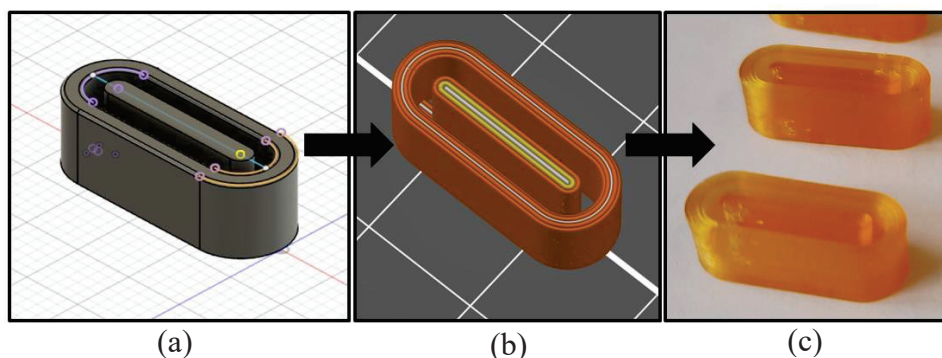
Figure 8: Creation process of a 3D printed object: a) object design with a CAD program; b) slicing the object, setting the printing parameters, creating a G-code; c) the desired object is printed with the selected material.

A.3.1.2 Stereolithography

The stereolithography (SLA) process was developed in 1986 by Charles Hull as the first commercially available 3DP method for manufacturing various solid geometries and objects [149]. In SLA 3DP, liquid resin is solidified by photopolymerization through a radical polymerization at the selected coordinates, triggered by a focused laser beam [127,146,150]. A tank is filled with the appropriate resin, in which a movable build platform is integrated. The previously generated G-code provides the information for the designed print object and gives the laser-print head the coordinates, laser speed (mm/s), and laser power (mW). After photopolymerization has taken place and the first layer of resin has solidified, the build platform is lowered in height by one layer and laser scanning is repeated until the 3D object has been built. Subsequently, excess resin often has to be removed with solvents [142,151,152].

One of the advantages this method offers is the resolution. SLA allows a resolution of up to 0.20 μm, while other 3DP processes have an average resolution of 50-200 μm [151–154]. Furthermore, since powder mixture is not used, the flow properties of the raw materials are irrelevant. In addition, the thermal stress during printing is low, which is advantageous for thermosensitive APIs. Nevertheless, this process has some weak points, too. Few

polymers are suitable for the SLA technique, as most of them are not generally recognized as safe (GRAS). Most of these polymers are designed for engineering purposes. Thus, they have resistant and tough structures, which are not desirable for oral medicines due to the risk of passing sharp tablet fragments into the gastrointestinal tract. In addition, residual monomer substances and photo initiator molecules may get entrapped in the photopolymerized geometry, which can become cytotoxic when leached from the structure and lead to uncontrollable and unpredictable effects. The photosensitivity of the resins may cause stability problems during the storage of the solid oral dosage forms, resulting in quality changes. Since the APIs are often poorly soluble to insoluble in the polymers, sedimentation and inhomogeneous distribution of the materials can occur. In addition, commercial printers often allow working on only one polymer at a time and in only large quantities, resulting in a high wastage of resin and, consequently, some economic and environmental discrepancies [135,146,152].

This technique has been used to print not only medical devices such as hearing aids [155] but also microneedles for insulin skin delivery [156] and a printed insert for bladder disease [157]. In a study, Robles-Martinez et al. printed a polypill with six different APIs with a modified release for a solid oral dosage form and an ibuprofen-loaded hydrogel [158,159]. The SLA technique is also frequently used for tissue engineering [160,161] and dental applications [162,163].

A.3.1.3 Powder Bed Printing

A.3.1.3.1 Selective Laser Sintering

In 1990, the selective laser sintering (SLS) process was developed and patented by Deckard and Beaman [146,164]. Similar to SLA 3DP, the SLS 3DP process also uses a focused high-energy laser beam. Polymer powder or a mixture of different polymers and API components is placed on a build platform (powder bed or print bed) and heated to temperatures just below or at the melting point of the used polymer [15]. The laser beam follows the commands of the G-code and heats the powder surface on the build platform above the melting point of the polymer in the predetermined pattern. The individual powder particles sinter, melt and fuse, forming a solid first layer. Subsequently, the build platform is lowered by one layer, and a new layer of powder is deposited. This procedure is repeated layer by layer until the desired object has been completely built up [127,165]. In the G-code, besides the coordinates of the printed object, laser power (W), laser focus on the powder bed, and

the laser speed (mm/s) can be specified, impacting the resolution of the printing process (particle size of the raw materials used and precision of the laser) and the mass variation of the printed oral dosage form (speed of the laser) [166]. Furthermore, the porosity of the printed object can be influenced by the printing speed. Since only individual, predetermined areas on the build platform are sintered and the rest are left as powder, these remnants can be removed after the printing process is completed. One advantage the SLS 3DP process presents is that it is a one-step process, which means that the raw material is manufactured directly into the final dosage form [167]. This is particularly beneficial for fragile APIs and is economical and time-saving. In addition, no further solvents are needed in the process, reducing toxicity. Moreover, there is no need for a drying step. Additional supports are not needed when constructing the object, since the powder bed is always completely refilled and thus no overhangs can occur. However, this is also disadvantageous since the unused material has to be discarded and hollow geometries cannot be formed without powder inside the interior. In addition, the heating of the material and the high energy input of the laser beam can lead to the degradation of the APIs [127,135].

Research groups are trying to develop new polymers and release profiles. Due to the porous structure, SLS 3DP is suitable for developing rapidly disintegrating tablets and, thus, for good water-soluble APIs an immediate release dosage form. Often, orodispersible tablets (ODTs) are investigated with this 3DP process, disintegrating within four seconds [152,168,169]. In 2020, Awad et al. printed orally disintegrating `printlets` with Braille and Moon patterns on their surface for visually impaired patients to identify their medications [170,171]. Fina et al. demonstrated the approach of adjusting the tablet design by creating a gyroid lattice and bi-layer constructs to achieve an individualized drug release profile [169]. With the high porosity and the rapid disintegration time associated with it, the SLS 3DP process is suitable for printing small dosage forms for children and the elderly with swallowing difficulties. The dosage forms can disintegrate directly in the mouth and be swallowed with the saliva [172]. To increase compliance in patients, the surface structures of the tablets could be improved, as they are quite rough and can affect the tablets' acceptability. This technique is also used for the creation of dental implants, knee implants and tissue scaffolds [173–175].

A.3.1.3.2 Powder Bed Ink-Jetting (Binder Jetting)

Similar to the SLS 3DP process, powder bed ink-jetting uses a print bed of a polymer powder, such as hydroxypropyl cellulose or microcrystalline cellulose [176]. However, instead

of a laser beam, this technique employs a solution with a binding agent to bind the individual powder particles. With this solution, the specified coordinates provided by the G-Code are moved with the print head and the powder is wetted with the solution at the designated points. Afterward, the print bed is lowered, a thin layer of powder is applied again, and the process is repeated until the object has been printed [146,152,176]. The powder bed ink-jetting process does not require any support structures for printing, but it also does not allow the printing of hollow objects. Due to the non-heat-intensive nature of this process, this technique is also suitable for thermosensitive and thermolabile APIs. These can be dissolved in the binder solution or used as powder as part of the powder bed [177]. If the APIs are dissolved in the binder solution, a very low API concentration can be achieved in tablets (e.g., hormones, highly active drugs). Since the solution usually consists of organic solvents, the APIs must be compatible with them. However, since a powder surplus is used, the remnants are disposed of after printing, which can lead to high costs with expensive APIs and input materials, as well as cause pollution. Therefore, these materials must be disposed properly or reused. The precision of the process depends on the particle size of the powder, the powder flowability, as well as the flow behavior of the solution through the nozzle [178]. Depending on the properties of the solution, the nozzle may clog, resulting in printing errors. If the API is incorporated into the solution, incorrect dosing can occur.

This 3DP process was developed at the Massachusetts Institute of Technology in the early 1990s by Michael Cima and Emanuel Sachs [179,180]. Because of the many materials that can be used in this process, this technique is suitable for a variety of applications in many fields: dentistry, the automotive industry, and the pharmaceutical field for medical devices and pharmaceuticals. Due to the porous structure of the printed objects, the resulting tablets often have a fragile structure and a high friability, which often fails to meet the requirements of the friability test of the European Pharmacopoeia (2.9.7) [181,182]. The choice of the polymer and the geometry of the printed tablet can control the release of the API with erosion and diffusion API release mechanisms [183,184]. Tuning the tablet properties and microstructural design with different porosity degrees can achieve varying erosion and API releases [185]. However, due to the porous structure of the printed objects, this 3DP process is preferable for fast-disintegrating dosage forms. In 2015, the first 3D printed drug "Spritam" (Levetiracetam, made by Aprecia Pharmaceuticals) made with the ZipDose® technology was approved by the U.S. Food and Drug Administration (FDA) using this process. The highly porous structure of the tablet made rapid disintegration possible in an

average of 11 seconds, enabling a rapid onset of the action of the antiepileptic drug [186,187]. The porous structures of tablets often result in a rough surface, which can be further modified (e.g., with coating) after the printing process to increase acceptability in patients [188–190].

A.3.1.4 Melt Extrusion Deposition, Direct Powder Extrusion

Melt Extrusion Deposition (MED) was invented in 2015 by Triastek, Inc., an international pharmaceutical company [191], as a direct powder extrusion 3DP technique [192]. In this process, a powder mixture with an API is transported via a small hot-melt extruder included at the top of the print head to the nozzle, where it is melted and deposited layer by layer on the print bed, as per the desired design [135,191]. This single-step process bypasses the production of filaments, which are necessary for the Fused Deposition Modeling (FDM) process, thus saving both time and thermal stress for the APIs and excipients. Melting the powder mixture in the nozzle makes it possible to produce an ASD and, thus, convert poorly soluble APIs into a better soluble form, which the body can absorb more quickly [193]. In 2020, the U.S. FDA included the MED process in its Emerging Technology Program (ETP). With this technology, a wide variety of release profiles and controlled release onset times and durations can be realized due to the different polymers that can be used in this process and the possibilities of working on various geometry designs with compartments [192]. In April 2022, Triastek Inc. got approval for an Investigational New Drug (IND)-application by the U.S. FDA for T20 with 3DP formulation by design (3DFbD®). This drug is intended for the treatment of cardiovascular and blood clotting disorders and this 3DP product is to be administered only once per day, made possible by the programmed release technology of Triastek, Inc. [194].

A.3.1.5 Pressure Assisted Micro Syringe Printing (Semi-Solid Micro Extrusion)

This 3DP process was invented by Landers and Mülhaupt in 2000. In it, viscous pastes, suspensions, emulsions, nanocrystalline materials and gels can be used and printed in a layer-wise manner through mechanical, solenoid-based or pneumatical extrusion out of a cartridge or a syringe containing a nozzle with a given diameter, mostly depending on the viscosity of the printing formulation [15,134,195–197]. The syringe may be provided with a temperature-controllable jacket to affect the viscosity of the formulation. On the print bed, the predetermined coordinates in the x-, y-, or z- directions, as specified by the G-code, are traversed, dispensing the desired amount of the semi-solid compound. This is set

via a motorized plunger, piston, or pressurized air (normally at 3-5 bar) [146,198]. After the first layer has been printed, the print bed is moved down by one layer in the z-direction, or the print head is moved up one layer and the process is repeated until the desired object has been finalized. The selected formulation must have special quality attributes (QA) for this process: the viscosity should be known, and the diameter of the nozzle should be chosen accordingly to ensure a continuous flow [199,200]. Moreover, the particle size of the formulation should be considered regarding the diameter of the nozzle. Furthermore, the solidification behavior of the compound should be fast - otherwise, the object could collapse. Since solvents are used in the production of the formulation, these should be subsequently removed in a drying step [137]. This can lead to large pores in or even shrinkage of the printed object [137,201]. In addition, the drying step can take up to 48 h at 40°C and stress the APIs, which could lead to degradation. According to Ph. Eur. 2.4.24., the content of the residual solvents should be determined. If water was used in the formulation, it should also be removed as it could cause a hydrolytic reaction of the API as well as microbial growth [152,202,203]. The advantage of this 3DP process is that it exerts little or no thermal stress on the API, making it suitable for thermosensitive APIs, when a long drying step at a high temperature is not required. Since pastes can also be printed, the drug load can be increased up to 80% API [204]. However, depending on the particle size and viscosity, the nozzle size may need to be adjusted, reducing the resolution and precision of the print [137,146,195,196].

This technology can be used to print oral dosage forms such as tablets [15], gums [205], ODFs [206], polypills [202,207] and self-microemulsifying drug delivery systems (SMEDDs) [143,208], as well as parental applications such as bone-scaffolds [209], implants [210], inserts [137], but also wound dressings [211] and suppositories [208]. This 3DP technique can also be used for bioprinting since it can be used to print living cells, for the realization of printed organs and living tissue, e.g., multi-layered skin, tracheal splints, and heart tissue [212,213] .

A.3.1.6 Fused Deposition Modeling

The FDM or Fused Filament Fabrication (FFF) 3DP process is the most studied 3DP process for pharmaceuticals. It was developed and introduced by Scott S. Crump in 1988 and patented by Stratasys in 1989. Since 2005, many cheap 3D printers have become affordable, so this process has become very popular [146]. Due to the low-cost equipment,

versatility, and possibilities that this process offers, many research groups and industries have dedicated themselves to this method for personalized medicine for several years. In this technique, a filament must be first produced using HME [138,141,214–218]. At the beginning of FDM 3DP, only placebo filaments were produced mostly via HME and impregnated afterward with an API solution [129,219]. Placebo-filaments used for impregnation can be purchased commercially, for example containing polylactic acid (PLA) and polyvinyl alcohol (PVA), so the 3DP centre does not need an extruder. However, these filaments do not have a pharmaceutical grade. In addition, organic solvents are used in the impregnation process, which must later be removed with a drying step. Furthermore, since only small amounts of APIs ($< 2\%$) can be incorporated with this procedure, more drug-loaded filaments are directly produced using HME [138,214,216,220]. Nowadays, a powder mixture with a polymer and an API is prepared. Often, plasticizers and glidants are added to the mixture as well. The plasticizers can lower the melt temperature or glass transition temperature (T_G) and, thus, reduce the thermal stress for the API and makes the often hard and brittle filament more flexible, which is advantageous for FDM 3DP. If particle sizes of the raw materials are not homogeneous enough so that segregation can occur, or if the materials do not flow well, it is possible to process the mixture into granules beforehand and then process these into filaments via HME [216]. It is also possible to dissolve the API and add this solution to the powder mixture in the extruder via a port. The temperature in the extruder is adjusted to the T_G of the polymer and, depending on the melt temperature of the API, the API is dissolved or suspended in the filament. This allows the production of an ASD and improvement of the solubility of the API [221–223]. In the extruder barrel, the powder blend is kneaded and transported by certain screw elements of single- or twin-screws. The molten mass is carried out of the extruder through a nozzle or a die and removed by a conveyer belt. The nozzle's size and the conveyor belt's speed influence the diameter of the filament. Usually, a diameter of 1.75 mm is aimed for. The produced filament is then inserted into the print head of the FDM 3D printer, where it is transported to the nozzle by conveyor wheels or counter-rotating gears. Due to this conveying mechanism, the filament needs to have certain QA. It must be somewhat flexible so that it can easily bend around the conveyor wheels and not break or crumble, but it must also not be too flexible; otherwise, it will wrap around the conveyor wheels, cannot be conveyed, and will not push the molten mass out of the nozzle like a piston [215]. This must be kept constant, otherwise dosing inaccuracies may occur. The nozzle is located in a heating element (hot-end) so that the filament in the nozzle is reheated and melted, which allows it to flow out

through the 0.05 – 2.0 mm opening (mostly 0.4 mm) and be deposited as a strand layer by layer on the print bed. The print bed can also be heated so that the strands deposited on it melt and adhere to the surface. With this, the subsequent layers can be precisely placed on top of each other, and the lower part of the geometry does not detach. The process parameters of the 3D printer can be used to influence the quality of the print. The adhesion of the material strands on the print bed can be modified by adjusting the bed and nozzle temperature as well as the speed of the moving print head. Depending on the flexibility, viscosity, and melt flow behavior of the filament, the conveying speed of the conveyer wheels can also be adjusted to ensure a constant melt flow.

The cost-effective FDM process enables the production of individual dosage forms of various shapes and infills (infill refers to the amount (%) of fill in a 3D printed object. An object with an infill of 0% is hollow and one with an infill of 100% is completely solid. The pattern of the infill can be varied) [130]. This allows variable dosing as well as modeling of different release profiles. By varying the geometry and, thus, the SA/V ratio, a wide range of dosages and dissolution profiles can be achieved with one formulation, i.e., one filament [128,136,145,224,225]. In the future, if good-manufacturing-practice (GMP)-compliant 3D printers are installed in community pharmacies or hospitals, it would be possible to meet the needs of a wide range of patients by purchasing only one drug containing filament. For children or patients with swallowing difficulties, smaller geometries could be printed. If an up- or down-dosing during the course of therapy is necessary (titration of the dose), this can also be reproduced with only one filament formulation by printing different geometries with various volumes [136,218,226,227]. By using multiple print heads working in parallel or multiple material units, printing polypills with multiple APIs and different polymers is possible [224,228,229]. This also allows the APIs incompatible with each other to undergo processing in one dosage form, since they are not contained in one filament, or the APIs can be released at different times or different release rates by choosing a variety of polymers. Consequently, the frequency of administration and the number of tablets required per day can be reduced, thus increasing patients' adherence and compliance. Of course, the FDM 3DP process also has disadvantages. Thermolabile APIs are not suitable for this process due to the extreme thermal stress the process generates (FDM has two heating steps: HME and 3DP, both mostly at >120°C) [230]. Currently, several research groups are trying to circumvent this problem by synthesizing new polymers with lower T_{GS} that are suitable for FDM 3DP [144,231,232]. The industrial production of the filaments under

GMP conditions with pharmaceutical-grade excipients requires a time-consuming intermediate step for the FDM process. However, it allows this intermediate step to be officially registered and approved so that there is a quality monitoring step before the personalized dosage forms are produced in hospitals and community pharmacies as a prescription, which cannot be officially approved due to the process. Nevertheless, formulation development and the HME process are complex procedures, especially when the required filaments must comply with critical QAs in terms of flexibility, stiffness, viscosity, water absorption and surface properties. Since the FDM technique is the most widely used process of creating pharmaceutical dosage forms in 3DP research, several drug delivery systems (DDSs) have already been developed. Most research groups are engaged in printing oral dosage forms like tablets or capsules, which have different release properties, such as immediate, gastro-retentive and pulsatile, or have multiple APIs incorporated into them [132,220,224,233–238]. However, oro-mucosal films (fast dissolving and mucoadhesive buccal films), os-motic tablets and microneedles have also been printed, as well as implants, vaginal rings, and dermal patches, for example for pancreatic cancer growth suppression [239–247].

A.3.2 Challenges and Limitations

Alongside the many benefits 3DP technologies provide, they also face challenges and limitations. First, the 3D printers currently mostly in use are only commercial machines that do not meet GMP requirements. Some research groups have already recognized this gap and are in the process of building and establishing GMP- and quality controlled (QC)-capable 3D printers [135,218,248,249]. The commercial 3D printers cannot be cleaned easily and completely to prevent cross-contamination. Otherwise, one 3D printer has to be dedicated to one product. In addition, no process analytical technologies (PAT) and in-process control strategies (IPC) are installed to monitor the process and ensure a certain quality of the product. For example, in FDM printing, the temperature, extrusion rate and mass could be continuously tracked throughout the process to establish quality by design (QbD) [250]. Thus, batch releases might require fewer tests, which would be advantageous for the small batch sizes made in community pharmacies and hospitals, since these places usually do not have the necessary equipment, time, and personnel to inspect the batches in detail. Trenfield et al. investigated a non-destructive method for printed tablet content determination using Raman and Near-infrared spectroscopy (NIR) [251]. Such a PAT could facilitate batch release and ensure quality. In addition, 3DP is often time-consuming and cannot be compared to a rotary tablet press, which produces 10,000 tablets per minute. The trend in the newer

3D printers is shifting toward having multiple print heads that can print simultaneously so that the printing time of a batch can be reduced. Furthermore, post-printing processes (e.g., drying) can impact the quality of the printed dosage form in terms of porosity, mechanical behavior or appearance and should be monitored and controlled accordingly.

In addition, the availability of excipients is limited, which corresponds to the pharma requirements. For health care applications and environmentally friendly conditions, the excipients should be non-toxic, biocompatible, erodible or biodegradable with non-toxic degradation products, stable, and meet the requirements of the 3DP technology to produce robust dosage forms.

One of the advantages of 3DP technology is that most devices are inexpensive to purchase. However, this is also a risk factor since anyone can quickly and easily get a 3D printer. Due to the variety of commercial filaments available on the market, the FDM printed drugs can be easily counterfeited. This 3DP process is particularly interesting for developing countries; due to the low-cost production and flexible dosage, a larger part of the population can be supplied with medicines and thus the health system can be strengthened. Currently, about 10% of the world's medicines on the market are counterfeit, in developing countries the percentage is even higher, at about 10-30% [252–254]. The falsified DDF usually contain no API, the wrong, or a reduced API content, so that the patient's therapy is at risk [255]. The most commonly counterfeited medicines include antibiotics, viral drugs or antimalarials (in developing countries), hormones, steroids, and antihistamines (in rich countries) [256,257]. A new traceability system (preferably directly in or on the DDF) is needed for personalized, tailored DDFs because they are not manufactured industrially on a large scale but individually in e.g., compounding centers and, accordingly, do not have serialized primary packaging [252]. Various research groups have discovered this gap and developed and tested different concepts that can be used to create an anti-counterfeit system [252,258–260]. For example, Trenfield et al. developed a track-and-trace system for 3D printed oral dosage forms. Using a combined 2D printing technology, QR codes and data matrices were printed on the surface of "printlets" and scanned with a smartphone [252,258].

Another hurdle is the approval process of 3D printed batches. Typically, a finished product is approved by regulatory agencies, with a statement of the underlying process, analytics, packaging materials, and in-vivo studies with a minimum of inter-batch variability with current chemistry, manufacturing, and control (CMC) standards, and other relevant

guidance. This is not possible for 3D printed medicines as they are produced on-demand by community pharmacies, compounding centers, or hospitals; do not have a fixed dosage as they are custom-made for the patient; and might have varying geometries and release profiles. In addition, no in-vivo studies are conducted on the finished product, as a batch is made for an individual patient [135]. For 3D printed medical devices and prosthetics without drug delivery function, the U.S. FDA published and approved a technical guidance in 2017 [261]. The raw materials used in the processes must of course comply with certain grades (e.g., Ph. Eur., USP). In FDM 3DP, the industrially produced intermediate, the filament, can meet certain regulatory requirements and be approved so that it can be further processed in pharmacies. This would mean additional quality assurance. The 3D printed medicine approved to date are not used for personalized medicine but are pre-produced on a large scale with given dosages and are accordingly approved using the standard process. This gap in the regulatory framework is known to the authorities, and guidelines for this procedure are being worked on. Recently, the FDA published a discussion paper for distributed manufacturing (DM) and point-of-care (POC) manufacturing in October 2022 [262]. It is intended to get input and public feedback from stakeholders outside the agency. The document discusses aspects such as how to proceed with possible inspections of DM and POC units, or how to deal with possible site-change regarding demonstration of bioequivalence, method transfer, and validation. Also, the question of the responsibility of medicine manufacturing POC units is addressed and the assurance of quality standards in POC units, as well as the circumvention of cross-contamination and approval process for manufactured drugs with a range of dose. This information and input will be considered in the development of future regulatory guidelines. These and other unanswered questions, such as which 3DP technologies can be approved, how can the in vivo studies be bypassed, and who is ultimately responsible when raw materials or intermediates are further processed in pharmacies, must be considered and answered in order to officially establish the 3D printing process in healthcare [263].

Another critical issue that must be considered is the patient acceptability of the 3D printed oral dosage forms. While the tablets can be customized in size and shape specifically for a patient, the FDM-, MED-, and SLS-printed tablets look particularly different from compressed tablets and may cause discomfort in swallowing. Some studies have been conducted on the acceptability of printed tablets [188]. If a patient shows scepticism about the innovative form, a trained dispensing pharmacist should ease the patient's fear. Since a film

coating would entail a further process step that cannot be carried out in this way in the pharmacy, this approach would not be expedient. If the API-containing layer tastes bitter or looks "unattractive", a placebo coating can be printed around the actual tablet that tastes neutral and is accepted by the patient in terms of color and structure.

A.3.3 Current Commercial Status of 3DP in Personalized Medicine

With 3DP, the supply of medicines and medical devices could be much faster and more widespread. Many different pharmaceutical companies are trying to gain a foothold in the field of this technology, and newer companies have also formed to rapidly develop this area. In 2015, the company Aprecia managed to get the world's first 3D printed tablet, Spritam®, Levetiracetam, approved by the FDA using Zip-dose technology via binder-jet printing. The tablet has a high drug- load (up to 1000 mg) and rapidly disintegrates. Although the tablet was produced using a new process, the manufacturing is not performed on- demand, instead, it is being produced on a large scale so that approval can be obtained through the standard route [264]. FabRx Ltd., a start-up biotech company founded by leading academics at University College London with profound knowledge in 3DP, has made some discoveries in the field of HME, 3DP [127,129,172], pharmaceutical 3D printers (M3dimaker™), software programming (M3diseen [265]), analytics, and formulation development [251,258]. Digital Health Systems GmbH (DiHeSys), an innovative company and health care provider, also focuses on the production of personalized pharmaceuticals, especially in the area of 2DP and 3DP. Here, too, a GMP- compliant FDM 3D printer is under development. In Germany, the *Federal Ministry for Education and Research* (German: Bundesministerium für Bildung und Forschung, BMBF) has focused on various applications of polymers, including 3DP with the project framework - ProMatLeben - "Polymere", in a wide variety of areas, such as implants, powder molding, electrospinning, bone replacements, and prosthesis. The "Innopoly" project uses biodegradable polymers for additive 3DP FDM, printing jaw implants [266]. The "Poly-IMPLANT-Druck" project team has explored the application of an industrial laser-based nano- 3DP process for hierarchically structured polymer-based cartilage-bone implants. The aim was to develop a nano-3DP process for the production of biphasic implants on an industrial scale with specifically adjustable geometric and mechanical functions for cartilage-bone therapy. The intention behind adding bioactive fillers and surface layers to the printed 3D constructs, is to realize the biological properties of natural cartilage-bone matrices [267]. The "PolyPrint" project team was tasked with producing printable polymer-drug filaments for individual

oral drug dosage forms. For this purpose, new polymers have been synthesized, methods were developed for characterization and various oral dosage forms for personalized medicine were printed using the FDM 3D printing technique [136,145,216,218,224,268–270]. This work comprises part of that project.

In 2019, FabRx Ltd. completed the world's first in-human clinical study (a single-center, prospective crossover experimental study) using their proprietary Printlets™ technology in a hospital setting, which relies on personalized 3DP dosage forms to treat children suffering from maple syrup urine disease [271]. Currently, the pharmaceutical industry lacks suitable oral treatments which is why 3DP is particularly useful here. The aim was to improve the safety and acceptability of isoleucine supplementation. The conventional capsule dosage form was compared against the 3DP chewable formulation by examining the children's isoleucine blood levels. In addition, the acceptability of the 3D printed forms was investigated with different flavors and colors. It was found that with the 3D printed form, the mean levels were closer to the target value with less variability and the 3D printed forms were well accepted.

A.4 Outlook for Personalized Medicine – Where Do We Go?

The various 3DP technologies enable the production of a wide range of medicines with varying porosity, appearance, release, and disintegration behavior. Due to the cost-effective and compact equipment involved in it, the production of 3D printed pharmaceuticals is possible in many places: community pharmacies, hospitals, industries, or contract manufacturers. With how easily 3DP produces different dosages and release profiles, the technology can produce clinical samples as well as dosage forms for use in areas with poor drug supply, like low- or middle-income countries, disaster zones, or outer space [272,273]. The formulation and the polymers utilized can influence which drug substance is to be released from the matrix and made available to the body for absorption. In clinical studies, initial investigations of new drugs are being carried out using experimental and animal models (mostly rodents), investigating efficacy profiles, and evaluating safety and pharmacokinetic behavior [274]. These studies are necessary to conduct the first clinical trials in humans, to determine dose regimens and to identify possible side effects. Mostly, small formulations such as mini-tablets, small capsule sizes, and liquid formulations are used on animals or humans, but these are usually inflexible in dose, time-consuming to manufacture, expensive, and they produce a lot of waste. For these requirements, 3DP offers plenty of flexibility; the dosages as well as the geometries can be easily changed without having to modify the formulation. In addition, the release profile can be quickly amended via the design of the DDF. Because of the cost-effective equipment and ease of handling, lab staff can quickly address needed changes and produce small batches on-site. However, this flexibility must be taken into account in the clinical studies and considerations must be made on how to adapt the dosage form to the patient's individual needs.

Furthermore, drug modeling and targeting is also becoming more and more present in the synthesis of the APIs, with protective groups or markers being added to drugs so that the APIs reach their site of action in a targeted manner and thus trigger fewer side effects. If this is combined with a dosage form that can be flexibly designed, therapy can be further customized and improved. Digitalization is also advancing more and more in modern medicine. The electronic patient file has been under discussion for several years. This will make it easier for both doctors and pharmacists to find the right treatment for a patient and prevent interactions. Digitalization can also make diagnoses faster, easier, and more accurate by matching patient data recorded worldwide. Artificial neural networks (ANN) may help in this. ANN consist of so-called artificial neurons (algorithms) that are able to sense and

interpret nonlinear processes. The input- and output-layers are interconnected via hidden layers that are capable of recognizing and extracting connections and patterns in data. In the process, the main features are extracted and functional relationships between the patterns are deliberated [275]. The ANN learns through continuous operation, not programming. The result is formed through the output layer. To build an ANN, a sufficiently large set of experimental data is needed as input. The connections and algorithms change their weights and links, critical parameters are identified, and the process is interpreted. A network is trained, validated, and tested with the experimentally obtained data so that there is confidence that its calculations and predictions can be relied upon [276]. ANNs are currently also being intensively investigated for 3DP. It has been found that with such databases, the extrudability, printability, viscosity, and release rates of formulations can be predicted [277–283]. In precision medicine, artificial intelligence is here to stay. Networking, collecting, and sharing volumes of data across countries and comparing the data quickly and cost-effectively help in making diagnoses, as well as therapeutic approaches and outcomes, and can thereby improve therapeutic success and reduce side effects. Because of the large amounts of data, ANNs can be used to make predictions in many areas, saving time, money, and energy.

With the developments that are taking place in the diagnosis and therapy, the synthesis of new substances, and the development of new dosage forms to treat a patient in the best possible way, to reduce adverse effects and increase therapy adherence and compliance, it may be possible to treat patients better, which will alleviate and shorten the course of the disease and increase life expectancy.

A.5 Future Application of Personalized Medicine in Parkinson's Disease

A possible application of personalized medicine could be the therapy of Parkinson's disease, since in this medical treatment special attention must be paid to the individual reactions of the patient to the drugs, highly potent APIs are administered and, over time, the adverse effects become more and more present during the therapy. Approximately one percent of the world's population over the age of 60 is affected by Parkinson's Disease, the second most common neurodegenerative disease in the world after Alzheimer's Disease [284,285]. Disease-related progressive degeneration of dopaminergic neurons in the substantia nigra leads to an imbalance in the transmitter system, resulting in dopamine deficiency and acetylcholine excess [224,286–288]. The primary symptoms of akinesia and bradyphrenia result from dopamine deficiency; rigor and tremor are consequences of the disinhibited cholinergic system [224]. As time progresses, symptoms increase and show a gradual progression associated with various motor, behavioral, and psychological disabilities [224,289]. To date, there is no cure, only symptomatic treatment. The disease can be diagnosed at a young age, as well as in older people. There are many different drugs that are used for therapy, but they must be individually adapted to the Parkinson's patient, because the course of the disease is different for each person. Levodopa (always prescribed in combination with dopamine- decarboxylase inhibitors (DDI, e.g., benserazide, carbidopa)) is the state-of-the-art therapy for patients >70 years of age. With this API, the symptoms are well controlled, but side effects set in after a short time interval of treatment and the therapeutic index becomes increasingly narrow. As the disease progresses, phases with good mobility (ON phases) and phases with low mobility (OFF phases) occur more frequently. Other non-motor disabilities and psychological changes may also occur. Due to this, the dosage of the API, combination of different APIs, and the intake intervals of the medication are constantly adjusted. Likewise, after a while in treatment, resistance to the API occurs, so that the dose must be continuously increased (Figure 9). Often dopamine agonists (DA, e.g., pramipexole, ropinirole) are chosen for a combined therapy. DA as mono therapy are the drug of choice for patients < 70 years of age [224,290]. However, even these young patients have to add levodopa + DDI after a certain period of time, because as the disease progresses, the effect of DA is not sufficient.
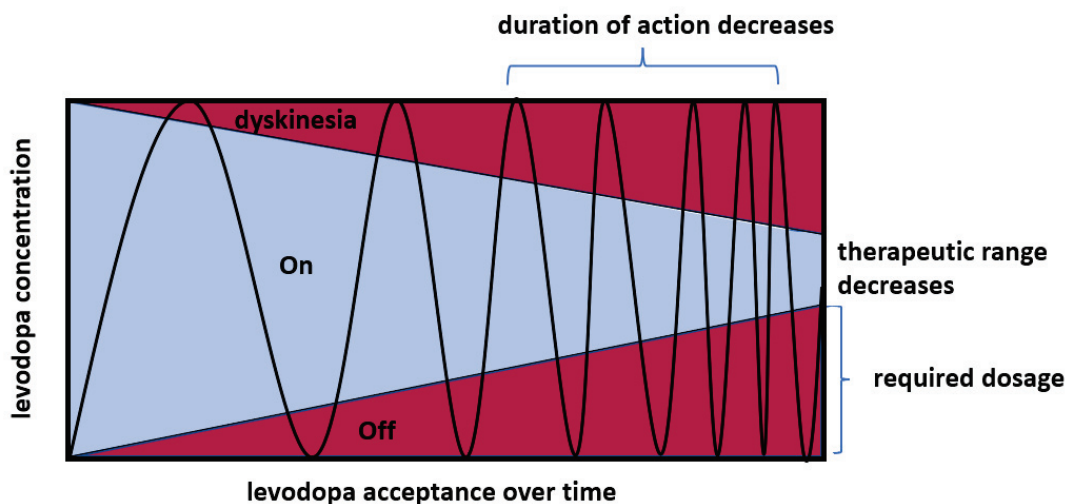
Figure 9: Schematic representation of the course of long-term levodopa therapy. Habituation to levodopa increases, with the consequence that a dose increase is necessary. The therapeutic range becomes smaller, due to which on-off fluctuations and dyskinesias occur [289].

Because of this progressive disease, limited patient motility, and large age range of the patients, personalized medicine is desirable for this disease. Since no cure exists, efforts should be made to preserve the quality of life of patients as much as possible with the available resources. Personalized medicine can also consider the existing dysphagia, prolonged gastric retention times, and different stages of the disease and improve compliance.

A.5.1 APIs Used for Personalized Medicine for Parkinson's Disease Treatment

Levodopa (Figure 10) is one of the drugs used to treat movement disorders in Parkinson's disease [290–292]. The API is a prodrug; it is converted to dopamine in the brain and is thus intended to compensate for the dopamine deficiency. The initial dose is 100 mg of levodopa once or twice daily. Every 3rd to 7th day, the dose should be increased until a maximum daily dose of 800 mg of levodopa is reached [224]. To prevent degradation of levodopa to dopamine in the body periphery, prior to passage of the blood-brain barrier, it is combined with either a DDI (carbidopa, benserazide) or a catechol-O-methyltransferase-inhibitor (entacapone, tolcapone). Levodopa and
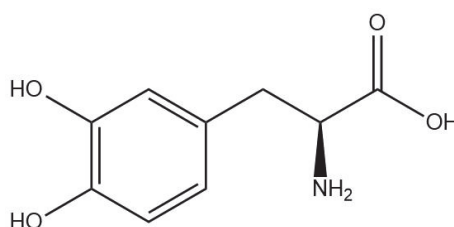
Figure 10: Chemical structure of levodopa. (Created with ChemDraw Version 21.0.0.28).
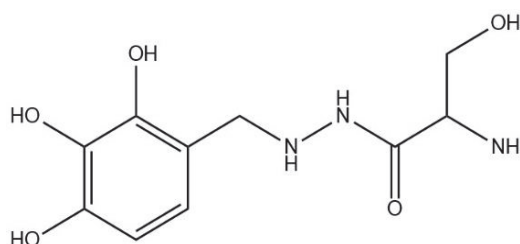
Figure 11: Chemical structure of benserazide. (Created with ChemDraw Version 21.0.0.28).

benserazide (Figure 11) are dosed in a 4:1 combination. The API levodopa is only absorbed in the upper section of the small intestine via amino acid transporters, which is why a wide variety of dosage forms exist on the market (e.g., floating DDF) that take the small absorption window into account. The dose of the API combination must be strictly monitored and constantly adjusted, since too low a dose will not free the patient from his body rigidity, and too high a dose can also lead to dyskinesia [224,291–293]. In addition, the dosage must be slowly titrated at the beginning of the pharmacotherapy and phased out when discontinuing the drug so that no withdrawal symptoms occur. Both levodopa and benserazide belong to BCS class I, so both are highly soluble and have high permeability properties.

Pramipexole (Figure 12) belongs to the group of DA and can be administered as monotherapy, but also in combination with levodopa [216,224,294]. The dopamine receptor agonist has high selectivity for the $D_{2/3}$ dopamine receptor and is thought to reverse the dopamine deficiency prevalent in Parkinson's disease. The lowest dose of a tablet on the market is 0.088 mg. The starting dose for monotherapy is 0.26 mg of pramipexole per day (equivalent to 0.375 mg of pramipexole dihydrochloride monohydrate,
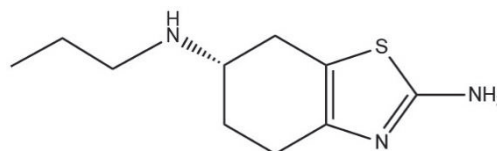
Figure 12: Chemical structure of pramipexole. (Created with ChemDraw Version 21.0.0.28).

PDM) which can be increased to a maximum dose of 3.15 mg per day (equivalent to 4.5 mg of PDM). At weekly intervals, the dose may be increased by 0.52 mg [224,290]. Pramipexole is standard therapy for patients < 70 years of age. The high-potency API must be dosed precisely to the patient to avoid triggering adverse effects. These include sleep attacks, as well as impulse control disorders. PDM is a highly soluble API and has good permeation properties, so it can be assigned to BCS class I [295,296].

A.6 Aims and Outline of the Thesis

As discussed in Section *A Introduction*, the FDM 3D printing process offers many opportunities for personalized medicine. In addition to varying dosages and release profiles, this process offers the advantage of creating polypills and the need for increased security for traceability. Due to the flexibility and versatility in terms of dosage and geometry of the DDF, dose-independent release should be considered. In other words, the release of the API from the DDF is independent of the dosage or strength of the drug and remains unchanged. Based on these characteristics, the following aims of this thesis were formulated. The advantages of FDM 3D printing should be transferred to personalized therapy using oral dosage forms. The principle of dose-independent release should be tested and a model for this approach should be developed. A polypill should be designed with different formulations and doses of filaments, resulting in varying API release, using Parkinson's disease therapy as an example. To close the gap in anti-counterfeiting, the possibility of a traceability concept for 3D printed oral dosage forms should be implemented.

The thesis is divided into five parts:

- Introduction (Section A)

- Overview: Quality of FDM 3D Printed Medicines for Pediatrics (Section B)

- Prediction of Drug Release Characteristics and 3DP Drug Dosage Form Design (Section C)

- Drug Dosage Form Design for Personalized Therapy with 3D Printed Oral Dosage Forms (Section D)
- Traceability Concept (Section E)

An overview of pharmaceutical and engineering considerations for FDM 3D printed dosage forms for personalized medicine for pediatrics is presented in Chapter B. The necessary properties of filaments for FDM 3D printing will be discussed and possible PAT for HME will be investigated. The 3D printed dosage forms for children developed to date will be outlined together with the changes in characterization of the new printed dosage forms associated with the innovative technology. In addition, the design of a GMP-compliant FDM 3D printer will be discussed.

> ➤ A review article on the quality of 3D printed pediatric dosage forms is presented in Section B. *Review: Quality of FDM 3D Printed Medicines for Pediatrics:*

> *Considerations for Formulation Development, Filament Extrusion, Printing Process and Printer Design.*

One of the advantages of FDM 3D printing is that many different geometries can be realized, with which different dosages and SA/V ratios can be implemented. Due to the influence of the SA/V ratio on the release behavior, the release of the API can also be influenced and specifically adapted to the patient. To predict the release behavior of the printed solid oral dosage forms, the obtained release profiles of different SA/V ratio should be described with mathematical formulas. Via a possible correlation, the resulting release curve is to be predicted based on the SA/V ratio. To select a suitable release rate and appropriate 3DP DDF design for a formulation, a predictive model should be designed. On this basis, when prescribing a printed dosage form, the required SA/V ratio for the DDF is to be selected via the required amount of API, SA, and the release time. To investigate a state-of-the-art approach, an ANN should be created using this data to test whether an artificial intelligence can assist in the design of the DDF geometries.

➢ Prediction of the release profiles from 3D printed oral dosage forms using MDT and descriptive mathematical models is presented in Section C.1: *Predicting Drug Release from 3D Printed Oral Medicines Based on the Surface Area to Volume Ratio of Tablet Geometry*.

➢ Investigations to predict the desired geometry using ANN is presented in Section C.2: *Investigations into the Use of Machine Learning to Predict Drug Dosage Form Design to Obtain Desired Release Profiles for 3D Printed Oral Medicines*.

Based on the concept that the SA/V ratio can be used to determine the release profile, a concept should be developed for a dose-independent drug release. This could allow multiple dosages to be served with only one formulation or filament, but the release profile would not change and thus continue to be appropriate for the particular patient. To be able to supply as many patients as possible with one formulation, a model for dose-independent release should be developed. The general dose-independent release approach should be implemented for Parkinson's disease patients. Due to the difficult therapy, the dosages have to be adjusted for the patients. In addition, the drug levodopa is only absorbed in the upper section of the small intestine, which should be taken into account in the development of the DDF. In the later course of therapy, other drugs are combined, e.g., DA, (e.g., pramipexole).

These APIs should be processed into a polypill using FDM 3D printing technique. To ensure that all APIs can be accurately analyzed during dissolution testing, a suitable analytical method must be developed that is able to reflect the respective content of the API released, regardless of the concentration used.

> ➤ A new representative dose-independent release approach is presented in Section D.1: *Dose-independent Drug Release from 3D Printed Oral Medicines for Patient-specific Dosing to Improve Therapy Safety.*

> ➤ The development of an analysis procedure for the parallel determination of levodopa, benserazide, and pramipexole is presented in Section D.2*: Embedding a Sensitive Liquid-Core Waveguide UV Detector into an HPLC-UV System for Simultaneous Quantification of Differently Dosed Active Ingredients during Drug Release.*

> ➤ The development of a 3D printed mini-floating polypill for Parkinson's disease therapy is described in Section D.3: *3D Printed Mini-Floating-Polypill for Parkinson's Disease: Combination of Levodopa, Benserazide, and Pramipexole in Various Dosing for Personalized Therapy.*

Due to the availability of cost-effective printers, the risk for falsified medicines increases for 3D printed dosage forms. To increase the safety of 3D printed drugs and counteract counterfeit drugs, an approach should be implemented to mark the printed tablets with blind watermarking.

> ➤ A proof-of-concept of a blind watermarking approach for 3D printed oral dosage forms is presented in Section E: *Blind-Watermarking—Proof-of-Concept of a Novel Approach to Ensure Batch Traceability for 3D Printed Tablets*.

These objectives are to explore the benefits of FDM 3D printing for personalized medicine, and to highlight the weaknesses and limitations of the process.

References

[1]   Weltbevölkerung 2022 - Weltbevölkerungsuhr, (2022). https://countryme-ters.info/de/World (accessed June 25, 2022).

[2]   R. Hodson, Precision medicine, Nature. 537 (2016) 49. https://doi.org/10.1038/537S49a.

[3]   E.A. Ashley, Towards precision medicine, Nature Reviews Genetics. 17 (2016) 507–522. https://doi.org/10.1038/NRG.2016.86.

[4]   F.S. Collins, H. Varmus, A new initiative on precision medicine, New England Journal of Medicine. 372 (2015) 793–795. https://doi.org/10.1056/nejmp1500523.

[5]   S.J. Balevic, A.C.P. Sagcal-Gironella, Precision medicine: Towards individualized dosing in pediatric rheumatology, Rheumatic Disease Clinics of North America. 48 (2022) 305–330. https://doi.org/10.1016/J.RDC.2021.09.010.

[6]   J. Breitkreutz, J. Boos, Paediatric and geriatric drug delivery, Expert Opinion on Drug Delivery. 4 (2007) 37–45. https://doi.org/10.1517/17425247.4.1.37.

[7]   M.A. Hamburg, F.S. Collins, The path to personalized medicine, New England Journal of Medicine. 363 (2010) 301–304. https://doi.org/10.1056/NEJMp1006304.

[8]   S.H. Oh, S.J. Lee, J. Park, Precision medicine for hypertension patients with type 2 Diabetes via reinforcement learning, Journal of Personalized Medicine. 12 (2022) 87–102. https://doi.org/10.3390/JPM12010087.

[9]   S.A. Dugger, A. Platt, D.B. Goldstein, Drug development in the era of precision medicine, Nature Reviews Drug Discovery. 17 (2018) 183–196. https://doi.org/10.1038/NRD.2017.226.

[10]   J.H. Ryu, S. Lee, S. Son, S.H. Kim, J.F. Leary, K. Choi, I.C. Kwon, Theranostic nanoparticles for future personalized medicine, Journal of Controlled Release. 190 (2014) 477–484. https://doi.org/10.1016/j.jconrel.2014.04.027.

[11]   F. Bono, C. Missale, C. Fiorentini, Induced pluripotent stem cells for defining Parkinsonian patient subtypes: a further step toward precision medicine, Neural Regeneration Research. 17 (2022) 767–769. https://doi.org/10.4103/1673-5374.322448.

[12]   K.B. Johnson, W.Q. Wei, D. Weeraratne, M.E. Frisse, K. Misulis, K. Rhee, J. Zhao, J.L. Snowdon, Precision medicine, AI, and the future of personalized health care, Clinical and Translational Science. 14 (2021) 86–93. https://doi.org/10.1111/CTS.12884.

[13]   M. McCarthy, E. Birney, Personalized profiles for disease risk must capture all facets of health, Nature. 597 (2021) 175–177. https://doi.org/10.1038/d41586-021-02401-0.

[14] M.B. Ayalew, H.G. Tegegn, O.A. Abdela, Drug related hospital admissions; A systematic review of the recent literatures, Bulletin of Emergency & Trauma. 7 (2019) 339–346. https://doi.org/10.29252/BEAT-070401.

[15] I. El-Aita, Manufacturing of solid dosage forms using pressure-assisted microsyringe 3D-printing, Dissertation, Heinrich-Heine Universität Düsseldorf. (2019).

[16] C. Limoges, Natural selection, phagocytosis, and preadaptation: Lucien Cuénot, 1886–1901, Journal of the History of Medicine and Allied Sciences. XXXI (1976) 176–214. https://doi.org/10.1093/JHMAS/XXXI.2.176.

[17] D.J. Galton, Archibald E. Garrod: The founding father of biochemical genetics, in: Pioneers of Medicine Without a Nobel Prize, Imperial College Press, 2014: pp. 1–22. https://doi.org/10.1142/9781783263851_0001.

[18] A. Piro, G. Tagarelli, P. Lagonia, A. Quattrone, A. Tagarelli, Archibald Edward Garrod and alcaptonuria: "Inborn errors of metabolism" revisited, Genetics in Medicine. 12 (2010) 475–476. https://doi.org/10.1097/GIM.0B013E3181E68843.

[19] A. Piro, A. Tagarelli, G. Tagarelli, P. Lagonia, A. Quattrone, Archibald Edward Garrod: The physician father of biochemistry, Metabolism: Clinical and Experimental. 58 (2009) 427–437. https://doi.org/10.1016/J.METABOL.2008.12.001.

[20] A.E. Garrod, F.R.C.P. Lond, The incidence of alkaptonuria: a study in chemical individuality, The Lancet. 160 (1902) 1616–1620. https://doi.org/10.1016/S0140-6736(01)41972-6.

[21] L. Mancinelli, M. Cronin, W. Sadée, Pharmacogenomics: The promise of personalized medicine, AAPS PharmSci. 2 (2000) 29–41. https://doi.org/10.1208/ps020104.

[22] L.H. Snyder, Inherited taste deficiency, Science. 74 (1931) 151–152. https://doi.org/10.1126/science.74.1910.151.

[23] H.N. Kirkman, Glucose-6-phosphate dehydrogenase and human erythrocytes: Characteristics of Glucose-6-phosphate dehydrogenase from normal and primaquine-sensitive erythrocytes, Nature. 184 (1959) 1291–1292. https://doi.org/10.1038/1841291a0.

[24] P.E. Carson, C.L. Flanagan, C.E. Ickes, A.S. Alving, Enzymatic deficiency in primaquine-sensitive erythrocytes, Science. 124 (1956) 484–485. https://doi.org/10.1126/SCIENCE.124.3220.484-A.

[25] D. Primorac, L. Bach-Rojecky, D. Vadunec, A. Juginović, K. Zunic, V. Matišić, A. Skelin, B. Arsov, L. Boban, D. Erceg, I.E. Ivkošić, V. Molnar, J. Catic, I. Mikula, L. Boban, L. Primorac, B. Esquivel, M. Donaldson, Pharmacogenomics at the center of precision medicine: Challenges and perspective in an era of big data, Pharmacogenomics. 21 (2020) 141–156. https://doi.org/10.2217/PGS-2019-0134.

[26] F.T. Evans, P.W.S. Gray, H. Lehmann, E. Silk, Sensitivity to succinylcholine in relation to serum-cholinesterase, The Lancet. 259 (1952) 1229–1230. https://doi.org/10.1016/S0140-6736(52)92059-X.

References

[27]   J.D. Watson, The human genome project: Past, present, and future, Science. 248 (1990) 44–49. https://doi.org/10.1126/SCIENCE.2181665.

[28]   S. Foote, D. Vollrath, A. Hilton, D.C. Page, The human Y chromosome: Overlapping DNA clones spanning the euchromatic region, Science. 258 (1992) 60–66. https://doi.org/10.1126/SCIENCE.1359640.

[29]   D. Vollrath, S. Foote, A. Hilton, L.G. Brown, P. Beer-Romero, J.S. Bogan, D.C. Page, The human Y chromosome: A 43-interval map based on naturally occurring deletions, Science. 258 (1992) 52–59. https://doi.org/10.1126/SCIENCE.1439769.

[30]   I. Dunham, N. Shimizu, B.A. Roe, S. Chissoe, I. Dunham, A.R. Hunt, J.E. Collins, R. Bruskiewich, D.M. Beare, M. Clamp, L.J. Smink, R. Ainscough, J.P. Almeida, A. Babbage, C. Bagguley, J. Bailey, K. Barlow, K.N. Bates, O. Beasley, C.P. Bird, S. Blakey, A.M. Bridgeman, D. Buck, J. Burgess, W.D. Burrill, J. Burton, C. Carder, N.P. Carter, Y. Chen, G. Clark, S.M. Clegg, V. Cobley, C.G. Cole, R.E. Collier, R.E. Connor, D. Conroy, N. Corby, G.J. Coville, A. v. Cox, J. Davis, E. Dawson, P.D. Dhami, C. Dockree, S.J. Dodsworth, R.M. Durbin, A. Ellington, K.L. Evans, J.M. Fey, K. Fleming, L. French, A.A. Garner, J.G.R. Gilbert, M.E. Goward, D. Grafham, M.N. Griffiths, C.H.R. Hall, G. Hall-Tamlyn, R.W. Heathcott, S. Ho, S. Holmes, S.E. Hunt, M.C. Jones, J. Kershaw, A. Kimberley, A. King, G.K. Laird, C.F. Langford, M.A. Leversha, C. Lloyd, D.M. Lloyd, I.D. Martyn, M. Mashreghi-Mohammadi, L. Matthews, O.T. Mccann, J. Mcclay, S. Mclaren, A.A. Mcmurray, S.A. Milne, B.J. Mortimore, C.N. Odell, R. Pavitt, A. v. Pearce, D. Pearson, B.J. Phillimore, S.H. Phillips, R.W. Plumb, H. Ramsay, Y. Ramsey, L. Rogers, M.T. Ross, C.E. Scott, H.K. Sehra, C.D. Skuce, S. Smalley, M.L. Smith, C. Soderlund, L. Spragon, C.A. Steward, J.E. Sulston, R.M. Swann, M. Vaudin, M. Wall, J.M. Wallis, M.N. Whiteley, D. Willey, L. Williams, S. Williams, H. Williamson, T.E. Wilmer, L. Wilming, C.L. Wright, T. Hubbard, D.R. Bentley, S. Beck, J. Rogers, N. Shimizu, S. Minoshima, K. Kawasaki, T. Sasaki, S. Asakawa, J. Kudoh, A. Shintani, K. Shibuya, Y. Yoshizaki, N. Aoki, S. Mitsuyama, B.A. Roe, F. Chen, L. Chu, J. Crabtree, S. Deschamps, A. Do, T. Do, A. Dorman, F. Fang, Y. Fu, P. Hu, A. Hua, S. Kenton, H. Lai, H.I. Lao, J. Lewis, S. Lewis, S.P. Lin, P. Loh, E. Malaj, T. Nguyen, H. Pan, S. Phan, S. Qi, Y. Qian, L. Ray, Q. Ren, S. Shaull, D. Sloan, L. Song, Q. Wang, Y. Wang, Z. Wang, J. White, D. Willingham, H. Wu, Z. Yao, M. Zhan, G. Zhang, S. Chissoe, J. Murray, N. Miller, P. Minx, R. Fulton, D. Johnson, G. Bemis, D. Bentley, H. Bradshaw, S. Bourne, M. Cordes, Z. Du, L. Fulton, D. Goela, T. Graves, J. Hawkins, K. Hinds, K. Kemp, P. Latreille, D. Layman, P. Ozersky, T. Rohlfing, P. Scheet, C. Walker, A. Wamsley, P. Wohldmann, K. Pepin, J. Nelson, I. Korf, J.A. Bedell, L. Hillier, E. Mardis, R. Waterston, R. Wilson, B.S. Emanuel, T. Shaikh, H. Kurahashi, S. Saitta, M.L. Budarf, H.E. Mcdermid, A. Johnson, A.C.C. Wong, B.E. Morrow, L. Edelmann, U.J. Kim, H. Shizuya, M.I. Simon, J.P. Dumanski, M. Peyrard, D. Kedra, E. Seroussi, I. Fransson, I. Tapia, C.E. Bruder, K.P. O'Brien, The DNA sequence of human chromosome 22, Nature. 402 (1999) 489–495. https://doi.org/10.1038/990031.

[31]   M. Hattori, A. Fujiyama, T.D. Taylor, H. Watanabe, T. Yada, H.S. Park, A. Toyoda, K. Ishii, Y. Totoki, D.K. Choi, E. Soeda, M. Ohki, T. Takagi, Y. Sakaki,

S. Taudien, K. Blechschmidt, A. Polley, U. Menzel, J. Delabar, K. Kumpf, R. Lehmann, D. Patterson, K. Reichwald, A. Rump, M. Schillhabel, A. Schudy, W. Zimmermann, A. Rosenthal, J. Kudoh, K. Shibuya, K. Kawasaki, S. Asakawa, A. Shintani, T. Sasaki, K. Nagamine, S. Mitsuyama, S.E. Antonarakis, S. Minoshima, N. Shimizu, G. Nordsiek, K. Homischer, P. Brandt, M. Scharfe, O. Schön, A. Desario, J. Reichelt, G. Kauer, H. Blöcker, J. Ramser, A. Beck, S. Klages, S. Hennig, L. Riesselmann, E. Dagand, T. Haaf, S. Wehrmeyer, K. Borzym, K. Gardiner, D. Nizetic, F. Francis, H. Lehrach, R. Reinhardt, M.L. Yaspo, The DNA sequence of human chromosome 21, Nature. 405 (2000) 311–319. https://doi.org/10.1038/35012518.

[32]   S. Reardon, A complete human genome sequence is close: How scientists filled in the gaps, Nature. 594 (2021) 158–159. https://doi.org/10.1038/D41586-021-01506-W.

[33]   J. Craig Venter, M.D. Adams, E.W. Myers, P.W. Li, R.J. Mural, G.G. Sutton, H.O. Smith, M. Yandell, C.A. Evans, R.A. Holt, J.D. Gocayne, P. Amanatides, R.M. Ballew, D.H. Huson, J.R. Wortman, Q. Zhang, C.D. Kodira, X.H. Zheng, L. Chen, M. Skupski, G. Subramanian, P.D. Thomas, J. Zhang, G.L. Gabor Miklos, C. Nelson, S. Broder, A.G. Clark, J. Nadeau, V.A. McKusick, N. Zinder, A.J. Levine, R.J. Roberts, M. Simon, C. Slayman, M. Hunkapiller, R. Bolanos, A. Delcher, I. Dew, D. Fasulo, M. Flanigan, L. Florea, A. Halpern, S. Hannenhalli, S. Kravitz, S. Levy, C. Mobarry, K. Reinert, K. Remington, J. Abu-Threideh, E. Beasley, K. Biddick, V. Bonazzi, R. Brandon, M. Cargill, I. Chandramouliswaran, R. Charlab, K. Chaturvedi, Z. Deng, V. di Francesco, P. Dunn, K. Eilbeck, C. Evangelista, A.E. Gabrielian, W. Gan, W. Ge, F. Gong, Z. Gu, P. Guan, T.J. Heiman, M.E. Higgins, R.R. Ji, Z. Ke, K.A. Ketchum, Z. Lai, Y. Lei, Z. Li, J. Li, Y. Liang, X. Lin, F. Lu, G. v. Merkulov, N. Milshina, H.M. Moore, A.K. Naik, V.A. Narayan, B. Neelam, D. Nusskern, D.B. Rusch, S. Salzberg, W. Shao, B. Shue, J. Sun, Z. Yuan Wang, A. Wang, X. Wang, J. Wang, M.H. Wei, R. Wides, C. Xiao, C. Yan, A. Yao, J. Ye, M. Zhan, W. Zhang, H. Zhang, Q. Zhao, L. Zheng, F. Zhong, W. Zhong, S.C. Zhu, S. Zhao, D. Gilbert, S. Baumhueter, G. Spier, C. Carter, A. Cravchik, T. Woodage, F. Ali, H. An, A. Awe, D. Baldwin, H. Baden, M. Barnstead, I. Barrow, K. Beeson, D. Busam, A. Carver, A. Center, M. Lai Cheng, L. Curry, S. Danaher, L. Davenport, R. Desilets, S. Dietz, K. Dodson, L. Doup, S. Ferriera, N. Garg, A. Gluecksmann, B. Hart, J. Haynes, C. Haynes, C. Heiner, S. Hladun, D. Hostin, J. Houck, T. Howland, C. Ibegwam, J. Johnson, F. Kalush, L. Kline, S. Koduru, A. Love, F. Mann, D. May, S. McCawley, T. McIntosh, I. McMullen, M. Moy, L. Moy, B. Murphy, K. Nelson, C. Pfannkoch, E. Pratts, V. Puri, H. Qureshi, M. Reardon, R. Rodriguez, Y.H. Rogers, D. Romblad, B. Ruhfel, R. Scott, C. Sitter, M. Smallwood, E. Stewart, R. Strong, E. Suh, R. Thomas, N. Ni Tint, S. Tse, C. Vech, G. Wang, J. Wetter, S. Williams, M. Williams, S. Windsor, E. Winn-Deen, K. Wolfe, J. Zaveri, K. Zaveri, J.F. Abril, R. Guigo, M.J. Campbell, K. v. Sjolander, B. Karlak, A. Kejariwal, H. Mi, B. Lazareva, T. Hatton, A. Narechania, K. Diemer, A. Muruganujan, N. Guo, S. Sato, V. Bafna, S. Istrail, R. Lippert, R. Schwartz, B. Walenz, S. Yooseph, D. Allen, A. Basu, J. Baxendale, L. Blick, M. Caminha, J. Carnes-Stine, P. Caulk, Y.H. Chiang, M. Coyne, C. Dahlke, A. Deslattes Mays, M.

Dombroski, M. Donnelly, D. Ely, S. Esparham, C. Fosler, H. Gire, S. Glanowski, K. Glasser, A. Glodek, M. Gorokhov, K. Graham, B. Gropman, M. Harris, J. Heil, S. Henderson, J. Hoover, D. Jennings, C. Jordan, J. Jordan, J. Kasha, L. Kagan, C. Kraft, A. Levitsky, M. Lewis, X. Liu, J. Lopez, D. Ma, W. Majoros, J. McDaniel, S. Murphy, M. Newman, T. Nguyen, N. Nguyen, M. Nodell, S. Pan, J. Peck, M. Peterson, W. Rowe, R. Sanders, J. Scott, M. Simpson, T. Smith, A. Sprague, T. Stockwell, R. Turner, E. Venter, M. Wang, M. Wen, D. Wu, M. Wu, A. Xia, A. Zandieh, X. Zhu, The sequence of the human genome, Science. 291 (2001) 1304–1351. https://doi.org/10.1126/SCIENCE.1058040.

[34] W.E. Evans, H.L. McLeod, Pharmacogenomics — Drug disposition, drug targets, and side effects, New England Journal of Medicine. 348 (2003) 538–549. https://doi.org/10.1056/NEJMRA020526.

[35] J.S. Ross, J.A. Fletcher, The HER-2/neu oncogene in breast cancer: Prognostic factor, predictive factor, and target for therapy, The Oncologist. 3 (1998) 237–252. https://doi.org/10.1634/THEONCOLOGIST.3-4-237.

[36] J. Baselga, L. Norton, J. Albanell, Y.M. Kim, J. Mendelsohn, Recombinant humanized anti-HER2 antibody (Herceptin) enhances the antitumor activity of paclitaxel and doxorubicin against HER2/neu overexpressing human breast cancer xenografts, Cancer Research. 58 (1998) 2825–2831.

[37] M.M. Goldenberg, Trastuzumab, a recombinant DNA-derived humanized monoclonal antibody, a novel agent for the treatment of metastatic breast cancer, Clinical Therapeutics. 21 (1999) 309–318. https://doi.org/10.1016/S0149-2918(00)88288-0.

[38] M. Gerlinger, A.J. Rowan, S. Horswell, J. Larkin, D. Endesfelder, E. Gronroos, P. Martinez, N. Matthews, A. Stewart, P. Tarpey, I. Varela, B. Phillimore, S. Begum, N.Q. McDonald, A. Butler, D. Jones, K. Raine, C. Latimer, C.R. Santos, M. Nohadani, A.C. Eklund, B. Spencer-Dene, G. Clark, L. Pickering, G. Stamp, M. Gore, Z. Szallasi, J. Downward, P.A. Futreal, C. Swanton, Intratumor heterogeneity and branched evolution revealed by multiregion sequencing, New England Journal of Medicine. 366 (2012) 883–892. https://doi.org/10.1056/NEJMOA1113205.

[39] S. Mallal, D. Nolan, C. Witt, G. Masel, A.M. Martin, C. Moore, D. Sayer, A. Castley, C. Mamotte, D. Maxwell, I. James, F.T. Christiansen, Association between presence of HLA-B*5701, HLA-DR7, and HLA-DQ3 and hypersensitivity to HIV-1 reverse-transcriptase inhibitor abacavir, The Lancet. 359 (2002) 727–732. https://doi.org/10.1016/S0140-6736(02)07873-X.

[40] S. Mallal, E. Phillips, G. Carosi, J.-M. Molina, C. Workman, J. Tomažič, E. Jägel-Guedes, S. Rugina, O. Kozyrev, J. Flores Cid, P. Hay, D. Nolan, S. Hughes, A. Hughes, S. Ryan, N. Fitch, D. Thorborn, A. Benbow, F. Royal, HLA-B*5701 screening for hypersensitivity to abacavir, New England Journal of Medicine. 358 (2008) 568–579. https://doi.org/10.1056/NEJMOA0706135.

[41] S. Hetherington, A.R. Hughes, M. Mosteller, D. Shortino, K.L. Baker, W. Spreen, E. Lai, K. Davies, A. Handley, D.J. Dow, M.E. Fling, M. Stocum, C. Bowman,

L.M. Thurmond, A.D. Roses, Genetic variations in HLA-B region and hypersensitivity reactions to abacavir, The Lancet. 359 (2002) 1121–1122. https://doi.org/10.1016/S0140-6736(02)08158-8.

[42]   L. Dean, Abacavir therapy and HLA-B*57:01 genotype, in: V.M. Pratt, S.A. Scott, M. Pirmohamed, B. Esquivel, B.L. Kattman, A.J. Malheiro (Eds.), Medical Genetics Summaries, National Center for Biotechnology Information (US), Bethesda (MD), 2018: pp. 7–16.

[43]   PharmGKB, (2001). https://www.pharmgkb.org/ (accessed November 11, 2022).

[44]   C.A.T.C. Lunenburg, C.H. van der Wouden, M. Nijenhuis, M.H. Crommentuijn-van Rhenen, N.J. de Boer-Veger, A.M. Buunk, E.J.F. Houwink, H. Mulder, G.A. Rongen, R.H.N. van Schaik, J. van der Weide, B. Wilffert, V.H.M. Deneer, J.J. Swen, H.J. Guchelaar, Dutch Pharmacogenetics Working Group (DPWG) guideline for the gene–drug interaction of DPYD and fluoropyrimidines, European Journal of Human Genetics . 28 (2019) 508–517. https://doi.org/10.1038/s41431-019-0540-0.

[45]   J.J. Swen, I. Wilting, A. de Goede, L. Grandia, H. Mulder, D.J. Touw, A. de Boer, J.M.H. Conemans, T.C.G. Egberts, O.H. Klungel, R. Koopmans, J. van der Weide, B. Wilffert, H.J. Guchelaar, V.H.M. Deneer, Pharmacogenetics: From bench to byte, Clinical Pharmacology & Therapeutics. 83 (2008) 781–787. https://doi.org/10.1038/SJ.CLPT.6100507.

[46]   J.J. Swen, M. Nijenhuis, A. de Boer, L. Grandia, A.H. Maitland-Van Der Zee, H. Mulder, G.A.P.J.M. Rongen, R.H.N. van Schaik, T. Schalekamp, D.J. Touw, J. van der Weide, B. Wilffert, V.H.M. Deneer, H.J. Guchelaar, Pharmacogenetics: From bench to byte— An update of guidelines, Clinical Pharmacology & Therapeutics. 89 (2011) 662–673. https://doi.org/10.1038/CLPT.2011.34.

[47]   M. Whirl-Carrillo, R. Huddart, L. Gong, et al., An evidence-based framework for evaluating pharmacogenomics knowledge for personalized medicine, Clinical Pharmacology & Therapeutics. 110 (2021) 563–572. https://doi.org/10.1002/CPT.2350.

[48]   Precision Medicine Initiative | The White House, (2015). https://obamawhitehouse.archives.gov/precision-medicine (accessed June 26, 2022).

[49]   Directorate-General for Research and Innovation - European Commission, Groundbreaking research demonstrates the power of using personalised approaches to select and correctly apply pharmaceuticals to patients, (2023). https://research-and-innovation.ec.europa.eu/news/all-research-and-innovation-news/groundbreaking-research-demonstrates-power-using-personalised-approaches-select-and-correctly-apply-2023-02-03_en (accessed February 9, 2023).

[50]   J.J. Swen, C.H. van der Wouden, L.E. Manson, H. Abdullah-Koolmees, K. Blagec, T. Blagus, S. Böhringer, A. Cambon-Thomsen, E. Cecchin, K.-C. Cheung, V.H. Deneer, M. Dupui, M. Ingelman-Sundberg, S. Jonsson, C. Joefield-Roka, K.S. Just, M.O. Karlsson, L. Konta, R. Koopmann, M. Kriek, T. Lehr, C. Mitropoulou, E.

References

Rial-Sebbag, V. Rollinson, R. Roncato, M. Samwald, E. Schaeffeler, M. Skokou, M. Schwab, D. Steinberger, J.C. Stingl, R. Tremmel, R.M. Turner, M.H. van Rhenen, C.L.D. Fajardo, V. Dolžan, G.P. Patrinos, M. Pirmohamed, G. Sunder-Plassmann, G. Toffoli, H.-J. Guchelaar, A. Buunk, H. Goossens, G. Baas, M. Algera, E. Schuil-Vlassak, T. Ambagts, L. de Hoog-Schouten, S. Musaafir, R. Bosch, C. Tjong, S. Steeman, M. van der Plas, G. Baldew, I. den Hollander, Z. de Waal, A. Heijn, L. Nelemans, K. Kouwen-Lubbers, M. van Leeuwen, S. Hoogenboom, J. van Doremalen, C. Ton, B. Beetstra, V. Meijs, J. Dikken, D. Dubero, M. Slager, T. Houben, T. Kanis, W. Overmars, M. Nijenhuis, M. Steffens, I. Bergs, K. Karamperis, S. Siamoglou, O. Ivantsik, G.-C. Samiou, Z. Kordou, E. Tsermpini, P. Ferentinos, A. Karaivazoglou, G. Rigas, H. Gerasimou, G. Voukelatou, E. Georgila, E.E. Tsermpini, E. Mendrinou, K. Chalikiopoulou, A. Kolliopoulou, K. Mitropoulos, A. Stratopoulos, I. Liopetas, A. Tsikrika, E. Barba, G. Emmanouil, T. Stamopoulou, A. Stathoulias, P. Giannopoulos, F. Kanellakis, M. Bartsakoulia, T. Katsila, A. Douzenis, F. Gourzis, K. Assimakopoulos, A. Bignucolo, L.D. Cin, F. Comello, S. Mezzalira, F. Puglisi, M. Spina, L. Foltran, M. Guardascione, A. Buonadonna, M. Bartoletti, S. Corsetti, E. Ongaro, L. da Ros, S. Bolzonello, S. Spazzapan, A. Freschi, P. di Nardo, E. Palazzari, F. Navarria, R. Innocente, M. Berretta, M. D'Andrea, F. Angelini, T. Diraimo, A. Favaretto, C.L. Dávila-Fajardo, X. Díaz-Villamarín, L.J. Martínez-González, A. Antúnez-Rodríguez, E. Moreno-Escobar, A.E. Fernández-Gonzalez, P. García-Navas, A.B.P. Bautista-Pavés, F. Burillo-Gómez, I. Villegas-Rodríguez, J.G. Sánchez-Ramos, M.J. Antolinos-Pérez, R. Rivera, S. Martínez-Huertas, J. Thomas-, J.J. Carazo, M.I. Yañez-Sanchez, R. Blancas-López-Navajas, B. García-Orta, C.J. González-Astorga, F.J. Rodríguez-González, M. Ruiz-Carazo, I. López-Pérez, R. Cano-Herrera, T. Herrera, Gil-Jiménez, M.T. Delgado-Ureña, J.M. Triviño-Juarez, S. Campos-Velázquez, S. Alcántara-Espadafor, M.R.M. Aguilar, M.C. Ontiveros-Ortega, L. Carnerero-Córdoba, M. Guerrero-Jiménez, M. Legeren-Álvarez, M. Yélamos-Vargas, I. Castillo-Pérez, I. Aomar-Millán, M. Anguita-Romero, M.J. Sánchez-García, S. Sequero-Lopez, N. Faro-Miguez, S. López-Fernández, R.N. Leyva-Ferrer, N. Herrera-Gómez, L. Pertejo-Manzano, E.M. Pérez-Gutierrez, A.J.M. la Higuera, J. Plaza-Carrera, F. Baena-Garzón, P. Toledo-Frías, I. Cruz-Valero, V. Chacón-McWeeny, I. Gallardo-Sánchez, A. Arrebola, L. Guillén-Zafra, Á. Ceballos-Torres, P. Guardia-Mancilla, E. Guirao-Arrabal, J. Canterero-Hinojosa, S. Velasco-Fuentes, D. Sánchez-Cano, M. del P. Aguilar-Jaldo, J. Caballero-Borrego, M. Praznik, U. Slapšak, B. Vončina, B. Rajter, A. Škrinjar, A.M. Ulčakar, A. Zidanšek, T.S. Ignjatvič, B.M. Poredoš, Ž.V. Pečnik, T.P. Susič, M. Juteršek, J. Klen, J. Skoporc, T. Kotar, M.P. Šter, M.Z. Dernovšk, J. Klen, G. Mlinšek, P. Miklavčič, A.P. Ilješ, C.G. Kuhar, I. Oblak, B. Stražišar, D. Štrbac, E. Matos, M. Mencinger, M. Vrbnjak, M. Saje, M. Radovanovič, K. Jeras, L. Bukovec, T. Terzič, I. Minichmayr, A. Nanah, E. Nielsen, Y. Zou, V. Lauschke, I. Johansson, Y. Zhou, Å. Nordling, C. Aigner, M. Dames-Ludwig, R. Monteforte, R. Sunder-Plassmann, C. Steinhauser, G. Sengoelge, W. Winnicki, A. Schmidt, F. Vasileios, V. Fontana, A. Hanson, M. Little, R. Hornby, C. dello Russo, S. French, J. Hampson, M. Gumustekin, G. Anyfantis, L. Hampson, D. Lewis, R. Westhead, C. Prince, A. Rajasingam, A 12-gene pharmacogenetic panel to prevent adverse drug reactions: an open-label, multicentre,

controlled, cluster-randomised crossover implementation study, The Lancet. 401 (2023) 347–356. https://doi.org/10.1016/S0140-6736(22)01841-4.

[51] A. Fahr, R. Voigt, Kapitel 7.7 Freisetzungs- und resorptionsbeeinflussende Faktoren, in: Voigt-Pharmazeutische Technologie, Deutscher Apotheker Verlag, Stuttgart, 2021: pp. 258–266.

[52] J. Kim, O. de Jesus, Medication routes of administration, StatPearls [Internet]. (2022). https://www.ncbi.nlm.nih.gov/books/NBK568677/ (accessed September 4, 2022).

[53] S. Klein, Transport von Arzneiformen durch den Gastrointestinaltrakt, Deutsche Apotheker Zeitung. 23 (2011) 53. https://www.deutsche-apotheker-zeitung.de/daz-az/2011/daz-23-2011/transport-von-arzneiformen-durch-den-gastrointestinaltrakt (accessed October 8, 2022).

[54] R. Löbenberg, G.L. Amidon, Modern bioavailability, bioequivalence and biopharmaceutics classification system. New scientific approaches to international regulatory standards, European Journal of Pharmaceutics and Biopharmaceutics. 50 (2000) 3–12. https://doi.org/10.1016/S0939-6411(00)00091-6.

[55] A. Langner, H.H. Borchert, W. Mehnert, Kapitel 3: Liberation, Absorption, Distribution, Metabolismus und Exkretion (LADME), in: Biopharmazie, Wissenschaftliche Verlagsgesellschaft mbH, Stuttgart, 2011: pp. 32–45.

[56] Y. Lu, S. Kim, K. Park, In vitro-in vivo correlation: Perspectives on model development, International Journal of Pharmaceutics. 418 (2011) 142–148. https://doi.org/10.1016/j.ijpharm.2011.01.010.

[57] K. Ewe, A.G. Press, S. Bollen, I. Schuhn, Gastric emptying of indigestible tablets in relation to composition and time of ingestion of meals studied by metal detector, Digestive Diseases and Sciences. 36 (1991) 146–152. https://doi.org/10.1007/BF01300748.

[58] F. Schneider, M. Koziolek, W. Weitschies, In vitro and in vivo test methods for the evaluation of gastroretentive dosage forms, Pharmaceutics. 11 (2019) 416. https://doi.org/10.3390/PHARMACEUTICS11080416.

[59] V.R. Devadasu, P.K. Deb, R. Maheshwari, P. Sharma, R.K. Tekade, Physicochemical, pharmaceutical, and biological considerations in GIT absorption of drugs, Dosage Form Design Considerations. 1 (2018) 149–178. https://doi.org/10.1016/B978-0-12-814423-7.00005-8.

[60] C. Brown, H. Chokshi, B. Nickerson, Acceptable analytical practices for dissolution testing of poorly soluble compounds, Pharmaceutical Technology. 28 (2004) 56–65.

[61] J. Siepmann, F. Siepmann, Mathematical modeling of drug dissolution, International Journal of Pharmaceutics. 453 (2013) 12–24. https://doi.org/10.1016/j.ijpharm.2013.04.044.

References

[62]   Committee for Medicinal Products for Human Use, ICH M9 biopharmaceutics classification system-based biowaivers guidance for industry, (2021). https://www.fda.gov/vaccines-blood-biologics/guidance-compliance-regulatory-information-biologics/biologics-guidances (accessed September 18, 2022).

[63]   G.L. Amidon, H. Lennernäs, V.P. Shah, J.R. Crison, A theoretical basis for a biopharmaceutic drug classification: The correlation of in vitro drug product dissolution and in vivo bioavailability, Pharmaceutical Research. 12 (1995) 413–420. https://doi.org/10.1023/A:1016212804288.

[64]   C.A. Challener, Enabling technologies advance poorly soluble highly potent APIs, Pharmaceutical Technology. 43 (2019) 20–22. https://www.pharmtech.com/view/enabling-technologies-advance-poorly-soluble-highly-potent-apis (accessed September 18, 2022).

[65]   K. Göke, T. Lorenz, A. Repanas, F. Schneider, D. Steiner, K. Baumann, H. Bunjes, A. Dietzel, J.H. Finke, B. Glasmacher, A. Kwade, Novel strategies for the formulation and processing of poorly water-soluble drugs, European Journal of Pharmaceutics and Biopharmaceutics. 126 (2018) 40–56. https://doi.org/10.1016/J.EJPB.2017.05.008.

[66]   D. Dahlgren, H. Lennernäs, Intestinal permeability and drug absorption: Predictive experimental, computational and in vivo approaches, Pharmaceutics. 11 (2019) 411–429. https://doi.org/10.3390/PHARMACEUTICS11080411.

[67]   H. Bohets, P. Annaert, G. Mannens, L. van Beijsterveldt, K. Anciaux, P. Verboven, W. Meuldermans, K. Lavrijsen, Strategies for absorption screening in drug discovery and development, Current Topics in Medicinal Chemistry. 1 (2001) 367–383. https://doi.org/10.2174/1568026013394886.

[68]   S. Misaka, F. Müller, M.F. Fromm, Clinical relevance of drug efflux pumps in the gut, Current Opinion in Pharmacology. 13 (2013) 847–852. https://doi.org/10.1016/J.COPH.2013.08.010.

[69]   T. Murakami, M. Takano, Intestinal efflux transporters and drug absorption, Expert Opinion on Drug Metabolism and Toxicology. 4 (2008) 923–939. https://doi.org/10.1517/17425255.4.7.923.

[70]   A. Dokoumetzidis, P. Macheras, A century of dissolution research: From Noyes and Whitney to the Biopharmaceutics Classification System, International Journal of Pharmaceutics. 321 (2006) 1–11. https://doi.org/10.1016/j.ijpharm.2006.07.011.

[71]   A.A. Noyes, W.R. Whitney, The rate of solution of solid substances in their own solutions, Journal of the American Chemical Society. 19 (1897) 930–934. https://doi.org/10.1021/JA02086A003.

[72]   W. Nernst, Theorie der Reaktionsgeschwindigkeit in heterogenen Systemen, Zeitschrift Für Physikalische Chemie. 47U (1904) 52–55. https://doi.org/10.1515/ZPCH-1904-4704.

[73] E. Brunner, Reaktionsgeschwindigkeit in heterogenen Systemen, Zeitschrift Für Physikalische Chemie. 47U (1904) 56–102. https://doi.org/10.1515/ZPCH-1904-4705.

[74] M. Bisrat, E.K. Anderberg, M.I. Barnett, C. Nyström, Physicochemical aspects of drug release. XV. Investigation of diffusional transport in dissolution of suspended, sparingly soluble drugs, International Journal of Pharmaceutics. 80 (1992) 191–201. https://doi.org/10.1016/0378-5173(92)90277-9.

[75] A.W. Hixson, J.H. Crowell, Dependence of reaction velocity upon surface and agitation: II—Experimental procedure in study of surface, Industrial and Engineering Chemistry. 23 (1931) 1002–1009. https://doi.org/10.1021/ie50261a009.

[76] K. Gowthamarajan, S.K. Singh, Dissolution testing for poorly soluble drugs: A continuing perspective, Dissolution Technologies. (2010) 24–32. https://doi.org/10.14227/DT170310P24.

[77] European Pharmacopoeia Commission, 5.17.1. Recommendations on dissolution testing, in: European Pharmacopoeia, EDQM, 2020: pp. 801–807.

[78] A. Maroni, L. Zema, M. Cerea, M.E. Sangalli, Oral pulsatile drug delivery systems, Expert Opinion on Drug Delivery. 2 (2005) 855–871. https://doi.org/10.1517/17425247.2.5.855.

[79] P. Costa, J.M. Sousa Lobo, Modeling and comparison of dissolution profiles, European Journal of Pharmaceutical Sciences. 13 (2001) 123–133. https://doi.org/10.1016/S0928-0987(01)00095-1.

[80] J. Siepmann, F. Siepmann, Mathematical modeling of drug delivery, International Journal of Pharmaceutics. 364 (2008) 328–343. https://doi.org/10.1016/j.ijpharm.2008.09.004.

[81] J. Siepmann, N.A. Peppas, Higuchi equation: Derivation, applications, use and misuse, International Journal of Pharmaceutics. 418 (2011) 6–12. https://doi.org/10.1016/J.IJPHARM.2011.03.051.

[82] T. Higuchi, Mechanism of sustained-action medication. Theoretical analysis of rate of release of solid drugs dispersed in solid matrices, Journal of Pharmaceutical Sciences. 52 (1963) 1145–1149. https://doi.org/10.1002/jps.2600521210.

[83] T. Higuchi, Rate of release of medicaments from ointment bases containing drugs in suspension, Journal of Pharmaceutical Sciences. 50 (1961) 874–875. https://doi.org/10.1002/jps.2600501018.

[84] R.W. Korsmeyer, R. Gurny, E. Doelker, P. Buri, N.A. Peppas, Mechanisms of solute release from porous hydrophilic polymers, International Journal of Pharmaceutics. 15 (1983) 25–35. https://doi.org/10.1016/0378-5173(83)90064-9.

[85] A. Fahr, R. Voigt, Kapitel 7.3.1 Biokinetische Modelle - Pharmakokinetik, in: Voigt - Pharmazeutische Technologie, Deutscher Apotheker Verlag, Stuttgart, 2021: pp. 243–250.

References

[86] P. Mistry, H. Batchelor, Evidence of acceptability of oral paediatric medicines: A review, Journal of Pharmacy and Pharmacology. 69 (2017) 361–376. https://doi.org/10.1111/jphp.12610.

[87] T. Vallet, H. Michelon, M. Orlu, Y. Jani, P. Leglise, S. Laribe-Caget, M. Piccoli, A. Fur, F. le Liu, F. Ruiz, V. Boudy, Acceptability in the older population: The importance of an appropriate tablet size, Pharmaceutics. 12 (2020) 746. https://doi.org/10.3390/PHARMACEUTICS12080746.

[88] F. Liu, S. Ranmal, H.K. Batchelor, M. Orlu-Gul, T.B. Ernest, I.W. Thomas, T. Flanagan, C. Tuleu, Patient-centered pharmaceutical design to improve acceptability of medicines: Similarities and differences in paediatric and geriatric populations, Drugs. 74 (2014) 1871–1889. https://doi.org/10.1007/S40265-014-0297-2.

[89] S.R. Ranmal, A. Cram, C. Tuleu, Age-appropriate and acceptable paediatric dosage forms: Insights into end-user perceptions, preferences and practices from the Children's Acceptability of Oral Formulations (CALF) Study, International Journal of Pharmaceutics. 514 (2016) 296–307. https://doi.org/10.1016/J.IJPHARM.2016.07.054.

[90] J.T. Schiele, R. Quinzler, H.D. Klimm, M.G. Pruszydlo, W.E. Haefeli, Difficulties swallowing solid oral dosage forms in a general practice population: Prevalence, causes, and relationship to dosage forms, European Journal of Clinical Pharmacology. 69 (2013) 937–948. https://doi.org/10.1007/S00228-012-1417-0.

[91] Z. Shariff, D. Kirby, S. Missaghi, A. Rajabi-Siahboomi, I. Maidment, Patient-centric medicine design: Key characteristics of oral solid dosage forms that improve adherence and acceptance in older people, Pharmaceutics. 12 (2020) 905. https://doi.org/10.3390/PHARMACEUTICS12100905.

[92] K. Wening, J. Breitkreutz, Oral drug delivery in personalized medicine: Unmet needs and novel approaches, International Journal of Pharmaceutics. 404 (2011) 1–9. https://doi.org/10.1016/j.ijpharm.2010.11.001.

[93] E. van Santen, D.M. Barends, H.W. Frijlink, Breaking of scored tablets: A review, European Journal of Pharmaceutics and Biopharmaceutics. 53 (2002) 139–145. https://doi.org/10.1016/S0939-6411(01)00228-4.

[94] R. Quinzler, C. Gasse, A. Schneider, P. Kaufmann-Kolle, J. Szecsenyi, W.E. Haefeli, The frequency of inappropriate tablet splitting in primary care, European Journal of Clinical Pharmacology. 62 (2006) 1065–1073. https://doi.org/10.1007/s00228-006-0202-3.

[95] Y. Thabet, V. Klingmann, J. Breitkreutz, Drug formulations: Standards and novel strategies for drug administration in pediatrics, The Journal of Clinical Pharmacology. 58 (2018) 26–35. https://doi.org/10.1002/JCPH.1138.

[96] D. Khan, D. Kirby, S. Bryson, M. Shah, A. Rahman Mohammed, Paediatric specific dosage forms: Patient and formulation considerations, International Journal of Pharmaceutics. 616 (2022) 121501. https://doi.org/10.1016/J.IJPHARM.2022.121501.

[97]   J.A. Cramer, Relationship between medication compliance and medical outcomes, American Journal of Health-System Pharmacy. 52 (1995) 27–29. https://doi.org/10.1093/AJHP/52.14_SUPPL_3.S27.

[98]   N. Col, J.E. Fanale, P. Kronholm, The role of medication noncompliance and adverse drug reactions in hospitalizations of the elderly, Archives of Internal Medicine. 150 (1990) 841–845. https://doi.org/10.1001/ARCHINTE.150.4.841.

[99]   R. Balkrishnan, Predictors of medication adherence in the elderly, Clinical Therapeutics. 20 (1998) 764–771. https://doi.org/10.1016/S0149-2918(98)80139-2.

[100]   E. Schirm, H. Tobi, T.W. de Vries, I. Choonara, L.T.W. de Jong-Van Den Berg, Lack of appropriate formulations of medicines for children in the community, Acta Paediatrica. 92 (2003) 1486–1489. https://doi.org/10.1080/08035250310006728.

[101]   H. Shonna Yin, R.M. Parker, L.M. Sanders, B.P. Dreyer, A.L. Mendelsohn, S. Bailey, D.A. Patel, J.J. Jimenez, K.Y.A. Kim, K. Jacobson, L. Hedlund, M.C.J. Smith, L.M. Harris, T. McFadden, M.S. Wolf, Liquid medication errors and dosing tools: A randomized controlled experiment, Pediatrics. 138 (2016) 1–11. https://doi.org/10.1542/PEDS.2016-0357.

[102]   I. Neves, L. Proença, M.D. Auxtero, Reproducibility and accuracy of measurement of oral liquid pharmaceutical forms, using a dosing spoon, Annals of Medicine. 51 (2019) 86. https://doi.org/10.1080/07853890.2018.1561800.

[103]   V. Klingmann, N. Spomer, C. Lerch, I. Stoltenberg, C. Frömke, H.M. Bosse, J. Breitkreutz, T. Meissner, Favorable acceptance of mini-tablets compared with syrup: A randomized controlled trial in infants and preschool children, The Journal of Pediatrics. 163 (2013) 1728–1732. https://doi.org/10.1016/J.JPEDS.2013.07.014.

[104]   D.A. van Riet-Nales, A.F.A.M. Schobben, H. Vromans, T.C.G. Egberts, C.M.A. Rademaker, Safe and effective pharmacotherapy in infants and preschool children: Importance of formulation aspects, Archives of Disease in Childhood. 101 (2016) 662–669. https://doi.org/10.1136/ARCHDISCHILD-2015-308227.

[105]   P. Lennartz, J.B. Mielck, Minitabletting: Improving the compactability of paracetamol powder mixtures, International Journal of Pharmaceutics. 173 (1998) 75–85. https://doi.org/10.1016/S0378-5173(98)00206-3.

[106]   C. Tissen, K. Woertz, J. Breitkreutz, P. Kleinebudde, Development of mini-tablets with 1 mm and 2 mm diameter, International Journal of Pharmaceutics. 416 (2011) 164–170. https://doi.org/10.1016/J.IJPHARM.2011.06.027.

[107]   I. Stoltenberg, J. Breitkreutz, Orally disintegrating mini-tablets (ODMTs)--A novel solid oral dosage form for paediatric use, European Journal of Pharmaceutics and Biopharmaceutics. 78 (2011) 462–469. https://doi.org/10.1016/J.EJPB.2011.02.005.

[108]   A. Hejduk, J. Lulek, Dispensing of minitablets – Has the problem been resolved?, International Journal of Pharmaceutics. 619 (2022) 121666. https://doi.org/10.1016/J.IJPHARM.2022.121666.

References

[109] T. Comoglu, E. Dilek Ozyilmaz, Orally disintegrating tablets and orally disintegrating mini tablets–novel dosage forms for pediatric use, Pharmaceutical Development and Technology. 24 (2019) 902–914. https://doi.org/10.1080/10837450.2019.1615090.

[110] A. Lura, Systematic investigations for the development and manufacturing of pharmaceutical mini-tablets, Dissertation Heinrich-Heine Universität Düsseldorf. (2021).

[111] S.M. Aquilonius, D. Nyholm, Development of new levodopa treatment strategies in Parkinson's disease-from bedside to bench to bedside, Upsala Journal of Medical Sciences. 122 (2017) 71–77. https://doi.org/10.1080/03009734.2017.1285374.

[112] J. Goole, P. Deleuze, F. Vanderbist, K. Amighi, New levodopa sustained-release floating minitablets coated with insoluble acrylic polymer, European Journal of Pharmaceutics and Biopharmaceutics. 68 (2008) 310–318. https://doi.org/10.1016/J.EJPB.2007.06.017.

[113] J. Goole, B. van Gansbeke, G. Pilcer, P. Deleuze, D. Blocklet, S. Goldman, M. Pandolfo, F. Vanderbist, K. Amighi, Pharmacoscintigraphic and pharmacokinetic evaluation on healthy human volunteers of sustained-release floating minitablets containing levodopa and carbidopa, International Journal of Pharmaceutics. 364 (2008) 54–63. https://doi.org/10.1016/J.IJPHARM.2008.08.016.

[114] S. Bredenberg, D. Nyholm, S.M. Aquilonius, C. Nyström, An automatic dose dispenser for microtablets - A new concept for individual dosage of drugs in tablet form, International Journal of Pharmaceutics. 261 (2003) 137–146. https://doi.org/10.1016/S0378-5173(03)00294-1.

[115] Y. Thabet, D. Lunter, J. Breitkreutz, Continuous manufacturing and analytical characterization of fixed-dose, multilayer orodispersible films, European Journal of Pharmaceutical Sciences. 117 (2018) 236–244. https://doi.org/10.1016/J.EJPS.2018.02.030.

[116] S. Niese, J. Quodbach, Formulation development of a continuously manufactured orodispersible film containing warfarin sodium for individualized dosing, European Journal of Pharmaceutics and Biopharmaceutics. 136 (2019) 93–101. https://doi.org/10.1016/J.EJPB.2019.01.011.

[117] Y. Thabet, J. Breitkreutz, Orodispersible films: Product transfer from lab-scale to continuous manufacturing, International Journal of Pharmaceutics. 535 (2018) 285–292. https://doi.org/10.1016/J.IJPHARM.2017.11.021.

[118] R. Jani, D. Patel, Hot melt extrusion: An industrially feasible approach for casting orodispersible film, Asian Journal of Pharmaceutical Sciences. 10 (2015) 292–305. https://doi.org/10.1016/J.AJPS.2015.03.002.

[119] S. Niese, J. Breitkreutz, J. Quodbach, Development of a dosing device for individualized dosing of orodispersible warfarin films, International Journal of Pharmaceutics. 561 (2019) 314–323. https://doi.org/10.1016/J.IJPHARM.2019.03.019.

[120] A. Göbel, J. Breitkreutz, Concept of orodispersible or mucoadhesive "Tandem Films" and their pharmaceutical realization, Pharmaceutics. 14 (2022) 264. https://doi.org/10.3390/PHARMACEUTICS14020264.

[121] M. Scarpa, S. Stegemann, W.-K. Hsiao, H. Pichler, S. Gaisford, M. Bresciani, A. Paudel, M. Orlu, Orodispersible films: Towards drug delivery in special populations, International Journal of Pharmaceutics. 523 (2017) 327–335. https://doi.org/10.1016/j.ijpharm.2017.03.018.

[122] R. Krampe, Orodispersible Filme mit schwerlöslichem, hochdosiertem Arzneistoff: Herstellungstechniken und biorelevante Beurteilung, Dissertation Heinrich-Heine Universität Düsseldorf. (2015).

[123] European Pharmacopoeia Commission, Oromucosal Preparations, in: European Pharmacopoeia, 2022: pp. 985–987.

[124] O. Kiefer, B. Fischer, J. Breitkreutz, Fundamental investigations into metoprolol tartrate deposition on orodispersible films by inkjet printing for individualised drug dosing, Pharmaceutics. 13 (2021) 247. https://doi.org/10.3390/PHARMACEUTICS13020247.

[125] O. Kiefer, J. Breitkreutz, Comparative investigations on key factors and print head designs for pharmaceutical inkjet printing, International Journal of Pharmaceutics. 586 (2020) 119561. https://doi.org/10.1016/J.IJPHARM.2020.119561.

[126] M. Alomari, P.R. Vuddanda, S.J. Trenfield, C.C. Dodoo, S. Velaga, A.W. Basit, S. Gaisford, Printing T3 and T4 oral drug combinations as a novel strategy for hypothyroidism, International Journal of Pharmaceutics. 549 (2018) 363–369. https://doi.org/10.1016/J.IJPHARM.2018.07.062.

[127] F. Fina, A. Goyanes, S. Gaisford, A.W. Basit, Selective laser sintering (SLS) 3D printing of medicines, International Journal of Pharmaceutics. 529 (2017) 285–293. https://doi.org/10.1016/J.IJPHARM.2017.06.082.

[128] A. Goyanes, P. Robles Martinez, A. Buanz, A.W. Basit, S. Gaisford, Effect of geometry on drug release from 3D printed tablets, International Journal of Pharmaceutics. 494 (2015) 657–663. https://doi.org/10.1016/j.ijpharm.2015.04.069.

[129] A. Goyanes, A.B.M. Buanz, A.W. Basit, S. Gaisford, Fused-filament 3D printing (3DP) for fabrication of tablets, International Journal of Pharmaceutics. 476 (2014) 88–92. https://doi.org/10.1016/J.IJPHARM.2014.09.044.

[130] C. Korte, J. Quodbach, 3D-printed network structures as controlled-release drug delivery systems: Dose adjustment, API release analysis and prediction, AAPS PharmSciTech. 19 (2018) 3333–3342. https://doi.org/10.1208/s12249-018-1017-0.

[131] M. Sadia, B. Arafat, W. Ahmed, R.T. Forbes, M.A. Alhnan, Channelled tablets: An innovative approach to accelerating drug release from 3D printed tablets, Journal of Controlled Release. 269 (2018) 355–363. https://doi.org/10.1016/j.jconrel.2017.11.022.

References

[132] M. Sadia, A. Sośnicka, B. Arafat, A. Isreb, W. Ahmed, A. Kelarakis, M.A. Alhnan, Adaptation of pharmaceutical excipients to FDM 3D printing for the fabrication of patient-tailored immediate release tablets, International Journal of Pharmaceutics. 513 (2016) 659–668. https://doi.org/10.1016/j.ijpharm.2016.09.050.

[133] T.C. Okwuosa, D. Stefaniak, B. Arafat, A. Isreb, K.-W. Wan, M.A. Alhnan, A lower temperature FDM 3D printing for the manufacture of patient-specific immediate release tablets, Pharmaceutical Research. 33 (2016) 2704–2712. https://doi.org/10.1007/s11095-016-1995-0.

[134] M.A. Alhnan, T.C. Okwuosa, M. Sadia, K.W. Wan, W. Ahmed, B. Arafat, Emergence of 3D printed dosage forms: Opportunities and challenges, Pharmaceutical Research. 33 (2016) 1817–1832. https://doi.org/10.1007/s11095-016-1933-1.

[135] I. Seoane-Viaño, S.J. Trenfield, A.W. Basit, A. Goyanes, Translating 3D printed pharmaceuticals: From hype to real-world clinical applications, Advanced Drug Delivery Reviews. 174 (2021) 553–575. https://doi.org/10.1016/J.ADDR.2021.05.003.

[136] H. Windolf, R. Chamberlain, J. Quodbach, Dose-independent drug release from 3D printed oral medicines for patient-specific dosing to improve therapy safety, International Journal of Pharmaceutics. 616 (2022) 121555. https://doi.org/10.1016/J.IJPHARM.2022.121555.

[137] J. Rahman-Yildir, B. Fischer, J. Breitkreutz, Development of sustained-release drug-loaded intravesical inserts via semi-solid micro-extrusion 3D-printing for bladder targeting, International Journal of Pharmaceutics. 622 (2022) 121849. https://doi.org/10.1016/J.IJPHARM.2022.121849.

[138] H. Ponsar, R. Wiedey, J. Quodbach, Hot-melt extrusion process fluctuations and their impact on critical quality attributes of filaments and 3D-printed dosage forms, Pharmaceutics. 12 (2020) 511. https://doi.org/10.3390/pharmaceutics12060511.

[139] Y. Zhang, Y. Yu, H. Chen, I.T. Ozbolat, Characterization of printable cellular micro-fluidic channels for tissue engineering, Biofabrication. 5 (2013) 025004. https://doi.org/10.1088/1758-5082/5/2/025004.

[140] A. Melocchi, M. Uboldi, M. Cerea, A. Foppoli, A. Maroni, S. Moutaharrik, L. Palugan, L. Zema, A. Gazzaniga, A graphical review on the escalation of fused deposition modeling (FDM) 3D printing in the pharmaceutical field, Journal of Pharmaceutical Sciences. 109 (2020) 2943–2957. https://doi.org/10.1016/J.XPHS.2020.07.011.

[141] A. Melocchi, F. Parietti, A. Maroni, A. Foppoli, A. Gazzaniga, L. Zema, Hot-melt extruded filaments based on pharmaceutical grade polymers for 3D printing by fused deposition modeling, International Journal of Pharmaceutics. 509 (2016) 255–263. https://doi.org/10.1016/j.ijpharm.2016.05.036.

[142] P.R. Martinez, A. Goyanes, A.W. Basit, S. Gaisford, Influence of geometry on the drug release profiles of stereolithographic (SLA) 3D-printed tablets, AAPS PharmSciTech. 19 (2018) 3355–3361. https://doi.org/10.1208/s12249-018-1075-3.

[143] K. Vithani, A. Goyanes, V. Jannin, A.W. Basit, S. Gaisford, B.J. Boyd, A proof of concept for 3D printing of solid lipid-based formulations of poorly water-soluble drugs to control formulation dispersion kinetics, Pharmaceutical Research. 36 (2019) 102. https://doi.org/10.1007/s11095-019-2639-y.

[144] G. Kollamaram, D.M. Croker, G.M. Walker, A. Goyanes, A.W. Basit, S. Gaisford, Low temperature fused deposition modeling (FDM) 3D printing of thermolabile drugs, International Journal of Pharmaceutics. 545 (2018) 144–152. https://doi.org/10.1016/J.IJPHARM.2018.04.055.

[145] H. Windolf, R. Chamberlain, J. Quodbach, Predicting drug release from 3D printed oral medicines based on the surface area to volume ratio of tablet geometry, Pharmaceutics. 13 (2021) 1453. https://doi.org/10.3390/PHARMACEUTICS13091453.

[146] I. El-Aita, H. Ponsar, J. Quodbach, A critical review on 3D-printed dosage forms, Current Pharmaceutical Design. 24 (2018) 4957–4978. https://doi.org/10.2174/1381612825666181206124206.

[147] N. Shahrubudin, T.C. Lee, R. Ramlan, An overview on 3D printing technology: Technological, materials, and applications, Procedia Manufacturing. 35 (2019) 1286–1296. https://doi.org/10.1016/J.PROMFG.2019.06.089.

[148] ASTM International, Standard terminology for additive manufacturing technologies : designation F2792-12a, ASTM International, West Conshohocken PA, 2012.

[149] C.W. Hull, Apparatus for production of three dimensional objects by stereolithography , USA: UVP, Inc. (1986). https://pubchem.ncbi.nlm.nih.gov/patent/US-6027324-A (accessed June 29, 2022).

[150] S. Mohapatra, R. Kumar Kar, P. Kumar Biswal, S. Bindhani, Approaches of 3D printing in current drug delivery, Sensors International. 3 (2022) 100146. https://doi.org/10.1016/j.sintl.2021.100146.

[151] S.C. Ligon, R. Liska, J. Stampfl, M. Gurr, R. Mülhaupt, Polymers for 3D printing and customized additive manufacturing, Chemical Reviews. 117 (2017) 10212–10290. https://doi.org/10.1021/ACS.CHEMREV.7B00074.

[152] C. Curti, D.J. Kirby, C.A. Russell, Current formulation approaches in design and development of solid oral dosage forms through three-dimensional printing, Progress in Additive Manufacturing. 5 (2020) 111–123. https://doi.org/10.1007/S40964-020-00127-5.

[153] F.P.W. Melchels, J. Feijen, D.W. Grijpma, A review on stereolithography and its applications in biomedical engineering, Biomaterials. 31 (2010) 6121–6130. https://doi.org/10.1016/J.BIOMATERIALS.2010.04.050.

[154] J. Goole, K. Amighi, 3D printing in pharmaceutics: A new tool for designing customized drug delivery systems, International Journal of Pharmaceutics. 499 (2016) 376–394. https://doi.org/10.1016/J.IJPHARM.2015.12.071.

[155] M. Vivero-Lopez, X. Xu, A. Muras, A. Otero, A. Concheiro, S. Gaisford, A.W. Basit, C. Alvarez-Lorenzo, A. Goyanes, Anti-biofilm multi drug-loaded 3D printed

References

hearing aids, Materials Science and Engineering: C. 119 (2021) 111606. https://doi.org/10.1016/J.MSEC.2020.111606.

[156] C.P.P. Pere, S.N. Economidou, G. Lall, C. Ziraud, J.S. Boateng, B.D. Alexander, D.A. Lamprou, D. Douroumis, 3D printed microneedles for insulin skin delivery, International Journal of Pharmaceutics. 544 (2018) 425–432. https://doi.org/10.1016/J.IJPHARM.2018.03.031.

[157] X. Xu, A. Goyanes, S.J. Trenfield, L. Diaz-Gomez, C. Alvarez-Lorenzo, S. Gaisford, A.W. Basit, Stereolithography (SLA) 3D printing of a bladder device for intravesical drug delivery, Materials Science and Engineering: C. 120 (2021) 111773. https://doi.org/10.1016/J.MSEC.2020.111773.

[158] P. Robles Martinez, A. Goyanes, A.W. Basit, S. Gaisford, Fabrication of drug-loaded hydrogels with stereolithographic 3D printing, International Journal of Pharmaceutics. 532 (2017) 313–317. https://doi.org/10.1016/j.ijpharm.2017.09.003.

[159] P. Robles-Martinez, X. Xu, S.J. Trenfield, A. Awad, A. Goyanes, R. Telford, A.W. Basit, S. Gaisford, 3D Printing of a multi-layered polypill containing six drugs using a novel stereolithographic method, Pharmaceutics. 11 (2019) 274. https://doi.org/10.3390/PHARMACEUTICS11060274.

[160] R. Langer, Selected advances in drug delivery and tissue engineering, Journal of Controlled Release. 62 (1999) 7–11. https://doi.org/10.1016/s0168-3659(99)00057-7.

[161] J.H. Kim, J.W. Lee, W.S. Yun, Fabrication and tissue engineering application of a 3D PPF/DEF scaffold using blu-ray based 3D printing system, Journal of Mechanical Science and Technology. 31 (2017) 2581–2587. https://doi.org/10.1007/S12206-017-0456-Y.

[162] T. Dostalova, A. Prochazka, P. Urbanova, H. Eliasova, 3D stereolithography print (SLA) in clinical orthodontic and dental applications, in: Lasers in Dentistry XXVIII, Society of Photo-Optical Instrumentation Engineers, San Francisco, 2022: p. 1194207. https://doi.org/10.1117/12.2608661.

[163] C. Curti, D.J. Kirby, C.A. Russell, Stereolithography apparatus evolution: Enhancing throughput and efficiency of pharmaceutical formulation development, Pharmaceutics. 13 (2021) 616. https://doi.org/10.3390/PHARMACEUTICS13050616.

[164] W. Weiss, D.L. Bourell, Selective laser sintering of intermetallics, Metallurgical Transactions A. 24 (1993) 757–759. https://doi.org/10.1007/BF02656644.

[165] S. Gaisford, 3D printed pharmaceutical products, 3D Printing in Medicine. (2017) 155–166. https://doi.org/10.1016/B978-0-08-100717-4.00007-7.

[166] E.O. Olakanmi, R.F. Cochrane, K.W. Dalgarno, A review on selective laser sintering/melting (SLS/SLM) of aluminium alloy powders: Processing, microstructure, and properties, Progress in Materials Science. 74 (2015) 401–477. https://doi.org/10.1016/J.PMATSCI.2015.03.002.

[167] M. Chung, N. Radacsi, C. Robert, E.D. McCarthy, A. Callanan, N. Conlisk, P.R. Hoskins, V. Koutsos, On the optimization of low-cost FDM 3D printers for accurate replication of patient-specific abdominal aortic aneurysm geometry, 3D Printing in Medicine. 4 (2018) 1–10. https://doi.org/10.1186/S41205-017-0023-2.

[168] F. Fina, C.M. Madla, A. Goyanes, J. Zhang, S. Gaisford, A.W. Basit, Fabricating 3D printed orally disintegrating printlets using selective laser sintering, International Journal of Pharmaceutics. 541 (2018) 101–107. https://doi.org/10.1016/j.ijpharm.2018.02.015.

[169] F. Fina, A. Goyanes, C.M. Madla, A. Awad, S.J. Trenfield, J.M. Kuek, P. Patel, S. Gaisford, A.W. Basit, 3D printing of drug-loaded gyroid lattices using selective laser sintering, International Journal of Pharmaceutics. 547 (2018) 44–52. https://doi.org/10.1016/J.IJPHARM.2018.05.044.

[170] A. Awad, A. Yao, S.J. Trenfield, A. Goyanes, S. Gaisford, A.W. Basit, 3D printed tablets (Printlets) with braille and moon patterns for visually impaired patients, Pharmaceutics. 12 (2020) 172. https://doi.org/10.3390/PHARMACEUTICS12020172.

[171] X. Zhu, H. Li, L. Huang, M. Zhang, W. Fan, L. Cui, 3D printing promotes the development of drugs, Biomedicine and Pharmacotherapy. 131 (2020) 110644. https://doi.org/10.1016/J.BIOPHA.2020.110644.

[172] A. Awad, F. Fina, S.J. Trenfield, P. Patel, A. Goyanes, S. Gaisford, A.W. Basit, 3D printed pellets (Miniprintlets): A novel, multi-drug, controlled release platform technology, Pharmaceutics. 11 (2019) 148. https://doi.org/10.3390/PHARMACEUTICS11040148.

[173] J.J. Water, A. Bohr, J. Boetker, J. Aho, N. Sandler, H.M. Nielsen, J. Rantanen, Three-dimensional printing of drug-eluting implants: Preparation of an antimicrobial polylactide feedstock material, Journal of Pharmaceutical Sciences. 104 (2015) 1099–1107. https://doi.org/10.1002/JPS.24305.

[174] N.A. Charoo, S.F. Barakh Ali, E.M. Mohamed, M.A. Kuttolamadom, T. Ozkan, M.A. Khan, Z. Rahman, Selective laser sintering 3D printing–An overview of the technology and pharmaceutical applications, Drug Development and Industrial Pharmacy. 46 (2020) 869–877. https://doi.org/10.1080/03639045.2020.1764027.

[175] F. Rouzé l'Alzit, R. Cade, A. Naveau, J. Babilotte, M. Meglioli, S. Catros, Accuracy of commercial 3D printers for the fabrication of surgical guides in dental implantology, Journal of Dentistry. 117 (2022) 103909. https://doi.org/10.1016/J.JDENT.2021.103909.

[176] S. Infanger, A. Haemmerli, S. Iliev, A. Baier, E. Stoyanov, J. Quodbach, Powder bed 3D-printing of highly loaded drug delivery devices with hydroxypropyl cellulose as solid binder, International Journal of Pharmaceutics. 555 (2019) 198–206. https://doi.org/10.1016/J.IJPHARM.2018.11.048.

References

[177] S.J. Trenfield, A. Awad, A. Goyanes, S. Gaisford, A.W. Basit, 3D printing pharmaceuticals: Drug development to frontline care, Trends in Pharmacological Sciences. 39 (2018) 440–451. https://doi.org/10.1016/J.TIPS.2018.02.006.

[178] L. Zema, A. Melocchi, A. Maroni, A. Gazzaniga, Three-dimensional printing of medicinal products and the challenge of personalized therapy, Journal of Pharmaceutical Sciences. 106 (2017) 1697–1705. https://doi.org/10.1016/J.XPHS.2017.03.021.

[179] E. Sachs, M. Cima, P. Williams, D. Brancazio, J. Cornie, Three dimensional printing: Rapid tooling and prototypes directly from a CAD model, Journal of Engineering for Industry. 114 (1992) 481–488. https://doi.org/10.1115/1.2900701.

[180] B.M. Wu, S.W. Borland, R.A. Giordano, L.G. Cima, E.M. Sachs, M.J. Cima, Solid free-form fabrication of drug delivery devices, Journal of Controlled Release. 40 (1996) 77–87. https://doi.org/10.1016/0168-3659(95)00173-5.

[181] D.G. Yu, C. Branford-White, Y.C. Yang, L.M. Zhu, E.W. Welbeck, X.L. Yang, A novel fast disintegrating tablet fabricated by three-dimensional printing, Drug Development and Industrial Pharmacy. 35 (2009) 1530–1536. https://doi.org/10.3109/03639040903059359.

[182] D.-G. Yu, X.-X. Shen, C. Branford-White, L.-M. Zhu, K. White, X.L. Yang, Novel oral fast-disintegrating drug delivery devices with predefined inner structure fabricated by three-dimensional printing., Journal of Pharmacy and Pharmacology. 61 (2009) 323–329. https://doi.org/10.1211/JPP/61.03.0006.

[183] W.E. Katstra, R.D. Palazzolo, C.W. Rowe, B. Giritlioglu, P. Teung, M.J. Cima, Oral dosage forms fabricated by three dimensional printing, Journal of Controlled Release. 66 (2000) 1–9. https://doi.org/10.1016/S0168-3659(99)00225-4.

[184] C.W. Rowe, W.E. Katstra, R.D. Palazzolo, B. Giritlioglu, P. Teung, M.J. Cima, Multimechanism oral dosage forms fabricated by three dimensional printing, Journal of Controlled Release. 66 (2000) 11–17. https://doi.org/10.1016/S0168-3659(99)00224-2.

[185] G.Y. Deng, L.Y. Xiang, D.H. Wei, J. Liu, G.W. Yun, H. Xu, Tablets with material gradients fabricated by three-dimensional printing, Journal of Pharmaceutical Sciences. 96 (2007) 2446–2456. https://doi.org/10.1002/JPS.20864.

[186] X. Li, E. Liang, X. Hong, X. Han, C. Li, Y. Wang, Z. Wang, A. Zheng, In vitro and in vivo bioequivalence study of 3d-printed instant-dissolving levetiracetam tablets and subsequent personalized dosing for chinese children based on physiological pharmacokinetic modeling, Pharmaceutics. 14 (2022) 20. https://doi.org/10.3390/PHARMACEUTICS14010020.

[187] L.K. Prasad, H. Smyth, 3D Printing technologies for drug delivery: A review, Drug Development and Industrial Pharmacy. 42 (2016) 1019–1031. https://doi.org/10.3109/03639045.2015.1120743.

[188] A. Goyanes, M. Scarpa, M. Kamlow, S. Gaisford, A.W. Basit, M. Orlu, Patient acceptability of 3D printed medicines, International Journal of Pharmaceutics. 530 (2017) 71–78. https://doi.org/10.1016/j.ijpharm.2017.07.064.

[189] V.M. Vaz, L. Kumar, 3D printing as a promising tool in personalized medicine, AAPS PharmSciTech. 22 (2021) 49. https://doi.org/10.1208/s12249-020-01905-8.

[190] S. Jacob, A.B. Nair, V. Patel, J. Shah, 3D printing technologies: Recent development and emerging applications in various drug delivery systems, AAPS PharmSciTech. 21 (2020) 220. https://doi.org/10.1208/S12249-020-01771-4.

[191] A. Goyanes, N. Allahham, S.J. Trenfield, E. Stoyanov, S. Gaisford, A.W. Basit, Direct powder extrusion 3D printing: Fabrication of drug products using a novel single-step process, International Journal of Pharmaceutics. 567 (2019) 118471. https://doi.org/10.1016/J.IJPHARM.2019.118471.

[192] Y. Zheng, F. Deng, B. Wang, Y. Wu, Q. Luo, X. Zuo, X. Liu, L. Cao, M. Li, H. Lu, S. Cheng, X. Li, Melt extrusion deposition (MED^{TM}) 3D printing technology – A paradigm shift in design and development of modified release drug products, International Journal of Pharmaceutics. 602 (2021) 120639. https://doi.org/10.1016/J.IJPHARM.2021.120639.

[193] M. Fanous, S. Gold, S. Muller, S. Hirsch, J. Ogorka, G. Imanidis, Simplification of fused deposition modeling 3D-printing paradigm: Feasibility of 1-step direct powder printing for immediate release dosage form production, International Journal of Pharmaceutics. 578 (2020) 119124. https://doi.org/10.1016/J.IJPHARM.2020.119124.

[194] Triastek, Inc-Triastek Receives FDA IND Clearance for 3D Printed Product of Blockbuster Molecule, (2022). https://www.triastek.com/detail/22.html (accessed July 1, 2022).

[195] J. Rahman, J. Quodbach, Versatility on demand - The case for semi-solid micro-extrusion in pharmaceutics, Advanced Drug Delivery Reviews. 172 (2021) 104–126. https://doi.org/10.1016/j.addr.2021.02.013.

[196] I. El-Aita, J. Breitkreutz, J. Quodbach, Investigation of semi-solid formulations for 3D printing of drugs after prolonged storage to mimic real-life applications, European Journal of Pharmaceutical Sciences. 146 (2020) 105266. https://doi.org/10.1016/J.EJPS.2020.105266.

[197] L. Lopez-Vidal, J.P. Real, D.A. Real, N. Camacho, M.J. Kogan, A.J. Paredes, S.D. Palma, Nanocrystal-based 3D-printed tablets: Semi-solid extrusion using melting solidification printing process (MESO-PP) for oral administration of poorly soluble drugs, International Journal of Pharmaceutics. 611 (2022) 121311. https://doi.org/10.1016/J.IJPHARM.2021.121311.

[198] S.A. Khaled, J.C. Burley, M.R. Alexander, C.J. Roberts, Desktop 3D printing of controlled release pharmaceutical bilayer tablets, International Journal of Pharmaceutics. 461 (2014) 105–111. https://doi.org/10.1016/j.ijpharm.2013.11.021.

References

[199] A. Tirella, A. Orsini, G. Vozzi, A. Ahluwalia, A phase diagram for microfabrication of geometrically controlled hydrogel scaffolds, Biofabrication. 1 (2009) 045002. https://doi.org/10.1088/1758-5082/1/4/045002.

[200] F. Dores, M. Kuźmińska, C. Soares, M. Bohus, L. A Shervington, R. Habashy, B.C. Pereira, M. Peak, A. Isreb, M.A. Alhnan, Temperature and solvent facilitated extrusion based 3D printing for pharmaceuticals, European Journal of Pharmaceutical Sciences. 152 (2020) 105430. https://doi.org/10.1016/J.EJPS.2020.105430.

[201] R. Ajdary, N.Z. Ezazi, A. Correia, M. Kemell, S. Huan, H.J. Ruskoaho, J. Hirvonen, H.A. Santos, O.J. Rojas, Multifunctional 3D-printed patches for long-term drug release therapies after myocardial infarction, Advanced Functional Materials. 30 (2020) 2003440. https://doi.org/10.1002/ADFM.202003440.

[202] S.A. Khaled, J.C. Burley, M.R. Alexander, J. Yang, C.J. Roberts, 3D printing of tablets containing multiple drugs with defined release profiles, International Journal of Pharmaceutics. 494 (2015) 643–650. https://doi.org/10.1016/j.ijpharm.2015.07.067.

[203] J.T. Carstensen, Effect of moisture on the stability of solid dosage forms, Drug Development and Industrial Pharmacy. 14 (2008) 1927–1969. https://doi.org/10.3109/03639048809151998.

[204] S.A. Khaled, M.R. Alexander, R.D. Wildman, M.J. Wallace, S. Sharpe, J. Yoo, C.J. Roberts, 3D extrusion printing of high drug loading immediate release paracetamol tablets, International Journal of Pharmaceutics. 538 (2018) 223–230. https://doi.org/10.1016/j.ijpharm.2018.01.024.

[205] H. Herrada-Manchón, D. Rodríguez-González, M. Alejandro Fernández, M. Suñé-Pou, P. Pérez-Lozano, E. García-Montoya, E. Aguilar, 3D printed gummies: Personalized drug dosage in a safe and appealing way, International Journal of Pharmaceutics. 587 (2020) 119687. https://doi.org/10.1016/J.IJPHARM.2020.119687.

[206] E. Sjöholm, N. Sandler, Additive manufacturing of personalized orodispersible warfarin films, International Journal of Pharmaceutics. 564 (2019) 117–123. https://doi.org/10.1016/J.IJPHARM.2019.04.018.

[207] S.A. Khaled, J.C. Burley, M.R. Alexander, J. Yang, C.J. Roberts, 3D printing of five-in-one dose combination polypill with defined immediate and sustained release profiles, Journal of Controlled Release. 217 (2015) 308–314. https://doi.org/10.1016/J.JCONREL.2015.09.028.

[208] I. Seoane-Viaño, J.J. Ong, A. Luzardo-Álvarez, M. González-Barcia, A.W. Basit, F.J. Otero-Espinar, A. Goyanes, 3D printed tacrolimus suppositories for the treatment of ulcerative colitis, Asian Journal of Pharmaceutical Sciences. 16 (2021) 110–119. https://doi.org/10.1016/J.AJPS.2020.06.003.

[209] T. Ahlfeld, A.R. Akkineni, Y. Förster, T. Köhler, S. Knaack, M. Gelinsky, A. Lode, Design and fabrication of complex scaffolds for bone defect healing: Combined 3D plotting of a calcium phosphate cement and a growth factor-loaded

hydrogel, Annals of Biomedical Engineering. 45 (2017) 224–236. https://doi.org/10.1007/S10439-016-1685-4.

[210] M. Kammerer, M. Fabritius, C. Carvalho, R. Mülhaupt, T.J. Feuerstein, R. Trittler, Valproate release from polycaprolactone implants prepared by 3D-bioplotting, Pharmazie. 66 (2011) 511–516. https://doi.org/10.1691/PH.2011.0882.

[211] J. Long, A.E. Etxeberria, A. v. Nand, C.R. Bunt, S. Ray, A. Seyfoddin, A 3D printed chitosan-pectin hydrogel wound dressing for lidocaine hydrochloride delivery, Materials Science and Engineering: C. 104 (2019) 109873. https://doi.org/10.1016/J.MSEC.2019.109873.

[212] I.T. Ozbolat, M. Hospodiuk, Current advances and future perspectives in extrusion-based bioprinting, Biomaterials. 76 (2016) 321–343. https://doi.org/10.1016/J.BIOMATERIALS.2015.10.076.

[213] S. v. Murphy, A. Atala, 3D bioprinting of tissues and organs, Nature Biotechnology. 32 (2014) 773–785. https://doi.org/10.1038/NBT.2958.

[214] C. Korte, J. Quodbach, Formulation development and process analysis of drug-loaded filaments manufactured via hot-melt extrusion for 3D-printing of medicines, Pharmaceutical Development and Technology. 23 (2018) 1117–1127. https://doi.org/10.1080/10837450.2018.1433208.

[215] C. Korte, 3D-Drug-Printing: Extrusion of printable drug-loaded filaments and development of novel solid dosage forms, Dissertation, Heinrich Heine Universität Düsseldorf. (2018).

[216] R. Chamberlain, H. Windolf, S. Geissler, J. Quodbach, J. Breitkreutz, Precise dosing of pramipexole for low-dosed filament production by hot melt extrusion applying various feeding methods, Pharmaceutics. 14 (2022) 216. https://doi.org/10.3390/PHARMACEUTICS14010216.

[217] M.A. Azad, D. Olawuni, G. Kimbell, A.Z.M. Badruddoza, M.S. Hossain, T. Sultana, Polymers for extrusion-based 3D printing of pharmaceuticals: A holistic materials–process perspective, Pharmaceutics. 12 (2020) 124. https://doi.org/10.3390/PHARMACEUTICS12020124.

[218] J. Quodbach, M. Bogdahn, J. Breitkreutz, R. Chamberlain, K. Eggenreich, A.G. Elia, N. Gottschalk, G. Gunkel-Grabole, L. Hoffmann, D. Kapote, T. Kipping, S. Klinken, F. Loose, T. Marquetant, H. Windolf, S. Geißler, T. Spitz, Quality of FDM 3D printed medicines for pediatrics: Considerations for formulation development, filament extrusion, printing process and printer design, Therapeutic Innovation & Regulatory Science. 56 (2022) 910–928. https://doi.org/10.1007/S43441-021-00354-0.

[219] J. Skowyra, K. Pietrzak, M.A. Alhnan, Fabrication of extended-release patient-tailored prednisolone tablets via fused deposition modelling (FDM) 3D printing, European Journal of Pharmaceutical Sciences. 68 (2015) 11–17. https://doi.org/10.1016/j.ejps.2014.11.009.

References

[220] J. Zhang, X. Feng, H. Patil, R. v. Tiwari, M.A. Repka, Coupling 3D printing with hot-melt extrusion to produce controlled-release tablets, International Journal of Pharmaceutics. 519 (2017) 186–197. https://doi.org/10.1016/j.ijpharm.2016.12.049.

[221] D.K. Tan, M. Maniruzzaman, A. Nokhodchi, Advanced pharmaceutical applications of hot-melt extrusion coupled with fused deposition modelling (FDM) 3D printing for personalised drug delivery, Pharmaceutics. 10 (2018) 203. https://doi.org/10.3390/pharmaceutics10040203.

[222] Z. Hu, P. Xu, J. Zhang, S. Bandari, M.A. Repka, Development of controlled release oral dosages by density gradient modification via three-dimensional (3D) printing and hot-melt extrusion (HME) technology, Journal of Drug Delivery Science and Technology. 71 (2022) 103355. https://doi.org/10.1016/J.JDDST.2022.103355.

[223] S. v. Bhujbal, B. Mitra, U. Jain, Y. Gong, A. Agrawal, S. Karki, L.S. Taylor, S. Kumar, Q. (Tony) Zhou, Pharmaceutical amorphous solid dispersion: A review of manufacturing strategies, Acta Pharmaceutica Sinica B. 11 (2021) 2505–2536. https://doi.org/10.1016/J.APSB.2021.05.014.

[224] H. Windolf, R. Chamberlain, J. Breitkreutz, J. Quodbach, 3D printed mini-floating-polypill for Parkinson's disease: Combination of levodopa, benserazide, and pramipexole in various dosing for personalized therapy, Pharmaceutics. 14 (2022) 931. https://doi.org/10.3390/PHARMACEUTICS14050931.

[225] T.D. Reynolds, S.A. Mitchell, K.M. Balwinski, Investigation of the effect of tablet surface area/volume on drug release from hydroxypropylmethylcellulose controlled-release matrix tablets, Drug Development and Industrial Pharmacy. 28 (2002) 457–466. https://doi.org/10.1081/DDC-120003007.

[226] S. Ayyoubi, J.R. Cerda, R. Fernández-García, P. Knief, A. Lalatsa, A.M. Healy, D.R. Serrano, 3D printed spherical mini-tablets: Geometry versus composition effects in controlling dissolution from personalised solid dosage forms, International Journal of Pharmaceutics. 597 (2021) 120336. https://doi.org/10.1016/J.IJPHARM.2021.120336.

[227] S. Vijayavenkataraman, J.Y.H. Fuh, W.F. Lu, 3D printing and 3D bioprinting in pediatrics, Bioengineering. 4 (2017) 63–74. https://doi.org/10.3390/BIOENGINEERING4030063.

[228] B.C. Pereira, A. Isreb, R.T. Forbes, F. Dores, R. Habashy, J.B. Petit, M.A. Alhnan, E.F. Oga, 'Temporary Plasticiser': A novel solution to fabricate 3D printed patient-centred cardiovascular 'Polypill' architectures, European Journal of Pharmaceutics and Biopharmaceutics. 135 (2019) 94–103. https://doi.org/10.1016/J.EJPB.2018.12.009.

[229] N. Keikhosravi, S.Z. Mirdamadian, J. Varshosaz, A. Taheri, Preparation and characterization of polypills containing aspirin and simvastatin using 3D printing technology for the prevention of cardiovascular diseases, Drug Development and

Industrial Pharmacy. 46 (2020) 1665–1675.
https://doi.org/10.1080/03639045.2020.1820034.

[230] C.R.M. Brambilla, O.L. Okafor-Muo, H. Hassanin, A. ElShaer, 3DP printing of oral solid formulations: A systematic review, Pharmaceutics. 13 (2021) 358. https://doi.org/10.3390/PHARMACEUTICS13030358.

[231] W. Kempin, V. Domsta, G. Grathoff, I. Brecht, B. Semmling, S. Tillmann, W. Weitschies, A. Seidlitz, Immediate release 3D-printed tablets produced via fused deposition modeling of a thermo-sensitive drug, Pharmaceutical Research. 35 (2018) 124. https://doi.org/10.1007/S11095-018-2405-6.

[232] S. Abdella, S.H. Youssef, F. Afinjuomo, Y. Song, P. Fouladian, R. Upton, S. Garg, 3D printing of thermo-sensitive drugs, Pharmaceutics. 13 (2021) 1524. https://doi.org/10.3390/PHARMACEUTICS13091524.

[233] A. Melocchi, F. Parietti, G. Loreti, A. Maroni, A. Gazzaniga, L. Zema, 3D printing by fused deposition modeling (FDM) of a swellable/erodible capsular device for oral pulsatile release of drugs, Journal of Drug Delivery Science and Technology. 30 (2015) 360–367. https://doi.org/10.1016/J.JDDST.2015.07.016.

[234] H. Wang, N. Dumpa, S. Bandari, T. Durig, M.A. Repka, Fabrication of taste-masked donut-shaped tablets via fused filament fabrication 3D printing paired with hot-melt extrusion techniques, AAPS PharmSciTech. 21 (2020) 243. https://doi.org/10.1208/S12249-020-01783-0.

[235] A. Goyanes, H. Chang, D. Sedough, G.B. Hatton, J. Wang, A. Buanz, S. Gaisford, A.W. Basit, Fabrication of controlled-release budesonide tablets via desktop (FDM) 3D printing, International Journal of Pharmaceutics. 496 (2015) 414–420. https://doi.org/10.1016/j.ijpharm.2015.10.039.

[236] K. Pietrzak, A. Isreb, M.A. Alhnan, A flexible-dose dispenser for immediate and extended release 3D printed tablets, European Journal of Pharmaceutics and Biopharmaceutics. 96 (2015) 380–387. https://doi.org/10.1016/j.ejpb.2015.07.027.

[237] T.C. Okwuosa, B.C. Pereira, B. Arafat, M. Cieszynska, A. Isreb, M.A. Alhnan, Fabricating a shell-core delayed release tablet using dual FDM 3D printing for patient-centred therapy, Pharmaceutical Research. 34 (2017) 427–437. https://doi.org/10.1007/s11095-016-2073-3.

[238] J.H. Kim, K. Kim, H.E. Jin, Three-dimensional printing for oral pharmaceutical dosage forms, Journal of Pharmaceutical Investigation. 52 (2022) 293–317. https://doi.org/10.1007/S40005-022-00561-3.

[239] N. Genina, J. Holländer, H. Jukarainen, E. Mäkilä, J. Salonen, N. Sandler, Ethylene vinyl acetate (EVA) as a new drug carrier for 3D printed medical drug delivery devices, European Journal of Pharmaceutical Sciences. 90 (2016) 53–63. https://doi.org/10.1016/J.EJPS.2015.11.005.

[240] J. Holländer, N. Genina, H. Jukarainen, M. Khajeheian, A. Rosling, E. Mäkilä, N. Sandler, Three-dimensional printed PCL-based implantable prototypes of medical

devices for controlled drug delivery, Journal of Pharmaceutical Sciences. 105 (2016) 2665–2676. https://doi.org/10.1016/J.XPHS.2015.12.012.

[241] H.G. Yi, Y.J. Choi, K.S. Kang, J.M. Hong, R.G. Pati, M.N. Park, I.K. Shim, C.M. Lee, S.C. Kim, D.W. Cho, A 3D-printed local drug delivery patch for pancreatic cancer growth suppression, Journal of Controlled Release. 238 (2016) 231–241. https://doi.org/10.1016/J.JCONREL.2016.06.015.

[242] A. Goyanes, U. Det-Amornrat, J. Wang, A.W. Basit, S. Gaisford, 3D scanning and 3D printing as innovative technologies for fabricating personalized topical drug delivery systems, Journal of Controlled Release. 234 (2016) 41–48. https://doi.org/10.1016/j.jconrel.2016.05.034.

[243] W. Jamróz, M. Kurek, E. Łyszczarz, J. Szafraniec, J. Knapik-Kowalczuk, K. Syrek, M. Paluch, R. Jachowicz, 3D printed orodispersible films with aripiprazole, International Journal of Pharmaceutics. 533 (2017) 413–420. https://doi.org/10.1016/J.IJPHARM.2017.05.052.

[244] C.I. Gioumouxouzis, E. Tzimtzimis, O.L. Katsamenis, A. Dourou, C. Markopoulou, N. Bouropoulos, D. Tzetzis, D.G. Fatouros, Fabrication of an osmotic 3D printed solid dosage form for controlled release of active pharmaceutical ingredients, European Journal of Pharmaceutical Sciences. 143 (2020) 105176. https://doi.org/10.1016/J.EJPS.2019.105176.

[245] J. Fu, X. Yu, Y. Jin, 3D printing of vaginal rings with personalized shapes for controlled release of progesterone, International Journal of Pharmaceutics. 539 (2018) 75–82. https://doi.org/10.1016/J.IJPHARM.2018.01.036.

[246] M.A. Luzuriaga, D.R. Berry, J.C. Reagan, R.A. Smaldone, J.J. Gassensmith, Biodegradable 3D printed polymer microneedles for transdermal drug delivery, Lab on a Chip. 18 (2018) 1223–1230. https://doi.org/10.1039/C8LC00098K.

[247] A.Q. Vo, J. Zhang, D. Nyavanandi, S. Bandari, M.A. Repka, Hot melt extrusion paired fused deposition modeling 3D printing to develop hydroxypropyl cellulose based floating tablets of cinnarizine, Carbohydrate Polymers. 246 (2020) 116519. https://doi.org/10.1016/J.CARBPOL.2020.116519.

[248] FabRx Limited, FabRx's pharmaceutical 3D printer for personalised medicines, M3DIMAKER™, is now available!, (2020). https://www.fabrx.co.uk/2020/04/06/fabrxs-pharmaceutical-3d-printer-for-personalised-medicines-m3dimaker-is-now-available/ (accessed July 10, 2022).

[249] DiHeSys, Digital-Health-Systems | 3D & 2D printed drugs | Deutschland, (2022). https://www.digital-health-systems.com/ (accessed July 10, 2022).

[250] A. Gosset, D. Barreiro-Villaverde, J.C.B. Permuy, M. Lema, A. Ares-Pernas, M.J.A. López, Experimental and numerical investigation of the extrusion and deposition process of a poly(lactic acid) strand with fused deposition modeling, Polymers. 12 (2020) 2885. https://doi.org/10.3390/POLYM12122885.

[251] S.J. Trenfield, A. Goyanes, R. Telford, D. Wilsdon, M. Rowland, S. Gaisford, A.W. Basit, 3D printed drug products: Non-destructive dose verification using a

rapid point-and-shoot approach, International Journal of Pharmaceutics. 549 (2018) 283–292. https://doi.org/10.1016/J.IJPHARM.2018.08.002.

[252] H. Windolf, R. Chamberlain, A. Delmotte, J. Quodbach, Blind-watermarking -- Proof-of-concept of a novel approach to ensure batch traceability for 3D printed tablets, Pharmaceutics. 14 (2022) 432. https://doi.org/10.3390/PHARMACEU-TICS14020432.

[253] D. McManus, B.D. Naughton, A systematic review of substandard, falsified, unlicensed and unregistered medicine sampling studies: A focus on context, prevalence, and quality, BMJ Global Health. 5 (2020) e002393. https://doi.org/10.1136/BMJGH-2020-002393.

[254] P. Feldschreiber, Public health issues with counterfeit medicines, Clinical Medicine, Journal of the Royal College of Physicians of London. 9 (2009) 63–64. https://doi.org/10.7861/CLINMEDICINE.9-1-63.

[255] M. Uddin, Blockchain Medledger: Hyperledger fabric enabled drug traceability system for counterfeit drugs in pharmaceutical industry, International Journal of Pharmaceutics. 597 (2021) 120235. https://doi.org/10.1016/J.IJPHARM.2021.120235.

[256] World Health Organization, WHO global surveillance and monitoring system for substandard and falsified medical products, World Health Organization. (2017). https://apps.who.int/iris/handle/10665/326708 (accessed January 24, 2023).

[257] A.S. Bolla, A.R. Patel, R. Priefer, The silent development of counterfeit medications in developing countries – A systematic review of detection technologies, International Journal of Pharmaceutics. 587 (2020) 119702. https://doi.org/10.1016/J.IJPHARM.2020.119702.

[258] S.J. Trenfield, H. Xian Tan, A. Awad, A. Buanz, S. Gaisford, A.W. Basit, A. Goyanes, Track-and-trace: Novel anti-counterfeit measures for 3D printed personalized drug products using smart material inks, International Journal of Pharmaceutics. 567 (2019) 118443. https://doi.org/10.1016/J.IJPHARM.2019.06.034.

[259] H.L. Liu, B. Zhang, T. Gao, X. Wu, F. Cui, W. Xu, 3D chiral color prints for anti-counterfeiting, Nanoscale. 11 (2019) 5506–5511. https://doi.org/10.1039/C8NR09975H.

[260] N. Alam, M.R. Hasan Tanvir, S.A. Shanto, F. Israt, A. Rahman, S. Momotaj, Blockchain based counterfeit medicine authentication system, in: IEEE 11th Symposium on Computer Applications and Industrial Electronics (ISCAIE), Institute of Electrical and Electronics Engineers Inc., Penang, Malaysia, 2021: pp. 214–217. https://doi.org/10.1109/ISCAIE51753.2021.9431789.

[261] FDA Guidance, Technical considerations for additive manufactured medical devices, Guidance for Industry and Food and Drug Administration Staff. (2017). https://www.fda.gov/regulatory-information/search-fda-guidance-documents/technical-considerations-additive-manufactured-medical-devices (accessed July 10, 2022).

References

[262] FDA, CDER, Distributed manufacturing and point-of-care manufacturing of drugs, Center for Drug Evaluation and Research - Discussion Paper. (2022) 1–21.

[263] M. Palo, J. Holländer, J. Suominen, J. Yliruusi, N. Sandler, 3D printed drug delivery devices: Perspectives and technical challenges, Expert Review of Medical Devices. 14 (2017) 685–696. https://doi.org/10.1080/17434440.2017.1363647.

[264] Spritam - A new formulation of levetiracetam for epilepsy, Medical Letter on Drugs and Therapeutics. 58 (2016) 78–79.

[265] M. Elbadawi, B. Muñiz Castro, F.K.H. Gavins, J.J. Ong, S. Gaisford, G. Pérez, A.W. Basit, P. Cabalar, A. Goyanes, M3DISEEN: A novel machine learning approach for predicting the 3D printability of medicines, International Journal of Pharmaceutics. 590 (2020) 119837. https://doi.org/10.1016/J.IJPHARM.2020.119837.

[266] T. Ahlfeld, V. Guduric, S. Duin, A.R. Akkineni, K. Schütz, D. Kilian, J. Emmermacher, N. Cubo-Mateo, S. Dani, M. v. Witzleben, J. Spangenberg, R. Abdelgaber, R.F. Richter, A. Lode, M. Gelinsky, Methylcellulose-a versatile printing material that enables biofabrication of tissue equivalents with high shape fidelity, Biomaterials Science. 8 (2020) 2102–2110. https://doi.org/10.1039/D0BM00027B.

[267] BMBF Poly-Implant, Reparatur von Gelenken: Die Schnittstelle zwischen Knochen und Knorpel (Poly-IMPLANT-Druck) | werkstofftechnologien.de, (2019). https://www.werkstofftechnologien.de/veranstaltungen/messepraesentation-auf-der-compamed-2021/reparatur-von-gelenken-die-schnittstelle-zwischen-knochen-und-knorpel-poly-implant-druck (accessed June 26, 2022).

[268] R. Chamberlain, H. Windolf, B.B. Burckhardt, J. Breitkreutz, B. Fischer, Embedding a sensitive liquid-core waveguide UV detector into an HPLC-UV system for simultaneous quantification of differently dosed active ingredients during drug release, Pharmaceutics. 14 (2022) 639. https://doi.org/10.3390/PHARMACEUTICS14030639.

[269] N. Gottschalk, M. Bogdahn, M. Harms, J. Quodbach, Brittle polymers in fused deposition modeling: An improved feeding approach to enable the printing of highly drug loaded filament, International Journal of Pharmaceutics. 597 (2021) 120216. https://doi.org/10.1016/J.IJPHARM.2021.120216.

[270] N. Gottschalk, J. Quodbach, A.G. Elia, F. Hess, M. Bogdahn, Determination of feed forces to improve process understanding of fused deposition modeling 3D printing and to ensure mass conformity of printed solid oral dosage forms, International Journal of Pharmaceutics. 614 (2022) 121416. https://doi.org/10.1016/J.IJPHARM.2021.121416.

[271] A. Goyanes, C.M. Madla, A. Umerji, G. Duran Piñeiro, J.M. Giraldez Montero, M.J. Lamas Diaz, M. Gonzalez Barcia, F. Taherali, P. Sánchez-Pintos, M.L. Couce, S. Gaisford, A.W. Basit, Automated therapy preparation of isoleucine formulations using 3D printing for the treatment of MSUD: First single-centre, prospective, crossover study in patients, International Journal of Pharmaceutics. 567 (2019) 118497. https://doi.org/10.1016/J.IJPHARM.2019.118497.

[272] C.R. Sagandira, M. Siyawamwaya, P. Watts, 3D printing and continuous flow chemistry technology to advance pharmaceutical manufacturing in developing countries, Arabian Journal of Chemistry. 13 (2020) 7886–7908. https://doi.org/10.1016/J.ARABJC.2020.09.020.

[273] S. Saunders, Astronauts 3D print the first medical supplies in space, which can also teach us more about healthcare on earth, (2017). https://3dprint.com/162241/3d-print-medical-supplies-in-space/ (accessed July 16, 2022).

[274] Y. Gao, C. Gesenberg, W. Zheng, Oral formulations for preclinical studies: Principle, design, and development considerations, Developing Solid Oral Dosage Forms: Pharmaceutical Theory and Practice: Second Edition. (2017) 455–495. https://doi.org/10.1016/B978-0-12-802447-8.00017-0.

[275] S. Agatonovic-Kustrin, R. Beresford, Basic concepts of artificial neural network (ANN) modeling and its application in pharmaceutical research, Journal of Pharmaceutical and Biomedical Analysis. 22 (2000) 717–727. https://doi.org/10.1016/S0731-7085(99)00272-1.

[276] P. Hassanzadeh, F. Atyabi, R. Dinarvand, The significance of artificial intelligence in drug delivery system design, Advanced Drug Delivery Reviews. 151–152 (2019) 169–190. https://doi.org/10.1016/J.ADDR.2019.05.001.

[277] Y. Yang, Z. Ye, Y. Su, Q. Zhao, X. Li, D. Ouyang, Deep learning for in vitro prediction of pharmaceutical formulations, Acta Pharmaceutica Sinica B. 9 (2019) 177–185. https://doi.org/10.1016/J.APSB.2018.09.010.

[278] Y. Peng, M. Geraldrajan, Q. Chen, Y. Sun, J.R. Johnson, A.J. Shukla, Prediction of dissolution profiles of acetaminophen beads using artificial neural networks, Pharmaceutical Development and Technology. 11 (2006) 337–349. https://doi.org/10.1080/10837450600769744.

[279] Y. Zhao, W. Li, Z. Shi, J.K. Drennen, C.A. Anderson, Prediction of dissolution profiles from process parameters, formulation, and spectroscopic measurements, Journal of Pharmaceutical Sciences. 108 (2019) 2119–2127. https://doi.org/10.1016/j.xphs.2019.01.023.

[280] J. Petru, P. Zamostny, Prediction of dissolution behavior of final dosage forms prepared by different granulation methods, Procedia Engineering. 42 (2012) 1463–1473. https://doi.org/10.1016/j.proeng.2012.07.539.

[281] M. Madzarevic, D. Medarevic, A. Vulovic, T. Sustersic, J. Djuris, N. Filipovic, S. Ibric, Optimization and prediction of ibuprofen release from 3D DLP printlets using artificial neural networks, Pharmaceutics. 11 (2019) 544. https://doi.org/10.3390/PHARMACEUTICS11100544.

[282] K. Takayama, S. Kawai, Y. Obata, H. Todo, K. Sugibayashi, Prediction of dissolution data integrated in tablet database using four-layered artificial neural networks, Chemical and Pharmaceutical Bulletin. 65 (2017) 967–972. https://doi.org/10.1248/cpb.c17-00539.

References

[283] A.P. Tinke, K. Vanhoutte, R. de Maesschalck, S. Verheyen, H. de Winter, A new approach in the prediction of the dissolution behavior of suspended particles by means of their particle size distribution, Journal of Pharmaceutical and Biomedical Analysis. 39 (2005) 900–907. https://doi.org/10.1016/j.jpba.2005.05.014.

[284] A. Samii, J.G. Nutt, B.R. Ransom, Parkinson's disease, The Lancet. 363 (2004) 1783–1793. https://doi.org/10.1016/S0140-6736(04)16305-8.

[285] A.E. Guttmacher, F.S. Collins, R.L. Nussbaum, C.E. Ellis, Alzheimer's disease and Parkinson's disease, The New England Journal of Medicine. 348 (2003) 1356–1364. https://doi.org/10.1056/NEJM2003RA020003.

[286] W. Poewe, K. Seppi, C.M. Tanner, G.M. Halliday, P. Brundin, J. Volkmann, A.E. Schrag, A.E. Lang, Parkinson disease, Nature Reviews Disease Primers. 3 (2017) 17013. https://doi.org/10.1038/nrdp.2017.13.

[287] J. Jankovic, Parkinson's disease: Clinical features and diagnosis, Journal of Neurology, Neurosurgery and Psychiatry. 79 (2008) 368–376. https://doi.org/10.1136/JNNP.2007.131045.

[288] J.A. Obeso, M. Stamelou, C.G. Goetz, W. Poewe, A.E. Lang, D. Weintraub, D. Burn, G.M. Halliday, E. Bezard, S. Przedborski, S. Lehericy, D.J. Brooks, J.C. Rothwell, M. Hallett, M.R. DeLong, C. Marras, C.M. Tanner, G.W. Ross, J.W. Langston, C. Klein, V. Bonifati, J. Jankovic, A.M. Lozano, G. Deuschl, H. Bergman, E. Tolosa, M. Rodriguez-Violante, S. Fahn, R.B. Postuma, D. Berg, K. Marek, D.G. Standaert, D.J. Surmeier, C.W. Olanow, J.H. Kordower, P. Calabresi, A.H.V. Schapira, A.J. Stoessl, Past, present, and future of Parkinson's disease: A special essay on the 200th anniversary of the shaking palsy, Movement Disorders. 32 (2017) 1264–1310. https://doi.org/10.1002/mds.27115.

[289] R. Chamberlain, H. Windolf, J. Breitkreutz, Arzneizubereitungen für die Therapie des idiopathischen Parkinson-Syndroms, Pharmakon. 10 (2022) 216–226.

[290] Deutsche Gesellschaft für Neurologie (DGN), S3 Leitlinie Idiopathisches Parkinson-Syndrom, AWMF-Register-Nummer: 030-010. 1 (2016) 1–77.

[291] J.E. Ahlskog, M.D. Muenter, Frequency of levodopa-related dyskinesias and motor fluctuations as estimated from the cumulative literature, Movement Disorders. 16 (2001) 448–458. https://doi.org/10.1002/MDS.1090.

[292] R.A. Hauser, Levodopa: Past, present, and future, European Neurology. 62 (2009) 1–8. https://doi.org/10.1159/000215875.

[293] S. Fahn, Levodopa-induced neurotoxicity: Does it represent a problem for the treatment of Parkinson's disease?, CNS Drugs. 8 (1997) 376–393. https://doi.org/10.2165/00023210-199708050-00004.

[294] S. Heinzel, D. Berg, S. Binder, G. Ebersbach, L. Hickstein, H. Herbst, M. Lorrain, I. Wellach, W. Maetzler, G. Petersen, N. Schmedt, J. Volkmann, D. Woitalla, V. Amelung, Do we need to rethink the epidemiology and healthcare utilization of Parkinson's disease in germany?, Frontiers in Neurology. 9 (2018) 1–9. https://doi.org/10.3389/FNEUR.2018.00500/FULL.

[295] European Pharmacopoeia Commission, Monograph Pramipexole Dihydrochloride Monohydrate, in: European Pharmacopoeia, 2020: pp. 5382–5384.

[296] M. Łaszcz, K. Trzcinska, M. Kubiszewski, B. Kosmacinska, M. Glice, Stability studies and structural characterization of pramipexole, Journal of Pharmaceutical and Biomedical Analysis. 53 (2010) 1033–1036. https://doi.org/10.1016/j.jpba.2010.06.018.

[297] A. Delmotte, K. Tanaka, H. Kubo, T. Funatomi, Y. Mukaigawa, Blind watermarking for 3-D printed objects by locally modifying layer thickness, IEEE Transactions on Multimedia. 22 (2020) 2780–2791. https://doi.org/10.1109/TMM.2019.2962306.

Chapter B:

Overview: Quality of FDM 3D Printed Medicines for Pediatrics

Quality of FDM 3D Printed Medicines for Pediatrics: Considerations for Formulation Development, Filament Extrusion, Printing Process and Printer Design

Julian Quodbach, Malte Bogdahn, Jörg Breitkreutz, Rebecca Chamberlain, Karin Eggenreich, Alessandro Giuseppe Elia, Nadine Gottschalk, Gesine Gunkel-Grabole, Lena Hoffmann, Dnyaneshwar Kapote, Thomas Kipping, Stefan Klinken, Fabian Loose, Tristan Marquetant, Hellen Windolf, Simon Geißler, Tilmann Spitz

Pretext

FDM 3D printing is particularly suitable for special patient groups, such as children, multimorbid patients, patients with swallowing difficulties, and patients with rare diseases. A wide variety of formulations can be used and processed into filaments using HME. Subsequent 3D printing shapes these into suitable dosage forms. This review article discusses the specifics of this process, how to monitor and ensure quality, and the challenges that still need to be overcome. The filaments required must meet certain criteria so that they can be used for FDM 3D printing. Possible in- and off-line PAT are evaluated. The subsequent 3D printing has so far been carried out with commercial printers. For official use in pharmacies and hospitals, a cGMP-capable printer must be developed to ensure pharmaceutical quality. The printed tablets have physically different properties and characteristics than pressed tablets. Accordingly, other analysis techniques are more often used here. In addition, a non-destructive analysis technique is advantageous for HME as well as for 3D printing, since the process is very time-consuming and only small batches can be produced. Furthermore, pharmacies and hospitals lack the equipment, personnel, and environment to perform wide-ranging analyses of printed batches.

Evaluation of authorship

author	idea [%]	study design [%]	experimental [%]	evaluation [%]	manuscript [%]
Julian Quodbach	12.5	5.9	0	5.9	15
Malte Bogdahn	5	5.9	0	5.9	5
Jörg Breitkreutz	5	5.9	0	5.9	5
Rebecca Chamberlain	5	5.9	100	5.9	5
Karin Eggenreich	5	5.9	0	5.9	5
Alessandro-Guiseppe Elia	5	5.9	0	5.9	5
Nadine Gottschalk	5	5.9	0	5.9	5
Gesine Gunkel-Grabole	5	5.9	0	5.9	5
Lena Hoffmann	5	5.9	0	5.9	5
Dnyaneshwar Kapote	5	5.9	0	5.9	5
Thomas Kipping	5	5.9	0	5.9	5
Stefan Klinken	5	5.9	0	5.9	5
Fabian Loose	5	5.9	0	5.9	5
Tristan Marquetant	5	5.9	0	5.9	5
Hellen Windolf	5	5.9	0	5.9	5
Simon Geißler	12.5	5.9	0	5.9	5
Tilmann Spitz	5	5.9	0	5.9	10

Evaluation of Copyright permission:

Quality of FDM 3D Printed Medicines for Pediatrics: Considerations for Formulation Development, Filament Extrusion, Printing Process and Printer Design

Julian Quodbach, Malte Bogdahn, Jörg Breitkreutz, Rebecca Chamberlain, Karin Eggenreich, Alessandro Giuseppe Elia, Nadine Gottschalk, Gesine Gunkel-Grabole, Lena Hoffmann, Dnyaneshwar Kapote, Thomas Kipping, Stefan Klinken, Fabian Loose, Tristan Marquetant, Hellen Windolf, Simon Geißler,   Tilmann Spitz

Abstract

3d printing is capable of providing dose individualization for pediatric medicines and translating the precision medicine approach into practical application. In pediatrics, dose individualization and preparation of small dosage forms is a requirement for successful therapy, which is frequently not possible due to the lack of suitable dosage forms. For precision medicine, individual characteristics of patients are considered for the selection of the best possible API in the most suitable dose with the most effective release profile to improve therapeutic outcome. 3d printing is inherently suitable for manufacturing of individualized medicines with varying dosages, sizes, release profiles and drug combinations in small batch sizes, which cannot be manufactured with traditional technologies. However, understanding of critical quality attributes and process parameters still needs to be significantly improved for this new technology. To ensure health and safety of patients, cleaning and process validation needs to be established. Additionally, adequate analytical methods for the in-process control of intermediates, regarding their printability as well as control of the final 3d printed tablets considering any risk of this new technology will be required. The PolyPrint consortium is actively working on developing novel polymers for fused deposition modeling (FDM) 3d printing, filament formulation and manufacturing development as well as optimization of the printing process, and the design of a GMP-capable FDM 3d printer. In this manuscript, the consortium shares its views on quality aspects and measures for 3d printing from drug-loaded filaments, including formulation development, the printing process, and the printed dosage forms. Additionally, engineering approaches for quality assurance during the printing process and for the final dosage form will be presented together with considerations for a GMP-capable printer design.

DIA

REVIEW

Quality of FDM 3D Printed Medicines for Pediatrics: Considerations for Formulation Development, Filament Extrusion, Printing Process and Printer Design

Julian Quodbach[1] · **Malte Bogdahn**[2] · **Jörg Breitkreutz**[1] · **Rebecca Chamberlain**[1] · **Karin Eggenreich**[4] ·
Alessandro Giuseppe Elia[3] · **Nadine Gottschalk**[2] · **Gesine Gunkel-Grabole**[3] · **Lena Hoffmann**[1] ·
Dnyaneshwar Kapote[4] · **Thomas Kipping**[3] · **Stefan Klinken**[1] · **Fabian Loose**[5] · **Tristan Marquetant**[3] · **Hellen Windolf**[1] ·
Simon Geißler[2] · **Tilmann Spitz**[5]

Abstract

3d printing is capable of providing dose individualization for pediatric medicines and translating the precision medicine approach into practical application. In pediatrics, dose individualization and preparation of small dosage forms is a requirement for successful therapy, which is frequently not possible due to the lack of suitable dosage forms. For precision medicine, individual characteristics of patients are considered for the selection of the best possible API in the most suitable dose with the most effective release profile to improve therapeutic outcome. 3d printing is inherently suitable for manufacturing of individualized medicines with varying dosages, sizes, release profiles and drug combinations in small batch sizes, which cannot be manufactured with traditional technologies. However, understanding of critical quality attributes and process parameters still needs to be significantly improved for this new technology. To ensure health and safety of patients, cleaning and process validation needs to be established. Additionally, adequate analytical methods for the in-process control of intermediates, regarding their printability as well as control of the final 3d printed tablets considering any risk of this new technology will be required. The PolyPrint consortium is actively working on developing novel polymers for fused deposition modeling (FDM) 3d printing, filament formulation and manufacturing development as well as optimization of the printing process, and the design of a GMP-capable FDM 3d printer. In this manuscript, the consortium shares its views on quality aspects and measures for 3d printing from drug-loaded filaments, including formulation development, the printing process, and the printed dosage forms. Additionally, engineering approaches for quality assurance during the printing process and for the final dosage form will be presented together with considerations for a GMP-capable printer design.

✉ Julian Quodbach
julian.quodbach@hhu.de

1 Institute of Pharmaceutics and Biopharmaceutics, Heinrich Heine University Düsseldorf, Universitätsstr. 1, 40225 Düsseldorf, Germany

2 Merck Healthcare KGaA, Frankfurter Str. 250, Darmstadt, Germany

3 Merck Life Science KGaA, Frankfurter Str. 250, Darmstadt, Germany

4 Gen-Plus GmbH & Co. KG, Staffelseestr. 6, München, Germany

5 Laboratory for Manufacturing Systems, University of Applied Sciences Cologne, Betzdorfer Str. 2, 50679 Cologne, Germany

Introduction

The general principle of pharmaceutical 3d printing, or additive manufacturing, renders this approach a promising candidate for the automated manufacturing of solid pediatric medicines [1]. Solid medicines have significant benefits over the use of liquids for the treatment of children. They provide a high microbial stability, good chemical and physical stability, enable controlled release properties and demonstrate high dosing accuracy [2]. With common manufacturing approaches, dosages can be varied only incrementally in certain ranges. 3d printing enables manufacturing of medicines with precise and fully variable dosing. Dosage forms are printed layer-by-layer in a shape predefined in a computer aided design (CAD) software. In theory, every imaginable size and shape can be printed. A

direct consequence of this approach is the ability to modify the dosage simply and conveniently, a lack of which is widely recognized as a major hurdle in pediatric therapy [3]. Besides the inherently possible size adaption, which is key to improve acceptability [4], 3d printing techniques also allow the manufacturing of small batches down to a single individual dosage form for a given patient.

While several 3d printing techniques exist and are investigated for pharmaceutical use [5], *fused deposition modeling* (FDM) emerges as one of the most interesting technologies for the manufacturing of pediatric medicines. In FDM, filaments, drug-loaded polymer wires, are fed into the printhead of the 3d printer. In the printhead, the filament is heated and extruded through a nozzle on a temperature-controlled print bed. A kinematic system allows movement of the printhead in *x*-, *y*-, and *z*-direction respective to the printhead, enabling the layer-wise deposition of the polymer-drug matrix until the dosage form is printed. Filaments are manufactured in a hot-melt extrusion (HME) step, which has to be performed industrially due to the required equipment, environment, and process understanding. This results in two main advantages. Firstly, a properly developed formulation and hot-melt extrusion process result in a high-quality intermediate that undergoes proper quality testing. Secondly, the active pharmaceutical ingredient (API) is bound in a polymer matrix within the filament, significantly reducing the risk of drug exposure for the professional operating the printer. The combination of these advantages makes FDM the most promising candidate for manufacturing of (pediatric) medicines also in decentralized settings, e.g., hospitals, compounding centers and community pharmacies. Other technologies require either the manufacturing of aqueous intermediates that cannot be prepared easily industrially due to the risk of contamination during storage [6] or the handling of powders in the final printing step, e.g., binder jetting and selective laser sintering [5], which bears a high risk of operator exposure. If a semi-solid formulation is prepared in decentralize settings, proper quality control of the API distribution within the semi-solid and printed dosage forms requires significant analytical effort that cannot be performed for individual batches.

While many publications cover proof-of-concept studies of novel dosage form designs and approaches to formulation and process development [7, 8] quality consideration of excipients, formulations, processes, filaments and medicines are frequently mentioned but rarely formalized. This lack was recognized by the United States Pharmacopeia (USP) and the International Association for Pharmaceutical Technology (APV) who co-organized a 4-day workshop on quality and standards considerations of 3d printed medicines (Homepage workshop). Even though quality aspects are mentioned for dosage forms for adult drug therapy, no

publications about the quality of pediatric 3d printing are available until now.

This publication aims to remedy this issue. The authors are members of the PolyPrint project [9] a project funded by the German Federal Ministry of Education and Research (BMBF). The project consortium exists of the companies Merck KGaA and Gen-Plus, the Laboratory for Manufacturing Systems of the University of Applied Sciences Cologne and the Institute of Pharmaceutics and Biopharmaceutics at Heinrich Heine University Düsseldorf. In the project, novel polymers for pharmaceutical FDM 3d printing are developed and thoroughly tested and benchmarked. Additionally, a novel type of FDM printer is developed to enable high-quality and cGMP compliant 3d printing of medicines. Here, we reflect on the status of the complete manufacturing process of 3d printed pediatric medicines beginning with the raw materials and ending with the final dosage form. We highlight existing shortcomings and provide guidance based on the experience gathered in the PolyPrint project.

Key Attributes of Raw Materials

Quality Aspects of Pharmaceutical Excipients

Pediatric formulation developments are obliged to follow the guidance of the EMA ensuring the overarching goal: "The development of pediatric formulations and presentations is necessary to ensure that children of all ages and their caregivers have access to safe and accurate dosage forms of medicines."[10]

More detailed information is provided in the "Guideline on pharmaceutical development of medicines for pediatric use" [11]. In general, solid oral dosage forms such as tablets and capsules can offer advantages of greater stability, accuracy of dosing and improved portability over liquid formulations. To assure suitable swallowability the size of tablets and capsules should be kept as small as possible [2].

The choice of excipients plays an important role in pediatric formulation development, both for safety and acceptability of the resulting dosage forms. The physiology of neonates and infants differs considerably from that of adults. They exhibit significantly different clearance and volume of distribution as well as differences in the metabolic profile [12]. Prominent excipient examples for the resulting challenges and issues are propylene glycol or sorbitol in infants. Also, polyethylene glycol (PEG)—a useful additive for filament plasticity and solubility enhancement—needs careful consideration regarding maximum intake. While studies confirm safe use of, e.g., PEG 3350–4000 as laxative, undesired laxative effects and potential gastrointestinal disorders limit the use of PEG to 10 mg/kg/d [13].

Looking at FDM based 3d printed formulations, usually the polymer makes up more than 50% of the formulation. Given the comparatively high intake of these excipients, the safety of polymers and additives (glidants, plasticizers) in pediatric formulations is a very important factor, especially if (partial) degradation of the polymer in the gastrointestinal tract (GIT) is to be expected. Therefore, not only polymer but also degradants and synthesis constituents of the polymer need to be carefully integrated into the safety assessment for pediatric medications. To date, several pharmaceutical polymers, such as methacrylates and ethylcellulose, are commercialized in pediatric products. Unfortunately, most polymers are used in comparatively low amounts as coating agents for taste masking and release modification [14]. Little information is available for polymers used as matrix agent and related high daily intake. Although observed adverse reactions from coated formulations might be used to prevent further incompatibilities, the maximum acceptable intake for children is critical and not easily derived from toxicological studies performed in adults. An important tool for assessing the safety of relevant excipients is the STEP database (Safety and Toxicity of Excipients for Pediatrics) [15].

In addition to safety, the taste sensation of excipients needs to be carefully considered. Polymers and additives should be taste- and odorless and ideally offer opportunities for obscuration of taste (see subsection on taste masking).

The important decision factors affecting the use of excipients are summarized by Yochana et al.: "Excipients for pediatric formulations should be carefully selected with reference to the age of the pediatric population, ADME developmental changes, and duration of treatment to ensure safety and efficacy of such formulations in pediatric population." [16]

Polymer Requirements—Limitations in FDM

In recent years, the application of thermoplastic polymers in pharmaceutical development of 3d printed products via FDM has gained increasing interest. A multitude of different material requirements need to be fulfilled by the polymer for these applications, as illustrated in Fig. 1 (further details on these parameters can be found in the supplementary information in Table S1). Here, we summarized relevant properties and parameters, which influence the suitability of given polymers or APIs, respectively. For an overview of different polymer families and a selection of marketed products in the field of hot-melt extrusion, the reader is referred to Simoes et al. [17, 18]. 3d printing using the FDM technique requires further polymer prerequisites [19] in addition to the parameters important in HME development, which typically depend

on the product properties and the utilized API. During an FDM 3d printing process, the polymeric filament is subject to significant mechanical forces. A specific mechanical profile is required due to "pinching" of these filaments between two feeding gears in the printhead. Filaments carrying a high Young's modulus (> 300 N/mm^2, depending on printhead) can be conveyed without breakage or deformation [20, 21]. At the same time, the tensile strength and the brittleness of the extrudates are crucial parameters for successful printing [19, 21–28]. The latter of which may be assessed using the three-point bending test (breaking distance > 1–1.5 mm [21, 22] and breaking stress > 2941–3126 g/mm^2 [22]). Nasereddin et al. evaluated a selection of the most commonly used polymers in FDM and developed a screening method to assess their brittleness including these parameters and thus evaluate printability [24].

Taste Masking

Taste is an important sensation to be considered in pharmaceutical development. Taste aversiveness might impact patients' compliance and medication adherence. Sensory components of both the olfactory and the gustatory sensations have to be distinguished. Whereas substances which should develop the smell as an olfactory signal need to be volatile under the conditions of drug administration, the gustatory system is directly based on the tongue comprising different types of taste buds and papillae where the sensory receptors and ion channels for salty, sour, sweet, bitter, and umami taste are located. Depending on the properties of the poorly tasting components, various taste-masking techniques are available [14]. In pharmaceutical printing technologies, most of the proposed taste-masking approaches can be applied although scientific papers or patents are scarce:

(a) One obvious approach is to mask the unpleasant taste of a printed object by the addition of differently tasting excipients, e.g., sweet carbohydrates (sucrose, fructose, glucose), sugar alcohols (mannitol, xylitol, sorbitol) or artificial sweeteners (saccharine, aspartame, cyclamate or acesulfame). An olfactory signal can be added to the printing formulation using volatile substances such as menthol or more complex organic or synthetic flavors [29]. However, it should be noted that one or more components of these mixtures will partly evaporate during the manufacturing and over storage time changing taste sensation as a key property to be controlled in stability studies.

(b) Unpleasant tasting ingredients can be physically bound within inclusion complexes, e.g., by use of cyclo-
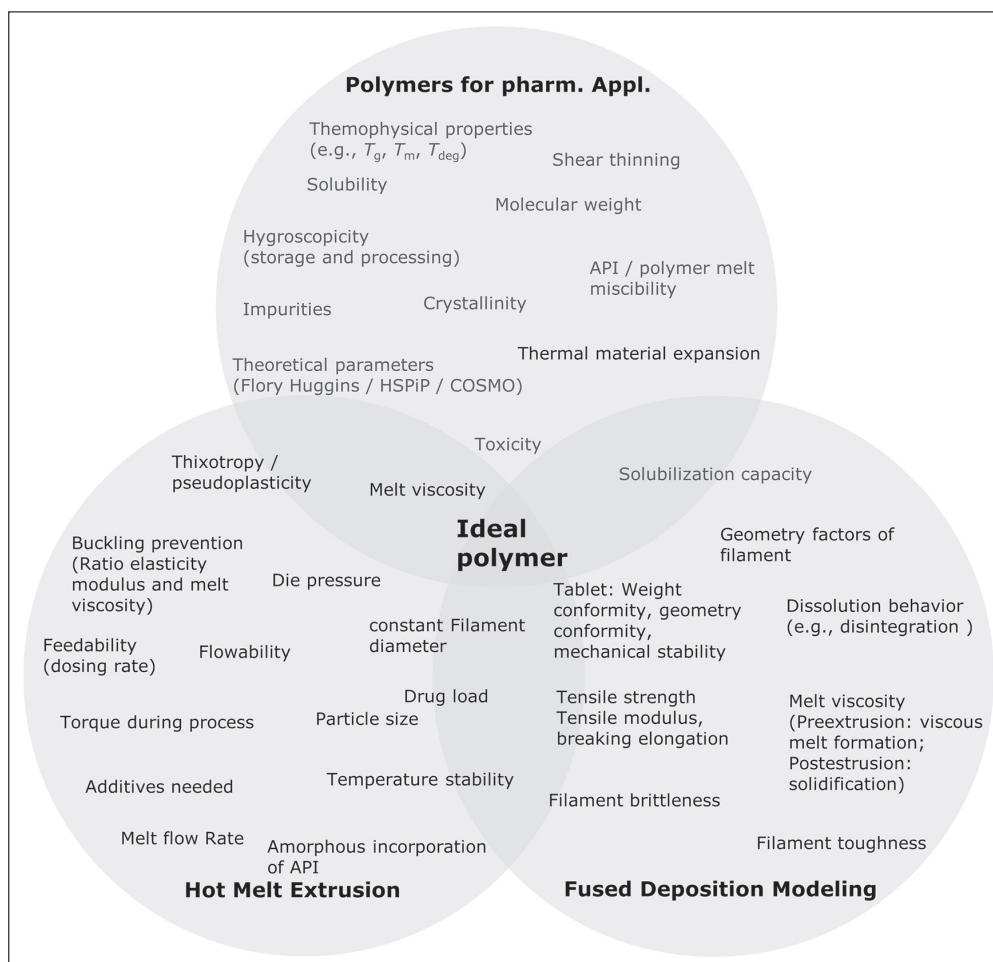
Figure 1 Selection of Parameters That are Relevant for Pharmaceutical Application of Polymers, Particularly in HME and FDM.

dextrins, or to polyelectrolytes (anionic or cationic polymers) which can also be part of the solid matrix. Entrapping by the printed polymers may be sufficient for taste masking of bitter compounds [30, 31].

(c) High viscosity hydrophilic polymers may prevent fast hydration and dissolution of the dosage form, thereby reducing the migration to the taste receptors on the tongue and the resulting taste sensation.

(d) Barriers inside or outside the printed dosage form may shield against quick dissolution and saliva contact.

The taste-masking effect of the applied pharmaceutical measures are usually demonstrated by using advanced dissolution setups [30] or electronic tongues in vitro [32], and human taste panels [31] or animal experiments like the BATA (brief-access taste aversion) model in vivo [33].

Hot-Melt Extrusion of Intermediates for Pediatric 3d Printing

Filament Extrusion—a Question of Homogeneity

The filament required for FDM 3d printing is generated as endless strand via twin-screw hot-melt extrusion. Filament extrusion comprises multiple individual unit operations and processes that must be considered to obtain an overview of relevant quality attributes. To meet quality attributes of products and establish robust processes, the Food and Drug Administration (FDA) recommends quality-by-design (QbD) approaches for formulation and process development [34]. This led to different implementations of QbD in pharmaceutical melt extrusion processes [34–36]. As mentioned in the section on polymer requirements, the mechanical properties

of filaments must allow proper feeding and extrusion from the printhead. Additionally, diameter homogeneity and API distribution are much more important compared to regular hot-melt extrusion processes. Usually, the obtained extrudate is milled or pelletized and a subsequent homogenization of the individual particles is performed. In FDM, the filament is commonly kept intact and printed as it exited the extrusion die. This means that diameter and API distribution inhomogeneities directly reflect in the printed amount of filament and API. This can be an issue for regularly sized dosage forms [37] and even more so for pediatric medicines of lower dose and mass. In this case, even small variations of diameter and API distribution can lead to non-compliance with monographs on the uniformity of dosage units and must be avoided. The API distribution is influenced primarily by the powder feeding process and hot-melt extrusion, the diameter homogeneity by the hot-melt extrusion process.

Powder Feeding

In twin-screw filament extrusion processes feeding of polymers, solid additives and APIs is a critical aspect. Unlike single-screw extruders, twin-screw extruders are run partially filled. Thus, the material flow inside the extruder depends on the flow rate of the feeder used. Process parameters like the specific feed load (SFL) and residence time distribution (RTD) are directly influenced by the feeding [38]. In Fig. 2 left, a typical residence time distribution curve of a filament extrusion process is shown. On the right, feeding fluctuations are shown in black and the resulting output fluctuations after extrusion are shown in red. The reduction in fluctuations demonstrates the mixing and homogenizing abilities of extruders. As the reduction is not absolute, feeding should be as homogeneous as possible, to reduce output variations.

Several types of dispensing devices are available for feeding bulk solids. Vibrating trays or screws are a widespread method of conveying the material [39]. Simple devices feed

in volumetric mode at a constant actuating variable. In contrast, loss-in-weight or gravimetric feeders are equipped with an integrated load cell that detects fluctuations in the feed rate. The actuating variable is adjusted via a control mechanism, leading to a compensation of fluctuations [40]. Material properties as well as the target feed rate must be considered in selection of the most suitable dosing device [41]. Low dosing rates and poor flow properties result in particularly high demands on equipment attributes [42]. Matarazzo et al. has provided a checklist to assist in the selection of proper feeder equipment [43].

Bulk solid feed is evaluated in several studies usually by using an external scale where the fed material is collected. Data analysis of the dosing curve or its integral can be conducted using statistic parameters like measure of dispersion or target-actual-ratio of moving measures of central tendency [44, 45]. Another way is using discrete Fourier transform of dosing fluctuations, which provides information about the materials dosed [46].

Extruding Filaments as Intermediates

The efficiency of the melting process of polymers in HME depends on the properties of the excipients and the extruder design. In general, polymers with low melt viscosities and high thermal conductivities exhibit a more efficient melting process. Changes in the screw design are often necessary to improve the melting process of the powders and to improve mass flow of the melt through the extruder. Otherwise, solid material may block the screws transiently, which can result in increased torque if the melting process is incomplete.

Ponsar et al. highlighted the effect of the extruder barrel fill level on filament homogeneity. The higher the fill level, the lower are the fluctuation of the mean diameter (Fig. 3 left) [37]. Frequently, as diameter fluctuations are not necessarily normal distributed, the inter quartile range of the diameter is used to describe fluctuations. Besides having

Figure 2 Exemplary Drawing of: (left) a Typical Residence Time Distribution Function of a Hot-Melt Extrusion Process; (right) Fluctuations of the Feed Rate (Black) and Output Fluctuations After Extruder (Red).
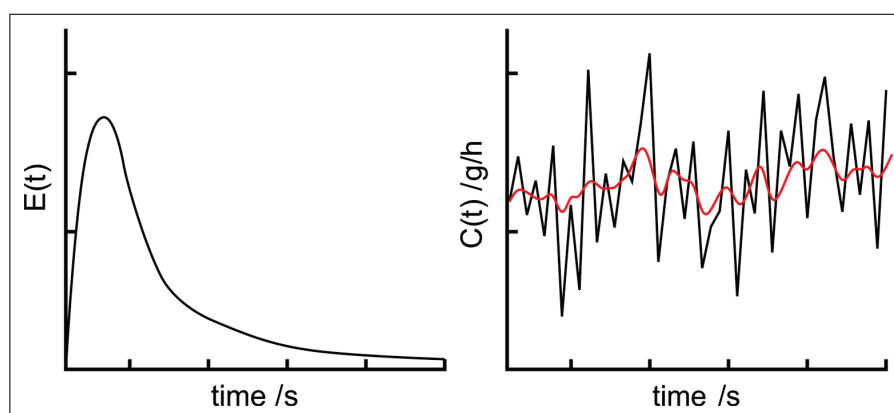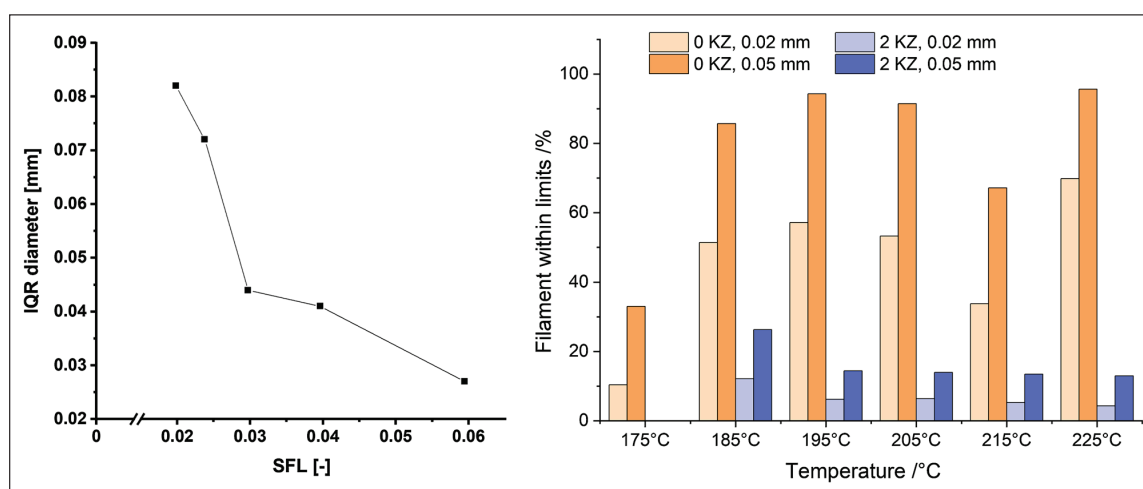
Figure 3 (Left) Interquartile Ranges of Diameter Measurements During Extrusion Correlated with SFL of the Extrusion Process [37], (Right) Amount of Filament Within ± 0.02 and 0.05 mm Specification With or Without Two Kneading Zones (KZ 1: 4×90°,4×60°, 2×30°, KZ 2: 8×60°, Unpublished Data).

a measure for fluctuations, it is as important to set limitations for said variations. Usually, deviations of ± 0.02 mm or 0.05 mm from the set value are considered tolerable. By varying the temperature, the polymers, the process setting and the screw configuration in an extruder, the limits are met with varying degrees of success. In Fig. 3 right, the same formulation was extruded at different temperatures and with different screw designs (no kneading zones or two kneading zones). The best batch was extruded at a high temperature of 225 °C with no kneading zone and the worst at the same temperature with two kneading zones. These data show the decrease of filament diameter within the ± 0.02 mm or 0.05 mm specification when adding two kneading zones. This observation indicates the importance of a continuous melt flow in the extruder, which is better provided by a screw configuration of only conveying elements. When adding kneading elements, the melt is retained before the kneading zones until enough pressure is build up by the following melt. To increase the homogeneity of the filament diameter further, a melt pump can be attached between the end of the extruder barrel and the die. The purpose of this attachment is to stabilize inevitable melt fluctuations that occur within the hot-melt extrusion process. The pump aligns those fluctuations by metering the melt flow to a very constant rate and therefore a very constant pressure level [47]. This leads to an increase of filament homogeneity since the fluctuations mentioned before are reduced drastically. This was shown by in-process monitoring of filament diameters [48].

After extrusion, it must be considered how to properly cool down the obtained filament. Commercial FDM filaments such as acrylonitrile butadiene styrene copolymer

(ABS) or polyether ether ketone (PEEK) are not water soluble and can therefore be cooled down in a water bath. Polymers for pharmaceutical FDM applications are frequently at least partially water soluble and they contain one or more APIs. Consequently, cooling in a water bath cannot be performed, even though it is a highly effective and efficient cooling process. For pharmaceutical applications, proper cooling can be achieved by either passive cooling on a conveyor belt at atmospheric conditions or by using an air ring or air tunnel [49].

While polymer melt is being pushed out of the nozzle, a phenomenon can occur known in HME as "die swell". Die swell is the expansion of molten polymer to a larger diameter than determined by the die itself, resulting in a filament thicker than desired. This effect is mainly related to the energy preserved by compression and force alignment of polymer chains being forced through the die, followed by the relaxation of those chains when exiting the die again [50]. The viscoelastic behavior of the melt as well as process parameters are major factors when die swell shall be reduced [37, 51]. A reduction of die swell can be achieved by increasing the temperature at the die. Even with thorough optimization, a larger mean diameter than desired will frequently result. To further adjust the mean diameter after extrusion, a pulling unit, e.g., a conveyor belt or the haul-off unit of a winder [37] can be implemented. The speed of haul-off units is variable and defines the final mean diameter of the filament, which can be wound or used as individual strands. Commercial filament diameters are typically 1.75 or 2.85 mm. For pharmaceutical purposes, a lower diameter is beneficial,

as potential inhomogeneities of diameter and content will have less of an impact relatively.

In Fig. 4, two prototype extrusion lines are shown. They consist of gravimetric powder feeders, twin-screw hot-melt extruders, cooling units (conveyor belt or cooling line with ring air-knives), laser-based diameter measurement system and optionally a filament winder.

Characterization of Filaments

To evaluate, optimize and monitor the process of filament production, different analytical tools can be used off-line and in-line.

Off-line Characterization

A simple and useful approach is the visual assessment of API-loaded filaments. This way, it is frequently possible to initially assess potential degradation via color changes and possible recrystallization of the active ingredient(s) especially for higher drug loadings and APIs that exhibit thermal sensitivity. As already discussed in the section on polymer requirements, the mechanical properties of filaments are an important factor for the feedability of the formulation that must be analyzed. The mechanical properties of filaments may change over time due to enthalpy relaxation [21] or because the included excipients are hygroscopic. Water

absorbed during processing or storage is a powerful plasticizer that lowers the glass transition temperature. Is does not only affect the mechanical properties and appearance, but also drug stability, may induce degradation, and needs to be quantified for this reason [52, 53]. In vitro dissolution as per compendial monographs is used to determine the amount of drug dissolved over time and thereby to assess the performance of the formulation (filament/tablet) in regard to release behavior [54]. For the content determination and examination of homogeneous drug distribution as well as characterization of related substances within filaments and tablets, most frequently HPLC analysis is used [55].

In-line Characterization of Filaments via PAT

The physicochemical properties of filaments produced by HME are crucial for the 3d printing process. Quality and performance of the 3d printed tablet and can be examined with PAT tools like spectroscopy, rheometry and optical coherence tomography (OCT) [56]. These tools enable capturing real-time information of process and filament properties during HME non-destructively. Some of the data can be easy to interpret, e.g., diameter and sphericity of filaments determined via multi-axes laser scanning modules (see Fig. 4). Some can be difficult to interpret and may require the preparation of multivariate, quantitative models, for example spectral information. Independent
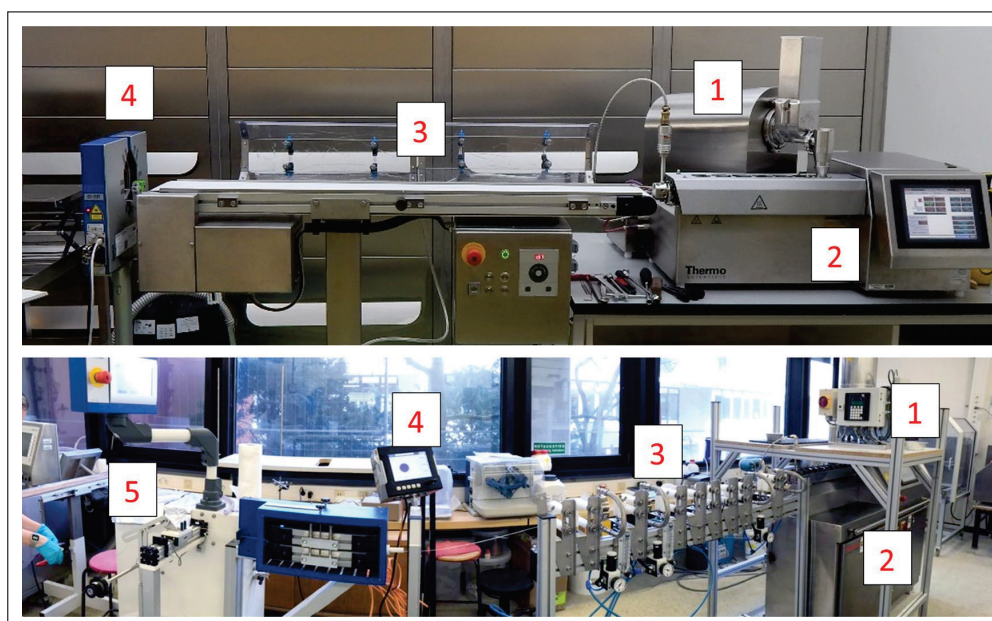
Figure 4 Two Filament Production Lines. (1) Gravimetric Feeders, (2) Twin-Screw Extruders, (3) Cooling via Conveyor Belt (Top) and Ring Air-Knives (Bottom), (4) Three-Axis Laser Micrometers, (5) Winding Unit.

of the data complexity, it can be utilized to monitor the process and initiate corrective actions to reach a desired state and potentially to allow real-time release [57]. In the following, relevant technologies are listed.

In-line Spectroscopy

UV–vis spectroscopy has been used and established as PAT tool in HME. Spoerk et al. used in-line UV–vis spectroscopy as an analytical tool for characterizing of active ingredients (Estradiol, Estriol, Ibuprofen) and polymer matrices (ethylene vinyl acetate, Eudragit RL-PO). The studies focused on the quantification of the drug for cleaning-in-place strategies [58]. Wesholowski et al. have investigated in-line UV–vis spectroscopy as a PAT tool for preparing solid dispersions of two APIs (carbamazepine and theophylline) with one polymer (copovidone) [59]. The obtained results revealed the suitability of the implemented tool to quantify the drug load in a typical range for pharmaceutical applications. The range of linearity differed with different formulation and was 5–30% for carbamazepine, whereas that for the theophylline formulations was 2.5–10%. They reported that the efforts to evaluate data was minimal due to univariate data analysis and in combination with a measurement frequency of 1 Hz, the system is sufficient for the real-time data acquisition. In-line near infrared (NIR) spectroscopy has also been used to investigate drug–polymer interactions and to validate a method for continuous API quantification during HME processing [60]. Vo et al. demonstrated the use of Fourier transform NIR spectroscopy in conjunction with multivariate analysis (MVA) for in-line API concentration monitoring during a HME process [61]. In this study, they used ketoprofen as model drug, Eudragit L100-55 as matrix polymer and stearic acid as processing aid. A principal component analysis (PCA) model was used to monitor the process state shift in response to disturbances of parameters, such as temperature and material feed rate. Thus, an NIR based quality monitoring methodology can be easily transferred from process development to manufacturing. Saerens et al. evaluated the suitability of Raman spectroscopy as PAT tool for the in-line determination of API concentration and the polymer-drug solid state during HME process [60]. They used different concentration of metoprolol tartrate (10%, 20%, 30%, and 40%) with Eudragit RL-PO mixtures, which were extruded and monitored in-line in the die using Raman spectroscopy. A PLS model was developed and validated, which allowed the real-time API concentration determination. They also investigated application of Raman spectroscopy in solid-state characterization and found that the mixtures containing solid

solution showed broadened Raman peak compared with the solid dispersion.

In-line Rheometry

In-line measurements of the rheological characteristics play an important role in real-time monitoring of torque, influence of drug load, and effect of formulation ingredients on the process. The real-time evaluation of rheology data in the extrusion process can be determined by pressure drop inside an extruder die connected to suitable instruments. In-line rheological characterization can enhance process control and understanding [62].

Optical Coherence Tomography (OCT)

OCT, a non-invasive method, is used as an off-line tool for semi-transparent and turbid media. It can be applied to measure parameters such as surface properties of filaments and layer thicknesses, e.g., of coating layers or filaments produced in hot-melt co-extrusion, and uniformity [63]. Koutsamanis and Eggenreich et al. reported the application of OCT to evaluate the integrity of the core/membrane interface and membrane thickness of vacuum compression molding formulations containing progesterone with ethylene vinyl acetate polymer [64].

Characterization of the Solid State

Even though some of the above-mentioned analytical tools can determine certain aspects of solid-state properties, other approaches are commonly used that provide a better understanding of materials. The solid state of an API incorporated in a polymer matrix can have a large impact on the performance of the final dosage form in terms of dissolution rate and bioavailability [65]. Poorly soluble APIs, which make up a large proportion of potential drug candidates [66], can be formulated as amorphous solid dispersions (ASD) where the crystalline structure of the API is broken up and the resulting molecular dispersions are stabilized by a polymer matrix. In contrast, an API can also be incorporated in filaments maintaining a crystalline structure [67, 68]. The presence or absence of crystalline structures strongly influences printability, such as mechanical [69] and rheological properties of filaments [70]. Consequently, the assessment of crystallinity in filaments is important in process development, quality control and stability studies. Even though this assessment can be supported by in-line measurements, traditional techniques are more widespread.

The formation and stability of the ASD is influenced by solubility and miscibility of the API and the polymer matrix [71]. Thermal and mechanical energy uptake during manufacturing facilitates the dispersion and reduces

the number and size of crystal nuclei, which may lead to premature precipitation of API in vivo or reduce physical stability during storage. To maintain the solid state during shipment and storage is important for the ASD itself, but for FDM the second heating cycle during printing needs to be considered, additionally. The thermal impact may not only impair the chemical stability of the formulation but can also lead to recrystallisation of API [28].

Several techniques can be applied to determine the solid state. Differential scanning calorimetry (DSC) as well as well as X-ray powder diffraction (XRPD) are well-established analytical methods to investigate the solid state of API dispersed in polymer matrices [72]. One caveat is the limit of detection of crystalline fractions in mostly amorphous systems [73]. The detection of small traces of crystalline fraction is possible by the use of polarized light microscopy [74]. However, this method lacks quantitative determination and selectivity.

In regard to the assessment of crystallinity in intermediate and final product the manufacturing process should be considered end to end for FDM printed solid dosage forms.

FDM Printing at Site of Care—Stricter Requirements for Dosing Precision and Quality Control

3d printing based on FDM has been state of the art for years and is used primarily in the consumer sector but also in industrial environments. Particularly in industry, a quality demand is placed on the products to be printed from the ground up. Unlike in pharmaceutical industry, however, the focus is primarily on geometric aspects.

Different consumer 3d printers are already being used in pharmaceutical research. One of several issues with off-the-shelf printers is that the amount of active ingredient processed cannot be verified. Thus, the quality of the pharmaceutical products is not verifiable. In contrast to classical manufacturing methods, 3d manufacturing is slow and only few dosage forms are printed [5]. Therefore, destructive quality control approaches are not profitable and in-line testing is unavoidable. Furthermore, there is hardly any system on the market that meets the cleaning requirements of pharmaceutical equipment [75].

In addition to the common requirements of mechanical engineering for the development and market placement of production machines, special requirements are part of the GMP guidelines [76]. For these reasons, it is imperative to rethink 3d printer design and adapt it to the needs of pharmaceutical manufacturing. The following sections highlight some of the most critical components.

Motion System and Overall Printer Design

The most common design in FDM 3d printing is the Cartesian printer, but other forms like the delta printer and the polar printer exist [77]. Cartesian printers operate by linear movement of the printhead in x-, y-, and z-direction respective to the print bed. In most cases, the axes, motors, and drives are designed for general industrial and mechanical engineering purposes and the requirements of the pharmaceutical industry are not considered. For example, many of the moving parts, which are usually lubricated, are not encapsulated and are, therefore, exposed to potential contaminants from filament and product. Since it is required for pharmaceutical production that all surfaces in contact with the product are cleanable, these elements do not meet the GMP standard [78].

During the development of new machines all requirements for the system need to be defined beforehand. In addition to the basic functions for a 3d printer almost all machines are designed to be as compact and as inexpensive as possible. To achieve this, many functions are implemented in a small space. When looking at existing printing systems under the prerequisites of the GMP guideline, several problems become apparent. In regular 3d printing systems, all subsystems such as material handling, material processing, build plate, and motions system are implemented openly in a very confined space. For a GMP-compliant implementation, however, it is recommended to separate all elements and to design individual and well controlled areas (Fig. 5).

For industrial and non-pharmaceutical applications, the print chamber usually does not have to be kept particle-free or sanitized. Axis systems for moving print head or print bed can be placed directly in the printing space. Since outgassing, particle detachment and other sources for (cross-)contamination must be contained or avoided during the print job, this arrangement is not applicable for GMP printers. The printing chamber should be as isolated as possible from all moving elements. In addition, surfaces should not have complex geometries or sharp angles to ensure cleanability.

In addition to the risk of contamination of the printer parts, attention must also be paid to the safety of the operator. During the processing of APIs, the user may be exposed to harmful chemicals. For example, in the case of outgassing, it must be ensured that substances cannot endanger the user. For this purpose, the printer should be equipped with appropriate protective devices such as air filters. In the pharmaceutical sector, little research has been done on the possible safety aspects of using 3d printing for the manufacture of pharmaceutical products [78].

Here, it is advisable to use approaches from industrial 3d printing as a starting point. Powder-based printing technologies in particular place great emphasis on user safety. The GMP guidelines stipulate that all surfaces in contact
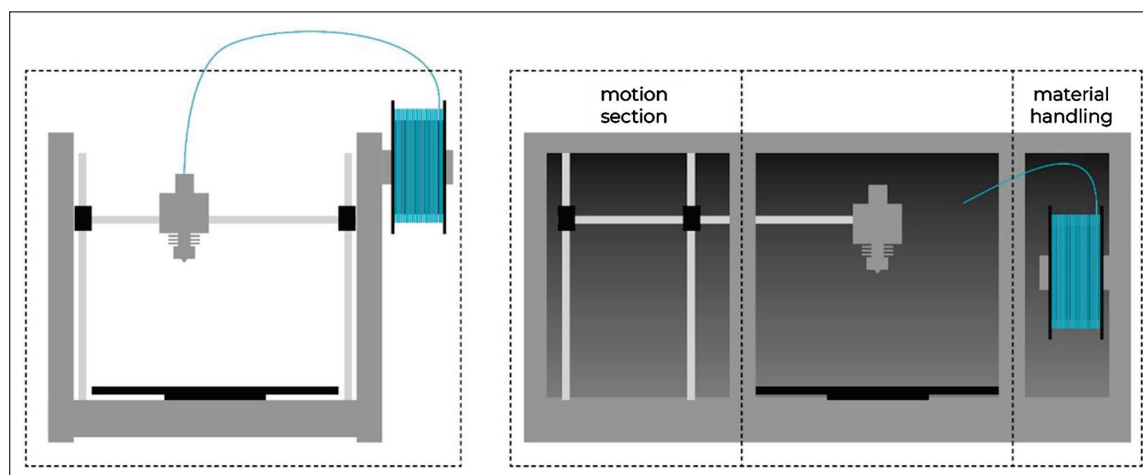
Figure 5 Schematic of an Off-the-Shelf 3D Printer (Left) and a 3D Printer with Separate Build, Motion, and Material Handling Section (Right).

with the product must be made of approved and cleaning-resistant materials, and that these must not have any edges, joints, undercuts or similar [79]. For this reason, all elements should be milled or machined from a single piece of material, if possible.

Feeding Mechanism, Filament, and Filament Storage

In commercially available printers, filament is conveyed in the extruder by two counter-rotating rollers. To increase the conveying force, at least one of the rollers is a gear wheel. This approach to filament transport is not suitable for pharmaceutical materials. The force exerted on the filament might become too high, resulting in slippage. Slippage, in turn, leads to small, usually statically charged filament grains that accumulate in the cavities of the feed roller and on other elements in the printhead. At high conveying resistances, i.e., high melt viscosities, this effect can even lead to breakage and creation of dislodged filament pieces. The consequence of this behavior is that the extruder must be cleaned extensively to avoid cross-contamination. In particular, the complex geometry of the gear wheel(s) with its many cavities prevents efficient cleaning. In addition, damage to the material leads to an undefined geometry of the filament and, thus, to an uncontrolled quantity of deposited material. Breakage of the filament will lead to printing process failure and manual intervention will be required to restart the process.

Traditional FDM 3d printing is based on a spool-based filament supply system. Technical polymers for classical FDM printing are designed and manufactured to display sufficient flexibility to be wound on a spool, but also enough

stiffness to be processed by a standard feeding mechanism. As described in the section on key attributes of excipients, pharmaceutical polymers often do not allow reliable feeding and printing easily due to their brittleness or undesirable deformation behavior. A filament provision and supply system must be developed that can handle a greater diversity of mechanical properties. To achieve this, both the bearing and the extruder technology must be completely revised.

Up to 450 m of filament can be wound onto a spool. When printing multiple large components this is an advantage. For the production of small dosage forms in lower quantities this is not necessary. If a lower amount of material is required, a smaller filament supply that is used up quicker reduces potential issues with the storage stability. Particularly in view of the API cost, smaller units of filaments are to be preferred. In addition, cross-contamination of filament must be avoided during handling so that encapsulation of the filament is necessary. For this reason, the currently selected filament geometry ("endless") and the bearing units (coils) must be questioned.

The material storage, commonly designed as filament reel, should also be redesigned as part of a separate area. This is realized by some commercial printers that have cartridge systems, but large amounts of material are still wound on spools. We recommended to reduce the amount of material stored in or on the material accumulator. With reduced material amounts, coiled-up, long filaments strands that require feeding rollers or gears are not necessary, solving multiple issues with the current printer design. Omitting spools enables a new design of the storage system which can offer hermetic encapsulation of the filament. This would allow filament storage and transport under controlled conditions, similar to a tablet in a blister. Initial approaches can

already be found in printers from the company Stratasys [80]. Yet, these are not suitable for pharmaceutical manufacturing machines without significant modifications.

If filaments are not a continuous long strand anymore and new bearing units are designed, the conveying mechanism needs to be revised, too. Roller or gear-based feeding mechanisms should not be used for this purpose as they facilitate cross-contamination. Piston based mechanisms similar to those already used in certain bioprinters [81, 82] would be a superior approach, as slippage and breakage could be prevented.

Hotend and Coldend

One of the most central parts in a 3d printer is the hotend. With the help of electrical heating, the polymer is melted and extruded through a nozzle. Conventional hotends are optimized for high throughput and printing speeds. Technical polymers allow processing at temperatures well above the melting or glass transition temperature to reduce duration of melt formation. The result is a high temperature gradient from the core to the edge of the filament [83]. The use of additive manufacturing in the pharmaceutical environment, on the other hand, requires processing that is particularly gentle on the material, as many APIs are thermo-labile. Nevertheless, high printing speeds must still be achieved for a productive process. It is necessary to optimize the hotend in terms of uniform heat input to reduce the heat strain put on pharmaceutical filaments.

The other components of a common printhead are also not suitable for use in the pharmaceutical manufacturing. To compensate for the high temperatures, the upper parts of the printing core, the coldend, are cooled to prevent or reduce softening of the filament before the actual hotend. Commonly, active air cooling with cooling fins is used. Due to their complex and fine geometry these parts are particularly difficult to clean and increase the risk of cross-contamination. As the hotend is located directly above the product, evaporation of residual solvents, plasticisers and other volatile components is to be expected. They will be distributed in the printing chamber via the cooling air, further increasing the risk of cross-contamination and reducing cleanability. Pharmaceutical print heads must be completely cleanable. Purging with cleaning filaments, what is the common procedure in research, will not suffice to prevent cross-contamination. Since the material is fed through coldend and hotend, all elements that come into contact with the product must be cleaned without residues after each use and before each material change. To avoid changing the complete print head, a system design similar to the design of hot-melt extruders is recommended. Similar to the barrels, the printhead should be demountable and the material touching parts easily accessible [58]. The coldend of the printhead is placed in the print chamber as well and its cooling fins cannot be cleaned properly. Switching to water cooling would solve this issue and provide a more accurate control of the temperature. This has been realized in some non-pharmaceutical systems such as the x500pro from German RepRap [84].

Sensors and Quality Control

A few years ago, 3d printing gained a detrimental reputation of being usable only for prototyping, due to frequent print failures, limited resolution, anisotropic mechanical properties, low production speeds and rough surface finish [85]. The reason for this is a lack of process and quality control. Even though the implementation of in-line quality is beginning in some 3d printing technologies, in FDM such methods are still at the experimental or research stage. The focus is mostly on thermal monitoring (melt pool analysis in selective laser sintering / melting) and layer monitoring [86]. Even though some of these approaches can also be used in a pharmaceutical context, they focus mostly on quality attributes for other manufacturing industries. Relevant pharmaceutical quality attributes cannot be captured with such systems. The use of the sensors applied for control issues only allows accurate control and regulation of the process. However, a quality statement regarding the solid state, API content or printed quantity is not possible. For 3d printers to be used for pharmaceutical manufacturing in the future, additional measures must be undertaken in addition to adapting the mechanical components. A major point is the quality control of the printed product.

Various types of defects in 3d printed parts are described in the literature [86, 87]. While structural integrity is key for technical applications of FDM, the doses of incorporated API in the final dosage form is the crucial parameter for medication manufactured by FDM. Especially medications to be used by children need to be manufactured in an accurate way, because the doses for children are typically lower and small deviations in the content of a dosage form result in higher relative over or underdosing potentially harming the patient.

To improve the quality of dosage forms, process control has to be improved as well. In general, three groups of parameters can be identified for in-process control.

1. Machine parameters derived from the control electronics. For example, motor and heater current, temperature of nozzle and cooling zone, vibrations etc.
2. Monitoring of the extruded volume or mass of the filament, either derived from measurements described in 1 or measured by dedicated sensors attached to the printer.
3. Non-destructive chemical analysis of the raw material and / or intermediate and final printed product.

The monitoring of machine parameters can be implemented in industrial control systems and do not necessarily rely on additional sensors which might lead to higher machine costs in the end. It has been described in literature to use the current of the feeding motor to detect a blocked nozzle [87, 88]. Chemical degradation and under-extrusion related to blocked nozzles is a major concern for the quality and accurate dosing of pharmaceutical dosage forms. In another example, Becker et al. [87, 89] used accelerometers to monitor the state of the printer and detect fluctuations in the flow of extruded raw material during the printing process. These substitute parameters can only be used if comparative data are available of the printing process for a specific raw material on a specific printer limiting the application to well understood processes. To circumvent these issues, dedicated sensors can be introduced into the printing system to directly measure the extruded volume or mass. Calculation of the printed dosage may act as a valuable in-process control, assuming that the active ingredient is homogenously distributed in the raw material.

Optical systems were described to measure the distance between printed object and nozzle detecting under-extrusion [90, 91] providing error detection during a print process. It is also possible to monitor the movement and quality of filament by a camera [92]. Dosage forms with defects can then be discarded after the printing process and documented in a batch report for documentation. Of course, specialized sensors as well as integrated balances measuring the actual printed mass of filament could be an option to further improve the accuracy of 3d printed oral dosage forms, assuring the quality. For printing at the site of care, implementation of feedback loops based of the obtained data to automatically adjust the printing process of each individual dosage form will enable to meet the claimed dose and lead to an efficient manufacturing process with reduced waste and higher yields resulting in fast supply of high-quality medication to the patients.

Focusing more on the final product than the process itself, chemical analysis of the API incorporated in the printed dosage form could enable real-time release in a clinical printing setup. Different spectroscopic methods were described in the literature to analyze pharmaceutical dosage forms without destroying the samples. It was shown that NIR-chemical imaging of 3d printed objects can be used to measure the amount of printed API [93]. Transmission Raman measurements were reported in literature to investigate the amorphous and crystalline fraction of fenofibrate in solid oral dosage forms [94]. Such methods could be used in future pharmaceutical 3d printers to assure the quality of amorphous solid dispersions. Chemical analysis of printed objects can lead to full batch real-time release of medications printed at site of care ensuring that the quality of the final product was not negatively influenced by the printing

process. Downsides of non-destructive chemical imaging are high costs and large equipment, which might not be easily integrated in the printing platform.

Still, FDM as a digitally controlled manufacturing process opens the opportunity to integrate multiple sensors to not only monitor the quality of the printing process and product but furthermore adjusting critical process parameter on the fly to resemble a true rapid manufacturing process.

3d Printed Dosage Forms for Pediatric Use

General Consideration

Only few solid dosage forms have been investigated for their acceptability in children [95]. Of those, even less can be manufactured by 3d printing: minitablets, orodispersible films, (orodispersible) tablets, and capsules. A definite advantage of 3d printing is a freedom of design previously not possible. This is demonstrated by many novel dosage form designs [7, 96]. It is likely that such novel designs will also demonstrate high acceptability in children, e.g., because of more appealing coloring and dimensions. However, this has not been demonstrated in clinical trials and this section will focus mostly on the above-mentioned dosage forms. As the resolution of FDM printing is limited, small capsules suitable for pediatric treatment are not sensible to manufacturing via this route. Similarly, printing of orodispersible tablets and minitablets has not been established, yet.

Minitablets and Small Oblong Tablets

Tablets of < 4 mm diameter are usually considered to be minitablets [97]. As they have demonstrated acceptability in neonates, infants and children [2, 98] minitablets of 2 mm diameter are developed and manufactured more frequently than larger ones. Accurate printing of small objects is challenging in general. A typical nozzle diameter is 0.4 mm and tablets with a diameter of 2 mm are only five times larger than the nozzle diameter. These small geometries are on the lower limit of what is possible with the FDM process [99] and dimensional accuracy is difficult to achieve. Due to the small surface area of a single layer the cool down period of the material before the nozzle passes an area a second time is short, which may lead to insufficient mechanical stability of already printed layer. Several strategies are suitable to circumvent such issues. Reduction of print speed is generally associated with higher dimensional accuracy and improved surface quality. However, throughput and productivity will decrease with lower print speed. The manufacturing order of objects on one build plate can also be changed from sequential printing (complete all layers of one object, then

moving on to the next object) to layer-wise printing where the printing layer is changed after the specific layer of all objects is completed. While cooling time per object layer is associated with beneficial effects on dimensional accuracy, frequent changes between objects may introduce additional classes of printing errors like stringing and blobs [100]. Every additional travel movement comes with the risk of oozing filament and, therefore, inaccuracy of dose. The dosing of smaller tablets is even more challenging than with larger objects because the relative change of incorporated API due to printing defects is more significant. Krause et al. printed objects with a diameter of 4 mm, 3 mm, 2 mm and 1.5 mm with decreasing tablet mass and calculated the acceptance value according to Ph. Eur. 2.9.40. While the standard deviation of tablet mass was higher for the largest objects, their acceptance value was lower compared to smaller tablets. These results show that dosing accuracy is especially important for mini tablets and low dose drug forms [99].

Ayyoubi et al. printed spherical tablets with a diameter of 6 mm with channels to improve dissolution rate [101]. Small oblong tablets (9 mm × 5 mm × 4 mm (width × length × height)) were manufactured for children > 6 years old by Fanous et al. [102].

Another aspect besides the dimensionally accuracy is the geometric flexibility. Geometrical flexibility offers the opportunity to increase the compliance in pediatric patient as well as to reduce the resistance of taking medication in children. The reason lies in the possibility of 3d printing for personalized medicine to choose the color, shape and design of the tablet according to the child's wishes [103]. Scoutaris et al. imitated chewable STARMIX® sweets by printing objects in the shape of a heart, ring, bottle, bear and lion, which contained the model substance indomethacin, hypromellose acetate succinate (HPMCAS) and polyethylene glycol (PEG) as polymers. The aim for the development of this pediatric dosage forms with the STARMIX® design via hot-melt extrusion (HME) and FDM 3d printing was also to enhance the palatability [104].

Besides the flexibility in geometry FDM can also be used to manufacture layer-wise polypills [105]. Multiple APIs were printed into one solid oral dosage form. In case of the layer-based FDM process, chemical compatibility of these APIs is not as limiting as in traditional manufacturing processes since the compounds are separately printed into different compartments of the dosage form. The flexibility of a computer-controlled manufacturing process opens the possibilities to match the exact needs for pediatric patients, but deep understanding of the underlaying processes and optimized print settings are necessary to ensure high quality of the final product.

Orodispersible Films

Orodispersible films are accepted by infants and children [95, 106, 107] and are dosage forms of choice for patient centric applications. The European Pharmacopoeia defines orodispersible films as solid oromucosal preparations intended for the administration in the mouth, where they disperse rapidly to deliver active substances (Ph. Eur. Monograph "Oromucosal preparations"). Dose adaption is possible by (1) modifying the API concentration in the formulation, (2) adapting the film thickness, and (3) by cutting films to the desired size, as both thickness and size defines the amount of incorporated API. However, the cutting approach can be accompanied by material waste and is prone to human errors.

Manufacturing routes of orodispersible films include solvent casting [108–110] and 2d and 3d printing technologies. In 2D printing [111, 112], the printing fluid consists of the drug dissolved in a suitable solvent or dispersed in a dispersant, which is printed onto a substrate which contains polymer(s) and additives (e.g., plasticizers, flavors) and is made in a separate manufacturing step. As for the solvent casting technique, the process parameters (drying temperature, humidity) need to be precisely controlled, as they significantly influence the final film properties [113, 114].

3d printing offers a waste-less route of precise manufacturing medicines for children. Jamróz and colleagues accurately printed orodispersible films containing aripiprazole [115], whereas Ethezazi et al. printed multi-layered films containing individual layers with paracetamol, ibuprofen and a taste-masking agent [29]. Cho et al. applied a variation of FDM printing to prepare an orodispersible film containing the poorly water soluble drug olanzapine [116]. They heated a polymer-API mixture until it melted and used pneumatic extrusion to drive the printing process, a approach similar to the one published by Musazzi et al. [108]. In another study, a bi-layer film was FDM printed with a mucoadhesive chitosan layer and drug containing layer and an ethyl cellulose backing layer that formed a permeation barrier, thus creating a unidirectional drug release [117].

Even though none of these studies directly investigated the suitability of FDM 3d printing to individualize the dose, they demonstrated sufficient mechanical properties to enable robust handling and acceptable accuracy that strongly hints at technological proficiency to produce pediatric orodispersible films. However, acceptability of orodispersible films was assessed with solvent-casted films and the different appearance of FDM printed films will have to be investigated separately in future studies.

Dosage Form Characterization

To ensure that printed dosage forms meet the requirements, physical properties need to be characterized, and the homogeneous distribution of the API has to be controlled to guarantee that patients receive the necessary therapeutical amount of API. For physical characterization, various tests are listed in the pharmacopeia: test for friability (Ph. Eur. 2.9.7), crushing strength (Ph. Eur. 2.9.8) and disintegration (Ph. Eur. 2.9.1). To check the homogeneity of the drug distribution, the content of the API in the tablets is determined via the uniformity of the mass or content (Ph. Eur. 2.9.5 / 2.9.6) or the uniformity of dosage units (Ph. Eur. 2.9.40). In addition, it is tested how the drug is released from the tablet over time (Ph. Eur. 2.9.3).

However, FDM printed tablets have different physical properties than compressed tablets, so further methods have been developed for physical characterization. Often, the printed tablets are less porous than the pressed ones, due to the individual layers fused together [118, 119]. Depending on the polymers used, the tablets cannot be crushed, do not disintegrate, or disintegrate very slowly, and do not exhibit abrasion [101, 120]. The porosity of the tablets can be easily controlled by the pattern and percentage of the infill of the design [120, 121]. To check the accuracy of the printing, as well as to determine the porosity of the printed tablets, μCT measurements are often used [102, 122]. The visualization of the internal structure of dosage forms reveals the structural quality, how well the layers adhere to each other, and how well the geometry matches the desired design without destruction of the tablet [123, 124]. In a study by Alhijjaj et al., it was shown that the printing speed, printing temperature, build plate leveling and polymer viscosity (melt flow index) have a high influence on the precision of the print, weight of the object and print reproducibility [125]. The effects of these parameters can be registered in the μCT and contribute to the improvement of the process.

As 3d printing is suitable for small, personalized batches, and produces a smaller throughput than industrial manufacturing machines, non-destructive methods are advantageous for this process. In addition, for the determination of the mass or content uniformity, the tablets must be dissolved, or the API must be extracted from the matrix. Therefore, there is also a growing interest in non-destructive content analysis, which is possible using NIR and Raman technology [102, 104]. This technique enables in-line and off-line implementation [126]. To verify the release of the API from the dosage form, in vitro studies must be performed. Here, the ingestion of the tablet, the residence time in the stomach and GIT are simulated. For children the dissolution studies were often adapted. For example, Starmix® candy-like dosage forms were dissolved in 2 ml saliva for 2 min, because children often are expected to chew the tablets [104, 127]. In addition, volumes and dwell times can also be adjusted for the specific patient group. Accurate dosing is especially important for children, which can be realized with FDM printing. The individually produced batch can be adapted to the needs of the children. Not only the dose, but also the release behavior can be varied. This is possible with the choice of polymer, as well as with the SA/V ratio, which can be implemented with the choice of geometry [99, 128, 129]. Various approaches are also currently being pursued to predict release curves using ANNs so that non-destructive methods can be established here as well [130–132]. These predictions are based, among other things, on the infill pattern of the tablets and their influences on the release pattern. In the study of Obeid et al. the influence of the SA/V ratio was used to predict the resulting release profile of the printed tablet [131].

Outlook

This manuscript aims to provide an overview of pharmaceutical as well as engineering considerations for FDM printed medication for children. We reflected on current liabilities and intended to depict ways for further innovation in the engineering of unit operations to enhance suitability of equipment and dosage forms. As for 3d printing of solid dosage forms in general, formulation and print technology need to be considered in a holistic manner taking into account all aspects from raw materials to final dosage forms. We conclude that there is strong need to advance FDM printing technologies and excipients to accommodate for pharmaceutical needs—with even more elevated quality requirements for pediatric patients especially in the fields of excipient safety, acceptability, printing control and accuracy. Good news is that remedy is underway with commercial start-ups (e.g., Triastek) as well es public–private consortia such as PolyPrint actively working on the necessary technical innovation to meet pharma requirements. Also, the pediatric patient population will benefit from future capabilities of individualized therapy with precise dose adjustment and possibilities to enhance compliance via tablet morphology and size. First small clinical trials on medications for children applying other additive manufacturing techniques clearly demonstrated the future potential of the tech field [133] and we speculate that FDM—due to its technical maturity and accessibility—will be one of the key enabling technologies to advance and establish pharmaceutical 3d printing for individualized and decentralized production of dosage forms—for adults as well as children.

Author contributions

JQ: conceptualization, writing, editing; MB: conceptualization, writing, editing; JB: writing; RC: writing; KE: conceptualization, writing, editing; A-GE: writing; NG: writing; GG-G: writing; LH: writing; DK: writing, editing; TK: conceptualization, writing, editing; SK: writing; FL: writing; TM: writing; HW: writing; SG: conceptualization, writing, editing; TS: writing, editing.

Funding

Declarations

Conflict of interest

The authors declare that they have no conflict of interest.

Open Access

Supplementary Information

References

1. Moreira M, Sarraguça M. How can oral paediatric formulations be improved? A challenge for the XXI century. *Int J Pharm*. 2020. https://doi.org/10.1016/J.IJPHARM.2020.119905.
2. Klingmann V, Spomer N, Lerch C. Favorable acceptance of mini-tablets compared with syrup: a randomized controlled trial in infants and preschool children. *J Pediatr*. 2013. https://doi.org/10.1016/J.JPEDS.2013.07.014.
3. Breitkreutz J, Boos J. Paediatric and geriatric drug delivery. *Expert Opin Drug Deliv*. 2007;4:37–45. https://doi.org/10.1517/17425247.4.1.37.
4. Liu F, Ranmal S, Batchelor HK. Patient-centered pharmaceutical design to improve acceptability of medicines: similarities and differences in paediatric and geriatric populations. *Drugs*. 2014;74:1871–89. https://doi.org/10.1007/S40265-014-0297-2.
5. el Aita I, Ponsar H, Quodbach J. A critical review on 3D-printed dosage forms. *Curr Pharm Des*. 2018;24:4957–78. https://doi.org/10.2174/1381612825666181206124206.
6. el Aita I, Breitkreutz J, Quodbach J. Investigation of semi-solid formulations for 3D printing of drugs after prolonged storage to mimic real-life applications. *Eur J Pharm Sci*. 2020;146: 105266. https://doi.org/10.1016/J.EJPS.2020.105266.
7. Melocchi A, Uboldi M, Cerea M. A graphical review on the escalation of fused deposition modeling (FDM) 3D printing in the pharmaceutical field. *J Pharm Sci*. 2020;109:2943–57. https://doi.org/10.1016/J.XPHS.2020.07.011.
8. Shaqour B, Samaro A, Verleije B. Production of drug delivery systems using fused filament fabrication: a systematic review. *Pharmaceutics*. 2020;12:517. https://doi.org/10.3390/PHARMACEUTICS12060517.
9. PolyPrint | ProMatLeben—Polymere n.d. https://promatleben.de/de/projekte/projekte-alphabetisch/polyprint/. Accessed 2 Sep 2021.
10. Paediatric formulations | European Medicines Agency n.d. https://www.ema.europa.eu/en/human-regulatory/research-development/paediatric-medicines/paediatric-investigation-plans/paediatric-formulations. Accessed 2 Sep 2021.
11. Reflection paper: formulations choice paediatric population n.d. https://www.ema.europa.eu/en/documents/scientific-guideline/reflection-paper-formulations-choice-paediatric-population_en.pdf. Accessed 2 Sep 2021.
12. Thabet Y, Klingmann V, Breitkreutz J. Drug formulations: standards and novel strategies for drug administration in pediatrics. *J Clin Pharmacol*. 2018;58:S26-35. https://doi.org/10.1002/JCPH.1138.
13. Rouaz K, Chiclana-Rodríguez B, Nardi-Ricart A. Excipients in the paediatric population: a review. *Pharmaceutics*. 2021. https://doi.org/10.3390/PHARMACEUTICS13030387.
14. Walsh J, Cram A, Woertz K. Playing hide and seek with poorly tasting paediatric medicines: do not forget the excipients. *Adv Drug Deliv Rev*. 2014;73:14–33. https://doi.org/10.1016/J.ADDR.2014.02.012.
15. STEP Database—EuPFI n.d. http://www.eupfi.org/step-database-info/. Accessed 2 Sep 2021.
16. Yochana S, Yu M, Alvi M. Pharmaceutical excipients and pediatric formulations. *Chim Oggi*. 2012;30:56–61.
17. Simões MF, Pinto RMA, Simões S. Hot-melt extrusion in the pharmaceutical industry: toward filing a new drug application. *Drug Discov Today*. 2019;24:1749–68. https://doi.org/10.1016/J.DRUDIS.2019.05.013.
18. Simões MF, Pinto RMA, Simões S. Hot-melt extrusion: a roadmap for product development. *AAPS PharmSciTech*. 2021. https://doi.org/10.1208/S12249-021-02017-7.
19. Bandari S, Nyavanandi D, Dumpa N. Coupling hot melt extrusion and fused deposition modeling: critical properties for successful performance. *Adv Drug Deliv Rev*. 2021;172:52–63. https://doi.org/10.1016/J.ADDR.2021.02.006.
20. Melocchi A, Parietti F, Maroni A. Hot-melt extruded filaments based on pharmaceutical grade polymers for 3D printing by fused deposition modeling. *Int J Pharm*. 2016;509:255–63. https://doi.org/10.1016/j.ijpharm.2016.05.036.
21. Korte C, Quodbach J. Formulation development and process analysis of drug-loaded filaments manufactured via hot-melt extrusion for 3D-printing of medicines. *Pharm Dev Technol*. 2018;23:1117–27. https://doi.org/10.1080/10837450.2018.1433208.

22. Zhang J, Feng X, Patil H. Coupling 3D printing with hot-melt extrusion to produce controlled-release tablets. *Int J Pharm.* 2017;519:186–97. https://doi.org/10.1016/j.ijpharm.2016.12.049.

23. Fuenmayor E, Forde M, Healy AV. Material considerations for fused-filament fabrication of solid dosage forms. *Pharmaceutics.* 2018;10:44. https://doi.org/10.3390/PHARMACEUTICS10020044.

24. Nasereddin JM, Wellner N, Alhijjaj M. Development of a simple mechanical screening method for predicting the feedability of a pharmaceutical FDM 3D printing filament. *Pharm Res.* 2018;35:1–13. https://doi.org/10.1007/S11095-018-2432-3.

25. Zhang J, Xu P, Vo A. Development and evaluation of pharmaceutical 3D printability for hot melt extruded cellulose-based filaments. *J Drug Deliv Sci Technol.* 2019;52:292. https://doi.org/10.1016/J.JDDST.2019.04.043.

26. Azad MA, Olawuni D, Kimbell G. Polymers for extrusion-based 3D printing of pharmaceuticals: a holistic materials-process perspective. *Pharmaceutics.* 2020;12:124. https://doi.org/10.3390/PHARMACEUTICS12020124.

27. Thakkar R, Thakkar R, Pillai A. Systematic screening of pharmaceutical polymers for hot melt extrusion processing: a comprehensive review. *Int J Pharm.* 2020;576: 118989. https://doi.org/10.1016/J.IJPHARM.2019.118989.

28. Gottschalk N, Bogdahn M, Harms M. Brittle polymers in fused deposition modeling: an improved feeding approach to enable the printing of highly drug loaded filament. *Int J Pharm.* 2021;597: 120216. https://doi.org/10.1016/J.IJPHARM.2021.120216.

29. Ehtezazi T, Algellay M, Islam Y. The application of 3D printing in the formulation of multilayered fast dissolving oral films. J Pharm Sci. 2018;107:1076–85. https://doi.org/10.1016/J.XPHS.2017.11.019.

30. Boniatti J, Januskaite P, da Fonseca LB. Direct powder extrusion 3D printing of praziquantel to overcome neglected disease formulation challenges in paediatric populations. *Pharmaceutics.* 2021. https://doi.org/10.3390/PHARMACEUTICS13081114.

31. Wang H, Dumpa N, Bandari S. Fabrication of taste-masked donut-shaped tablets via fused filament fabrication 3D printing paired with hot-melt extrusion techniques. *AAPS PharmSciTech.* 2020. https://doi.org/10.1208/S12249-020-01783-0.

32. Woertz K, Tissen C, Kleinebudde P. Taste sensing systems (electronic tongues) for pharmaceutical applications. *Int J Pharm.* 2011;417:256–71. https://doi.org/10.1016/J.IJPHARM.2010.11.028.

33. Soto J, Keeley A, Keating AV. Rats can predict aversiveness of active pharmaceutical ingredients. *Eur J Pharm Biopharm.* 2018;133:77–84. https://doi.org/10.1016/J.EJPB.2018.09.027.

34. Patwardhan K, Asgarzadeh F, Dassinger T. A quality by design approach to understand formulation and process variability in pharmaceutical melt extrusion processes. *J Pharm Pharmacol.* 2015;67:673–84. https://doi.org/10.1111/JPHP.12370.

35. Islam MT, Maniruzzaman M, Halsey SA. Development of sustained-release formulations processed by hot-melt extrusion by using a quality-by-design approach. *Drug Deliv Transl Res.* 2014;4:377–87. https://doi.org/10.1007/S13346-014-0197-8.

36. Agrawal A, Dudhedia M, Deng W. Development of tablet formulation of amorphous solid dispersions prepared by hot melt extrusion using quality by design approach. *AAPS PharmSciTech.* 2016;17:214–32. https://doi.org/10.1208/S12249-015-0472-0.

37. Ponsar H, Wiedey R, Quodbach J. Hot-melt extrusion process fluctuations and their impact on critical quality attributes of filaments and 3D-printed dosage forms. *Pharmaceutics.* 2020;12:511. https://doi.org/10.3390/pharmaceutics12060511.

38. Kohlgrüber K. *Co-rotating twin-screw extruders: fundamentals | Hanser-Fachbuch.* Munich: Hanser; 2008.

39. Coperion Download Center n.d. https://download.coperion.com/index_.html?download=111413. Accessed 2 Sep 2021.

40. Hopkins M. LOSS in weight feeder systems. *Meas Control.* 2006;39:237–40. https://doi.org/10.1177/002029400603900801.

41. Schulze D. *Powders and bulk solids—behavior, characterization, storage and flow|Dietmar Schulze|, vol. 22. New York: Springer; 2008.

42. Fahlenbock TD. Selecting a screw feed device for low-rate loss-in-weight feeding. *Powder Bulk Eng.* 2007;21(12):27–31.

43. Matarazzo P. Checklist for selecting a volumetric or gravimetric feeder. *Powder Bulk Eng.* 2010.

44. NAMUR. *Dosiergenauigkeit von kontinuierlichen Waagen.* 2006.

45. Meier R, Thommes M, Rasenack N. Granule size distributions after twin-screw granulation—do not forget the feeding systems. *Eur J Pharm Biopharm.* 2016;106:59–69. https://doi.org/10.1016/J.EJPB.2016.05.011.

46. Engisch WE, Muzzio FJ. Method for characterization of loss-in-weight feeder equipment. *Powder Technol.* 2012;228:395–403. https://doi.org/10.1016/J.POWTEC.2012.05.058.

47. Bruce C, Manning M. *Melt extruded thin strips containing coated pharmaceutical actives*, 2011.

48. Merck KGAA. *Shaping the future of formulation development with melt-based 3d printing technologies [White Paper]. 2021. https://www.pharmaexcipients.com/wp-content/uploads/2021/06/Shaping-the-Future-of-Formulation-Development-with-Melt-based-3D-Printing-Technologies.pdf. Accessed Sept 21, 2021.

49. Vynckier A-K, Dierickx L, Voorspoels J. Hot-melt co-extrusion: requirements, challenges and opportunities for pharmaceutical applications. *J Pharm Pharmacol.* 2014;66:167–79. https://doi.org/10.1111/JPHP.12091.

50. Crowley MM, Zhang F, Repka MA. Pharmaceutical applications of hot-melt extrusion: part I. *Drug Dev Ind Pharm.* 2008;33:909–26. https://doi.org/10.1080/03639040701498759.

51. Liang JZ. Effects of extrusion conditions on die-swell behavior of polypropylene/diatomite composite melts. *Polym Test.* 2008;27:936–40. https://doi.org/10.1016/J.POLYMERTESTING.2008.08.001.

52. Öblom H, Zhang J, Pimparade M. 3D-printed isoniazid tablets for the treatment and prevention of tuberculosis—personalized dosing and drug release. *AAPS PharmSciTech.* 2019. https://doi.org/10.1208/S12249-018-1233-7.

53. Xie T, Taylor LS. Effect of temperature and moisture on the physical stability of binary and ternary amorphous solid dispersions of celecoxib. *J Pharm Sci.* 2017;106:100–10. https://doi.org/10.1016/J.XPHS.2016.06.017.

54. Awad A, Fina F, Trenfield SJ. 3D printed pellets (miniprintlets): a novel, multi-drug, controlled release platform technology. *Pharmaceutics.* 2019;11:148. https://doi.org/10.3390/PHARMACEUTICS11040148.

55. Eggenreich K, Windhab S, Schrank S. Injection molding as a one-step process for the direct production of pharmaceutical dosage forms from primary powders. *Int J Pharm.* 2016;505:341–51. https://doi.org/10.1016/J.IJPHARM.2016.03.034.

56. Repka M, Bandari S, Kallakunta V. Melt extrusion with poorly soluble drugs—an integrated review. *Int J Pharm.* 2018;535:68–85. https://doi.org/10.1016/J.IJPHARM.2017.10.056.

57. Saerens L, Vervaet C, Remon JP. Process monitoring and visualization solutions for hot-melt extrusion: a review. *J Pharm Pharmacol.* 2014;66:180–203. https://doi.org/10.1111/JPHP.12123.

58. Spoerk M, Koutsamanis I, Matic J. Novel cleaning-in-place strategies for pharmaceutical hot melt extrusion. *Pharmaceutics.* 2020;12:1–21. https://doi.org/10.3390/PHARMACEUTICS12060588.

59. Wesholowski J, Prill S, Berghaus A. Inline UV/Vis spectroscopy as PAT tool for hot-melt extrusion. *Drug Deliv Transl Res.* 2018;8:1595–603. https://doi.org/10.1007/S13346-017-0465-5.

60. Saerens L, Dierickx L, Lenain B. Raman spectroscopy for the in-line polymer–drug quantification and solid state characterization during a pharmaceutical hot-melt extrusion process. *Eur J Pharm Biopharm.* 2011;77:158–63. https://doi.org/10.1016/J.EJPB.2010.09.015.

61. Vo AQ, He H, Zhang J. Application of FT-NIR analysis for in-line and real-time monitoring of pharmaceutical hot-melt extrusion: a technical note. *AAPS PharmSciTech.* 2018;19:3425. https://doi.org/10.1208/S12249-018-1091-3.

62. Kallakunta VR, Sarabu S, Bandari S. An update on the contribution of hot-melt extrusion technology to novel drug delivery in the twenty-first century: part I. *Expert Opin Drug Deliv.* 2019;16:539. https://doi.org/10.1080/17425247.2019.1609448.

63. Kim EJ, Kim JH, Kim M-S. Process analytical technology tools for monitoring pharmaceutical unit operations: a control strategy for continuous process verification. *Pharmaceutics.* 2021;13:919. https://doi.org/10.3390/PHARMACEUTICS13060919.

64. Koutsamanis I, Paudel A, Nickisch K. Controlled-release from high-loaded reservoir-type systems—a case study of ethylene-vinyl acetate and progesterone. *Pharmaceutics.* 2020. https://doi.org/10.3390/PHARMACEUTICS12020103.

65. Auch C, Harms M, Mäder K. How changes in molecular weight and PDI of a polymer in amorphous solid dispersions impact dissolution performance. *Int J Pharm.* 2019;556:372–82. https://doi.org/10.1016/J.IJPHARM.2018.12.012.

66. Ting J, William W, Porter I, Mecca JM. Advances in polymer design for enhancing oral drug solubility and delivery. *Bioconjug Chem.* 2018;29:939–52. https://doi.org/10.1021/ACS.BIOCONJCHEM.7B00646.

67. Đuranović M, Obeid S, Madžarevic M, et al. Paracetamol extended release FDM 3D printlets: evaluation of formulation variables on printability and drug release. *Int J Pharm.* 2021. https://doi.org/10.1016/J.IJPHARM.2020.120053.

68. Gorkem Buyukgoz G, Soffer D, Defendre J. Exploring tablet design options for tailoring drug release and dose via fused deposition modeling (FDM) 3D printing. *Int J Pharm.* 2020. https://doi.org/10.1016/J.IJPHARM.2020.119987.

69. Prasad E, Islam MT, Goodwin DJ. Development of a hot-melt extrusion (HME) process to produce drug loaded Affinisol[TM] 15LV filaments for fused filament fabrication (FFF) 3D printing. *Addit Manuf.* 2019. https://doi.org/10.1016/J.ADDMA.2019.06.027.

70. Aho J, van Renterghem J, Arnfast L. The flow properties and presence of crystals in drug-polymer mixtures: rheological investigation combined with light microscopy. *Int J Pharm.* 2017;528:383–94. https://doi.org/10.1016/J.IJPHARM.2017.06.012.

71. Qian F, Huang J, Hussain M. Drug-polymer solubility and miscibility: stability consideration and practical challenges in amorphous solid dispersion development. *J Pharm Sci.* 2010;99:2941–7. https://doi.org/10.1002/JPS.22074.

72. Baird J, van Eerdenbrugh B, Taylor L. A classification system to assess the crystallization tendency of organic molecules from undercooled melts. *J Pharm Sci.* 2010;99:3787–806. https://doi.org/10.1002/JPS.22197.

73. Dedroog S, Pas T, Vergauwen B. Solid-state analysis of amorphous solid dispersions: why DSC and XRPD may not be regarded as stand-alone techniques. *J Pharm Biomed Anal.* 2020. https://doi.org/10.1016/J.JPBA.2019.112937.

74. Ma X, Williams RO III. Characterization of amorphous solid dispersions: an update. *J Drug Deliv Sci Technol.* 2019;50:113–24. https://doi.org/10.1016/j.jddst.2019.01.017.

75. Wadher K, Trivedi R, Wankhede N. 3D printing in pharmaceuticals: an emerging technology full of challenges. *Ann Pharm Fr.* 2021;79:107–18. https://doi.org/10.1016/J.PHARMA.2020.08.007.

76. Hauser G. *Hygienegerechte apparate und anlagen*, vol. 1. 1st ed. Weinheim: Wiley; 2008.

77. Kampker A, Triebs J, Kawollek S. Review on machine designs of material extrusion based additive manufacturing (AM) systems—status-Quo and potential analysis for future AM systems. *Procedia CIRP.* 2019;81:815–9. https://doi.org/10.1016/J.PROCIR.2019.03.205.

78. Melocchi A, Briatico-Vangosa F, Uboldi M. Quality considerations on the pharmaceutical applications of fused deposition modeling 3D printing. *Int J Pharm.* 2021. https://doi.org/10.1016/J.IJPHARM.2020.119901.

79. Leitlinien—EHEDG n.d. https://ehedg.de/leitlinien/. Accessed 2 Sep 2021.

80. Fortus 450mc | Stratasys[TM] Support Center n.d. https://support.stratasys.com/en/printers/fdm/fortus-450mc. Accessed 2 Sep 2021.

81. BIO X Syringe Pump Printhead—CELLINK n.d. https://www.cellink.com/product/bio-x-syringe-pump-printhead/. Accessed 2 Sep 2021.

82. SDS-5 3d printer Extruder| Hyrel3D n.d. https://www.hyrel3d.com/portfolio/sds-5-extruder/. Accessed 2 Sep 2021.

83. Serdeczny MP, Comminal R, Mollah MT. Numerical modeling of the polymer flow through the hot-end in filament-based material extrusion additive manufacturing. *Addit Manuf.* 2020. https://doi.org/10.1016/J.ADDMA.2020.101454.

84. x500pro | German RepRap GmbH n.d. https://www.germanreprap.com/printer/x500pro.aspx. Accessed 2 Sep 2021.

85. van Bracht R, Piller FT, Marquardt E. Das Potenzial der additiven Fertigung: digitale Technologien im Unternehmenskontext : Auswert 2019.

86. Kim H, Lin Y, Tseng TLB. A review on quality control in additive manufacturing. *Rapid Prototyping* J. 2018;24:645–69. https://doi.org/10.1108/RPJ-03-2017-0048.

87. Becker P, Gebert J, Roennau A et al. Online error detection in additive manufacturing: a review. In: *Proceedings of the 2021 IEEE 8th International Conference on Industrial Engineering and Applications, ICIEA 2021,* pp. 167–75. https://doi.org/10.1109/ICIEA52957.2021.9436729.

88. Tlegenov Y, Lu WF, Hong GS. A dynamic model for current-based nozzle condition monitoring in fused deposition modelling. *Progress Addit Manuf.* 2019;4:211–23. https://doi.org/10.1007/S40964-019-00089-3.

89. Rao P, Liu J, Mathew Roberson D, et al. Online real-time quality monitoring in additive manufacturing processes using heterogeneous sensors additive manufacturing view project fatigue life prediction from defect criticality for L-PBF parts view project online real-time quality monitoring in additive manufacturing processes using heterogeneous sensors. *J Manuf Sci Eng.* 2014. https://doi.org/10.1115/1.4029823.

90. Baumann F, Roller D. Vision based error detection for 3D printing processes. *MATEC Web Conf.* 2016;59:1–7. https://doi.org/10.1051/conf/2016.

91. Becker P, Spielbauer N, Roennau A. Real-time in-situ process error detection in additive manufacturing. In: *Proceedings of the 4th IEEE International Conference on Robotic Computing, IRC 2020,* 2020, pp 426–427. https://doi.org/10.1109/IRC.2020.00077.

92. Greeff GP, Schilling M. Closed loop control of slippage during filament transport in molten material extrusion. *Addit Manuf.* 2017;14:31–8. https://doi.org/10.1016/j.addma.2016.12.005.

93. Khorasani M, Edinger M, Raijada D, et al. Near-infrared chemical imaging (NIR-CI) of 3D printed pharmaceuticals. *Int J*

95

Pharm. 2016;515:324–30. https://doi.org/10.1016/j.ijpharm.2016.09.075.

94. Theil F, Milsmann J, Anantharaman S, et al. Manufacturing amorphous solid dispersions with a tailored amount of crystallized API for biopharmaceutical testing. *Mol Pharm.* 2018;15:1870–7. https://doi.org/10.1021/acs.molpharmaceut.8b00043.

95. Alessandrini E, Brako F, Scarpa M. Children's Preferences for Oral Dosage Forms and Their Involvement in Formulation Research via EPTRI (European Paediatric Translational Research Infrastructure). *Pharmaceutics.* 2021;13:730. https://doi.org/10.3390/PHARMACEUTICS13050730.

96. Jamróz W, Szafraniec J, Kurek M. 3D printing in pharmaceutical and medical applications—recent achievements and challenges. *Pharm Res.* 2018. https://doi.org/10.1007/S11095-018-2454-X.

97. Lennartz P, Mielck JB. Minitabletting: improving the compactability of paracetamol powder mixtures. *Int J Pharm.* 1998;173:75–85. https://doi.org/10.1016/S0378-5173(98)00206-3.

98. Klingmann V, Seitz A, Meissner T. Acceptability of uncoated mini-tablets in neonates—a randomized controlled trial. *J Pediatr.* 2015;167:893-896.e2. https://doi.org/10.1016/J.JPEDS.2015.07.010.

99. Krause J, Müller L, Sarwinska D. 3D printing of mini tablets for pediatric use. *Pharmaceuticals.* 2021;14:1–16. https://doi.org/10.3390/PH14020143.

100. Parhi R. A review of three-dimensional printing for pharmaceutical applications: quality control, risk assessment and future perspectives. *J Drug Deliv Sci Technol.* 2021. https://doi.org/10.1016/J.JDDST.2021.102571.

101. Ayyoubi S, Cerda JR, Fernández-García R. 3D printed spherical mini-tablets: geometry versus composition effects in controlling dissolution from personalised solid dosage forms. *Int J Pharm.* 2021. https://doi.org/10.1016/J.IJPHARM.2021.120336.

102. Fanous M, Bitar M, Gold S. Development of immediate release 3D-printed dosage forms for a poorly water-soluble drug by fused deposition modeling: study of morphology, solid state and dissolution. *Int J Pharm.* 2021;599: 120417. https://doi.org/10.1016/J.IJPHARM.2021.120417.

103. Vijayavenkataraman S, Fuh JYH, Lu WF. 3D printing and 3D bioprinting in pediatrics. *Bioengineering.* 2017. https://doi.org/10.3390/BIOENGINEERING4030063.

104. Scoutaris N, Ross S, Douroumis D. 3D printed "Starmix" drug loaded dosage forms for paediatric applications. *Pharm Res.* 2018. https://doi.org/10.1007/S11095-017-2284-2.

105. Pereira BC, Isreb A, Forbes RT. 'Temporary Plasticiser': a novel solution to fabricate 3D printed patient-centred cardiovascular 'Polypill' architectures. *Eur J Pharm Biopharm.* 2019;135:94–103. https://doi.org/10.1016/J.EJPB.2018.12.009.

106. Klingmann V, Pohly CE, Meissner T. Acceptability of an orodispersible film compared to syrup in neonates and infants: a randomized controlled trial. *Eur J Pharm Biopharm.* 2020;151:239–45. https://doi.org/10.1016/J.EJPB.2020.03.018.

107. Orlu M, Ranmal SR, Sheng Y. Acceptability of orodispersible films for delivery of medicines to infants and preschool children. Drug Deliv. 2017;24:1243–8. https://doi.org/10.1080/10717544.2017.1370512.

108. Musazzi UM, Selmin F, Ortenzi MA. Personalized orodispersible films by hot melt ram extrusion 3D printing. *Int J Pharm.* 2018;551:52–9. https://doi.org/10.1016/J.IJPHARM.2018.09.013.

109. Liu C, Chang D, Zhang X. Oral fast-dissolving films containing lutein nanocrystals for improved bioavailability: formulation development, in vitro and in vivo evaluation. *AAPS*

PharmSciTech. 2017;18:2957–64. https://doi.org/10.1208/S12249-017-0777-2.

110. Foo WC, Khong YM, Gokhale R. A novel unit-dose approach for the pharmaceutical compounding of an orodispersible film. *Int J Pharm.* 2018;539:165–74. https://doi.org/10.1016/J.IJPHARM.2018.01.047.

111. Huanbutta K, Sriamornsak P, Singh I. Manufacture of 2D-printed precision drug-loaded orodispersible film prepared from tamarind seed gum substrate. *Appl Sci.* 2021;11:5852. https://doi.org/10.3390/APP11135852.

112. Öblom H, Sjöholm E, Rautamo M. towards printed pediatric medicines in hospital pharmacies: comparison of 2D and 3D-printed orodispersible warfarin films with conventional oral powders in unit dose sachets. *Pharmaceutics.* 2019. https://doi.org/10.3390/PHARMACEUTICS11070334.

113. Landová H, Vetchý D. Evaluation of the influence of formulation and process variables on mechanical properties of oral mucoadhesive films using multivariate data analysis. *BioMed Res Int.* 2014. https://doi.org/10.1155/2014/179568.

114. Evans SE, Harrington T, Rodriguez Rivero MC, et al. 2D and 3D inkjet printing of biopharmaceuticals—a review of trends and future perspectives in research and manufacturing. *Int J Pharm.* 2021;599: 120443. https://doi.org/10.1016/J.IJPHARM.2021.120443.

115. Jamróz W, Kurek M, Łyszczarz E, et al. 3D printed orodispersible films with Aripiprazole. *Int J Pharm.* 2017;533:413–20. https://doi.org/10.1016/J.IJPHARM.2017.05.052.

116. Cho HW, Baek SH, Lee BJ, et al. Orodispersible polymer films with the poorly water-soluble drug, olanzapine: hot-melt pneumatic extrusion for single-process 3D printing. *Pharmaceutics.* 2020;12:1–16. https://doi.org/10.3390/PHARMACEUTICS12080692.

117. Eleftheriadis GK, Ritzoulis C, Bouropoulos N, et al. Unidirectional drug release from 3D printed mucoadhesive buccal films using FDM technology: In vitro and ex vivo evaluation. *Eur J Pharm Biopharm.* 2019;144:180–92. https://doi.org/10.1016/J.EJPB.2019.09.018.

118. Than YM, Titapiwatanakun V. Tailoring immediate release FDM 3D printed tablets using a quality by design (QbD) approach. *Int J Pharm.* 2021;599: 120402. https://doi.org/10.1016/J.IJPHARM.2021.120402.

119. Nukala PK, Palekar S, Patki M, et al. Abuse deterrent immediate release egg-shaped tablet (Egglets) using 3D printing technology: quality by design to optimize drug release and extraction. *AAPS PharmSciTech.* 2019. https://doi.org/10.1208/S12249-019-1298-Y.

120. Zhang J, Thakkar R, Zhang Y. Structure-function correlation and personalized 3D printed tablets using a quality by design (QbD) approach. *Int J Pharm.* 2020. https://doi.org/10.1016/J.IJPHARM.2020.119945.

121. Palekar S, Nukala P, Mishra S. Application of 3D printing technology and quality by design approach for development of age-appropriate pediatric formulation of baclofen. *Int J Pharm.* 2019;556:106–16. https://doi.org/10.1016/J.IJPHARM.2018.11.062.

122. Goyanes A, Fina F, Martorana A, et al. Development of modified release 3D printed tablets (printlets) with pharmaceutical excipients using additive manufacturing. *Int J Pharm.* 2017;527:21–30. https://doi.org/10.1016/J.IJPHARM.2017.05.021.

123. Markl D, Zeitler JA, Rasch C. Analysis of 3D prints by X-ray computed microtomography and terahertz pulsed imaging. *Pharm Res.* 2016;34:1037–52. https://doi.org/10.1007/S11095-016-2083-1.

124. Gioumouxouzis CI, Katsamenis OL, Fatouros DG. X-ray microfocus computed tomography: a powerful tool for structural

and functional characterisation of 3D printed dosage forms. J Microsc. 2019. https://doi.org/10.1111/JMI.12798.

125. Alhijjaj M, Nasereddin J, Belton P. Impact of processing parameters on the quality of pharmaceutical solid dosage forms produced by fused deposition modeling (FDM). *Pharmaceutics.* 2019;11:633. https://doi.org/10.3390/PHARMACEUTICS11120633.

126. Trenfield SJ, Goyanes A, Telford R, et al. 3D printed drug products: non-destructive dose verification using a rapid point-and-shoot approach. *Int J Pharm.* 2018;549:283–92. https://doi.org/10.1016/J.IJPHARM.2018.08.002.

127. Rachid O, Rawas-Qalaji M, Estelle F. Dissolution testing of sublingual tablets: a novel in vitro method. *AAPS PharmSciTech.* 2011;2011(12):544–52. https://doi.org/10.1208/s12249-011-9615-0.

128. Reynolds TD, Mitchell SA, Balwinski KM. Investigation of the effect of tablet surface area/volume on drug release from hydroxy-propylmethylcellulose controlled-release matrix tablets. *Drug Dev Ind Pharm.* 2002. https://doi.org/10.1081/DDC-120003007.

129. Goyanes A, Robles Martinez P, Buanz A, et al. Effect of geometry on drug release from 3D printed tablets. *Int J Pharm.* 2015. https://doi.org/10.1016/j.ijpharm.2015.04.069.

130. Madzarevic M, Medarevic D, Vulovic A. Optimization and prediction of ibuprofen release from 3D DLP printlets using artificial neural networks. *Pharmaceutics.* 2019. https://doi.org/10.3390/PHARMACEUTICS11100544.

131. Obeid S, Madžarević M, Krkobabić M, et al. Predicting drug release from diazepam FDM printed tablets using deep learning approach: Influence of process parameters and tablet surface/volume ratio. *Int J Pharm.* 2021;601: 120507. https://doi.org/10.1016/J.IJPHARM.2021.120507.

132. Novák M, Boleslavská T, Grof Z, et al. Virtual prototyping and parametric design of 3D-printed tablets based on the solution of inverse problem. *AAPS PharmSciTech.* 2018;19:3414–24. https://doi.org/10.1208/s12249-018-1176-z.

133. Goyanes A, Madla CM, Umerji A, et al. Automated therapy preparation of isoleucine formulations using 3D printing for the treatment of MSUD: First single-centre, prospective, crossover study in patients. *Int J Pharm.* 2019;567: 118497. https://doi.org/10.1016/J.IJPHARM.2019.118497.

Chapter C:

Prediction of Drug Release Characteristics and 3DP Drug Dosage Form Design

C.1 Predicting Drug Release from 3D Printed Oral Medicines Based on the Surface Area to Volume Ratio of Tablet Geometry

Hellen Windolf, Rebecca Chamberlain, Julian Quodbach

Pretext

For personalized therapy to be shaped in the best possible way for the patient, it is important to be able to cover different time periods for the release of the API. If the effect is to occur quickly and directly, an unmodified, immediate release is necessary; if a constant release over as long a period as possible is desired, the dissolution rate can be influenced by the choice of polymer, as well as the geometry and thus the SA/V ratio. The experimentally generated release curves can be described using various mathematical equations and models. In the following study, a correlation between the SA/V ratio and the MDT was used to predict the MDT and the underlying release curve based on the SA/V ratio. By describing the curves more accurately using the Peppas Sahlin equation and the Weibull function, accurate predictions could be made about the resulting release profiles, which were confirmed experimentally.

Evaluation of authorship:

author	idea [%]	study design [%]	experimental [%]	evaluation [%]	manuscript [%]
Hellen Windolf	80	90	90	80	80
Rebecca Chamberlain	10	5	10	10	10
Julian Quodbach	10	5	0	10	10

Evaluation of Copyright permission:

Predicting drug release from 3D printed oral medicines based on the surface area to volume ratio of the tablets

Hellen Windolf, Rebecca Chamberlain, Julian Quodbach

Abstract

3D printing offers the advantage to modify dosage form geometry, which can be exploited to modify release characteristics. In this study, we investigate the influence of the surface area to volume ratio (SA/V) to change and predict release profiles of 3D printed dosage forms. Geometries with varying SA/V and dosages were designed, printed, and drug dissolution investigated. Three drug substances were used: pramipexole, levodopa (both BCS I) and praziquantel (BCS II). Two polymers were chosen as matrix formers: polyvinyl alcohol (water-soluble) and ethylene vinyl acetate (inert). Drug release was characterized using the Mean Dissolution Time (MDT) and applying established equations that describe complete dissolution curves. Predictions were validated with previously un-printed dosage forms. Based on an identified MDT-SA/V correlation, the MDT can be predicted with a deviation of ≤ 5 min for given SA/V. Using correlations of fit parameters and SA/V, RMSEP values of 0.6-2.8 % and 1.6-3.4 % were obtained for the BCS I formulations and RMSEP values of 1.0-3.8 % for the BCS II formulation, indicating accurate prediction over a wide range of dissolution profiles. With this approach, MDT and release profiles of dosage forms with given SA/V can be precisely predicted without performing dissolution tests and vice versa, the required SA/V can be predicted for a desired release profile.

Article

Predicting Drug Release from 3D Printed Oral Medicines Based on the Surface Area to Volume Ratio of Tablet Geometry

Hellen Windolf [ID], Rebecca Chamberlain and Julian Quodbach *[ID]

Institute of Pharmaceutics and Biopharmaceutics, Heinrich Heine University, Universitätsstr. 1,
40225 Düsseldorf, Germany; hellen.windolf@hhu.de (H.W.); rebecca.chamberlain@hhu.de (R.C.)
* Correspondence: julian.quodbach@hhu.de; Tel.: +49-211-81-15693

Abstract: 3D printing offers the advantage of being able to modify dosage form geometry, which can be exploited to modify release characteristics. In this study, we investigated the influence of the surface area to volume ratio (SA/V) to change and predict release profiles of 3D printed dosage forms. Geometries with varying SA/V and dosages were designed and printed, and drug dissolution was investigated. Three drug substances were used: pramipexole, levodopa (both BCS I) and praziquantel (BCS II). Two polymers were chosen as matrix formers: polyvinyl alcohol (water-soluble) and ethylene vinyl acetate (inert). Drug release was characterized using the mean dissolution time (MDT) and established equations that describe complete dissolution curves were applied. Predictions were validated with previously un-printed dosage forms. Based on an identified MDT-SA/V correlation, the MDT can be predicted with a deviation of ≤ 5 min for a given SA/V. Using correlations of fit parameters and SA/V, RMSEP values of 0.6–2.8% and 1.6–3.4% were obtained for the BCS I formulations and RMSEP values of 1.0–3.8% were obtained for the BCS II formulation, indicating accurate prediction over a wide range of dissolution profiles. With this approach, MDT and release profiles of dosage forms with a given SA/V can be precisely predicted without performing dissolution tests and vice versa, the required SA/V can be predicted for a desired release profile.

Keywords: 3D printing; oral dosage form; drug dissolution; mean dissolution time; drug release prediction; personalized medicine

1. Introduction

Personalized pharmaceutical therapies are increasingly moving into focus to match the individual needs of patients [1–3]. There is a constantly improving understanding of the organism and metabolism of children and elderly patients, and it is becoming increasingly clear that drug substances may be metabolized differently compared to adults, especially if comorbidities are present. The efficacy of the active pharmaceutical ingredient (API) varies depending on age, body type, gender, health, and the individual metabolic state [4–6]. To adjust the dose of medicine for patients based on these dependencies, several approaches are available. Liquid or semi-solid preparations can be measured and dosed individually with the help of dosing aids, such as spoons, syringes, or cups. With solid dosage forms, it becomes more difficult to provide exact doses. Some tablets can be split into halves or quarters by hand or with the help of a tablet cutter, but these methods lead to inaccurate dosing [7,8]. Tablets with modified release especially demonstrate a major challenge if the release-determining factor is controlled by a functional coating, which loses its integrity when a tablet is split or mortared [9]. The requirements for dose variability and the constraining demand for an equivalent release profile despite the change in dose strength cannot be addressed industrially. The small batches needed for personalized medicine are not technically and economically feasible to manufacture on large-scale equipment. To provide patients with customized medicines, 3D printing to manufacture individualized medicine has been investigated [10–14]. Most commercial 3D printers

are not only inexpensive, but also easy to operate and able to produce small batches for patients on demand. With individually manufactured dosage forms, it is possible to adapt the dosage of the API and the release kinetics of the API to the patient. In this way, a wide range of therapeutic regimens can be covered and side effects reduced, as the most effective dose with the least adverse effects can be administered precisely [15]. In the future, the production of these individual batches could be realized by community pharmacies, hospitals and regional manufacturing hubs.

In fused deposition modeling (FDM) 3D printing, intermediates containing the API, so-called filaments, are produced by hot-melt extrusion [3,16–18]. Filaments have to meet certain mechanical properties in order to enable the subsequent printing process [16,19,20]. The drug-loaded filament is fed into the print head, molten in the nozzle, and deposited on a heated print bed. Because of these two heat-intensive steps, FDM 3D printing is limited in terms of the APIs that can be used. The APIs should be thermostable and only decompose at high temperatures. Although it is possible to work with polymers that melt at low temperatures, this severely limits the choice of polymers [21]. The desired object is designed in advance using computer-aided design (CAD) software and converted via a slicer software into a machine language, the G-code. This G-code determines the temperature, movement, and the speed of the print head and print bed. The design of the object should consider the volume, which determines the dosage depending on the drug-load of the filament. There are two opportunities to influence the drug release properties of 3D printed objects: changing the composition of the filaments and adapting the surface area to volume (SA/V) ratio [22–25]. Since printing technologies allow one to manufacture a wide range of geometries without further development efforts, changing the SA/V ratio is the preferred option. It has been shown that the API release is faster, when the SA/V ratio is higher and slower when the ratio is smaller [22,23,26]. The absolute volume and the selected geometry were found to be negligible [23]. In order to reduce the elaborate production of filaments, there is a need to achieve different release profiles with only one filament.

To enable an individual dosage form with a defined dissolution profile, one must understand how the underlying formulation performs and according to which kinetic the API is released from the polymer matrix. Release profiles can be fitted using mathematical equations that consider the dissolution behaviour of the API and the polymer, as well as the diffusion pathways the API and the medium must overcome [27–29]. So far, various approaches have been used to try to predict the drug release from solid dosage forms [30–41]. Korte et al. investigated the approach of changing the dose of the 3D geometry via the percent of infill and predicted the release kinetics depending on the infill density [42]. Likewise, in another study, an infill in the form of honeycomb was modified, thereby also changing the drug release profile and predicting the resulting release profiles [43]. Artificial neural networks (ANN) are also being implemented to identify the influence of formulation and process parameters on the release behaviour and to improve predictions [28,34,44–47]. For example, Novák investigated the influence of varying infills and resulting tablet porosities on drug release using an ANN. This resulted in an in-silico design method of infill variations for 3D printed dosage geometries [48].

In this work, two different approaches were applied to predict dissolution characteristics and complete dissolution profiles of 3D printed geometries. This should ensure that individual batches can be produced in hospitals and community pharmacies without having to spend a lot of material, time and money on release testing. Firstly, the release behaviour of various geometries should be predicted via correlations between the SA/V ratio of the printed objects and the mean dissolution time (MDT) of the printed dosage forms. Secondly, complete release profiles should be predicted based on correlations between the SA/V ratio and suitable mathematical equations. Validation experiments should be performed in all cases to appraise the quality of the prediction approaches.

2. Materials and Methods

2.1. Materials

Formulation 1, referred to as the PVA-PDM formulation, consisted of 5% (*w/w*) pramipexole dihydrochloride monohydrate (PDM, Chr. Olesen, Denmark) as an API of the biopharmaceutics classification system (BCS) class I, declared as good water solubility ($c_s \geq 200$ mg/mL) [49,50]. Mannitol (Parteck M®, Merck, Germany) was used as a plasticizer at 10% (*w/w*) content. Polyvinyl alcohol (84%, PVA, Parteck MXP®, Merck, Germany) was selected as a polymer. Formulation 2, referred to as the EVA-LD formulation, consisted of 10% (*w/w*) levodopa (Zhejiang Wild Wind Pharmaceutical, Dongyang, China), and was also a BCS class I API ($c_s \geq 12$ mg/mL) [51]. As water soluble component, a vinylpyrrolidone-vinyl acetate copolymer (VP-VA) was used (39.5%, Kollidon VA 64®, BASF, Ludwigshafen, Germany) and 10% mannitol was added as a plasticizer. The matrix consisted of ethylene vinyl acetate (EVA) with a content of 18% vinyl acetate (39.5%, Escorene® FL 01418, TER Chemicals, Hamburg, Germany). To improve flowability, 1% fumed silica (Aerosil® 200 VV Pharma, Evonik, Germany) was added to both formulations. Formulation 3, referred to as the PVA-PZQ formulation, consisted of 5% (*w/w*) praziquantel (PZQ, donated from Bayer AG, Leverkusen, Germany) as an API of BCS class II ($c_s = 0.4$ mg/mL) [52–54], declared as poorly water-soluble. As a polymer basis, PVA was chosen with 95% content. All filament formulations were systematically developed to minimize diameter fluctuations of the filaments and to ensure highest printability with the available equipment. The criteria for the drug selection were heat stability and different classifications in the BCS. The melting point of PDM is also the decomposition point at 296–305 °C [20,55–57]. LD melts and decomposes at 260–330 °C [58]. PZQ has its melting point already at 140–143 °C but decomposes only at temperatures >400 °C [59,60]. The investigated dose ranges do not correspond to therapeutic dosages and result from the drug loading of the filament and the volume of the objects. The polymer matrix of the first formulation should be water soluble and generate prolonged drug release. PVA fulfils both criteria as the polymer forms a water-soluble hydrocolloid matrix [61]. To test the transferability of the predictive model to other formulations, an inert, non-swelling matrix, EVA, was chosen [62]. To improve the printability and hydrophilicity of the filament, VP-VA was added. PVA was again chosen for transferring the model to the BCS class II drug, for the extended drug release as well as better printability. Thus, variations resulting from the process could be eliminated and the differences clearly attributed to the API.

2.2. Methods

2.2.1. Hot Melt Extrusion

The drug-containing filaments of formulation 1, 2 and 3 were produced via hot-melt extrusion with a co-rotating twin-screw extruder (Pharmalab HME 16, Thermo Fisher Scientific, Waltham, USA) using an in-house manufactured die with a diameter of 1.85 mm. The feed rate was set to 5 g/min and the screw speed to 30 rpm. The temperatures of the heating zones as well as the screw configurations are shown in Table 1. The filaments were hauled off with a winder (Model 846700, Brabender, Duisburg, Germany) at a speed of 1.8 m/min to the target diameter of 1.75 mm. The diameter was controlled using a laser-based diameter measurement module (Laser 2025 T, Sikora, Bremen, Germany).

2.2.2. 3D Printing of Tablets

The drug-loaded filaments were printed on a FDM 3D printer (Prusa i3 Mk3, Prusa Research, Prague, Czech Republic) to oral dosage forms in various geometries. The geometries were designed with Fusion 360® (Autodesk, San Rafael, CA, USA) and sliced in Simplify3D® (Simplify3D, Cincinnati, OH, USA) to obtain the desired G-code. The print temperature for the PVA-PDM filaments was set to 185 °C, the bed temperature to 60 °C and the printing speed was 20 mm/s. The printing temperature had to be increased for the EVA-LD formulation, as the filament was very flexible and could not be transported reliably through the nozzle by the conveying wheels in the print head at lower temperatures, as

the filament would otherwise wrap around the wheels. To ensure a constant filament-flow through the nozzle, the temperature of the nozzle was set to 220 °C and the printing speed was reduced to 10 mm/s. For the PVA-PZQ formulation, a nozzle temperature of 185 °C could again be used, but the bed temperature had to be increased to 90 °C because the printed objects adhered poorly to the print bed and detached from the bed more often. Therefore, a printing speed of 10 mm/s was also selected here. To obtain high print accuracy, the layer height was set to 0.1 mm and the extrusion width to 0.4 mm using a nozzle with a diameter of 0.4 mm. The infill percentage of the concentric infill was set to 100%.

Table 1. Extrusion settings (temperature profile and screw configuration) for the used formulations.

Temperature Profile in Zone 2–10/°C									
Zone/-	**2**	**3**	**4**	**5**	**6**	**7**	**8**	**9**	**10**
PVA-PDM formulation/°C	30	100	180	180	180	180	180	195	195
PVA-PZQ formulation/°C	21	31	78	180	180	180	180	180	190
EVA-LD formulation/°C	25	28	78	130	140	155	155	120	100
Screw Configuration (Die–Gear)									
PVA/EVA formulation	die-10 CE 1 L/D-KZ: 5 × 60°-3 × 30°-5 CE 1 L/D-KZ: 4 × 90°-5 × 60°-3 × 30°-10 CE 1 L/D-2 CE 3/2 L/D-gear CE = conveying element, KZ = kneading zone								

2.2.3. Dissolution Test

According to Ph. Eur. monographs 2.9.3 and 5.17.1 [63,64], release studies ($n \geq 3$) were performed with the basket method (Method 1) in a dissolution tester (DT 726, Erweka, Langen, Germany). The baskets were 3D printed from water insoluble polylactide acid (PLA). They had to be adapted for printed tablets, since the mesh size of the regular Ph. Eur. baskets is small (0.36–0.44 mm) and the baskets were clogged by the swollen polymer of the PVA formulation. This affected the hydrodynamic medium flow around the printed oral dosage forms. The self-printed baskets have the same outer dimensions as the Ph. Eur. baskets, except that the mesh width was changed to 3 mm. The dissolution test for PDM containing tablets was performed in 500 mL of degassed 0.1 N hydrochloric acid at pH 1.2 under sink conditions ($c_s \geq 200$ mg/mL [50]; maximum concentration 0.08 mg/mL) and stirred at 50 rpm at a temperature of 37 ± 0.5 °C. The released API was measured using an UV-Vis spectral photometer (UV-1800 Shimadzu, Japan) at a wavelength of 263 nm. Dissolution testing of the levodopa containing geometries was performed in 1000 mL of degassed 0.1 N hydrochloric acid at pH 1.2 under sink conditions ($c_s \geq 12$ mg/mL [51]; maximum concentration 0.05 mg/mL) and stirred at 50 rpm at a temperature of 37 ± 0.5 °C. The API release was recorded with the same UV-Vis spectral photometer at a wavelength of 280 nm. The dissolution tests with PZQ were performed in 750 mL of degassed 0.1 N hydrochloric acid at pH 1.2 for the first 120 min and then transferred to 1000 mL phosphate buffer pH 6.8 with 250 mL of degassed 0.2 N tri-sodium phosphate dodecahydrate solution. The temperature was adjusted to 37 ± 0.5 °C. The drug release was measured at a wavelength of 210 nm. The tests were performed under sink conditions ($c_s = 0.4$ mg/mL [54]; maximum concentration: 0.03 mg/mL). Samples were taken every 5 min for the first 30 min, then every 10 min for the next 90 min, followed by sampling in 20 min intervals. After a release time of 240 min, samples were taken every 30 min.

2.2.4. Mathematical Description
Release Modeling

The mean dissolution time (MDT) is used as a characteristic value that describes the drug release and was calculated according to Equation (1). It is expressed in units of time, usually in minutes, and indicates how long an API molecule is retained in a dosage form on average during dissolution [27,65].

$$\text{MDT} = \frac{\text{ABC}}{c_\infty} = \frac{\sum_{i=0}^{\infty}\left[(c_{i+1} - c_i) * \frac{(t_i + t_{i+1})}{2}\right]}{c_\infty} \tag{1}$$

ABC stands for the area between the curves and is calculated via the trapezoidal equation with c as the concentration of the API released over time t and c_∞ as the initial drug load of the dosage form. Values up to 100% of the release curve were used for the calculation since the ABC does not change afterwards.

Various mathematical models were tested to fit the complete release profiles for prediction. First, the Korsmeyer–Peppas equation, or power law, was applied (Equation (2)) [27,66].

$$\frac{M_t}{M_\infty} = k * t^n \tag{2}$$

The released amount of the API over time t is described by the term M_t. The total amount of the API in the dosage form at the beginning of the release process is represented by M_∞. The constant k describes the structural and geometrical characteristics of the dosage form (cylinder, sphere, film), also known as the reaction rate constant or release velocity constant. The diffusional constant n describes the underlying drug release mechanism. Only the first 60% of the release curve should be used for the calculation. The model can be used to analyse the underlying release properties of the system, when the mechanism is unknown, or more than one release mechanism is involved. It should be taken into account that the equation requires some properties of the matrix to be valid: the drug in the matrix must be distributed homogeneously, show unidirectional diffusion, and during dissolution, sink conditions should be maintained. Depending on the value of n, the release behaviour can be categorized into Fickian Diffusion, anomalous transport, or case-II transport (see Table 2) [29,66].

Table 2. Characterization of the diffusion exponent *n* depending on the dosage form geometry.

n			
Thin Film	**Cylinder**	**Sphere**	**Drug Release Mechanism**
0.50	0.45	0.43	Fickian diffusion
0.50 < *n* < 1.00	0.45 < *n* < 0.89	0.43 < *n* < 0.85	Anomalous transport
1.00	0.89	0.85	Case-II transport

The second equation used for the description of the release profile was the Peppas Sahlin equation (Equation (3)) [29].

$$\frac{M_t}{M_\infty} = k_1 \times t^n + k_2 \times t^{2n} \tag{3}$$

Using this equation, it is possible to describe the anomalous drug release process: the first term describes the Fickian diffusion and the second the Case-II relaxational contribution. The exponent n is, as in the Korsmeyer–Peppas equation, the diffusion exponent for any geometrical shape. The constants k_1, k_2 describe the kinetics. The equation refers only to the anomalous release of the API [67].

The drug release from an inert matrix is often described using the Higuchi equation (Equation (4)). The Higuchi equation describes the release of a suspended drug from an

insoluble matrix via diffusion and is also called square-root-of-time kinetic. This equation was initially intended for ointments but can also be used for solid dosage forms [68,69].

$$Q = \sqrt{D \times (2 \times c_0 - c_s) \times c_s \times t} \tag{4}$$

This calculation is used to calculate Q, the amount of API released at time t per unit area. It is composed of D, the diffusion coefficient of the API in the matrix, c_0, the initial dose in the dosage form and c_s, the saturation concentration of the API. The formula considers that the diffusion distance covered by the API does not remain constant but increases steadily during dissolution. The API concentration in the matrix decreases towards the medium since this is where the API is released first. Due to the growth of the diffusion distance, the concentration gradient decreases and, accordingly, the release rate. The Higuchi equation can be applied to suspension ointments and planar matrices (films) in which the API is dispersed as the equation describes a one-dimensional diffusion under sink conditions. The matrix should be inert and not undergo any change in structure, not even swelling, so that the diffusion coefficient remains constant. In addition, the drug concentration in the dosage form must be higher than the saturation solubility c_s. As soon as these conditions are no longer given, the equation is invalid, since the API is then no longer dispersed but dissolved. The application of this equation is limited to 60% of the released API [70].

Lapidus and Lordi modified the Higuchi equation for swellable hydroxypropyl methylcellulose (HPMC) tablets (Equation (5)) [22,71,72].

$$\frac{M_t}{M_0} = 2 \times \left(\frac{SA}{V}\right) \times \left(\frac{D \times t}{\pi}\right)^{0.5} \tag{5}$$

In this equation, M_t represents the released API at time t and M_0 indicates the initial amount of the API in the tablet. The formula directly includes the SA/V ratio and the diffusion coefficient D of the API in the matrix.

For eroding tablets, the release can be described by the Hixson Crowell equation (Equation (6)). The formula reflects the size decrease of the dosage form. It assumes that the surface of the form decreases proportionally over time and the geometrical form remains constant.

$$\sqrt[3]{W_0} = \sqrt[3]{W_i} + k \times t \tag{6}$$

W_0 reflects the initial amount of API and W_i is the remaining API content over time t. The constant k is the constant of incorporation, which describes the surface area and volume relation of the dosage form. For the Hixson Crowell model, the release described is limited by dissolution velocity and not by diffusion of the API through the polymer matrix. Throughout dissolution, it is assumed that the surface decreases as layers detach over time [27,73,74].

Furthermore, a release of an eroding matrix can be described by the Hopfenberg equation (Equation (7)). The Hopfenberg equation is used to describe the drug release from different geometries (plates, spheres, and cylinders). The assumption is that drug release occurs via erosion and is not affected by diffusion.

$$\frac{M_t}{M_\infty} = 1 - \left[1 - \frac{k_0 \times t}{c_o \times a_0}\right]^n \tag{7}$$

The term $\frac{M_t}{M_\infty}$ describes the release of the initial concentration c_o of the system over time t with M_t as API amount at the observed point of time and M_∞ as the total amount of API solute of the dissolved tablet at infinite time. The erosion constant is described by k_0. The variable a_0 presents the radius of the selected geometry (sphere, cylinder, plate). The factor n represents the shape of the dosage form: n = 1 for a plate, n = 2 for a cylinder and n = 3 for a sphere. The limiting factor of this model is erosion of the matrix, which is the

rate-limiting step of drug release and assumes that time-dependent diffusion resistances inside or outside the eroding matrix have no effect on it [27,75,76].

The Weibull equation (Equation (8)) can be used to describe release curve profiles, regardless of the underlying physical mechanisms (diffusion or erosion).

$$c_t = 1 - e^{\left(\frac{-(t-T_i)^b}{a}\right)} \tag{8}$$

The value of c_t is the concentration of the API at timepoint t. T_i represents the lag-time before the release of API starts. If there is no delayed release, T_i becomes zero. The parameter b describes the shape of the curve (exponential b = 1; sigmoid b > 1 or parabolic b < 1). The scale parameter a characterizes the time scale of the dissolution. As this equation is an empirical model without any kinetic basis, it does not provide any information about the underlying release properties, and only describes the curve profile. [27,77–79].

Prediction

In order to be able to evaluate how accurate the prediction of the release curves is, the root mean square error of prediction (RMSEP) was calculated (Equation (9)) [42,80].

$$\text{RMSEP} = \sqrt{\frac{\sum_{i=1}^{n}(y_i - \hat{y})^2}{n}} \tag{9}$$

The RMSEP value describes the differences between the predicted and the measured values. The factor y_i represents the experimental values and $\hat{y}$ represents the prediction values for every point of time of the release curve. The number of samples is indicated by n.

Comparison of the Dissolution Profiles

To compare the release curves, the similarity factor was used. This is approved by the FDA. The calculation was performed with Equation (10) [27,81,82].

$$f_2 = 50 \times \log\left\{\left[1 + \frac{1}{n}\sum_{t=1}^{n}(R_t - T_t)^2\right]^{-0.5} \times 100\right\} \tag{10}$$

In this equation, R_t and T_t stand for the mean released amounts of the API in % at time point t of the reference and the test product and n for the number of time points. A minimum of 12 measurement points was used as the mean to determine the f_2 value. The f_2 value is sensitive to the number of measurement points. For this reason, only one measurement point was included in the calculation after 85% released API. A f_2 value around 100 is desired, which indicates that the curves are identical. A value of 50 or more is accepted, which indicates that the values differ by max. 10%. Values below 50 indicate that the curves can no longer be considered similar.

2.2.5. Characterization of the Printed Tablets

To evaluate the precision of the printing and to see whether the designed SA/V ratio was also adhered to in the printed geometries, the printed tablets were measured with a caliper (CD-15CPXR, Mitutoyo, Kawasaki, Japan). The weight of the tablets was determined on a balance (Type 1702, Sartorius, Göttingen, Germany), and the tensile strength of the tablets was determined ($n = 10$) with the crushing force tester (TBH210, Erweka, Langen, Germany).

3. Results

3.1. Characterization of the Printed Tablets

To ensure the printed tablets corresponded to the designed SA/V ratio, they were characterized (Supplementary Material, Tables S1–S7). The printing precision is considered

very good for all three formulations and the deviations within a batch are very low, which indicates a good reproducibility. The largest weight variations were found for the PZQ-PVA formulation. The larger and heavier the printed tablet, the higher the variations in weight. In contrast, the API content is very similar, so the variations are small. These data suggest a good extrusion process with a homogeneous API distribution, as well as a robust printing process with small variations in precision. This leads to small variations in mass, which in turn leads to small variations in content. The printed PVA tablets have a high internal hardness, which means that they cannot be broken in the crushing force tester. The EVA tablets are very flexible, so that they also do not break in the crushing force tester but deform.

3.2. Drug Release from Dosage Forms with Defined SA/V Ratios

For initial release studies, various geometries of constant SA/V ratios with different doses were printed with the PVA-PDM formulation (Figure 1). The SA/V ratios were 1, 1.5, and 2 mm^{-1}, based on changes of the dimensions (Table 3). By keeping the SA/V ratio constant, the dose was varied according to the volume of the objects.
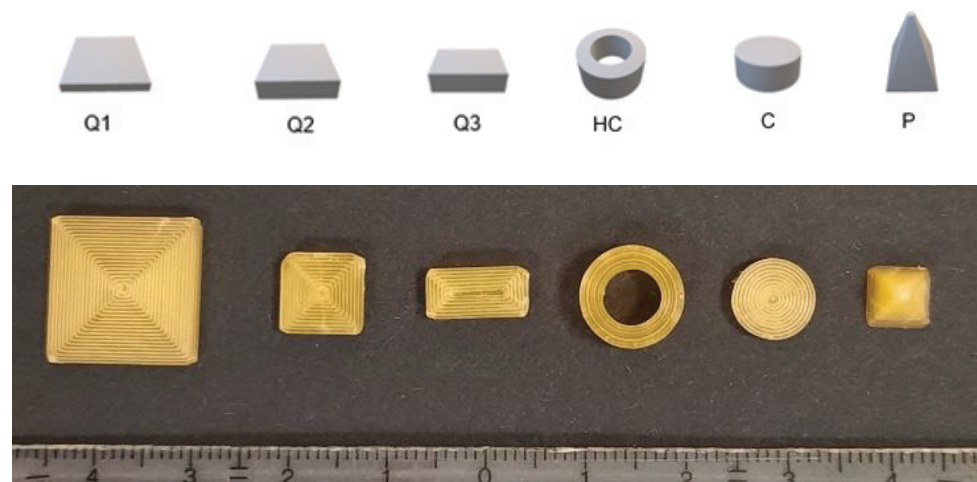
Figure 1. Designed geometries (from left to right): cube 1 (Q1), cube 2 (Q2), cube 3 (Q3), hollow cylinder (HC), cylinder (C) and pyramid (P). Upper image: CAD-Design, lower image: printed geometries of SA/V ratio 1.5 mm^{-1}.

The dissolution data (Figure 2) revealed that dose and size did not influence the relative drug release but only the SA/V ratio, which was expected. The PVA matrix forms a hydrocolloid structure that swells first and slowly dissolves over time.
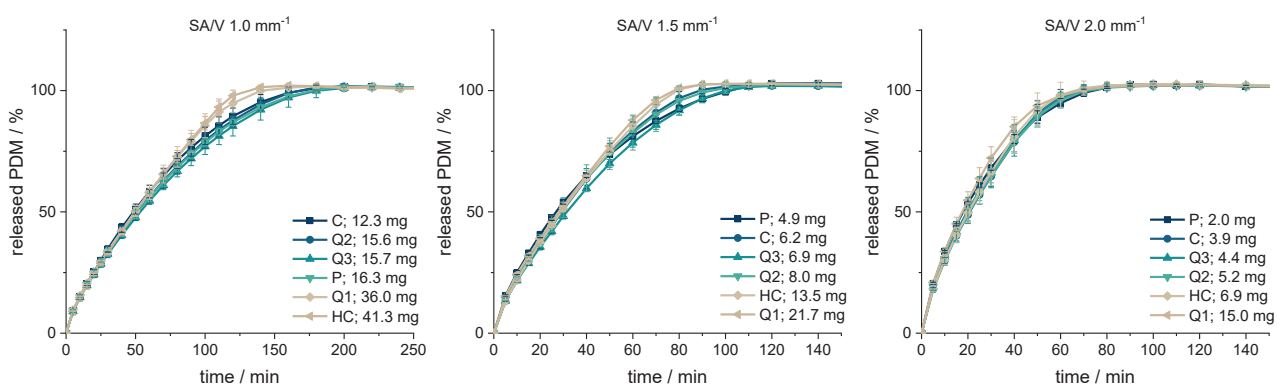
Figure 2. PDM-release curves of the geometries printed with SA/V ratios of 1, 1.5, 2 mm^{-1} ($n = 6$; $x \pm s$).

Table 3. Characteristics of the printed geometries including the calculated MDT of the PVA-PDM formulation.

Form	SA/mm^2	V/mm^3	SA/V/mm^{-1}	API/mg	MDT/min	f$_2$ Value
SA/V 1 mm^{-1}						
Q1	606.00	585.00	1.00	35.97	56.95	77.51
Q2	256.00	256.00	1.00	15.60	62.91	87.92
Q3	250.00	250.00	1.00	15.66	65.65	73.88
HC	667.59	667.59	1.00	41.34	56.84	71.87
C	201.06	201.06	1.00	12.29	60.67	Reference
P	273.05	265.97	1.03	16.25	64.30	82.89
SA/V 1.5 mm^{-1}						
Q1	546.00	360.00	1.52	21.74	32.81	78.20
Q2	192.00	128.00	1.50	8.00	35.67	92.54
Q3	166.00	110.00	1.51	6.92	38.07	73.19
HC	301.59	201.06	1.50	13.54	33.83	90.82
C	150.80	100.53	1.50	6.19	34.80	Reference
P	121.92	80.10	1.52	4.85	36.92	75.40
SA/V 2 mm^{-1}						
Q1	516.00	247.50	2.08	15.04	22.98	66.45
Q2	169.60	83.20	2.04	5.21	25.70	96.55
Q3	142.00	70.00	2.03	4.43	24.90	91.95
HC	201.06	100.50	2.00	6.87	25.02	92.37
C	133.20	65.35	2.04	3.92	25.14	Reference
P	66.02	32.24	2.05	1.99	24.86	75.79

The smaller the SA/V ratio was, the longer it took until 100% of the API was released as the diffusion pathways are longer and vice versa. The geometries with a SA/V ratio of 1 mm^{-1} released 80% of the API in 100 min, the geometries with a SA/V ratio of 1.5 mm^{-1} released 80% in 60 min and with a SA/V ratio of 2 mm^{-1}, 80% API was released in 45 min. The dosages varied by a factor of 7.5 for the SA/V ratio of 2 mm^{-1}, by a factor of 4.5 for the SA/V ratio of 1.5 mm^{-1} and by a factor of 3.4 for the ratio of 1 mm^{-1}.

The respective MDTs were calculated using Equation (1) and are listed in Table 3. Geometries with the same SA/V ratio have very similar MDTs that match the observed trend of the dissolution data. The MDT of geometries printed with a SA/V ratio of 1 mm^{-1} was 61 ± 3 min, with a SA/V ratio of 1.5 mm^{-1} 35 ± 2 min and with a SA/V ratio of 2 mm^{-1} 25 ± 1 min across all designs. The similarity of the curves was evaluated with the similarity factor (Equation (10)). The cylinder was used as a reference for each SA/V group. The f$_2$-values are above 50 in each group and show that the curves are similar to each other.

3.3. Correlation between MDT and SA/V Ratio

Based on this data, a correlation between the SA/V ratio and the MDT was hypothesized. For a better understanding of the correlation between these two features, geometries with additional SA/V ratios were printed and the API release tested with the PVA-PDM formulation. For this, a SA/V ratio of 0.8 mm^{-1} was chosen as minimum and 6.0 mm^{-1} as maximum. The obtained data is shown in Figure 3a.
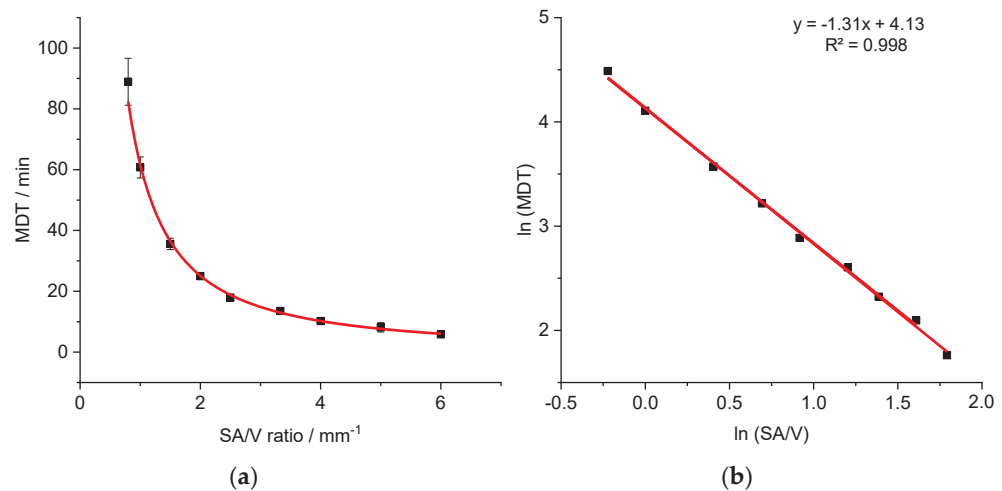
Figure 3. Correlation of MDT and SA/V ratio for the PVA-PDM formulation (**a**) and linearized version (**b**) ($n \geq 3$; x ± s).

The correlation between the variables SA/V and MDT results in a curve (MDT = $62.5 \times \left(\frac{SA}{V}\right)^{-1.3}$), which could be linearized by log-transformation of both axes (R^2: 0.9977). The linear equation of the regression was used to predict the MDT of 3D printed tablets with different SA/V ratios. The predictions were made exemplarily for four different SA/V ratios not used for the regression model and compared with the experimentally determined MDT of the corresponding printed geometries (Table 4).

Table 4. Comparison of MDT: predicted vs. experimental data of the PVA-PDM formulation ($n \geq 3$; x ± s).

SA/V Ratio/mm^{-1}	MDT Prediction/min	MDT Experiment/min	RMSEP/min
0.90	71.70	74.06 ± 11.45	2.36
1.60	33.83	31.04 ± 2.20	2.79
2.30	21.07	16.65 ± 0.46	4.42
4.67	8.36	6.93 ± 0.71	1.43

The predictions are very similar to the measured MDTs. The deviations are less than 5 min, which is acceptable with respect to small variations in the measured release curves. With this assessment, it is possible to categorize the SA/V ratios in terms of their release profiles.

Similar experiments were conducted for the EVA-LD formulation to assess the validity of the approach. Geometries with variable dosages and SA/V ratios of 0.9–6.0 mm^{-1} were printed, and the MDT was calculated from the obtained dissolution data (Figure 4).

A similar relationship was obtained as described earlier for the PVA-PDM formulation. The resulting curve (MDT = $209.43 \times \left(\frac{SA}{V}\right)^{-1.71}$) was linearized again via log-transformation of both axes (R^2: 0.9819).
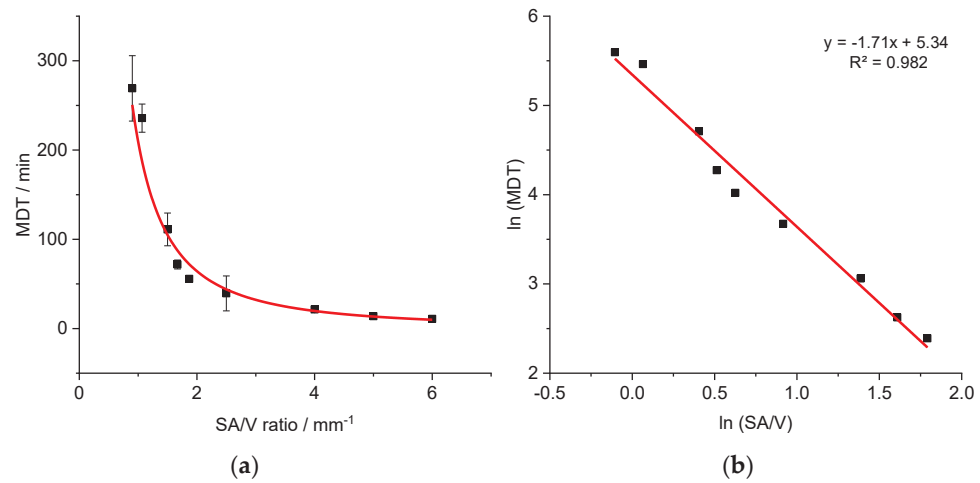
Figure 4. Correlation of MDT and SA/V ratio for the EVA-LD formulation (**a**) and linearized version (**b**) ($n \geq 3$; x ± s).

Additional geometries with defined SA/V ratios were printed and the MDTs resulting from the release curves were calculated. The measured and predicted MDTs are shown in Table 5.

Table 5. Comparison of MDT: predicted vs. experimental data of the EVA-LD formulation ($n \geq 3$; x ± s).

SA/V Ratio/mm^{-1}	MDT Prediction/min	MDT Experiment/min	RMSEP/min
1.73	82.25	78.79 ± 7.24	3.46
1.89	70.74	62.60 ± 5.90	8.14
4.67	15.13	14.40 ± 0.77	0.73

Again, predicted MDTs describe the obtained data well. The variations between the predicted values to the experimentally determined values are similar to the variations from the PVA-PDM formulation.

The approach for predicting MDT was also tested for BCS class II using the PVA-PZQ formulation (Figure 5).
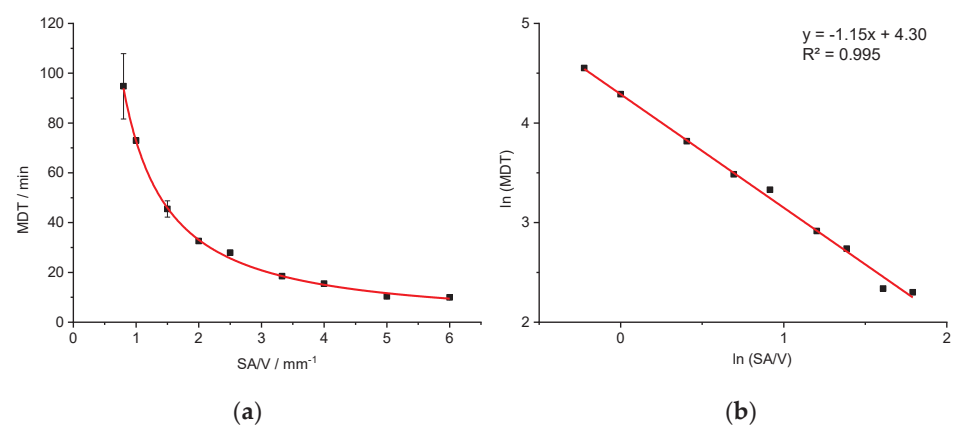
Figure 5. Correlation of MDT and SA/V ratio for the PVA-PZQ formulation (**a**) and linearized version (**b**) ($n \geq 3$; x ± s).

Likewise, a relationship between the SA/V ratio and the MDT (MDT $= 73.487 \times \left(\frac{SA}{V}\right)^{-1.145}$) is evident. A linearization is again obtained by a log-transformation of both axes (R^2: 0.9953).

Additional geometries with defined SA/V ratios were printed (not used for the regression model) and the MDTs resulting from the release curves were calculated. The measured and predicted MDTs are shown in Table 6.

Table 6. Comparison of MDT: predicted vs. experimental data of the PVA-PZQ formulation ($n \geq 3$; x ± s).

SA/V Ratio/mm^{-1}	MDT Prediction/min	MDT Experiment/min	RMSEP/min
1.30	54.42	55.91 ± 1.11	1.49
1.83	36.79	38.73 ± 1.07	1.94
2.30	28.32	27.88 ± 2.23	0.44
4.67	12.58	12.16 ± 0.96	0.42

Again, predicted MDTs describe the obtained data precisely. The variations between the predicted values and the experimentally determined values are similar to the variations from the PVA-PDM or EVA-LD formulation.

In the inert EVA matrix, which does not swell nor erode, the API can only be dissolved and transported by diffusion through the inert matrix into the dissolution medium. The API release is more prolonged compared to the PVA matrix. Considering geometries with a SA/V ratio of 1.5 mm^{-1}, the drug was released from the PVA-PDM matrix with a MDT of 35.58 ± 1.87 min, from the PVA-PZQ matrix with a MDT of 45.49 ± 3.27 min and from the EVA-LD matrix with a MDT of 111.07 ± 18.37 min. Despite the different behaviour of the matrix systems, the solubility properties of the APIs and the resulting differences in MDT, a correlation of the SA/V ratio and the MDT can be established for all three tested formulations. With the help of this correlation, the release time of an existing geometry with a given SA/V ratio can be predicted without having to waste material and perform dissolution tests. Similarly, the required SA/V ratio can be predicted for a desired MDT and the corresponding geometry can be designed and printed on this basis.

If it can be demonstrated that a linear relationship exists between ln(SA/V) and ln(MDT), a simple regression model can be generated using a two-point calibration with dissolution data only from geometries with a low and a high SA/V ratio. This would save further time and production costs and valid predictions could still be made.

3.4. Modeling and Prediction of Release Profiles

To predict the complete release curve and not only the MDT, different mathematical models were used to fit the data (Equations (2)–(8)) and the R^2 values of the fits were compared to evaluate the fit quality (Table 7). According to the Korsmeyer–Peppas model (KMP), the drug release from the PVA formulations follows an anomalous transport (diffusion constant $n = 0.7$ (PDM), $n = 0.8$ (PZQ), Table 2). Since anomalous transport can be described with different models (Equations (3) and (5)–(8)), only these equations were used to fit the data of the PVA formulations. For the EVA-LD formulation, $n = 0.55$ was obtained. This indicates a release according to square-root-of-t kinetic. This profile is often described with the Higuchi equation (Equation (4)). Additionally, the generally applicable Weibull equation (Equation (8)) as well as the Peppas Sahlin equation (Equation (3)) were used to fit the release profiles of the EVA formulation.

Table 7. R^2 values of model fits.

SA/V mm^{-1}	KMP	Hixson	Peppas Sahlin $n = 0.79$	Hopfenberg	Lapidus + Lordi	Weibull
PVA-PDM Formulation						
0.8	0.9837	0.9951	0.9991	0.9837	0.9837	0.1240
1.0	0.9971	0.9969	0.9989	0.9971	0.9971	0.1620
1.5	0.9981	0.9964	0.9995	0.9981	0.9981	0.2575
2.0	0.9966	0.9961	0.9996	0.9966	0.9966	0.9919
2.5	0.9783	0.9975	0.9978	0.9783	0.9783	0.9957
3.3	0.9982	0.9951	0.9997	0.9982	0.9982	0.9955
4.0	0.9949	0.9964	0.9995	0.9949	0.9949	0.9971
5.0	0.9931	0.9987	0.9999	0.9931	0.9931	0.9994
6.0	0.9970	0.9987	0.9999	0.9970	0.9970	0.9997

SA/V mm^{-1}	KMP	Hixson	Peppas Sahlin $n = 1.1$	Hopfenberg	Lapidus + Lordi	Weibull
PVA-PZQ Formulation						
0.8	0.9680	0.9922	0.9980	0.9680	0.9680	0.9993
1.0	0.9870	0.9832	0.9953	0.9870	0.9870	0.9972
1.5	0.9765	0.9727	0.9890	0.9765	0.9765	0.9976
2.0	0.9663	0.9646	0.9667	0.9663	0.9663	0.9973
2.5	0.9819	0.9292	0.9932	0.9819	0.9819	0.9963
3.3	0.9350	0.9408	0.9807	0.9350	0.9350	0.9980
4.0	0.9331	0.9361	0.9877	0.9331	0.9331	0.9975
5.0	0.9143	0.9787	0.9823	0.9143	0.9143	0.9994
6.0	0.9429	0.9299	0.9888	0.9429	0.9429	0.9992

SA/V mm^{-1}	KMP	Weibull	Peppas Sahlin $n = 0.66$	Higuchi
EVA-LD Formulation				
0.9	0.9941	0.9986	0.9808	0.8760
1.1	0.9910	0.9936	0.9853	0.9304
1.5	0.9961	0.9961	0.9981	0.9945
1.7	0.9925	0.9884	0.9966	0.9880
1.9	0.9949	0.9894	0.9989	0.9941
2.5	0.9724	0.9979	0.9993	0.9282
4.0	0.9979	0.9928	0.9934	0.9730
5.0	0.9970	0.9944	0.9956	0.9583
6.0	0.9974	0.9946	0.9957	0.9600

For both BCS class I API formulations, the Peppas Sahlin equation provides the best fit. In order to also include enough data points for fast release dosage forms, the curves were fitted up to an API release of 98%. For the formulation with BCS class II API, the Weibull function provides the best fit (Figure 6).

In earlier works, the slope of the Higuchi plot, the rate constant of dissolution and the constant k of the Korsmeyer–Peppas equation were already related to the particle size and the SA/V ratio of tablets [22,83,84]. In this study, all dissolution curves of BCS class I APIs were fitted with the Peppas Sahlin equation, as it provided the best fits and the constants k_1 and k_2 were determined (Table 8). For the PVA-PDM formulation, an average diffusion exponent of $n = 0.79$ was obtained, and for the EVA-LD formulation, an average diffusion exponent of $n = 0.66$ was obtained. The constants k_1 and k_2 were plotted in a graph as a function of the SA/V ratio. A linear correlation between k and the SA/V ratio was obtained by a log-transformation of both axes (Figure 7).
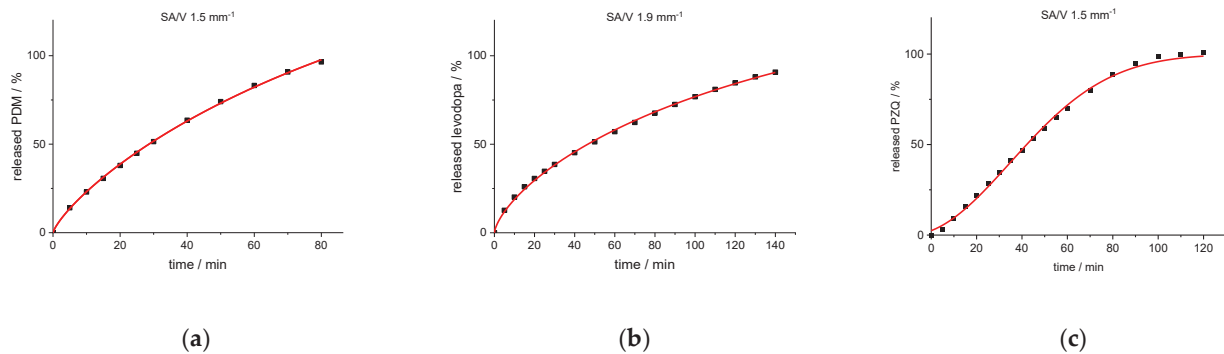
Figure 6. Experimental release data points (black cuboids) and predicted release curve (red line) calculated with Peppas Sahlin (PVA-PDM formulation (**a**); EVA-LD formulation (**b**)) and Weibull function (PVA-PZQ formulation (**c**)).

Table 8. Calculated constants for the SA/V ratios of both BCS I formulations.

SA/V	k_1	k_2	ln(SA/V)	ln(k_1)	ln(k_2)
PVA−PDM Formulation					
0.8	1.986	0.010	−0.223	0.686	−4.608
1.0	2.516	0.011	0.000	0.923	−4.549
1.5	3.920	0.027	0.405	1.366	−3.626
2.0	5.561	0.067	0.693	1.716	−2.704
2.5	7.362	0.135	0.916	1.996	−2.001
3.3	11.555	0.258	1.203	2.447	−1.353
4.0	15.459	0.545	1.386	2.738	−0.608
5.0	16.888	0.713	1.609	2.827	−0.338
6.0	20.856	1.069	1.792	3.038	0.066
EVA−LD Formulation					
0.9	1.952	0.010	−0.105	0.669	−4.614
1.1	2.286	0.014	0.065	0.827	−4.282
1.5	3.115	0.020	0.405	1.136	−3.928
1.7	4.087	0.031	0.513	1.408	−3.465
1.9	5.009	0.053	0.626	1.611	−2.944
2.5	7.636	0.153	0.916	2.033	−1.876
4.0	10.374	0.279	1.386	2.339	−1.277
5.0	14.444	0.540	1.609	2.670	−0.617
6.0	16.816	0.727	1.792	2.822	−0.319
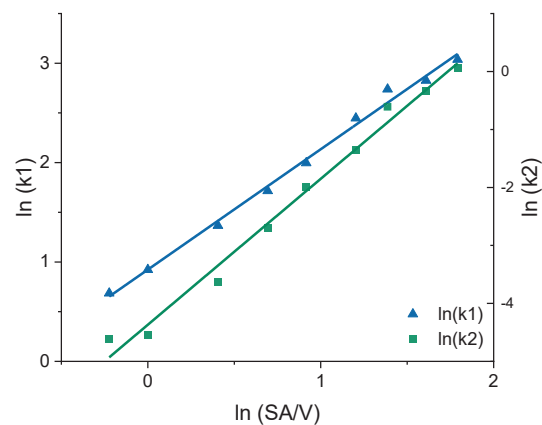
Figure 7. Correlation of the constants k_1 and k_2 of the Peppas Sahlin equation with the SA/V ratio for the PVA-PDM formulation.

Using this relation and the resulting linear regression, k_1 and k_2 can be determined for arbitrarily selected SA/V ratios. If these calculated values are inserted into the Peppas Sahlin equation with the diffusion exponent $n = 0.79$, a concentration curve of the released API can be calculated for the specific time points. These calculations were performed exemplarily for the four different SA/V ratios not used for the model creation. The graphs comparing the experimental data points with the prediction curve are shown in Figure 8.
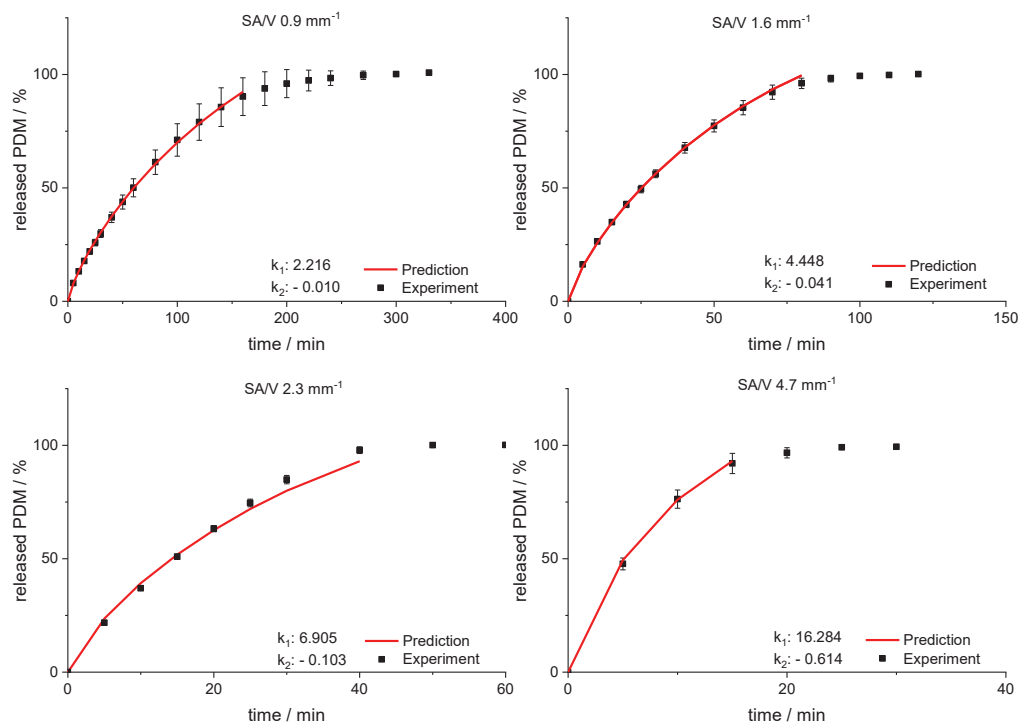
Figure 8. Predicted PDM release profiles vs. experimental results for SA/V ratio 0.9 mm^{-1}, 1.6 mm^{-1}, 2.3 mm^{-1} and 4.67 mm^{-1} of the PVA-PDM formulation.

The RMSEPs were calculated (Equation (9)) for the predictions and experimental results. The best predictive power was observed for a SA/V ratio of 1.6 mm^{-1} with a RMSEP of 0.56% and 0.9 mm^{-1} with a RMSEP of 0.74%. For the SA/V ratio of 2.3 mm^{-1}, the prediction above 70% API release underestimated the experimental data points, which results in a RMSEP of 2.85%. If only the release data points up to 70% released API are included, the RMSEP was 1.70%. Predicting the SA/V ratio of 4.7 mm^{-1} resulted in a RMSEP of 3.41%. If the prediction is only made up to 70% API release, the RMSEP is 1.18%, but only three time points are compared due to the quick drug release. Apparently, the predictions represent the experimental values better for smaller SA/V ratios because multiple time points can be considered and therefore the curves are not as sensitive to changes in k values. Nevertheless, the prediction approximated the experimental release curves well, especially in the early phase of drug release.

The prediction approach was tested for the EVA-LD formulation, respectively. Again, the constants k_1 and k_2 were plotted in a graph as a function of the SA/V ratio. A linear correlation between k and the SA/V ratio was obtained by a log-transformation of both values (Figure 9). Using this relation and the resulting linear regression, k_1 and k_2 can be determined for arbitrarily selected SA/V ratios. These calculations were exemplarily for the three different SA/V ratios, the MDT was already predicted in Section 3.2. The resulting graphs comparing the experimental data points with the prediction curve are shown in Figure 10.
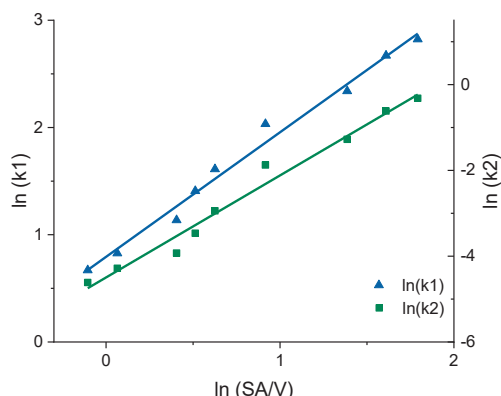
Figure 9. Correlation of the constants k_1 and k_2 of the Peppas Sahlin equation with the SA/V ratio for the EVA-LD formulation.
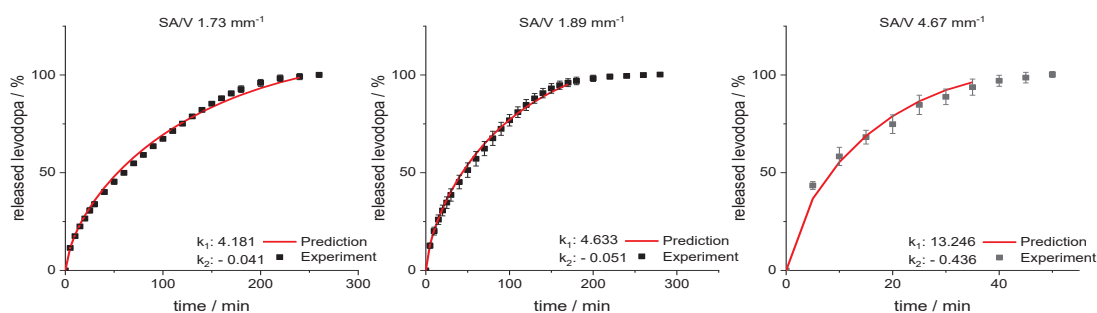
Figure 10. Predicted levodopa release vs. experimental levodopa release for SA/V ratios of 1.73 mm^{-1}, 1.89 mm^{-1} and 4.67 mm^{-1} of the EVA-LD formulation.

For the SA/V ratio of 1.89 mm^{-1}, the RMSEP value was 1.60% and for the SA/V ratio of 1.73 mm^{-1}, the RMSEP value was 1.95%. The RMSEP for the SA/V ratio 4.67 mm^{-1} results in a value of 3.42%. Again, the experimental data of the smaller SA//V ratios can be predicted better by the model, nevertheless, the prediction of higher SA/V ratios is still close to experimental data. The data implies that the developed prediction model also works for this formulation with an inert matrix.

For the PVA-PZQ formulation, the Weibull function provides the best fit (Table 7). Therefore, the approach for predicting the dissolution curves was tested for this equation. For the given SA/V ratio, the variables a and b were calculated (Table 9) and plotted with log-transformed axes (Figure 11). The resulting linear equations were used to calculate the required variables for the SA/V ratios, whose curves were to be predicted. The comparison of the predicted and experimentally determined release profiles is shown in Figure 12.

Table 9. Calculated constants for the SA/V ratios of the BCS II–formulation.

PVA-PZQ Formulation					
SA/V	a	b	ln(SA/V)	ln(a)	ln(b)
0.8	105.0	1.38	−0.223	4.654	0.322
1.0	81.0	1.45	0.000	4.394	0.372
1.5	52.0	1.63	0.405	3.951	0.489
2.0	38.0	1.80	0.693	3.638	0.588
2.5	31.5	1.91	0.916	3.450	0.647
3.3	20.8	2.05	1.194	3.035	0.718
4.0	17.1	2.15	1.386	2.836	0.765
5.0	11.5	2.29	1.609	2.442	0.829
6.0	11.2	2.40	1.792	2.414	0.875
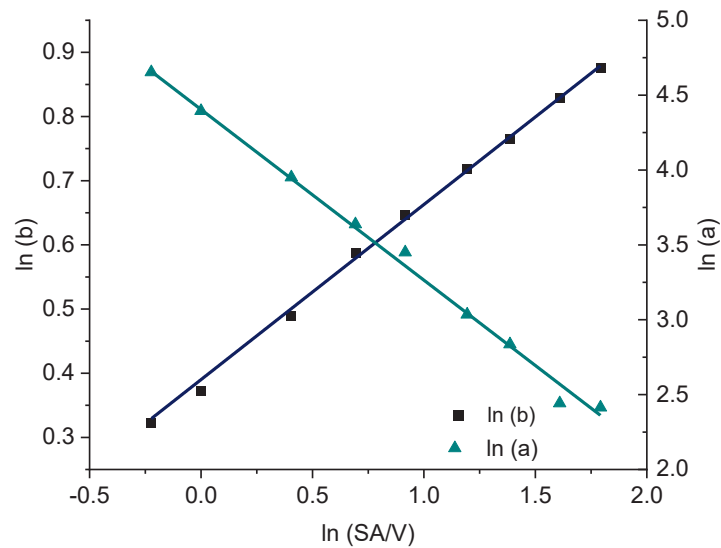
Figure 11. Correlation of the constants a and b of the Weibull function with the SA/V ratio for the PVA-PZQ formulation.
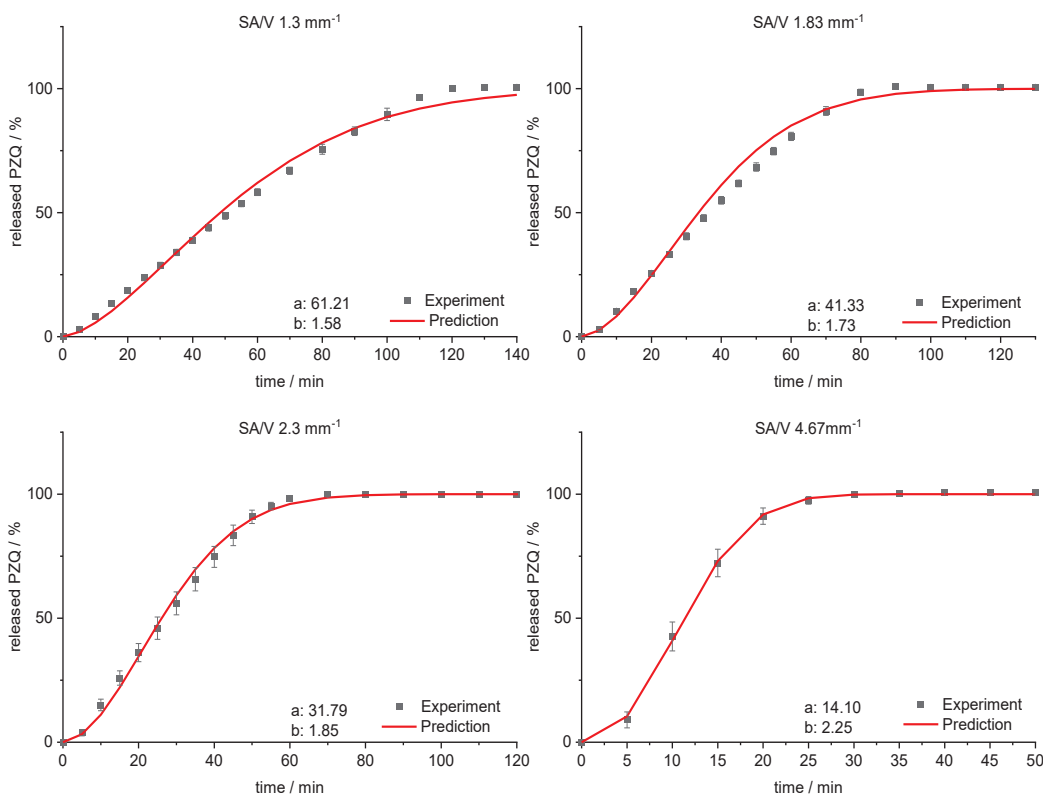
Figure 12. Predicted PZQ release vs. experimental PZQ release for SA/V ratios of 1.3 mm^{-1}, 1.83 mm^{-1}, 2.3 mm^{-1} and 4.67 mm^{-1} of the PVA-PZQ formulation.

The sigmoidal curve is described with the Weibull function. Initially, the amount of API released is somewhat underestimated, but as dissolution progresses, the mean value is predicted well. For the curves of lower SA/V ratios, the course of the release curve is overestimated from 55–80% released API and a stronger S-curve course is predicted. With increasing SA/V ratio, however, the Weibull curve predicts the release profile better. The

RMSEP for the SA/V ratio of 1.3 mm^{-1} is 2.5%, for 1.83 mm^{-1} 3.6%, for 2.3 mm^{-1} 2.1% and for 4.67 mm^{-1} 1.0%. The predicted value of the curve deviates from the experiment by 2.3% on average, which can be considered acceptable.

With this approach, it is possible to extend the prediction of the MDT as described in Section 3.2 and predict the release profile of different APIs of various BCS classes for a given SA/V ratio. As shown with the different formulations and APIs, this method can potentially be applied for various matrices and drug substances. This approach enables more accurate predictions to be made for the release behaviour of 3D printed dosage forms.

4. Discussion

A correlation between MDT and SA/V ratio was found in these experiments and used for a prediction of drug release profiles with three different formulations. With the help of this approach, the MDT of printed dosage forms with known SA/V ratios can be easily predicted and it is possible to categorize the SA/V ratios in terms of their release. MDT predictions are quite accurate for all three formulations, varying from experiment mostly by ≤5 min, which is acceptable. The largest variations are found for the EVA formulation, which may be due to the more difficult printing conditions. Due to the high flexibility of the filaments, the constant transport of the filament through the nozzle is not always given, resulting in less accurate printing of the tablets. In addition, the release of the API is longer than in the PVA formulations, resulting in larger standard deviations. Since inert matrices often lead to prolonged release kinetics and, therefore, require time consuming experiments, the identified relationship between MDT and SA/V ratio represents a helpful tool for dosage form design. Accurate predictions of release profiles of BCS class I APIs could be made using the Peppas Sahlin equation. This equation was used to describe the dissolution curves of two different matrix systems with different release characteristics. The constants of the equation were found to change in a predictable manner with the SA/V ratio. For both formulations, precise predictions of release profile could be made, with an average variation of 0.6–3% of API released per time point. Predictions for smaller SA/V were mostly more accurate than those for larger SA/V, which may be due to the number of time points included, making the curves more sensitive to changes in the constants. In the PVA formulation with the BCS class II compound, the Weibull function was found to be most suitable to describe the drug release (R^2: 0.999). Again, the linear relationship between the logarithmised constants and the SA/V ratio was used to calculate dissolution predictions. With an average deviation of 2% from the predicted to the experimentally determined release profile, it can be stated that dissolution curves of dosage forms with a poorly water-soluble API can also be modeled.

Future studies should include testing more formulations and drug substances to investigate the validity of this approach for other drugs and polymers, and expanding the database, as well as investigating the use of ANNs for these kinds of dosage forms. In addition, it should be tested whether the prediction model is also transferable to tablets or dosage forms manufactured by other 3D printing processes, e.g., by powder bed 3D printing or semi-solid 3D printing with different materials and porosity.

5. Conclusions

We demonstrated that the relationships between constants of established equations and the SA/V ratio can be exploited to predict complete dissolution curves for specific SA/V ratios. The validity of this approach was shown for water-soluble as well as poorly water-soluble drug substances and erodible and inert polymers. It might be possible to establish a dataset for polymer matrices with various APIs of different BCS classes and directly calculate the release curves of dosage forms with a known SA/V ratio. Such an approach would save additional costs and time-consuming dissolution studies of individual geometries and matrix systems, which is especially important for community pharmacies and hospitals. Future patient care with 3D printed oral dosage forms could be: 1. the optimal drug release for a patient is determined, 2. the appropriate formulation

and SA/V ratio are selected, 3. a suitable geometry is 3D printed with the required dose of the API. Therefore, with an established matrix system, not every drug release of oral dosage forms would need to be tested in dissolution studies but could be mathematically predicted. As a result, the dissolution rate could be individualized in decentralized settings, an approach that has not been easily adaptable before.

Supplementary Materials: The following are available online at https://www.mdpi.com/article/10.3390/pharmaceutics13091453/s1, Table S1: Physical characterization of the printed tablets for SA/V ratio 1–2 mm^{-1} ($n \geq 3$, x $\pm$ s), Table S2: Physical characterization of the printed tablets for the correlation generation with the PDM-PVA formulation ($n \geq 3$, x $\pm$ s), Table S3: Physical characterization of the printed tablets for the correlation generation with the LD-EVA formulation ($n \geq 3$, x $\pm$ s), Table S4: Physical characterization of the printed tablets for the correlation generation with the PZQ-PVA formulation ($n \geq 3$, x $\pm$ s), Table S5: Physical characterization of the printed tablets for the prediction validation with the PDM-PVA formulation ($n \geq 3$, x $\pm$ s), Table S6: Physical characterization of the printed tablets for the prediction validation with the LD-EVA formulation ($n \geq 3$, x $\pm$ s), Table S7: Physical characterization of the printed tablets for the prediction validation with the PZQ-PVA formulation ($n \geq 3$, x $\pm$ s).

References

1. Hamburg, M.A.; Collins, F.S. The path to personalized medicine. *N. Engl. J. Med.* **2010**, *363*, 301–304. [CrossRef] [PubMed]
2. Ryu, J.H.; Lee, S.; Son, S.; Kim, S.H.; Leary, J.F.; Choi, K.; Kwon, I.C. Theranostic nanoparticles for future personalized medicine. *J. Control. Release* **2014**, *190*, 477–484. [CrossRef]
3. Tan, D.K.; Maniruzzaman, M.; Nokhodchi, A. Advanced pharmaceutical applications of hot-melt extrusion coupled with Fused Deposition Modelling (FDM) 3D printing for personalised drug delivery. *Pharmaceutics* **2018**, *10*, 203. [CrossRef]
4. Breitkreutz, J.; Boos, J. Paediatric and geriatric drug delivery. *Expert Opin. Drug Deliv.* **2007**, *4*, 37–45. [CrossRef]
5. Collins, F.S.; Varmus, H. A New initiative on precision medicine. *N. Engl. J. Med.* **2015**, *372*, 793–795. [CrossRef] [PubMed]
6. Hodson, R. Precision medicine. *Nature* **2016**, *537*, S49. [CrossRef]
7. van Santen, E.; Barends, D.M.; Frijlink, H.W. Breaking of scored tablets: A review. *Eur. J. Pharm. Biopharm.* **2002**, *53*, 139–145. [CrossRef]
8. Quinzler, R.; Gasse, C.; Schneider, A.; Kaufmann-Kolle, P.; Szecsenyi, J.; Haefeli, W.E. The frequency of inappropriate tablet splitting in primary care. *Eur. J. Clin. Pharmacol.* **2006**, *62*, 1065–1073. [CrossRef]
9. Wening, K.; Breitkreutz, J. Oral drug delivery in personalized medicine: Unmet needs and novel approaches. *Int. J. Pharm.* **2011**, *404*, 1–9. [CrossRef]
10. Goyanes, A.; Det-Amornrat, U.; Wang, J.; Basit, A.W.; Gaisford, S. 3D Scanning and 3D printing as innovative technologies for fabricating personalized topical drug delivery systems. *J. Control. Release* **2016**, *234*, 41–48. [CrossRef] [PubMed]
11. Alhnan, M.A.; Okwuosa, T.C.; Sadia, M.; Wan, K.W.; Ahmed, W.; Arafat, B. Emergence of 3D printed dosage forms: Opportunities and challenges. *Pharm. Res.* **2016**, *33*, 1817–1832. [CrossRef] [PubMed]
12. Ibrahim, M.; Barnes, M.; McMillin, R.; Cook, D.W.; Smith, S.; Halquist, M.; Wijesinghe, D.; Roper, T.D. 3D printing of Metformin HCl PVA tablets by fused deposition modeling: Drug loading, tablet design, and dissolution studies. *AAPS PharmSciTech* **2019**, *20*, 195. [CrossRef] [PubMed]
13. Rahman, J.; Quodbach, J. Versatility on demand—The case for semi-solid micro-extrusion in pharmaceutics. *Adv. Drug Deliv. Rev.* **2021**, *172*, 104–126. [CrossRef] [PubMed]

14. Seoane-Viaño, I.; Januskaite, P.; Alvarez-Lorenzo, C.; Basit, A.W.; Goyanes, A. Semi-solid extrusion 3D printing in drug delivery and biomedicine: Personalised solutions for healthcare challenges. *J. Control. Release* **2021**, *332*, 367–389. [CrossRef]

15. el Aita, I.; Rahman, J.; Breitkreutz, J.; Quodbach, J. 3D-printing with precise layer-wise dose adjustments for paediatric use via pressure-assisted microsyringe printing. *Eur. J. Pharm. Biopharm.* **2020**, *157*, 59–65. [CrossRef] [PubMed]

16. Korte, C.; Quodbach, J. Formulation development and process analysis of drug-loaded filaments manufactured via hot-melt extrusion for 3D-printing of medicines. *Pharm. Dev. Technol.* **2018**, *23*, 1117–1127. [CrossRef]

17. Melocchi, A.; Parietti, F.; Maroni, A.; Foppoli, A.; Gazzaniga, A.; Zema, L. Hot-melt extruded filaments based on pharmaceutical grade polymers for 3D printing by fused deposition modeling. *Int. J. Pharm.* **2016**, *509*, 255–263. [CrossRef]

18. Ponsar, H.; Wiedey, R.; Quodbach, J. Hot-melt extrusion process fluctuations and their impact on critical quality attributes of filaments and 3D-printed dosage forms. *Pharmaceutics* **2020**, *12*, 511. [CrossRef]

19. Zhang, J.; Feng, X.; Patil, H.; Tiwari, R.V.; Repka, M.A. Coupling 3D printing with hot-melt extrusion to produce controlled-release tablets. *Int. J. Pharm.* **2017**, *519*, 186–197. [CrossRef]

20. Gültekin, H.E.; Tort, S.; Acartürk, F. An effective technology for the development of immediate release solid dosage forms containing low-dose drug: Fused deposition modeling 3D printing. *Pharm. Res.* **2019**, *36*, 128. [CrossRef]

21. Kollamaram, G.; Croker, D.M.; Walker, G.M.; Goyanes, A.; Basit, A.W.; Gaisford, S. Low temperature Fused Deposition Modeling (FDM) 3D printing of thermolabile drugs. *Int. J. Pharm.* **2018**, *545*, 144–152. [CrossRef]

22. Reynolds, T.D.; Mitchell, S.A.; Balwinski, K.M. Investigation of the effect of tablet surface area/volume on drug release from hydroxypropylmethylcellulose controlled-release matrix tablets. *Drug Dev. Ind. Pharm.* **2002**, *28*, 457–466. [CrossRef]

23. Goyanes, A.; Robles Martinez, P.; Buanz, A.; Basit, A.W.; Gaisford, S. Effect of geometry on drug release from 3D printed tablets. *Int. J. Pharm.* **2015**, *494*, 657–663. [CrossRef]

24. Sadia, M.; Arafat, B.; Ahmed, W.; Forbes, R.T.; Alhnan, M.A. Channelled tablets: An innovative approach to accelerating drug release from 3D printed tablets. *J. Control. Release* **2018**, *269*, 355–363. [CrossRef] [PubMed]

25. Gorkem Buyukgoz, G.; Soffer, D.; Defendre, J.; Pizzano, G.M.; Davé, R.N. Exploring tablet design options for tailoring drug release and dose via Fused Deposition Modeling (FDM) 3D printing. *Int. J. Pharm.* **2020**, *591*, 119987. [CrossRef] [PubMed]

26. Narayana Raju, P. Effect of tablet surface area and surface area/volume on drug release from lamivudine extended release matrix tablets. *Int. J. Pharm. Sci. Nanotechnol.* **2010**, *3*, 872–876. [CrossRef]

27. Costa, P.; Sousa Lobo, J.M. Modeling and comparison of dissolution profiles. *Eur. J. Pharm. Sci.* **2001**, *13*, 123–133. [CrossRef]

28. Siepmann, J.; Siepmann, F. Mathematical modeling of drug delivery. *Int. J. Pharm.* **2008**, *364*, 328–343. [CrossRef]

29. Peppas, N.A.; Sahlin, J.J. A simple equation for the description of solute release. III. Coupling of diffusion and relaxation. *Int. J. Pharm.* **1989**, *57*, 169–172. [CrossRef]

30. Siepmann, J.; Kranz, H.; Peppas, N.A.; Bodmeier, R. Calculation of the required size and shape of hydroxypropyl methylcellulose matrices to achieve desired drug release profiles. *Int. J. Pharm.* **2000**, *201*, 151–164. [CrossRef]

31. Siepmann, J.; Streubel, A.; Peppas, N.A. Understanding and predicting drug delivery from hydrophilic matrix tablets using the "Sequential Layer" model. *Pharm. Res.* **2002**, *3*, 306–314. [CrossRef]

32. Tsunematsu, H.; Hifumi, H.; Kitamura, R.; Hirai, D.; Takeuchi, M.; Ohara, M.; Itai, S.; Iwao, Y. Analysis of available surface area can predict the long-term dissolution profile of tablets using short-term stability studies. *Int. J. Pharm.* **2020**, *586*, 119504. [CrossRef] [PubMed]

33. Baishya, H. Application of mathematical models in drug release kinetics of carbidopa and levodopa ER tablets. *J. Dev. Drugs* **2017**, *6*, 1–8. [CrossRef]

34. Petru, J.; Zamostny, P. Prediction of dissolution behavior of final dosage forms prepared by different granulation methods. *Procedia Eng.* **2012**, *42*, 1463–1473. [CrossRef]

35. Madzarevic, M.; Medarevic, D.; Vulovic, A.; Sustersic, T.; Djuris, J.; Filipovic, N.; Ibric, S. Optimization and prediction of ibuprofen release from 3D DLP printlets using artificial neural networks. *Pharmaceutics* **2019**, *11*, 544. [CrossRef] [PubMed]

36. Siepmann, J. A new model combining diffusion, swelling, and dissolutions mechanisms and predicting the release kinetics. *Pharm. Res.* **1999**, *16*, 1748–1756. [CrossRef] [PubMed]

37. Siepmann, J.; Peppas, N.A. Hydrophilic matrices for controlled drug delivery: An improved mathematical model to predict the resulting drug release kinetics the "Sequential Layer" model). *Pharm. Res.* **2000**, *17*, 1290–1298. [CrossRef] [PubMed]

38. Borgquist, P.; Körner, A.; Piculell, L.; Larsson, A.; Axelsson, A. A model for the drug release from a polymer matrix tablet-effects of swelling and dissolution. *J. Control. Release* **2006**, *113*, 216–225. [CrossRef]

39. Narasimhan, B. Mathematical models describing polymer dissolution: Consequences for drug delivery. *Adv. Drug Deliv. Rev.* **2001**, *48*, 195–210. [CrossRef]

40. Siepmann, J.; Siegel, R.A.; Siepmann, F. Diffusion controlled drug delivery systems. In *Fundamentals and Applications of Controlled Release Drug Delivery*; Siepmann, J., Siegel, R.A., Eds.; Springer: New York, NY, USA, 2012; pp. 127–152. ISBN 9781461408819.

41. Siepmann, J.; Siepmann, F. Swelling controlled drug delivery systems. In *Fundamentals and Applications of Controlled Release Drug Delivery*; Springer: New York, NY, USA, 2012; pp. 153–170, ISBN 9781461408819.

42. Korte, C.; Quodbach, J. 3D-printed network structures as controlled-release drug delivery systems: Dose adjustment, API release analysis and prediction. *AAPS PharmSciTech* **2018**, *19*, 3333–3342. [CrossRef]

43. Kyobula, M.; Adedeji, A.; Alexander, M.R.; Saleh, E.; Wildman, R.; Ashcroft, I.; Gellert, P.R.; Roberts, C.J. 3D inkjet printing of tablets exploiting bespoke complex geometries for controlled and tuneable drug release. *J. Control. Release* **2017**, *261*, 207–215. [CrossRef]

44. Pishnamazi, M.; Ismail, H.Y.; Shirazian, S.; Iqbal, J.; Walker, G.M.; Collins, M.N. Application of lignin in controlled release: Development of predictive model based on artificial neural network for API release. *Cellulose* **2019**, *26*, 6165–6178. [CrossRef]

45. Takayama, K.; Kawai, S.; Obata, Y.; Todo, H.; Sugibayashi, K. Prediction of dissolution data integrated in tablet database using four-layered artificial neural networks. *Chem. Pharm. Bull.* **2017**, *65*, 967–972. [CrossRef]

46. Peng, Y.; Geraldrajan, M.; Chen, Q.; Sun, Y.; Johnson, J.R.; Shukla, A.J. Prediction of dissolution profiles of acetaminophen beads using artificial neural networks. *Pharm. Dev. Technol.* **2006**, *11*, 337–349. [CrossRef]

47. Ghennam, A.; Rebouh, S.; Bouhedda, M. Application of artificial neural network-genetic algorithm model in the prediction of ibuprofen release from microcapsules and tablets based on plant protein and its derivatives. *Lect. Notes Netw. Syst.* **2021**, *174*, 625–634. [CrossRef]

48. Novák, M.; Boleslavská, T.; Grof, Z.; Waněk, A.; Zadražil, A.; Beránek, J.; Kovačík, P.; Štěpánek, F. Virtual prototyping and parametric design of 3D-printed tablets based on the solution of inverse problem. *AAPS PharmSciTech* **2018**, *19*, 3414–3424. [CrossRef]

49. Komal, C.; Dhara, B.; Sandeep, S.; Shantanu, D.; Priti, M.J. Dissolution-controlled salt of pramipexole for parenteral administration: In Vitro assessment and mathematical modeling. *Dissolution Technol.* **2019**, *26*, 28–36. [CrossRef]

50. Tzankov, B.; Voycheva, C.; Yordanov, Y.; Aluani, D.; Spassova, I.; Kovacheva, D. Development and In Vitro safety evaluation of pramipexole-loaded Hollow Mesoporous Silica (HMS) particles. *Biotechnol. Biotechnol. Equip.* **2019**, *33*, 1204–1215. [CrossRef]

51. Krisai, K.; Charnvanich, D.; Chongcharoen, W. Increasing the solubility of levodopa and carbidopa using ionization approach. *Thai J. Pharm. Sci. TJPS* **2020**, *44*, 251–255.

52. Liu, Y.; Wang, T.; Ding, W.; Dong, C.; Wang, X.; Chen, J.; Li, Y. Dissolution and oral bioavailability enhancement of praziquantel by solid dispersions. *Drug Deliv. Transl. Res.* **2018**, *8*, 580–590. [CrossRef] [PubMed]

53. Dinora, G.E.; Julio, R.; Nelly, C.; Lilian, Y.M.; Cook, H.J. In Vitro characterization of some biopharmaceutical properties of Praziquantel. *Int. J. Pharm.* **2005**, *295*, 93–99. [CrossRef]

54. Lombardo, F.C.; Perissutti, B.; Keiser, J. Activity and pharmacokinetics of a praziquantel crystalline polymorph in the Schistosoma Mansoni Mouse model. *Eur. J. Pharm. Biopharm.* **2019**, *142*, 240–246. [CrossRef]

55. Łaszcz, M.; Trzcí Nska, K.; Kubiszewski, M.; Zenna Kosmacińska, B.; Glice, M. Stability studies and structural characterization of Pramipexole. *J. Pharm. Biomed. Anal.* **2010**, *53*, 1033–1036. [CrossRef]

56. Pawar, S.M.; Khatal, L.D.; Gabhe, S.Y.; Dhaneshwar, S.R. Establishment of inherent stability of Pramipexole and development of validated stability indicating LC–UV and LC–MS method. *J. Pharm. Anal.* **2013**, *3*, 109–117. [CrossRef]

57. Panditrao, V.M.; Sarkate, A.P.; Sangshetti, J.N.; Wakte, P.S.; Shinde, D.B. Stability-indicating HPLC determination of Pramipexole dihydrochloride in bulk drug and pharmaceutical dosage form. *J. Braz. Chem. Soc.* **2011**, *22*, 1253–1258. [CrossRef]

58. Ledeti, A.; Olariu, T.; Caunii, A.; Vlase, G.; Circioban, D.; Baul, B.; Ledeti, I.; Vlase, T.; Murariu, M. Evaluation of thermal stability and kinetic of degradation for levodopa in non-isothermal conditions. *J. Therm. Anal. Calorim.* **2018**, *131*, 1881–1888. [CrossRef]

59. Kinetiği, D.; Vitro, I.; Çalışmaları Ve Bağlanmış, Ç.; Emisyon, P.; Spektroflurimetri, Y.; Tayini, M. Degradation kinetics, In Vitro dissolution studies, and quantification of Praziquantel, anchored in emission intensity by spectrofluorimetry. *Turk. J. Pharm. Sci.* **2019**, *16*, 82–87. [CrossRef]

60. Mainardes, R.M.; Gremião, M.P.D.; Evangelista, R.C. Thermoanalytical study of Praziquantel-loaded PLGA nanoparticles. *Revista Brasileira de Ciências Farmacêuticas* **2006**, *42*, 523–530. [CrossRef]

61. Freichel, O.L. Hydrokolloidretardarzneiformen Mit Endbeschleunigter Freisetzung. Ph.D. Thesis, Heinrich-Heine-Universität, Düsseldorf, Germany, 2002.

62. Genina, N.; Holländer, J.; Jukarainen, H.; Mäkilä, E.; Salonen, J.; Sandler, N. Ethylene Vinyl Acetate (EVA) as a new drug carrier for 3D printed medical drug delivery devices. *Eur. J. Pharm. Sci.* **2016**, *90*, 53–63. [CrossRef]

63. European Pharmacopoeia Comission 2.9.3. Dissolution test for solid dosage forms. In *European Pharmacopoeia*; EDQM: Strasbourg, France, 2020; Volume 10.2, pp. 326–333.

64. European Pharmacopoeia Comission 5.17.1. Recommendations on dissolution testing. In *European Pharmacopoeia*; EDQM: Strasbourg, France, 2020; Volume 10.2, pp. 801–807.

65. Tanigawara, Y.; Yamaoka, K.; Nakagawa, T.; Uno, T. New method for the evaluation of In Vitro dissolution time and disintegration time. *Chem. Pharm. Bull.* **1982**, *30*, 1088–1090. [CrossRef]

66. Korsmeyer, R.W.; Gurny, R.; Doelker, E.; Buri, P.; Peppas, N.A. Mechanisms of solute release from porous hydrophilic polymers. *Int. J. Pharm.* **1983**, *15*, 25–35. [CrossRef]

67. Siepmann, J.; Peppas, N.A. Modeling of drug release from delivery systems based on Hydroxypropyl Methylcellulose (HPMC). *Adv. Drug Deliv. Rev.* **2001**, *48*, 139–157. [CrossRef]

68. Higuchi, T. Rate of release of medicaments from ointment bases containing drugs in suspension. *J. Pharm. Sci.* **1961**, *50*, 874–875. [CrossRef]

69. Higuchi, T. Mechanism of sustained-action medication. Theoretical analysis of rate of release of solid drugs dispersed in solid matrices. *J. Pharm. Sci.* **1963**, *52*, 1145–1149. [CrossRef]

70. Siepmann, J.; Peppas, N.A. Higuchi equation: Derivation, applications, use and misuse. *Int. J. Pharm.* **2011**, *418*, 6–12. [CrossRef]

71. Lapidus, H.; Lordi, N.G. Drug release from compressed hydrophilic matrices. *J. Pharm. Sci.* **1968**, *57*, 1292–1301. [CrossRef]
72. Lapidus, H.; Lordi, N.G. Some factors affecting the release of a water-soluble drug from a compressed hydrophilic matrix. *J. Pharm. Sci.* **1966**, *55*, 840–843. [CrossRef] [PubMed]
73. Hixson, A.W.; Crowell, J.H. Dependence of reaction velocity upon surface and agitation: II—Experimental procedure in study of surface. *Ind. Eng. Chem.* **1931**, *23*, 1002–1009. [CrossRef]
74. Bruschi, M.L. *Strategies to Modify the Drug Release from Pharmaceutical Systems*; Woodhead Publishing: Sawston, UK, 2015; pp. 63–86.
75. Hopfenberg, H.B. Controlled release from erodible slabs, cylinders, and spheres. In *Division of Organic Coatings and Plastics Chemistry: Preprints-Advantages and Problems*; American Chemical Society: Washington, DC, USA, 1976; Volume 36, pp. 229–234.
76. Katzhendler, I.; Hoffman, A.; Goldberger, A.; Friedman, M. Modeling of drug release from erodible tablets. *J. Pharm. Sci.* **1997**, *86*, 110–115. [CrossRef] [PubMed]
77. Langenbucher, F. Letters to the editor: Linearization of dissolution rate curves by the weibull distribution. *J. Pharm. Pharmacol.* **1972**, *24*, 979–981. [CrossRef] [PubMed]
78. Dokoumetzidis, A.; Papadopoulou, V.; Macheras, P. Analysis of dissolution data using modified versions of Noyes-Whitney Equation and the Weibull function. *Pharm. Res.* **2006**, *23*, 256–261. [CrossRef] [PubMed]
79. Waloddi Weibull, B. A Statistical distribution function of wide applicability. *J. Appl. Mech.* **1951**, *18*, 293–297. [CrossRef]
80. Kenney, J.F.; Keeping, E.S. "Root mean square". In *Mathematics of Statistics: Part 1*; Van Nostrand: Princeton, NJ, USA, 1962; pp. 59–60.
81. FDA. *FDA Guidance for Industry—Dissolution Testing of Immediate Release Solid Oral Dosage Forms*; FDA Center for Drug Evaluation and Research: Silver Spring, MD, USA, 1997; Volume 1, pp. 1–17.
82. Shah, V.P.; Tsong, Y.; Sathe, P.; Liu, J.-P. In Vitro dissolution profile comparison—Statistics and analysis of the similarity factor, F2. *Pharm. Res.* **1998**, *15*, 889–896. [CrossRef]
83. Skoug, J.W.; Borin, M.T.; Fleishaker, J.C.; Cooper, A.M. In Vitro and In Vivo evaluation of whole and half tablets of sustained-release Adinazolam Mesylate. *Pharm. Res. Off. J. Am. Assoc. Pharm. Sci.* **1991**, *8*, 1482–1488. [CrossRef]
84. Tinke, A.P.; Vanhoutte, K.; de Maesschalck, R.; Verheyen, S.; de Winter, H. A new approach in the prediction of the dissolution behavior of suspended particles by means of their particle size distribution. *J. Pharm. Biomed. Anal.* **2005**, *39*, 900–907. [CrossRef] [PubMed]

C.2   Investigations into the Use of Machine Learning to Predict Drug Dosage Form Design to Obtain Desired Release Profiles for 3D Printed Oral Medicines

Hellen Mazur, Leon Erbrich, Julian Quodbach

Pretext

The concept from Section C.1 should be adapted to the modern standard and it should be investigated whether the mathematical, manually created prediction model can also be replaced by an artificial intelligence. It should be tested whether an ANN can support the DDF design and thus be integrated into the process of a physician's prescription of 3DP DDF. The data set of about 200 geometries and resulting in about 1000 release curves was used as input data for this purpose. Different ANN architectures were created based on this data to see if the underlying geometries and SA/V ratios can be predicted from the release curves. The different networks were trained, validated, and tested and compared with respect to their accuracy and loss function, as well as their mean square error evaluated.

Evaluation of authorship:

author	idea [%]	study design [%]	experimental [%]	evaluation [%]	manuscript [%]
Hellen Windolf	100	30	100	30	45
Leon Erbrich	-	40	-	70	45
Julian Quodbach	-	30	-	-	10

Evaluation of Copyright permission:

Investigations into the Use of Machine Learning to Predict Drug Dosage Form Design to Obtain Desired Release Profiles for 3D Printed Oral Medicines

Hellen Mazur, Leon Erbrich, Julian Quodbach

Abstract

Three-dimensional (3D) printing, digitalization, and artificial intelligence (AI) are gaining increasing interest in modern medicine. All three aspects are combined in personalized medicine where 3D printed dosage forms are advantageous because of their variable geometry design. The geometry design can be used to determine the surface area to volume (SA/V) ratio, which affects drug release from the dosage forms. This study investigated artificial neural networks (ANN) to predict suitable geometries for the desired dose and release profile. Filaments with 5% API load and polyvinyl alcohol were 3D printed using Fused Deposition Modeling to provide a wide variety of geometries with different dosages and SA/V ratios. These were dissolved in vitro, and the API release profiles were described mathematically. Using these data, ANN architectures were designed with the goal of predicting a suitable dosage form geometry. Poor accuracies of 68.5% in the training and 44.4% in the test settings were achieved with a classification architecture. However, the SA/V ratio could be predicted accurately with a mean squared error loss of only 0.05. This study shows that the prediction of the SA/V ratio using AI works, but not of the exact geometry. For this purpose, a global database could be built with a range of geometries to simplify the prescription process.

Investigations into the use of machine learning to predict drug dosage form design to obtain desired release profiles for 3D printed oral medicines

Hellen Mazur, Leon Erbrich & Julian Quodbach

Published online: 16 Feb 2023.

Submit your article to this journal ⬚

Article views: 1366

View related articles ⬚

View Crossmark data ⬚

Taylor & Francis
Taylor & Francis Group

RESEARCH ARTICLE

OPEN ACCESS | Check for updates

Investigations into the use of machine learning to predict drug dosage form design to obtain desired release profiles for 3D printed oral medicines

Hellen Mazur[a], Leon Erbrich[a] and Julian Quodbach[a,b]

[a]Institute of Pharmaceutics and Biopharmaceutics, Heinrich Heine University, Düsseldorf, Germany; [b]Department of Pharmaceutics, Utrecht Institute for Pharmaceutical Sciences, Utrecht University, Utrecht, The Netherlands

ABSTRACT

Three-dimensional (3D) printing, digitalization, and artificial intelligence (AI) are gaining increasing interest in modern medicine. All three aspects are combined in personalized medicine where 3D-printed dosage forms are advantageous because of their variable geometry design. The geometry design can be used to determine the surface area to volume (SA/V) ratio, which affects drug release from the dosage forms. This study investigated artificial neural networks (ANN) to predict suitable geometries for the desired dose and release profile. Filaments with 5% API load and polyvinyl alcohol were 3D printed using Fused Deposition Modeling to provide a wide variety of geometries with different dosages and SA/V ratios. These were dissolved in vitro, and the API release profiles were described mathematically. Using these data, ANN architectures were designed with the goal of predicting a suitable dosage form geometry. Poor accuracies of 68.5% in the training and 44.4% in the test settings were achieved with a classification architecture. However, the SA/V ratio could be predicted accurately with a mean squared error loss of only 0.05. This study shows that the prediction of the SA/V ratio using AI works, but not of the exact geometry. For this purpose, a global database could be built with a range of geometries to simplify the prescription process.

1. Introduction

Artificial intelligence (AI) and precision medicine are two important aspects of modern medicine. Both promise to revolutionize healthcare worldwide (Ashley 2016; Hodson 2016; Deng et al. 2021; Johnson et al. 2021; Maceachern and Forkert 2021). With precision medicine, which aims to personalize therapy for individuals, several approaches are utilized to stratify patient groups. For example, the genome has been examined to characterize disease risks and responses to treatment because of its genetic layout, environmental influences, and other characteristics (Jorgensen et al. 2019; Uddin et al. 2019). By cross-referencing with databases, a diagnosis can be made quickly and specifically, and appropriate therapy with the correct dosage and dosing regimen can be established. Owing to the digitalization of health-related data and the rapid proliferation of technologies across countries, changes and progress in the development and use of AI in healthcare are driven (Topol 2019). Despite the promised advantages, modern electronic medicine faces some challenges, such as data integrity and safety, privacy, bias, and model performance. Nevertheless, the field of AI in medicine is growing; in screening, diagnostics, prevention, therapy, and aftercare, databases are used to monitor processes, detect trends at an early stage, and react to them. For example, AI can support medical diagnostics by analyzing image data. Based on existing images and associated diagnoses, AI recognizes patterns in the image that are assigned to disease patterns. The analysis and availability of large amounts of data make it possible to recognize pathological changes in the image quickly and reliably, to adapt therapies individually to the patient, and to provide prognoses for further disease progression (Lundervold and Lundervold 2019; Schork 2019; Deng et al. 2021). The use of AI is also becoming increasingly prevalent in pharmaceutical research. Groups are identifying new chemical structures with desired properties based on large datasets and algorithms, which is accelerating the development of new drugs and helping fight diseases (Baskin et al. 2016; Paul et al. 2021; Karthikeyan and Priyakumar 2022). AI is also helpful in the development of dosage forms, as experimental work, cost, and time can be saved. It can provide support for formulation development, stability testing, and release characterization, as well as optimizing the manufacturing process (Madzarevic et al. 2019; Yang et al. 2019; Elbadawi et al. 2020; Muñiz Castro et al. 2021). Obeid et al. predicted the diazepam release behavior of 3D printed tablets with the input parameters infill density and surface area to volume (SA/V) ratio (Obeid et al. 2021). A similar approach has been adopted by Benkö et al., Stanojevic et al. and Madzarevic et al. in their studies. Based on the geometries of the dosage forms, used excipients, and active pharmaceutical ingredient (API) load, the respective release profiles were predicted (Madzarevic et al. 2019; Stanojević et al. 2020; Benkő et al. 2022). Elbadawi et al. developed a web-based pharmaceutical software 'M3diseen' to predict the 3D printability of medicines for fused deposition modeling (FDM) (Elbadawi et al. 2020). The filaments required for FDM printing are produced using hot-melt extrusion (HME). As HME is

CONTACT Julian Quodbach ✉ j.h.j.quodbach@uu.nl 🖅 Institute of Pharmaceutics and Biopharmaceutics, Heinrich Heine University, Düsseldorf, Germany; Department of Pharmaceutics, Utrecht Institute for Pharmaceutical Sciences, Utrecht University, Utrecht, The Netherlands

a complicated process in which the optimization of the fabrication parameters requires a lot of time and knowledge, the software predicts key fabrication parameters for printability and filament properties.

3D printing is particularly suitable for personalized medicine and is currently being researched in detail for this purpose (Goyanes et al. 2014; Goyanes et al. 2015; Fina et al. 2017; el Aita et al. 2020; Rahman and Quodbach 2021). Relevant processes are being investigated and potential polymers are being tested and developed (Gottschalk et al. 2021; Chamberlain et al. 2022). FDM 3D printing enables the manufacturing of a variety of geometries through the layer-by-layer construction of dosage forms. The geometries can have a bespoke pore structure, built-in cavities, as well as shapes that are not attainable via tablet compression. With FDM, the patient's requirements can be precisely addressed. Limitations are given here by the properties of the polymers (e.g. swelling behavior, solidification behavior) and the swallowability of the individual geometry. FDM 3D printing is only suitable for smaller batches, because so far usually only one to two print heads work in parallel and the printing of one tablet, depending on the size, can take about 1 min. Especially for tailored medicine, 3D printing processes offer the advantage that geometries can be freely selected and designed. Adjustment of dosages and SA/V ratios can lead to the modification of the release rates (Sadia et al. 2018; Windolf et al. 2021; Windolf et al. 2022). Besides the individual dosage, it is of equal importance in personalized medicine that the duration of action and the onset of the effect are in line with the therapy and support compliance. This means that symptoms can be alleviated immediately with a rapid onset of action. But in the same way, with a prolonged release time, the effect can be sustained over a period of time, thus extending the ingestion intervals of the medicine. Due to the small batch sizes, non-destructive quality control processes and predictive tools are of interest. Therefore, AI technologies are used in this area to make predictions about the characteristics of the dosage form based for example on the formulation or geometry design.

In addition to the predictions of the resulting release profiles (Hassanzadeh et al. 2019), there are already a few approaches to predicting the design of the dosage form using an ANN (Novák et al. 2018; Grof and Štěpánek 2021). A computational design method for finding the internal structures for multi-component tablets that result in a preferred dissolution profile was developed by Grof and Štěpánek 2021.

Once the required API dose is known and the necessary release profile from the dosage form to achieve maximum therapeutic efficacy, reduce side effects, and increase compliance, an appropriate 3D printed dosage form geometry must be selected. In this study, the underlying geometry should be predicted to result in a predetermined dissolution profile with a given API load. This could streamline the workflow from prescription to 3D-printed tablets. Prediction by ANN is intended to bypass the design step that currently must be performed by skilled personnel, thus eliminating potential errors, and saving cost and effort. Previous studies have shown that the release behavior is independent of geometry and depends only on the SA/V ratio of the dosage form (Reynolds et al. 2002; Goyanes et al. 2015; Windolf et al. 2021; Windolf et al. 2022). Based on the generated release data for different SA/V ratios, the associated dissolution profile can be predicted using mathematical equations such as the Peppas Sahlin equation (Windolf et al. 2021). In the first approach, an ANN should be created to predict the geometry from the input data of the release curve and the desired API content. The predicted geometry should include the necessary SA/V ratio, which reflects the desired drug load in volume and ensures the release progression through the SA/V ratio. Subsequently, another neural net was created to backtrack the attempt, in which an appropriate SA/V ratio should be predicted for the desired curve.

2. Materials and methods

2.1. Materials

The formulation consisted of 5% (w/w) pramipexole dihydrochloride monohydrate (PDM, Chr. Olesen, Denmark) as a readily soluble API of the biopharmaceutics classification system (BCS) class I (Łaszcz et al. 2010; Komal et al. 2019; Tzankov et al. 2019). Mannitol (Parteck M®, Merck, Germany) was used as a plasticizer at 10% (w/w) content. Polyvinyl alcohol (84%, PVA, Parteck MXP®, Merck, Germany) was selected as a polymer. To improve flowability, 1% fumed silica (Aerosil® 200 VV Pharma, Evonik, Germany) was added to the formulation. This formulation has been used in previous studies (Windolf et al. 2021; Windolf et al. 2022).

2.2. Methods

2.2.1. Hot-melt extrusion

The drug-containing filament was produced via HME with a co-rotating twin-screw extruder (Pharmalab HME 16, Thermo Fisher Scientific, USA) using an in-house manufactured die with a diameter of 1.85 mm. The feed rate was set to 5 g/min and the screw speed to 30 rpm. The temperatures of the heating zones as well as the screw configurations are shown in Table 1. The filaments were hauled off with a winder (Model 846700, Brabender, Germany) at a speed of 1.8 m/min to a target diameter of 1.75 mm. The diameter was controlled in-line using a laser-based diameter measurement module (Laser 2025 T, Sikora, Germany).

2.2.2 3D Printing of geometries

The drug-loaded filament was printed on a FDM 3D printer (Prusa i3 Mk3, Prusa Research, Czech Republic) into dosage forms with various geometries. These forms were designed by considering the SA/V ratio using the computer-aided design (CAD) software Fusion 360® (Autodesk, USA) and were sliced in PrusaSlicer® (Prusa Research, Czech Republic) to obtain the desired G-code. The printing temperature for the filament was 185 °C, the bed temperature was 60 °C, and printing speed was 20 mm/s. The infill percentage was 100%, printed in a concentric shape. In total, 196 different geometries were printed.

2.2.3. Description of the geometries for dataset

The printed geometries were numerically described as accurately as possible for processing using ANN. The parameters recorded were surface area (SA), volume (V), SA/V ratio, total weight, and API mass (mg total and mg API), layer height (lh), and extrusion width (ew) as printing parameters, number of layers in total, length, height, and width of the 3D geometry, as well as the diameter of pores and their surface area, amount of beam-layers, their height, and amount of cylinders/hollow cylinders connected by the beams (see Figure 1). Numbers were used for the fundamental geometric shapes, i.e. cylinder =1, hollow cylinder =2, pyramid =3 (Table 2).

The amount of API contained covered a range of 1.7 − 49.2 mg. For each API content, a spectrum of SA/V ratios was attempted to be printed from the lowest possible to the highest possible SA/V using different designs (Figure 2). This was restricted by the limits that the forms should serve as oral dosage forms and, thus, be swallowable. For example, for a geometry with 2 mg of API, it was

Table 1. Extrusion data (temperature profile and screw configuration).

Temperature profile in zone 1-10 / °C									
zone / -	2	3	4	5	6	7	8	9	10
temperature / °C	30	100	180	180	180	180	180	195	195

screw configuration (die - gear)

die − 10 CE 1 L/D − KZ: 5 × 60°-3 × 30°- 5 CE 1 L/D- KZ: 4 × 90°-5 × 60°-3 × 30°- 10 CE 1 L/D − 2 CE 3/2 L/D – gear
CE = conveying element KZ = kneading zone

SA in mm²	841.63
V in mm³	613.25
SA/V in mm⁻¹	1.37
mg total	720.1
mg API	36.54
lh / ew in mm	0.2 / 0.4
No. layer total	50
l x h x w in mm	10 x 10 x 10
Ø pore in mm	2
pore SA in mm²	32
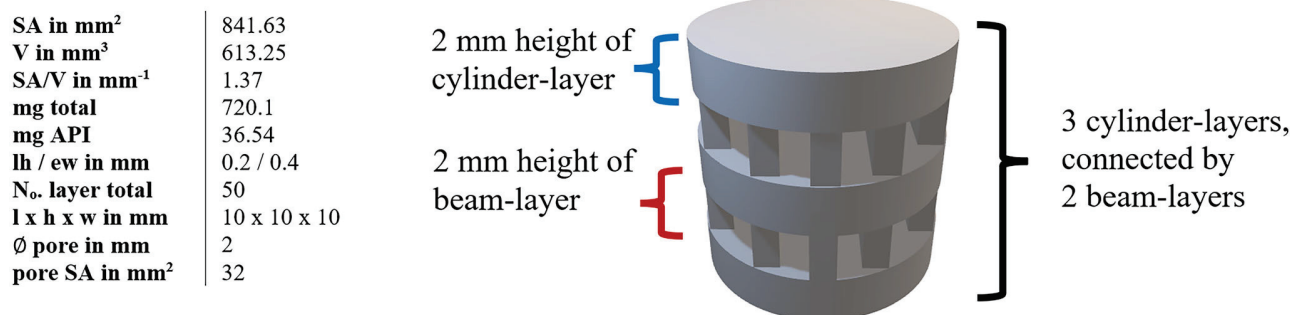
Figure 1. Example for description of the geometries for dataset. Variation of cylindrical shaped tablet. SA: surface area; V: volume; lh: layer height; ew: extrusion width.

only possible to achieve $1.6\,\text{mm}^{-1}$ as the smallest SA/V ratio (egg-shaped). The higher the volume (more API), the larger the geometries could become and, thus, the SA/V ratio is smaller. With 10 mg API, for example, a range of $0.9–2.5\,\text{mm}^{-1}$ SA/V ratio could be covered. With an API load of 20–39 mg, the maximum achievable SA/V ratio was only $2\,\text{mm}^{-1}$, as the volume was too large and a correspondingly large surface area led to very large tablets, which in turn are difficult to swallow (Figure 3). The focus was on ingestible shapes (round and oval), but to cover a wider range, several geometries not suitable for ingestion (e.g. cuboid and pyramid) were also printed.

2.2.4. Dissolution test

According to the European Pharmacopoeia (Ph. Eur.) monographs 2.9.3 and 5.17.1 (European Pharmacopoeia Commission 2.9.3 2020; European Pharmacopoeia Commission 5.17.1 2020), release studies ($n = 3–9$) were performed with the basket method (Method 1) in a dissolution tester (DT 726, Erweka, Germany). The baskets were 3D printed from water-insoluble polylactide acid (PLA). They had to be adapted for printed tablets since the mesh size of the regular Ph. Eur. baskets is small (0.36−0.44 mm) and the baskets were clogged by the swollen polymer of the PVA formulation. This affected the hydrodynamic medium flow around the printed oral dosage forms. The self-printed baskets have the same outer dimensions as the Ph. Eur. baskets except that the mesh width was changed to 3 mm. The dissolution test for PDM-containing tablets was performed in 500 mL of degassed 0.1 N hydrochloric acid at pH 1.2 under sink conditions ($c_s \geq 200\,\text{mg/mL}$ (Tzankov et al. 2019); maximum achieved concentration 0.1 mg/mL) and stirred at 50 rpm at a temperature of $37 \pm 0.5\,°\text{C}$. The released API was measured using a UV-Vis spectral photometer (UV-1800 Shimadzu, Japan) at a wavelength of 263 nm. Samples were taken every 5 min for the first 30 min, then every 10 min for the next 90 min, followed by sampling in 20 min intervals. After a release time of 240 min, samples were taken every 30 min. A total of 1001 single dissolution curves were measured ($n = 3–9$ for each geometry).

2.2.5. Description of the dissolution curves

For the data input, the release curves were saved in an array with the released percentage of API over time. The dissolution profiles were also described with the *Mean Dissolution Time* (MDT, Equation 1), $t_{50\%}$ (time in which 50% API were released), $t_{80\%}$, $t_{100\%}$.

$$\text{MDT} = \frac{ABC}{c_\infty} = \frac{\sum_{i=o}^{\infty}\left[(c_{i+1} - c_i) \times \frac{(t_i+t_{i+1})}{2}\right]}{c_\infty} \quad (1)$$

MDT indicates the average time an API molecule remains in a dosage form during release. The **MDT** (min) is calculated from the **ABC** (area between the curves) via the trapezoidal equation. c_∞ represents the initial amount of API in the dosage form. c_i is the concentration of the API released over time (Costa and Sousa Lobo 2001; Tanigawara et al. 1982).

When dissolution data showed linear regions, the slope of these regions was also recorded as potential input parameter for analysis. In previous publications, it has been described that the release profile of the used formulation can be expressed with the Peppas Sahlin equation (Equation 2). Therefore, the descriptive parameters k_1, k_2, and n were calculated for the individual curves and also included in the dataset.

$$\frac{M_t}{M_\infty} = k_1 \times t^n + k_2 \times t^{2n} \quad (2)$$

The exponent **n** is the diffusion exponent for any geometric shape. The constants k_1, k_2 describe the kinetics for erosion and diffusion (Siepmann and Peppas 2001; Windolf et al. 2021).

2.2.6. Dataset for ANN

A dataset was generated from the designed geometries (Section 2.2.3) and release curves (Section 2.2.5). A part of the dataset was already used in some previous studies (Windolf et al. 2021; Windolf et al. 2022). As different numbers of experiments ($n = 3 – 9$) were executed for each geometry, the dissolution curves were averaged to obtain a mean curve for each printed tablet. While originally 12 different geometry

Table 2. Categorization of printed geometries.

Number	Name	Shape Examples
1	Cylinder	
2	Hollow Cylinder	
3	Pyramid	
4	Double HollowCylinder	
5	Hollow Cylinder with included Cylinder	
6	Oblong	
7	Spiral	
8	Rectangle	
9	Cuboid	
10	Hollow Oblong	
11	Egg-shaped	
12	Hexagon	

categories were printed (Section 2.2.3, Table 2), the classes were limited to less refined categories: 'cylinder', 'hollow cylinder', 'oblong' and 'other'. The class 'other' was created so it was possible to use input data of unusual geometric shapes such as rectangular or spiral shapes while retaining the complexity of the overall classification problem. The problem gets more difficult if more classes of fewer examples are introduced and therefore the creation of the 'other' class was accepted as a compromise between complexity and the obtainable information and variance from unusual geometries. Tablets with large surface areas lead to large tablets that are difficult to swallow and additionally, the release curves no longer differ strongly with increasing SA/V ratio (Windolf et al. 2021). Therefore, tablets with large SA/V ratios were
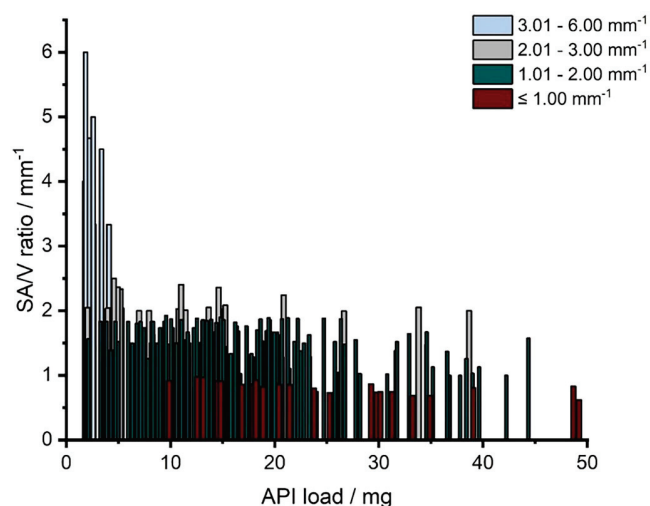
Figure 2. Distribution of API load (1.7 – 49.2 mg) and SA/V ratio (0.6 – 6.0 mm^{-1}) of printed geometries.
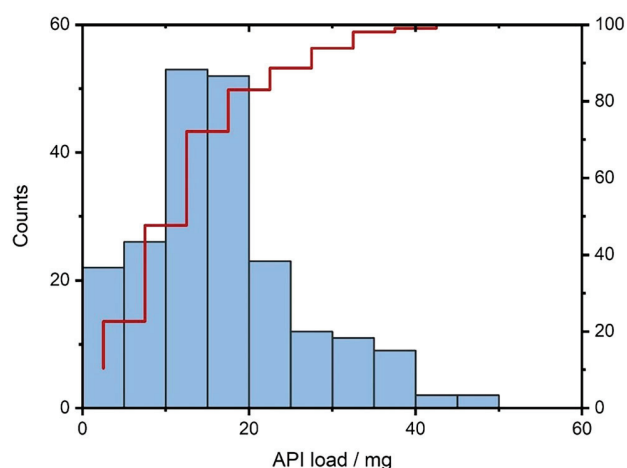
Figure 3. Quantity distribution of the printed tablets regarding the API content, $n = 196$. Blue columns: absolute counts; red line: cumulative percent (We refer the reader to the online version for the color coded graphs).

Figure 4. Class imbalance of 3D printed geometries. Hollow cylinder: 46.4%; cylinder: 26.3%; oblong: 5.0%; other: 22.4%.

removed from the dataset, where outliers were defined by the interquartile range (IQR) of the SA/V ratio where $q_n(0.75)$, $q_n(0.25)$ describe the upper quartile (75%) and lower quartile (25%) respectively (Dekking and Kraaikamp 2005) (Equation 3).

$$IQR = q_n(0.75) - q_n(0.25) \qquad (3)$$

Each tablet with a SA/V ratio that was below $q_n(0.25) - 1.5 \ IQR$ and above $q_n(0.75) + 1.5 \ IQR$ was considered an outlier and removed from the dataset as proposed in the literature (Tukey 1977). Although this is a simple approach to classify outliers, we consider it sufficient for this application. Based on the IQR of the SA/V ratio, tablet geometries that represent SA/V ratios above 2.97 mm^{-1} were excluded. Removal of outliers and deletion of replicates resulted in a dataset consisting of 179 distinct data points, each representing a geometry. The dataset is significantly imbalanced: The most prevalent class is *hollow cylinder* making up 46.4% of the tablets or 83 geometries in total, while only 5% (9 geometries) of the dataset are oblong-shaped tablets (Figure 4). The imbalance results from the fact that the data were first used for other studies (Windolf et al 2021; Windolf 2022) and some

forms are particularly suitable for representing different volumes and surface areas without the geometries becoming too large and thus 'unswallowable'. This must be considered during the training process and when assessing the performance of the classifier. The term 'classifier' is interchangeably used with 'neural network' in this study to describe the proposed architectures in the next section that are used to classify the input data into the underlying geometric shape. If the performance of the classifier is below 46.4% it can be considered unsuitable because any classifier that predicts the most prevalent class, i.e. hollow cylinder, every time, is equally good. Therefore 46.4% should be considered as a lower threshold for accuracy in this setting.

2.2.7. Neural Network architectures

Artificial Neural Networks (ANN) are at the heart of most modern Machine Learning applications and connect input data to output data. ANN only provides the net architecture composed of different numbers of input and output neurons and different layers, while the specific weights and biases are computed by error backpropagation as an optimization method (Bishop 2006). The term 'layers' generally refers to a specific computational function, which is directly applied to the original input data or to the output of a different layer. The latter implies, that layers can be stacked and that the stack of layers constitutes the ANN architecture. The goal is to minimize a loss function so that the neural net provides concise output predictions when receiving appropriate input data. In this paper, ANNs were leveraged for two optimization goals: geometry classification and SA/V ratio prediction. For classification, three different architectures are investigated. The first architecture and most basic approach consisted of 7 linear layers, 2 dropout layers, 6 applications of batch normalization and exponential linear units (ELU) as nonlinear activation functions and each computational unit has a different purpose. Linear layers are one of the basic building blocks of most simple feed-forward neural network architectures and represent a linear transformation of the input vector (Bishop 2006). Applying a linear transformation to the input vector yields an output vector, where the output size of this transformation is a freely adjustable parameter. Linear layers can be thought of as calculating a matrix-vector multiplication first and then adding a bias term to the result (Bishop 2006). Because the weights (i.e. the entries of the matrix) are optimized through error backpropagation, linear layers with

reduced output size can represent a lower-dimensional transformation of the input with a (potentially) reduced loss. Dropout layers act as regularization in deep neural networks and are often used to avoid overfitting where robustness is achieved by randomly dropping neuronal connections of the network (Srivastava et al. 2014). The fraction of discarded connections is controlled through a parameter p, which is also freely adjustable (Srivastava et al. 2014). Another technique in machine learning is batch normalization which leads to faster convergence while also acting as a regularization (Ioffe and Szegedy 2015). The idea is to apply both rescalings and mean shifting to every output dimension of a certain layer (Ioffe and Szegedy 2015). The training inputs for ANNs are often processed in batches (or mini-batches), which correspond to a fixed number of training examples (Ioffe and Szegedy 2015). The statistical properties of those batches such as the mini-batch variance and the mini-batch mean are used for the rescaling and the mean shifting respectively, resulting in normalized values between 0 and 1 for the certain layer (Ioffe and Szegedy 2015). Another key component of every neural network architecture is the concept of a nonlinear activation function. In multilayer neural network architectures, nonlinear activation functions are necessary. Otherwise, multiple linear layers collapse into a single linear layer if they are stacked together without some form of nonlinearity (Bishop 2006). If no nonlinear activation functions are implemented between linear layers, the neural net will result into a simple linear matrix-vector product with a bias component. These functions are therefore required for every multilayer perceptron to become 'universal approximators' (Bishop 2006). ELU layers were used as nonlinear neuron activation functions, which were first introduced by Clevert at al (Clevert et al. 2016). and represent a less known variant of the Rectified Linear Unit (RELU). Instead of setting negative inputs to zero, the ELU layer interpolates for $x \leq 0$. In other cases, the activations are the same as for the RELU layer, shown in Equation 4.

$$ELU(x) = \begin{cases} x, & \text{if } x > 0 \\ \alpha * (\exp(x) - 1), & \text{if } x \leq 0 \end{cases} \quad (4)$$

The hyperparameter α is frequently set to 1, which is also the default in this work. Both RELU and ELU activations are the same for $x > 0$. However, the ELU activation is smoother for negative values. The first architecture is named 'StandardNet' and is depicted in Figure 5. The net receives a total of 132 features consisting of the dissolution data (128 features) and the four inputs 'mg API', as well as 'k_1', 'k_2' and 'n' from fitting with the Peppas Sahlin equation. The input is passed in batches of 32 through the fully connected layer fc1 which outputs a 64-dimensional representation. Subsequently, batch normalization and the nonlinear ELU activation layer are applied. Note that neither the batch normalization nor the nonlinear activation changes the output dimension. In the next step, the output is passed through the first dropout layer with dropout probability p1, which is determined by hyperparameter optimization. The stack consisting of a fully connected layer, batch normalization, ELU, and dropout is repeated with an output dimension set to 32. This is the last application of dropout and in the next steps, the data is only passed through 4 stacks of fully connected layers, batch normalization and ELU where the output dimensions are 16, 8, 6 and 6. This output is processed by the last linear layer fc7, where the output dimension is set to the number of distinct geometry shapes (in this case 4 shapes). From this output that indicates the predicted class labels, the cross-entropy loss is calculated to obtain the gradient, which is passed on to the optimizer.

The second architecture which is called 'InterpretableNet' can be seen in Figure 6. The conceptual difference between the previous and this architecture is that certain tablet characteristics such as SA/V Ratio, surface area, volume, inner diameter, and mean dissolution time (MDT) should be predicted from the desired dissolution characteristics, the required drug amount (mg API) and the mentioned dynamical parameters of the Peppas Sahlin equations. These predictions are used within the same net to obtain a score for each tablet geometry. This score is used to predict the corresponding geometrical shape.

The last architecture that was used as a classifier exhibits the sequential and time-dependent nature of the dissolution curve and is referred to as 'SequentialNet' (Figure 7). It is composed of two stacked Recurrent Neural Networks (RNN) and the same stack of layers which were already described before in Figure 5. RNN are a common way to address time dependency by utilizing hidden states. These hidden states can represent connections to previous states of the system and can act as a memory (Elman 1990). The used RNN architecture was a simple Elman Net (Elman 1990). The dissolution curve is first passed through the two stacked RNN and the resulting representation of this curve is concatenated with the Peppas Sahlin coefficients and with the desired drug amount. In the previous architecture, the curve was passed along with these coefficients in the first place.

A neural net that should predict the SA/V ratio given the dissolution data was also constructed. SvPredictionNet is similar to the StandardNet and is shown in Figure 8.

2.2.8. Loss Functions and hyperparameter optimization

Loss functions are functions that are commonly used to compare the values predicted by neural nets to the prior known ground truth scalar values or class labels. Assume that y is the true vector of class labels of size C, where C is the number of distinct classification labels. Furthermore, let x be the output of the last layer of some neural net, where x is a matrix with dimensions $N \times C$ $N \times C$ and N is the number of training inputs the neural net receives per forward pass (batch size). Then, for a single training input i the following is true (Bishop 2006; Sammut and Webb 2010) (Equation 5):

$$l_n = -\log \frac{\exp(x_{n,y_n})}{\sum_{c=1}^{C} \exp(x_{n,c})} \text{ for } n = 1, \ldots, N \quad (5)$$

where the total loss $l(x, y)$ is obtained by calculating the average over each l_n from 1 to N. The cross-entropy loss is used within the classification task in the StandardNet, InterpretableNet, and SequentialNet to compare the class label predictions to the ground truth class labels. To control for the class imbalance, which was mentioned in 2.2.6, the loss of a particular prediction was weighted with a weight function that takes the skewed distribution of each subclass into account. The reciprocal of the relative frequency of each class was used as a weight function (Sammut and Webb 2010), which results in low weights for frequent classes such as hollow cylinder and higher importance for less common classes (e.g. oblong class). This implicitly sets the focus on the least frequent classes which often leads to better results for these classes. The other loss function is the commonly used mean squared error loss (MSE). Let $\hat{y}$ be a N-dimensional vector that contains scalar predictions of the ground truth values y. Then, the total MSE loss is calculated via Equation 6 (Sammut and Webb 2010).

$$MSE = \frac{1}{N} \sum_{n=1}^{N} (\hat{y}_n - y_n)^2 \quad (6)$$

The MSE loss is used to assess the predictive performance of the SvPredictionNet. The hyperparameters, such as the dropout
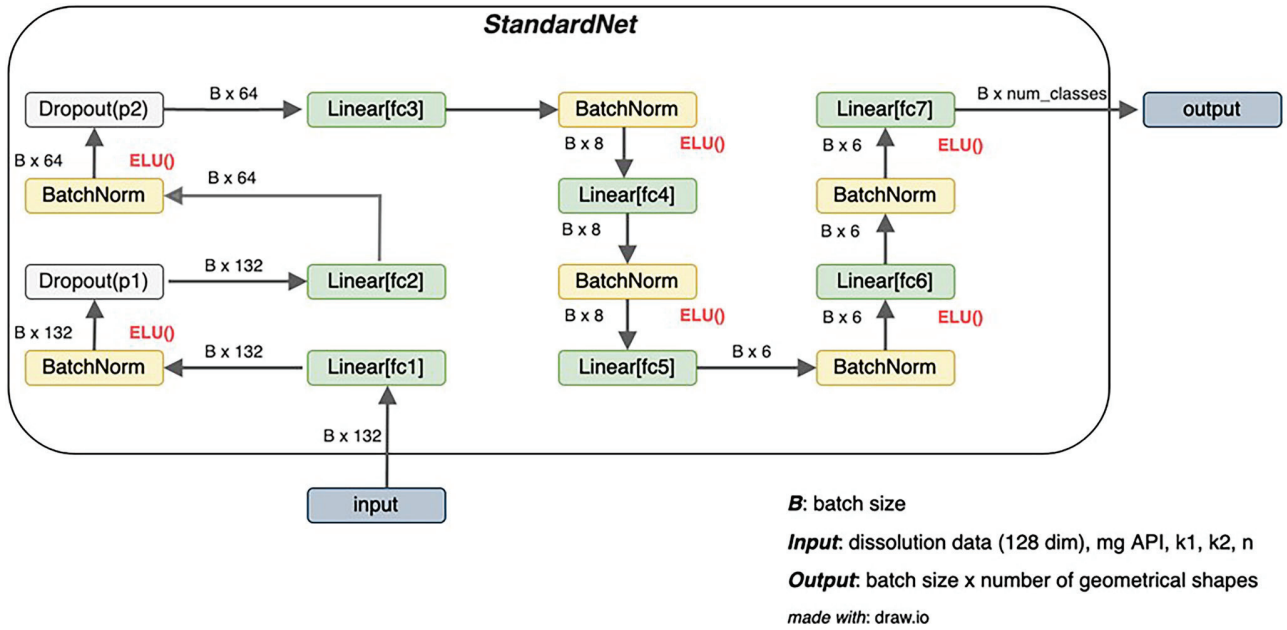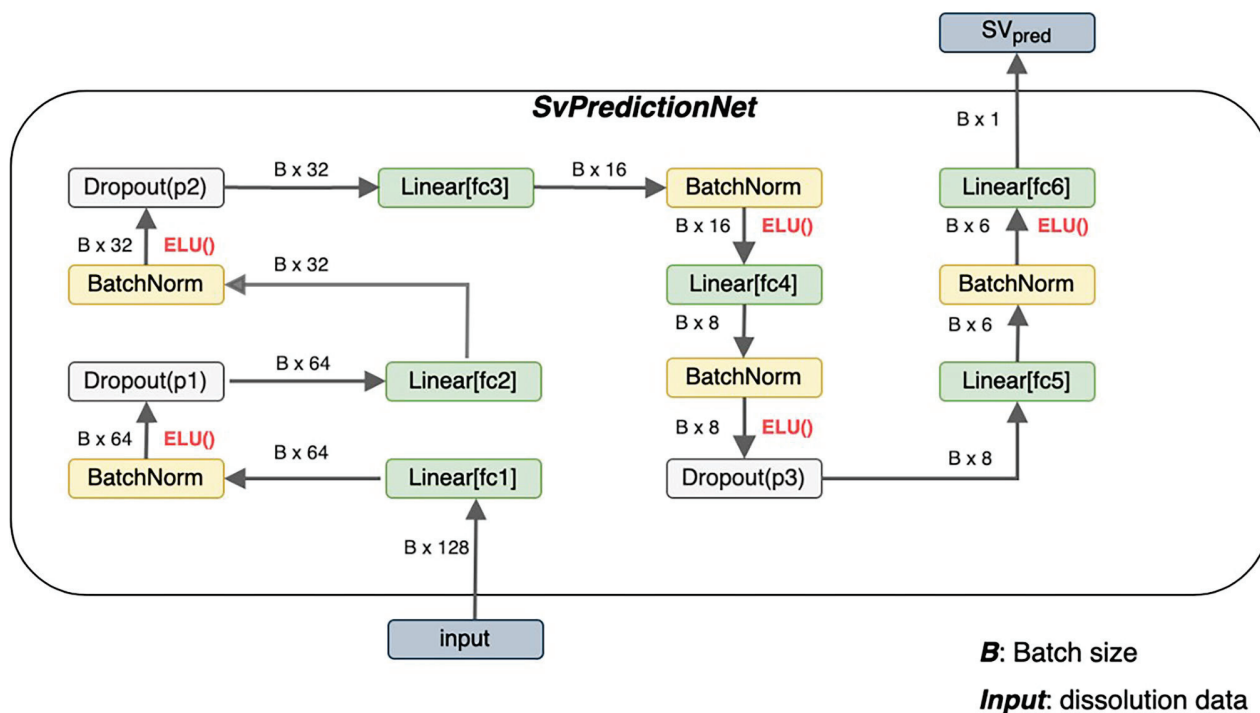
Figure 5. Architecture of StandardNet. *B* is the number of training examples, that are processed in parallel (batch size). The *fc* abbreviation in the linear layers stands for fully connected, which is a synonym for linear layers. *ELU* stands for exponential linear units and is the nonlinear activation function introduced in 2.2.7. *mg API* is the abbreviation of the drug amount and k_1, k_2, and n are descriptive parameters of the Peppas Sahlin equation (Equation 2).
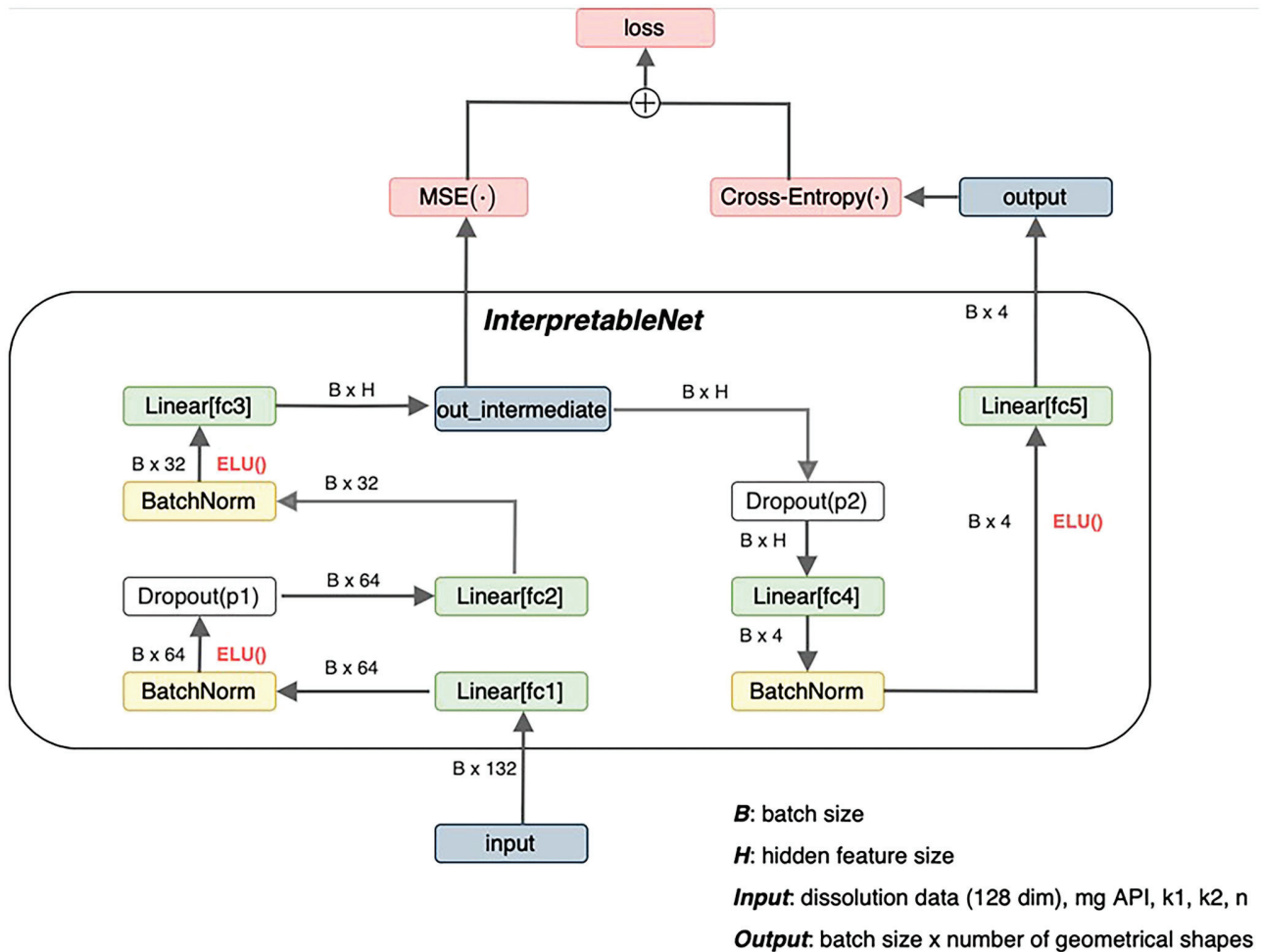
Figure 6. Architecture of InterpretableNet. *B* is the number of training examples, that are processed in parallel (batch size). The *fc* abbreviation in the linear layers stands for fully connected, which is a synonym for linear layers. *ELU* stands for exponential linear units and is the nonlinear activation function introduced in 2.2.7. *mg API* is the abbreviation of the drug amount and k_1, k_2, and n are descriptive parameters of the Peppas Sahlin equation (Equation 2). MSE refers to the mean-squared-error loss (Equation 6).
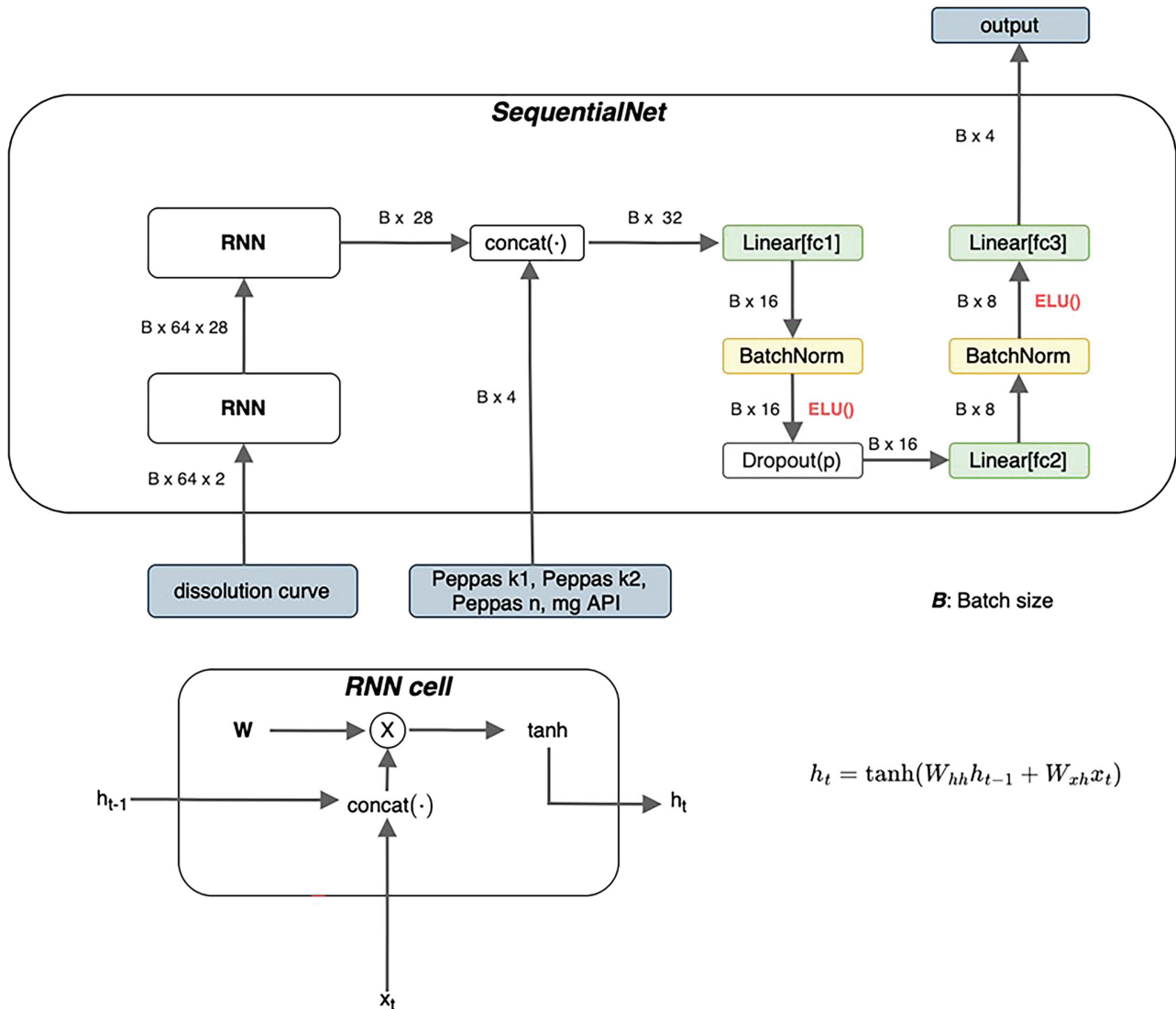
Figure 7. Architecture of SequentialNet. *B* is the number of training examples, that are processed in parallel (batch size). The *fc* abbreviation in the linear layers stands for fully connected, which is a synonym for linear layers. *ELU* stands for exponential linear units and is the nonlinear activation function introduced in 2.2.7. *mg API* is the abbreviation of the drug amount and k_1, k_2, and n are descriptive parameters of the Peppas Sahlin equation (Equation 2). h_t is the hidden state of the Recurrent Neural Network at time step t.

probability p and the learning rate, were optimized with the help of pytorch (Paszke et al. 2019) and optuna (Akiba et al. 2019).

3. Results and discussion

The used architectures can be categorized into two broad categories: classification architectures that should predict the suitable geometric shape (*StandardNet, SequentialNet, InterpretableNet*) and a scalar prediction architecture that return the SA/V ratio as a continuous positive value (*SvPredictionNet*). Accuracy is only meaningful in the context of classification architectures as this term is often considered as the ratio between correctly predicted classes and the total number of samples. Therefore, accuracy measures are only provided for *StandardNet, InterpretableNet* and *SequentialNet* and in the case of the *SvPredictionNet* architecture we refer to the loss metric described in Section 2.2.8. The dataset was split into training, validation, and test set, where 80% of the data were used to train weights of the neural nets and 10% of the data were used for validation and test sets, respectively.

Splitting the dataset into these three sets is standard practice and results in less biased and more accurate estimators for the reported accuracies and loss metrics. The additional validation set is used to tune hyperparameters whereas the test set is utilized to obtain estimates of classifier performance for unseen data.

3.1. Prediction of the geometry from dissolution curves

To implement the goal of predicting geometries for 3D-printed drug dosage forms with desired release profiles, different networks were constructed. First, it was attempted to predict the form as accurately as possible with class labels (cylinder, hollow cylinder, etc.) and in the next step with exact diameter, height, width, number of pores, etc., to reproduce the appearance of a possible geometry (Section 2.2.3, Figure 1). Since the SA/V ratio is set based on the release profile, the desired API content is given as additional information so that the volume is known, and the ANN can then output a suitable geometry for the desired volume and SA/V ratio.

Figure 8. Architecture of SvPredictionNet. *B* is the number of training examples, that are processed in parallel (batch size). The *fc* abbreviation in the linear layers stands for fully connected, which is a synonym for linear layers. *ELU* stands for exponential linear units and is the nonlinear activation function introduced in 2.2.7. SV_{pred} is the predicted surface-area-to-volume-ratio.

Three networks were used for this approach, which was set up differently (2.2.7: *StandardNet, InterpretableNet, SequentialNet*). For each of the 90 epochs, Figure 9 shows both accuracies and losses of the classification architectures. Each epoch represents a complete pass of every training example through the ANN (Nielsen 2015). The neural nets *StandardNet* and *InterpretableNet* show a moderate acceleration of both training and validation accuracy along the increasing number of epochs.

Furthermore, both validation and training loss also decreases over time for the *StandardNet* and the *InterpretableNet*. For the latter architecture, there is a pronounced peak in the validation loss around epoch 5. One possible explanation for this anomaly is the fact that the validation set was relatively small in absolute units (sample size 18), which may lead to unreliable loss estimates for some epochs. The fact that the validation loss reverts to its mean value in the 10th epoch supports this consideration. The more sophisticated design of the *SequentialNet* did not result in better performance. Specifically, the training accuracy of the mentioned neural net is stuck in a tight channel between 40% and 60% and settles to 52% in the last epoch. In relation to the lower accuracy threshold of 46% (Section 2.2.6), this is not a considerable improvement compared to the complexity of the architecture. The peak in the corresponding loss plot is not surprising, as the loss acceleration coincides with a drop in training accuracy. Figure 10 depicts the final accuracies of the last epoch for the different classification architectures. The training performance is influenced by the architecture type: The training accuracy of the basic approach, which is implemented by the *StandardNet,* outperforms the other architectures by some margin. Indeed, the training accuracy of 68.5% is 11.2 percentage points higher than the *InterpretableNet* and

16.7 percentage points higher than the accuracy of the *SequentialNet*. This suggests that a simple approach is superior to either presupposing the features which should be extracted or leveraging more sophisticated architectures such as RNN. It also translates to the test set with an accuracy of 44.4% for the *StandardNet* architecture compared to 44.4% for the *InterpretableNet*, which were surprisingly identical. The *SequentialNet* reaches a test accuracy of 38.9%. These test results show that none of the three architectures generalizes well on unseen data. The performance on the validation set is different. In this case, *SequentialNet* achieves the best performance with an accuracy of 72.2%. Both other architectures are accurate in 66.7% of the cases. The higher performance can also be interpreted as an outlier: as the validation set and test set are small, a misclassification of just one sample has large effect on the accuracy (± 5.6 pp. accuracy for $n = 18$). It is important to emphasize that the amount of data which is available for the test and validation set can lead to unreliable results.

The *StandardNet* is the best overall choice among the three architectures that are used for classification as its usage combines a simple architecture with moderate results. However, the overall training accuracies imply that no architecture was able to correctly adapt to the data.

Unfortunately, it became clear that these ANN-Designs were not able to predict the required information accurately so that the appropriate geometry can be designed based on predicted data. Ideally, the network should be able to infer from the given information which class label, height, diameter, etc. is needed to create a geometry with desired volume and surface area. However, the class label, i.e. the appropriate geometry, must first be selected for this procedure, but the release curves do not
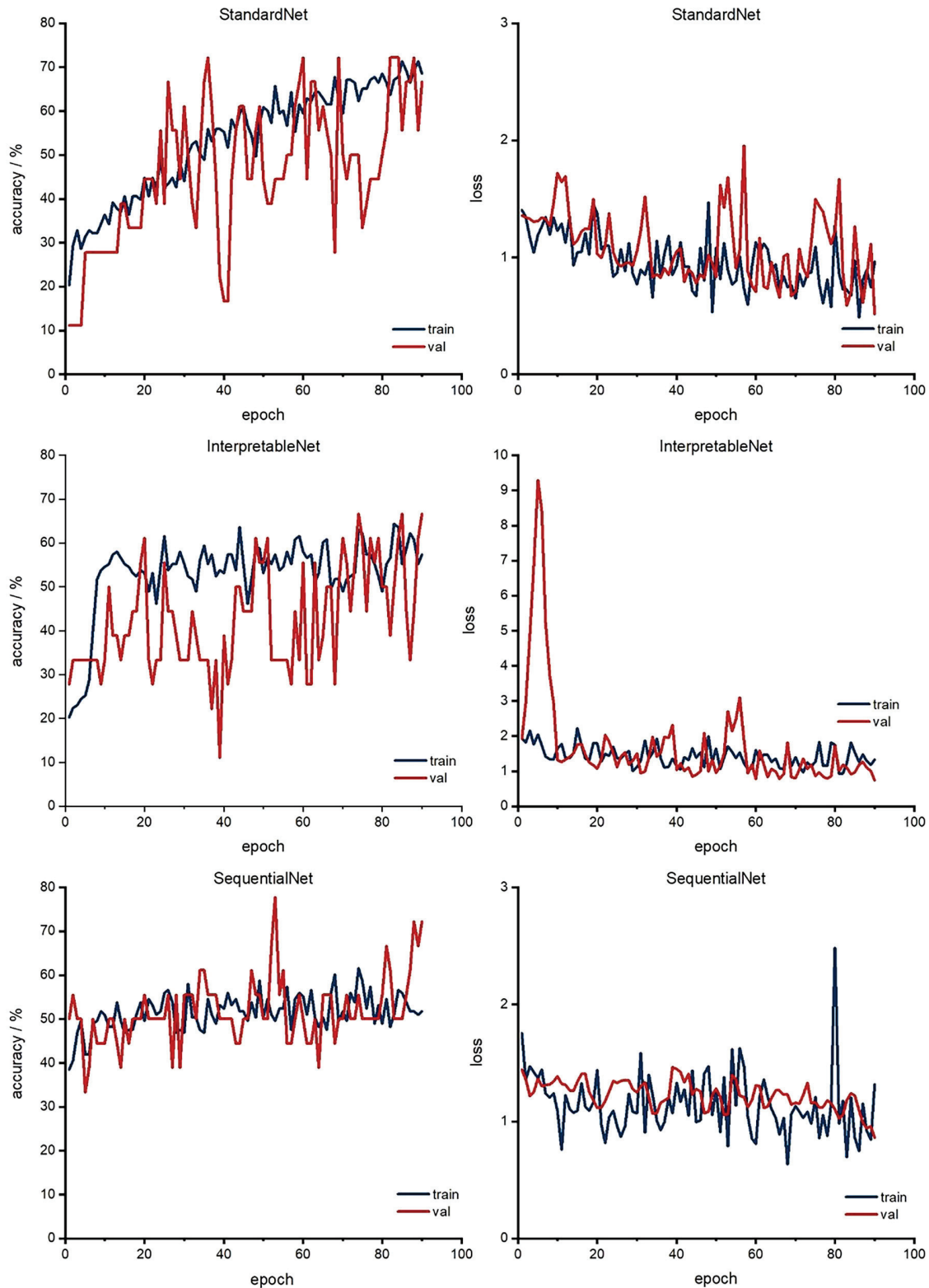
Figure 9. Accuracy (left column) and loss (right column) for each epoch for classification networks. Red: validation; blue: training (We refer the reader to the online version for the color coded graphs).

allow the necessary geometry to be inferred exactly. At least it was evaluated to see if it could identify a trend based on the dissolution profile as to which geometry was suitable so that this form could be used as a basis for the patient.

3.2. Prediction of SA/V ratio from dissolution curves

As the initial goal could not be attained, a different procedure was investigated. Since the release behavior is based on the SA/V ratio of the geometry, this ratio should be predicted from the
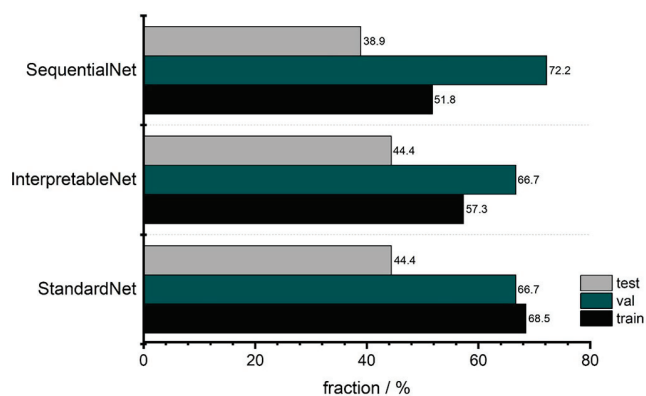
Figure 10. Accuracies for the last epoch for classification networks. Grey: test; green: validation; black: training (We refer the reader to the online version for the color coded graphs).
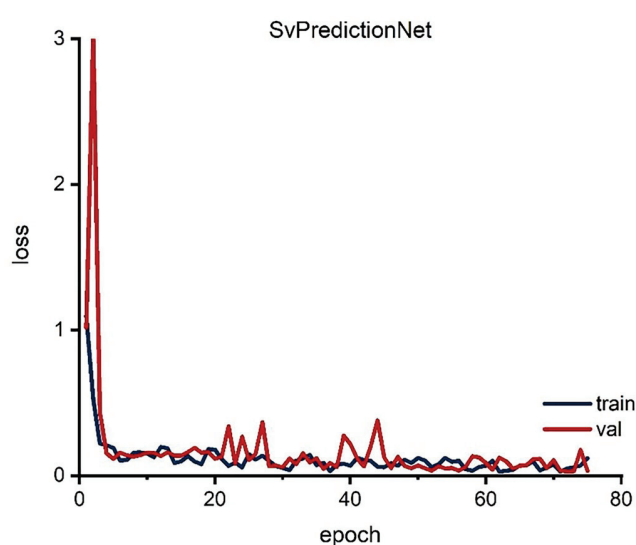
Figure 11. Loss for SvPredictionNet. Red: validation; blue: training (We refer the reader to the online version for the color coded graphs).

given data, so that subsequently the appropriate geometry could be selected from a database. This could offer the advantage that several geometries available for selection could be chosen during this screening process and thus limitations, such as the swelling behavior of the polymers used, could also be taken into account. The database with possible geometries could be fed by different persons independent of location, it would only be necessary to specify the volume and the surface with the resulting SA/V ratio and possible pore sizes based on the polymer swelling behavior. To implement this concept, the prediction approach of Windolf et al. (2021) was used. In this study, a correlation between the MDT and the SA/V ratio and between the Peppas Sahlin equation and the SA/V ratio was used to predict the resulting release profile based on the SA/V ratio. This approach was reversed here to predict the SA/V ratio based on the dissolution curve. With this information, the required surface area could be calculated for a desired dose and a corresponding geometry could be designed with the CAD software, or chosen from a possible database. As a scalar prediction net architecture, the *SvPredictionNet* was used. The results in Figure 11 indicate that the net learns a reasonable representation from which predictive SA/V ratios are obtained. The model however does also suffer from an incapability to

generalize well. While the overall test set MSE loss of 0.054 between predicted and ground truth is acceptable, there are some predictions that are off by a large margin, e.g. a predicted value of $1.44\,mm^{-1}$ with the ground truth value of $1.9\,mm^{-1}$, representing a squared error loss of 0.212. The inaccurate predictions for the test set are more common for geometries with higher SA/V ratios. For example, in 3 of 4 cases where the MSE was larger than 0.1, the SA/V ratios of the related tablets were larger than $2.3\,mm^{-1}$. This underlines the fact that acquiring more data is necessary for more reliable results, especially for dissolution curves where the underlying geometrical shapes represent higher SA/V ratios. The same argument can be made for the classification problem. As this problem is harder to solve than the prediction of SA/V ratios one would need at least as much data as for those.

4. Conclusion

In this study, four different approaches were pursued to use Machine Learning to make predictions for geometric designs suitable as oral dosage forms. The geometry should be designed with respect to its API content and desired release behavior. This would allow a prescription workflow to be established for 3D printed oral dosage forms. The approach of using the given data to predict a geometry with the required length, width, height, and underlying geometry such as a cylinder or hollow cylinder by an artificial neural network was unfortunately not possible. Therefore, a general approach was taken to predict only the geometry without exact dimensions from the available data. It was assumed that this would not work, since the shape should have little to no influence on the release profile. Nevertheless, the geometry corresponding to the dissolution curve could be predicted with an accuracy of 68.5% (training) and 44.4% (test). The generated accuracy was higher than expected. Another approach was to predict the required SA/V ratio for a given release profile. This was possible with a MSE loss of 0.05. With this procedure, the swelling behavior of the polymer can cause errors, since the digitally generated SA/V ratio can be affected *in vitro* by the swelling of pores and the release curves therefore do not match the generated SA/V ratio. Thus, studies on the swelling behavior of the polymer should be carried out in advance to ensure those properties do not falsify the data. Another strong influencing factor is the distribution of the data, which is unfortunately unevenly distributed due to the given constraints regarding swallowability in this study, making it difficult to predict the appropriate geometry. The scope of the study was limited to neural networks as a model architecture. It should be emphasized, that there are a lot of other different architectures and algorithms available. As all four approaches were either classification or regression setups, further studies for other algorithms such as Random Forest Classification or Random Forest Regression are left for future research. To take advantage of the opportunities 3D printing offers for personalized medicine, the geometry with the desired properties must still be created manually. Based on the SA/V ratio prediction and the desired API content, the required surface area and volume can be calculated, but the geometry containing these values must be created and tested manually, which in turn takes a lot of time and is prone to errors. To avoid having to perform these steps for every prescription, a database could be created with the associated surface area and volume information so that the required form only needs to be selected and printed. To create a working network for each formulation, much more data is needed, which is very unusual and uneconomical for the pharmaceutical field. For such an approach, a collaboration between

multiple institutions that publish their geometries with associated release data and formulations is necessary. This way it might be possible to create a database to select the drug dosage from geometry. For the particular formulation used, the required SA/V ratio can be predicted via the manual route of Windolf et al. 2021 or a neural network as described in Section 3.2. In the future, a program with a user-friendly interface could be designed, which is connected to the geometry database and suggests geometries for the calculated SA/V ratio and desired dosage, and the pharmacist or physician could select the appropriate form tailored to the patient, which also takes into account the properties of the formulation, such as the swelling behavior so that no pores can swell and thus change the release profile by reducing the required surface area. However, this could provide a method to establish a prescription process of 3D printed dosage forms.

Data availability statement

The data that support the findings of this study are available from the corresponding authors, [HM, LE], upon reasonable request.

References

Akiba T, Sano S, Yanase T, Ohta T, Koyama M. 2019. Optuna: a next-generation hyperparameter optimization framework. In Ankur Teredesai, Vipin Kumar (General chairs), Proceedings of the 25th ACM SIGKDD International Conference on Knowledge Discovery & Data Mining New York, NY, USA: Association for Computing Machinery; p. 2623–2631.

Ashley EA. 2016. Towards precision medicine. Nat Rev Genet. 17(9):507–522.

Baskin II, Winkler D, Tetko I. v 2016. A renaissance of neural networks in drug discovery. Expert Opin Drug Discov. 11(8):785–795.

Benkő E, Ilič IG, Kristó K, Regdon G, Csóka I, Pintye-Hódi K, Srčič S, Sovány T. 2022. Predicting drug release rate of implantable matrices and better understanding of the underlying mechanisms through experimental design and artificial neural network-based modelling. Pharmaceutics. 14(2):228.

Bishop CM. 2006. Pattern recognition. Mach Learn. 128:225–284.

Chamberlain R, Windolf H, Geissler S, Quodbach J, Breitkreutz J. 2022. Precise dosing of pramipexole for low-dosed filament production by hot melt extrusion applying various feeding methods. Pharmaceutics. 14(1):216.

Clevert D-A, Unterthiner T, Hochreiter S. 2016. Fast and accurate deep network learning by exponential linear units (ELUs). ICLR. Vol. 1, p. 1–14.

Costa P, Sousa Lobo JM. 2001. Modeling and comparison of dissolution profiles. Eur J Pharm Sci. 13(2):123–133.

Dekking FM,Kraaikamp C, LHP, MLE., 2005. Exploratory data analysis: numerical summaries. In George Casella, Stephen Fienberg, Ingram Olkin (Adv.), A modern introduction to probability and statistics: understanding why and how. London: Springer London; p. 231–243. ISBN 978-1-84628-168-6.

Deng J, Hartung T, Capobianco E, Chen JY, Emmert-Streib F. 2021. Editorial: artificial intelligence for precision medicine. Front Artif Intell. 4:834645.

el Aita I, Breitkreutz J, Quodbach J. 2020. Investigation of semi-solid formulations for 3d printing of drugs after prolonged storage to mimic real-life applications. Eur J Pharm Sci. 146:105266.

Elbadawi M, McCoubrey LE, Gavins FKH, Ong JJ, Goyanes A, Gaisford S, Basit AW. 2021. Harnessing artificial intelligence for the next generation of 3D printed medicines. Adv Drug Deliv Rev. 175:113805.

Elbadawi M, Muñiz Castro B, Gavins FKH, Ong JJ, Gaisford S, Pérez G, Basit AW, Cabalar P, Goyanes A. 2020. M3DISEEN: a novel machine learning approach for predicting the 3D printability of medicines. Int J Pharm. 590:119837.

Elman JL. 1990. Finding structure in time. Cognitive Science. 14(2): 179–211.

European Pharmacopoeia Commission 2.9.3 2020. Dissolution test for solid dosage forms. In European Pharmacopoeia; European Directorate for the Quality of Medicines & HealthCare of the Council of Europe (EDQM), Vol 10.2, p. 326–333.

European Pharmacopoeia Commission 5.17.1 2020. Recommendations on Dissolution Testing. In European Pharmacopoeia; European Directorate for the Quality of Medicines & HealthCare of the Council of Europe (EDQM), Vol 10.2, p. 801–807.

European Pharmacopoeia Commission 2020. Monograph pramipexole dihydrochloride monohydrate. In European Pharmacopoeia; European Directorate for the Quality of Medicines & HealthCare of the Council of Europe (EDQM), Vol 10.0, p. 5382–5384.

Fina F, Goyanes A, Gaisford S, Basit AW. 2017. Selective laser sintering (sls) 3d printing of medicines. Int J Pharm. 529(1-2):285–293.

Gottschalk N, Bogdahn M, Harms M, Quodbach J. 2021. Brittle polymers in fused deposition modeling: an improved feeding approach to enable the printing of highly drug loaded filament. Int J Pharm. 597:120216.

Goyanes A, Buanz ABM, Basit AW, Gaisford S. 2014. Fused-filament 3D printing (3DP) for fabrication of tablets. Int J Pharm. 476(1-2):88–92.

Goyanes A, Robles Martinez P, Buanz A, Basit AW, Gaisford S. 2015. Effect of geometry on drug release from 3D printed tablets. Int J Pharm. 494(2):657–663.

Grof Z, Štěpánek F. 2021. Artificial intelligence-based design of 3D-printed tablets for personalised medicine. Comput Chem Eng. 154:107492.

Hassanzadeh P, Atyabi F, Dinarvand R. 2019. The significance of artificial intelligence in drug delivery system design. Adv Drug Deliv Rev. 151-152:169–190.

Hodson R. 2016. Precision medicine. Nature. 537(7619):S49–S49.

Ioffe S, Szegedy C. 2015. Batch normalization: accelerating deep network training by reducing covariate shift. CoRR. abs/1502.03167. Vol. 37, p. 448–456.

Johnson KB, Wei W, Weeraratne D, Frisse ME, Misulis K, Rhee K, Zhao J, Snowdon JL. 2021. Precision medicine, AI, and the future of personalized health care. Clin Transl Sci. 14(1):86–93.

Jorgensen AL, Prince C, Fitzgerald G, Hanson A, Downing J, Reynolds J, Zhang JE, Alfirevic A, Pirmohamed M. 2019. Implementation of genotype-guided dosing of warfarin with point-of-care genetic testing in three UK clinics: a matched cohort study. BMC Med. 17(1):11.

Karthikeyan A, Priyakumar UD. 2022. Artificial intelligence: machine learning for chemical sciences. J Chem Sci . 134(1):2.

Komal C, Dhara B, Sandeep S, Shantanu D, Priti MJ. 2019. Dissolution-controlled salt of pramipexole for parenteral administration: in vitro assessment and mathematical modeling. Dissolution Technol. 26(1):28–35.

Łaszcz M, Trzcińska K, Kubiszewski M, Kosmacińska B, Glice M. 2010. Stability studies and structural characterization of pramipexole. J Pharm Biomed Anal. 53(4):1033–1036.

Lundervold AS, Lundervold A. 2019. An overview of deep learning in medical imaging focusing on MRI. Z Med Phys. 29(2):102–127.

Maceachern SJ, Forkert ND. 2021. Machine learning for precision medicine. Genome. 64(4):416–425.

Madzarevic M, Medarevic D, A Vulovic A, Sustersic T, Djuris J, Filipovic N, Ibric S. 2019. Optimization and prediction of ibuprofen release from 3D DLP printlets using artificial neural networks. Pharmaceutics. 11(10):544.

Muñiz Castro B, Elbadawi M, Ong JJ, Pollard T, Song Z, Gaisford S, Pérez G, Basit AW, Cabalar P, Goyanes A. 2021. Machine learning predicts 3D printing performance of over 900 drug delivery systems. J Control Release. 337:530–545.

Nielsen MA. 2015. Neural Networks and Deep Learning. San Francisco, CA: Determination Press, 25, p. 15–24.

Novák M, Boleslavská T, Grof Z, Waněk A, Zadražil A, Beránek J, Kovačík P, Štěpánek F. 2018. Virtual prototyping and parametric design of 3D-printed tablets based on the solution of inverse problem. AAPS PharmSciTech. 19(8):3414–3424.

Obeid S, Madžarević M, Krkobabić M, Ibrić S. 2021. Predicting drug release from diazepam fdm printed tablets using deep learning approach: influence of process parameters and tablet surface/volume ratio. Int J Pharm. 601:120507.

Paszke A, Gross S, Massa F, Lerer A. 2019. PyTorch: an imperative style, high-performance deep learning library. Adv Neural Inf Process Syst. 32:8026-8037.

Paul D, Sanap G, Shenoy S, Kalyane D, Kalia K, Tekade RK. 2021. Artificial intelligence in drug discovery and development. Drug Discov Today. 26(1):80–93.

PyTorch Foundation - Crossentropyloss. https://Pytorch.Org/Docs/Stable/Generated/Torch.Nn.CrossEntropyLoss.Html. (accessed 15.05.2022)

Rahman J, Quodbach J. 2021. Versatility on Demand – The case for semi-solid micro-extrusion in pharmaceutics. Adv Drug Deliv Rev. 172:104–126.

Reynolds TD, Mitchell SA, Balwinski KM. 2002. Investigation of the effect of tablet surface area/volume on drug release from hydroxypropylmethylcellulose controlled-release matrix tablets. Drug Dev Ind Pharm. 28(4):457–466.

Sadia M, Arafat B, Ahmed W, Forbes RT, Alhnan MA. 2018. Channelled tablets: an innovative approach to accelerating drug release from 3D printed tablets. J Control Release. 269:355–363.

Sammut C, Webb G. 2010. Mean squared error. In Claude Sammut, Geoffrey I. Webb (Eds.), Encyclopedia of Machine Learning; Springer US: Boston, MA, p. 653. ISBN 978-0-387-30164-8.

Schork NJ. 2019. Artificial intelligence and personalized medicine. Cancer Treat Res. 178:265–283.

Siepmann J, Peppas NA. 2001. Modeling of drug release from delivery systems based on hydroxypropyl methylcellulose (HPMC). Adv Drug Deliv Rev. 48(2-3):139–157.

Srivastava N, Hinton G, Krizhevsky A, Sutskever I, Salakhutdinov R. 2014. Dropout: a simple way to prevent neural networks from overfitting. J Mach Lear Res. 15:1929–1958.

Stanojević G, Medarević D, Adamov I, Pešić N, Kovačević J, Ibrić S. 2020. Tailoring atomoxetine release rate from DLP 3D-printed tablets using artificial neural networks: influence of tablet thickness and drug loading. Molecules. 26(1):111.

Tanigawara Y, Yamaoka K, Nakagawa T, Uno T. 1982. New method for the evaluation of in vitro dissolution time and disintegration time. Chem Pharm Bull. 30(3):1088–1090.

Topol EJ. 2019. High-performance medicine: the convergence of human and artificial intelligence. Nat Med. 25(1):44–56.

Tukey 1977. Chapter 2D: Fences, and outside values, Exploratory Data Analysis. In Frederick Mosteller (Ed.), Addison-Wesley Publishing Company, Reading, Mass 2:43–47. ISBN 0-201-07616-0.

Tzankov B, Voycheva C, Yordanov Y, Aluani D, Spassova I, Kovacheva D, Lambov N, Tzankova V. 2019. Development and invitro safety evaluation of pramipexole-loaded hollow mesoporous silica (HMS) particles. Biotechnol Biotechnol Equip. 33(1):1204–1215.

Uddin M, Wang Y, Woodbury-Smith M. 2019. Artificial intelligence for precision medicine in neurodevelopmental disorders. Npj Digit Med. 2(1)2019 2:1 :1–10.

Windolf H, Chamberlain R, Quodbach J. 2021. Predicting drug release from 3D printed oral medicines based on the surface area to volume ratio of tablet geometry. Pharmaceutics. 13(9):1453.

Windolf H, Chamberlain R, Quodbach J. 2022. Dose-independent drug release from 3D printed oral medicines for patient-specific dosing to improve therapy safety. Int J Pharm. 616:121555.

Yang Y, Ye Z, Su Y, Zhao Q, Li X, Ouyang D. 2019. Deep learning for in vitro prediction of pharmaceutical formulations. Acta Pharm Sin B. 9(1):177–185.

Chapter D:

Drug Dosage Form Design for Personalized Therapy with 3D Printed Oral Dosage Forms

D.1 Dose-independent Drug Release from 3D Printed Oral Medicines for Patient-specific Dosing to Improve Therapy Safety

Hellen Windolf, Rebecca Chamberlain, Julian Quodbach

Pretext

One of the special features and advantages of FDM 3D printing is the variety of geometries that can be realized. These can be adapted to the wishes and needs of the patient and thus improve adherence and compliance. The printed DDF can contain different volumes and thus variable dosages. The release behavior of the geometry is determined by the SA/V ratio, which can be easily changed by modifying the shape of the DDF. If only the dosage of the DDF is to be changed and not the release behavior (dose-independent release), the SA must be adjusted according to the V so that the SA/V ratio remains the same. In this manuscript, a geometry model is presented that allows the dose to be varied by a factor of 8 without changing the release profile.

Evaluation of authorship:

author	idea [%]	study design [%]	experimental [%]	evaluation [%]	manuscript [%]
Hellen Windolf	20	70	70	80	70
Rebecca Chamberlain	10	10	20	20	20
Julian Quodbach	70	20	10	0	10

Evaluation of Copyright permission:

Dose-independent drug release from 3D printed oral medicines for patient-specific dosing to improve therapy safety

Hellen Windolf, Rebecca Chamberlain, Julian Quodbach

Abstract

Fused deposition modeling (FDM) 3D printing provides the ability to address individual patients' therapeutic needs without having to change the formulation every time. This is particularly interesting for dosing and release modeling. In this study, a geometry model was developed that can represent variable dosages while keeping the surface area to volume (SA/V) ratio alike, so the drug release profiles remain similar. The model was tested on three different formulations. Two BCS I active pharmaceutical ingredients (API), pramipexole and levodopa, and one BCS II API, praziquantel, were used. Polyvinyl alcohol (PVA, water soluble) and a combination of vinylpyrrolidone-vinyl acetate copolymer (PVP-VA, water soluble) and ethylene–vinyl acetate (EVA, water insoluble) were used as the polymer matrix. The curves were compared using the similarity factor (f_2 value) and mean dissolution time (MDT). Using a hollow cylinder-based (HCb) geometry model, a dose-independent drug release could be realized. For the PVA formulations, an 8-fold dose change could be obtained and for the EVA- PVP-VA formulation a factor of 5.5 could be achieved, with $f_2 > 50$. Due to the layer structure of the printed objects, very fine dose variation of 0.13 mg per layer is possible within these models. This allows variable dosing in small steps with only one basis formulation.

D.2 Embedding a Sensitive Liquid-Core Waveguide UV Detector into an HPLC-UV System for Simultaneous Quantification of Differently Dosed Active Ingredients during Drug Release

Rebecca Chamberlain, Hellen Windolf, Björn B. Burckhardt, Jörg Breitkreutz, Björn Fischer

Pretext

In addition to flexible geometry design, FDM 3D printing also enables the printing of different APIs into one dosage form called a polypill. This is possible with a fixed combination, i.e., several APIs in one formulation with one polymer, but also the combination of several formulations of different APIs and polymers. This allows variable release of the active (IR and SR), but also dosage. For testing these dosage forms, analytical methods need to be developed that can measure multiple APIs simultaneously, but also cover a wide range of concentrations. In this study, a polypill was developed containing the fixed combination of levodopa (LD) and benserazide (BZ) (50-200 mg LD, 12.5-50 mg BZ) and another filament consisting of pramipexole (PDM) (0.375-3.5 mg). To detect the release of the APIs from the polypill, a liquid-core waveguide detector was coupled to an HPLC-UV system and the sensitivity for PDM detection was improved.

Evaluation of authorship:

author	idea [%]	study design [%]	experimental [%]	evaluation [%]	manuscript [%]
Rebecca Chamberlain	60	60	60	45	45
Hellen Windolf	30	40	40	35	35
Björn B. Burckhardt	-	-	-	5	5
Jörg Breitkreutz	-	-	-	5	5
Björn Fischer	10	-	-	10	10

Evaluation of Copyright permission:

Embedding a Sensitive Liquid-Core Waveguide UV Detector into an HPLC-UV System for Simultaneous Quantification of Differently Dosed Active Ingredients during Drug Release

Rebecca Chamberlain, Hellen Windolf, Björn B. Burckhardt, Jörg Breitkreutz, Björn Fischer

Abstract

Individual dosing of pharmaceutics and personalized medicine have become important with regard to therapeutic safety. Dose adjustments, biorelevant drug release and combination of multiple active substances in one dosage form for the reduction in polymedication are essential aspects that increase the safety and acceptance of the patient's pharmacotherapy. Therefore, not only innovative drug products but also new analytical methods are needed during the drug development phase and for quality control that can simultaneously determine different active ingredients and cover wide concentration ranges. We investigated a liquid-core waveguide UV absorbance flow cell detector coupled to an existing HPLC-UV system. A Teflon AF 2400 capillary tubing of 20 cm length was connected in series to the HPLC flow line and enabled a lower limit of quantification of 1 ng/mL pramipexole (increase in sensitivity by 20 compared to common 0.9 cm flow cells). This allowed the low-concentration of pramipexole and the higher concentrations of levodopa and benserazide occurring during drug release to be determined in a single chromatographic run within 22.5 min.

Article

Embedding a Sensitive Liquid-Core Waveguide UV Detector into an HPLC-UV System for Simultaneous Quantification of Differently Dosed Active Ingredients during Drug Release

Rebecca Chamberlain [1] , Hellen Windolf [1] , Bjoern B. Burckhardt [2] , Jörg Breitkreutz [1] and Björn Fischer [1,*]

1   Institute of Pharmaceutics and Biopharmaceutics, Heinrich Heine University, Universitätsstraße 1, 40225 Düsseldorf, Germany; rebecca.chamberlain@hhu.de (R.C.); hellen.windolf@hhu.de (H.W.); joerg.breitkreutz@hhu.de (J.B.)
2   Institute of Clinical Pharmacy and Pharmacotherapy, Heinrich Heine University, Universitätsstraße 1, 40225 Düsseldorf, Germany; bjoern.burckhardt@hhu.de
*   Correspondence: bjoern.fischer@hhu.de; Tel.: +49-211-81-10076

Abstract: Individual dosing of pharmaceutics and personalized medicine have become important with regard to therapeutic safety. Dose adjustments, biorelevant drug release and combination of multiple active substances in one dosage form for the reduction in polymedication are essential aspects that increase the safety and acceptance of the patient's pharmacotherapy. Therefore, not only innovative drug products but also new analytical methods are needed during the drug development phase and for quality control that can simultaneously determine different active ingredients and cover wide concentration ranges. We investigated a liquid-core waveguide UV absorbance flow cell detector coupled to an existing HPLC-UV system. A Teflon AF 2400 capillary tubing of 20 cm length was connected in series to the HPLC flow line and enabled a lower limit of quantification of 1 ng/mL pramipexole (increase in sensitivity by 20 compared to common 0.9 cm flow cells). This allowed the low-concentration of pramipexole and the higher concentrations of levodopa and benserazide occurring during drug release to be determined in a single chromatographic run within 22.5 min.

Keywords: liquid-core waveguide; hot melt extrusion; low-dosed dosage forms; analytics of extruded filaments; fused filament 3D printing; oral dosage form; personalized medicine

1. Introduction

Current therapy guidelines for the treatment of non-communicable diseases (e.g., ESC guideline on hypertension) have recently changed their recommendations based on the latest scientific data towards a dual combination at the initiation of therapy [1]. A rational extension of this approach is to offer such dual or multiple combinations directly in one dosage form to increase patient adherence by reducing the number of drug products to be taken [2]. According to the FDA, a combination product is defined as a dosage form containing two or more drugs in a single pill [3]. Not only is the combination of drugs of interest, but personalized medicine also focuses on individual dosing for each patient in terms of age, weight and comorbidities. The "one-size-fits-all" approach of APIs that have a narrow therapeutic window and therefore risk side effects with small differences in dosage is in the process of being replaced by new approaches, e.g., 3D printing of medicines [4]. With 3D printing it is possible to fabricate complex geometries that incorporate multiple APIs with diverse release kinetics [5–8]. This potentially allows various active ingredients to be combined in a single 3D printed tablet. In previous studies, we found that even if the dose is varied, the release profile remains the same if the surface area to volume ratio is kept constant [9]. In analyzing release kinetics of all incorporated APIs especially during the development phase, analytical methods that can quantify all incorporated APIs simultaneously are useful. To ensure the detection of

a low concentration of a high-potent drug during drug release from its dosage form, a sensitive analytical method must be selected, the dissolution apparatus can be adjusted, or the volume of the medium in the dissolution vessel can be reduced [10–14]. Wang et al. found that dissolution studies conducted in mini vessel led to the same results as in a vessel prescribed by European Pharmacopeia, but the paddle speed had to be increased [15]. Mini paddle apparatus is recommended by Klein et al. to be used for powders, multiparticulate dosage forms and small tablets or capsules [16]. However, it is important that the dissolution study proceeds under sink conditions to avoid influencing the drug release behavior of the corresponding API, which would no longer be the case with high-concentrated APIs in a combination product [17]. The combination of high-performance liquid chromatography UV detection with mass spectrometry (MS) detection and high dynamic range diode array detection (high dynamic range DAD) is capable of covering a wide concentration range [18,19]. For a cost-effective and easy-to-integrate detection system, liquid-core waveguide detection systems are used and described in literature by several research groups. Li et al. have developed a portable setup with extended light path that can be used to detect very low concentrations [20]. A modified detection system compared to the detection system used in this work with a charged-coupled device including optical fibers and a liquid-core waveguide was utilized by Kottke et al. to detect low concentrations of desmopressin during permeation studies. However, they used fluorescence measurements to be able to detect 9.5 ng/mL of desmopressin, a method that was tenfold more sensitive in comparison with reference HPLC detection systems [21]. In this study, drug preparations of three different APIs were analyzed with substantially different dosage ranges. Levodopa (LD), the precursor to the neurotransmitter dopamine, is used in the clinical treatment of Parkinson's disease in a single dose with oral administration of 25–200 mg [22]. The decarboxylase inhibitor benserazide (BZ) is routinely administered orally in combination with levodopa in a ratio of 1:4 (BZ/LD) to prevent peripheral degradation of levodopa [23]. This results in a dosage range between 12.5 and 50 mg for benserazide. The dopamine agonist, pramipexole, is administered at a lower drug amount. Here, only 0.088–3.15° mg is required for pharmacologically efficient drug concentrations after oral administration [24]. The combination of these three APIs should reduce the number of tablets for Parkinson's patients and guarantee individualized dosing. The fluorescence detection cannot be applied as pramipexole does not show fluorescence in aqueous medium, which leads to an exclusion of the detector selection option. Consequently, UV measurement of pramipexole was favored, and the suitability of detection by a liquid-core waveguide ultraviolet absorbance detection system (LCW-UV) was investigated, which is frequently used in literature [25–32]. The extended detection path of the LCW should result in the detection range of UV measurement being extended into the low concentration range (minimum of 1 ng/mL pramipexole) while at the same time also allowing APIs to be detected in the higher concentration range (maximum of 2 μg/mL levodopa) by the UV detector of the HPLC covering a difference in concentration by a factor of 2000.

2. Materials and Methods

2.1. Experimental Procedure of Hot Melt Extrusion Runs

Poly-(ethylene-vinyl acetate)-copolymer (82:18) (EVA; Escorene® FL01418, TER Chemicals, Hamburg, Germany) and polyvinyl alcohol (PVA; Parteck MXP®, Merck, Darmstadt, Germany) were used as polymer matrices. Pramipexole (P, Chr. Olesen, Denmark), levodopa (Zhejiang Wild Wind Pharmaceutical, Dongyang, China) and benserazide (s.p. quimica, s.a., Barcelona, Spain) were used as model drugs. PVA was chosen as a matrix for pramipexole, and EVA was used for the matrix of the fixed combination of levodopa and benserazide within one filament. Poly-(vinylpyrrolidone-vinyl acetate)-copolymer (60:40) (VA; Kollidon VA 64®, BASF, Ludwigshafen, Germany) was incorporated into formulation 2 to act as a pore-forming agent. The composition of the two formulations is listed in Table 1.

Table 1. Composition of filaments.

APIs and Excipients	Concentration in % (*w/w*)	Function
Formulation 1 (PVA-P):		
Pramipexole 2 HCl·H$_2$O (P)	0.5	API
Polyvinyl alcohol (PVA)	99.5	matrix
Formulation 2 (EVA-LD-BZ):		
Levodopa (LD)	40	API
Benserazide HCl (BZ)	10	API
Poly (ethylene-vinyl acetate)-copolymer (82:18) (EVA)	35	matrix
Poly (vinylpyrrolidone-vinyl acetate)-copolymer (60:40) (VA)	15	pore former

All filaments were prepared by hot melt extrusion (HME) with a co-rotating twin-screw extruder with a hot-melt extrusion die (Pharmalab HME 16, Thermo Fisher Scientific, Rockford, IL, USA). A gravimetric feeder (K-SFS-24/6, Coperion K-Tron, Niederlenz, Switzerland) was used for all experiments. A vent port was set between kneading zones 1 and 2 for all extrusions. An in-house manufactured die with a diameter of 1.85 mm was used. The desired filament diameter was achieved using a belt hauled-off unit of a winder (Brabender, Duisburg, Germany) with a belt speed of 0.8 m/min, and the filament was pulled through a roll-system with four 360° air flow ring nozzles (Super Air Wipe, Exair, Cincinnati, OH, USA) for active cooling of the melt. With a laser-based diameter measurement module (Laser 2025 T, Sikora, Bremen, Germany), we continuously measured and logged the filament diameter during the process with a readout rate of 1 Hz to ensure diameter homogeneity [33] of PVA-P and EVA-LD-BZ filaments. The screw speed was set to 20 rpm and powder feed rate was set to 2 g/min. The screw configuration and the temperatures of the heating zones were set according to the physical properties of the polymers for both formulations and are summarized in Table 2.

Table 2. Adjusted temperatures and screw configuration of performed extrusions.

Temperature Profile in Zones 2–10/°C									
Zone	2	3	4	5	6	7	8	9	10
PVA-P formulation	30	100	180	180	180	180	180	195	195
EVA-LD-BZ formulation	30	180	190	200	220	220	220	220	220
Screw Configuration (Die–Gear)									
PVA-P/ EVA-LD-BZ formulation	die–10 CE 1 L/D–KZ 1: 5 × 60°–3 × 30°–5 CE 1 L/D–KZ 2: 4 × 90°–5 × 60°–3 × 30°–16 CE 1 L/D–2 CE 3/2 L/D–1 L/D adapter–gear								

CE = conveying element, KZ = kneading zone.

2.2. Dissolution Testing

According to European Pharmacopoeia monographs 2.9.3 and 5.17.1, release studies were performed with the basket method (method 1) in a dissolution tester (DT 700, Erweka, Langen, Germany) [13,34]. The baskets were 3D printed from water insoluble polylactide acid. They had to be adapted for extruded filaments, since the mesh size of the regular Ph. Eur. baskets is small, and the baskets were clogged by the swollen polymer of the PVA formulation [35]. This affected the hydrodynamic medium flow around the filament. Vessels contained 1000 mL of degassed 0.1 N hydrochloric acid at pH 1.2 at a temperature of 37 ± 0.5 °C, and the baskets were stirred at 50 rpm. Dissolution tests were performed under sink conditions of pramipexole (c$_s$ = 200 mg/mL [36]; maximum concentration 0.1 µg/mL). For the comparison of released pramipexole from PVA matrix by MS vs. LCW-UV detection, 5 mL samples were taken from the dissolution medium after 5, 10, 15, 30, 45, 60, 90 and 120 min by a syringe. One 2.5 mL aliquot was used to fill HPLC vials for UV measurement, and another 2.5 mL was poured into a 96-well plate for mass spectrometric

analysis and mixed with 50 μL of internal standard (Figure 1, left side). No replenishment was conducted, but the amount of removed liquid volume by sampling was calculated for the corresponding subsequent sampling time point. The same dissolution testing setup was used for the simultaneous analysis of the PVA-P filament and EVA-LD-BZ filament, but samples were obtained by an autosampler (Vision® AutoFill™ + AutoPlus™, Teledyne Hanson Research, Chatsworth, CA, USA). The content of P, LD and BZ was analyzed by UV and LCW-UV detection (Figure 1, right side). To avoid oxidation processes of BZ, the whole dissolution tester was wrapped in aluminum foil for light protection, whenever filaments were released containing BZ [37].
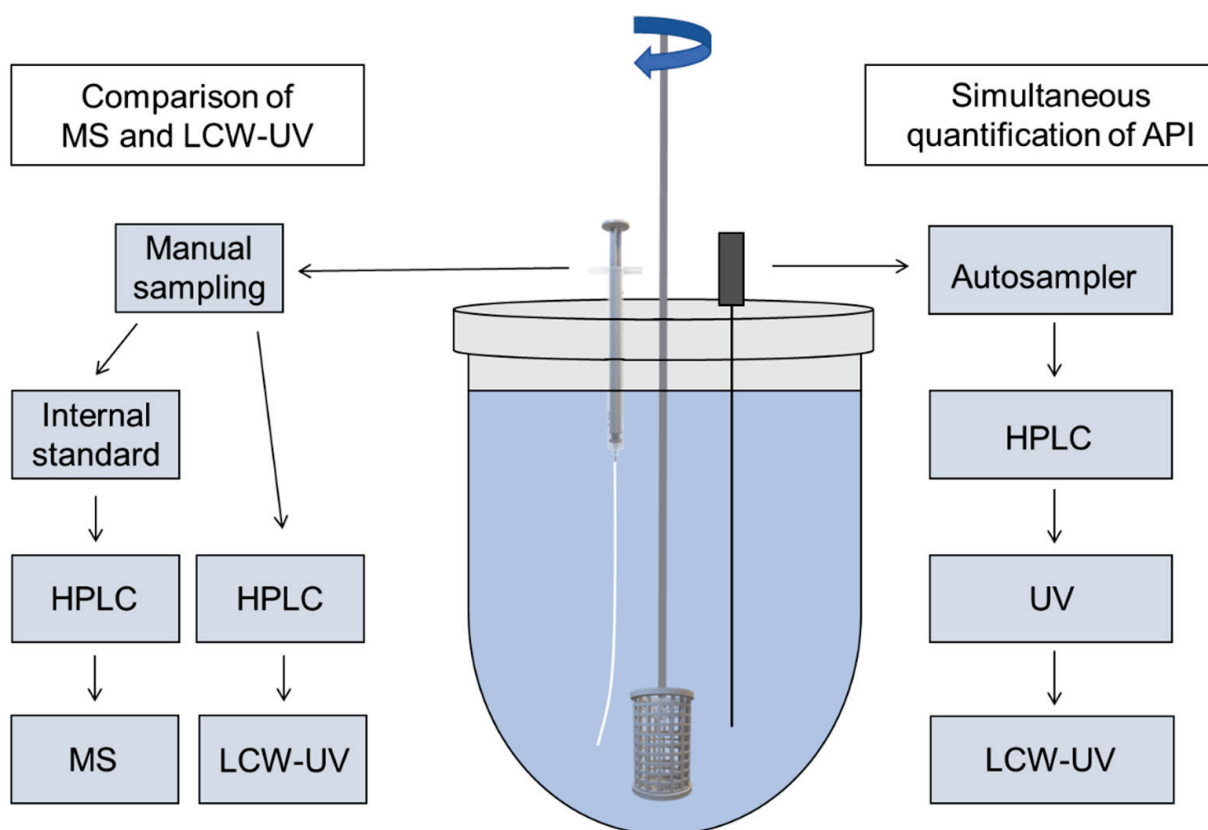
Figure 1. Modified dissolution testing with 3D printed basket based on Ph. Eur. monographs 2.9.3 and 5.17.1 with manual sampling (**left side**) for MS and LCW measurement of single pramipexole filaments and automatic sampling (**right side**) for the simultaneous content determination of three APIs (pramipexole, benserazide and levodopa) during dissolution by HPLC-UV and LCW-UV.

The dissolution tests were also performed under sink conditions of levodopa (c_s = 12 mg/mL [38]; maximum concentration 0.1 mg/mL) and benserazide (c_s = 33.5 mg/mL; maximum concentration 0.025 mg/mL). Samples (1.5 mL) were taken by the autosampler and were filled in HPLC vials every 5 min for the first 30 min, then every 10 min for the next 30 min, followed by sampling at time point 90 and 120 min. After a release time of 120 min, samples were taken every 120 min until 10 h had passed. At every time point, 1.5 mL of 0.1 N hydrochloric acid was returned to the dissolution medium, and the amount of API removed by sampling was calculated for the corresponding subsequent sampling time point.

2.3. LC-MS/MS Quantification of Pramipexole during Dissolution

The mass spectrometric quantification of pramipexole was carried out on an Agilent 1200 Serie HPLC system (Agilent, Ratingen, Germany) coupled to a triple-quadrupole

tandem mass spectrometer API 4000 (SCIEX, Vaughan, ON, Canada) with an electrospray ionization (ESI) interface. Samples were injected by a CTC HTC PAL autosampler (CTC Analytics AG, Zwingen, Switzerland) equipped with a 20 µL sample loop. Chromatographic separation was achieved on a Phenomenex Synergi Hydro RP (150.0 × 2.0 mm; 4 µm) column using isocratic condition with acetonitrile and 10 mM ammonium acetate in water as mobile phase (70/30 (*v/v*)). The compound specific parameters were as follows: declustering potential of 66 V/81 V, entrance potential of 8 V, cell entrance potential of 21 V/19 V and cell exit potential of 30 V/6 V. CAD gas was set to 7 psi, while gas 1 and gas 2 were adjusted to 32 and 45 psi, respectively. Curtain gas was 37 psi. Ion spray voltage was set to 5.5 kV with 600 °C ion source temperature. Time between injections was 2 min with retention times of 0.95 min for pramipexole and 1.1 min for talipexole. The mass-to-charge ratio of 212.2 to 153.1 *m/z* for pramipexole and 304.1 to 260.0 *m/z* for the internal standard talipexole was monitored utilizing multiple reaction monitoring and positive ionization mode. The method was characterized by a linear range from 0.19 to 100 ng/mL ($1/x^2$ weighing). The intra-run accuracy varied from −4.5 to 13.2% (n = 3 per quality control level). The collected data were analyzed using Analyst 1.6.2 (Applied Biosystems/MDS SCIEX, Concord, ON, Canada) with IntelliQuan ® as the integration algorithm without smoothing.

2.4. Chromatographic Conditions for UV and LCW-UV Measurements

For dissolution analysis, dissolution medium of pramipexole filaments was analyzed by UV measurements. The HPLC system (Dionex, Sunnyvale, CA, USA) was equipped with a quaternary pump (P 580 A, Dionex, Sunnyvale, CA, USA) and an autosampler (ASI-100, Dionex, Sunnyvale, CA, USA). For the first HPLC method (method 1) analyzing only pramipexole, a 150 × 4.6 mm column (Eurospher II 100-5 C18A, Knauer, Berlin, Germany) with an integrated precolumn was used. The mobile phase consisted of methanol (mobile phase B) and ammonium acetate buffer (0.05 M, pH 4). The flow rate was set to 1 mL/min, the oven temperature was set to 40 °C and the injection volume was 200 µL. The gradient was as follows: mobile phase B was increased from 5 to 95% (*v/v*) within the first 10 min, held for 5 min at 95% (*v/v*) and decreased to 5% (*v/v*) again until 20 min after the sample injection. The column was equilibrated for 3 min before the next sample was injected. Detection was achieved by measuring the UV absorbance of the sample at 264 nm. This UV detector is described as the reference UV detector (UV). Since the release of 88 µg pramipexole from a drug preparation is described (1% of released drug is 0.88 ng/mL), and thus the calibration curve must be extended, a liquid-core waveguide ultraviolet detection system (LCW-UV) was incorporated into the HPLC flow, which is described in Section 2.5. For the second HPLC method (method 2) encompassing all three APIs, a 250 × 4.6 mm column (Eurospher II 100-5 C18A, Knauer, Berlin, Germany) with an integrated precolumn was utilized (Figure 2). The same mobile phase, flow rate and column temperature were used. The gradient was as follows: Mobile phase B was increased from 1 to 5% (*v/v*), within the first min, held at 5% (*v/v*) for 4 min, increased from 5 to 10% (*v/v*) within 1 min, held at 10% (*v/v*) for 4 min, increased again from 10 to 20% (*v/v*) within 1 min, held for 4 min at 20% (*v/v*), increased again from 20 to 99% (*v/v*) within 5 min, held for 2 min at 99% (*v/v*) and decreased to 1% (*v/v*) within 0.5 min and again until 22.5 min after sample injection. An equilibration time of 3.5 min per run was allowed to pass before the next sample was injected. An injection volume of 200 µL was chosen to analyze the APIs during drug dissolution. Again, the second detector system (Section 2.5) was incorporated into the HPLC flow for the quantification of low pramipexole concentrations. Detection was achieved by measuring the absorbance of the sample at 264 nm using the UV detector (BZ, LD) and the LCW-UV detector (P) (Figure 2).
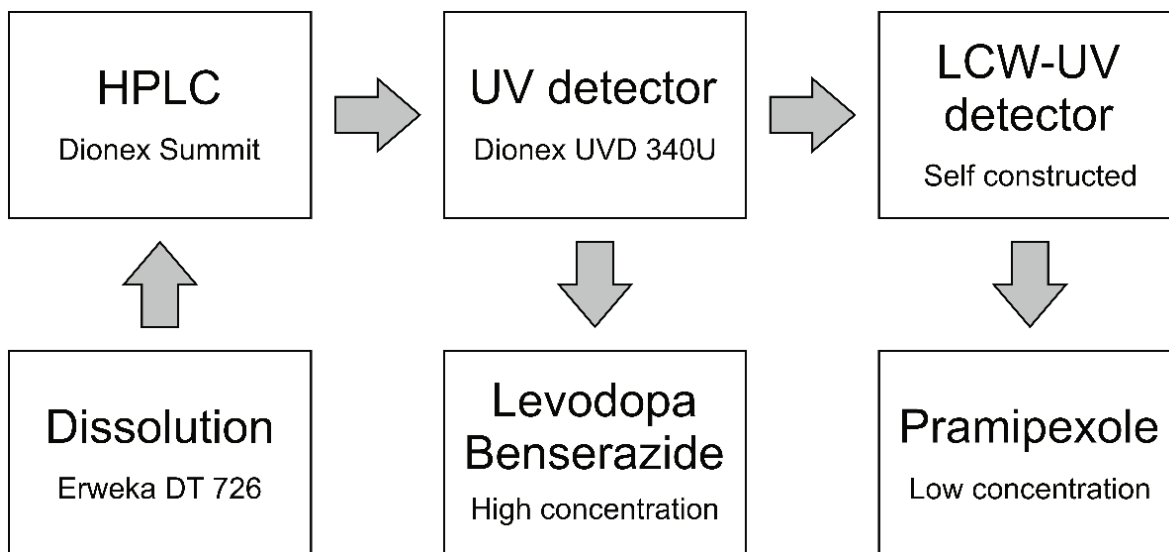
Figure 2. Inline coupling of a UV detector and LCW-UV detector for the simultaneous analysis of pramipexole, levodopa and benserazide.

2.5. Liquid-Core Waveguide Ultraviolet Detection System (LCW-UV)

Figure 3 shows the schematic composition of the LCW-UV detection system. Two stainless steel tees (U-428, 508 μm through hole, IDEX Health & Science, Oak Harbor, WA, USA) were applied to pass the eluent from the HPLC through a 20 cm liquid-core waveguide (LCW, Teflon AF 2400, RI = 1.29, d_{inner} = 200 μm, d_{outer} = 813 μm, Biogeneral, CA, USA). A UV-LED (LED33UV270-6060-100, LG Innotek, Seoul, Korea) was chosen as the light source providing a measured emission maximum at 275 nm. The light was guided into tee 1 at the pigtail end of an optical fiber (d_{inner} = 600 μm, FDP600660710, Laser Components GmbH, Olching, Germany). To avoid breakage of the fiber, the cladding of the fiber was not removed and the front side was optically polished together with the cladding. At the same time, the polymer cladding ensured sufficient tightness of the flow cell. Fluoropolymer sleeves (NanoTight Sleeve Green, d_{inner} = 838 μm, d_{outer} = 1588 μm, IDEX Health & Science, Oak Harbor, WA, USA) were used to match the dimensions between the LCW, the optical fibers and the tees.
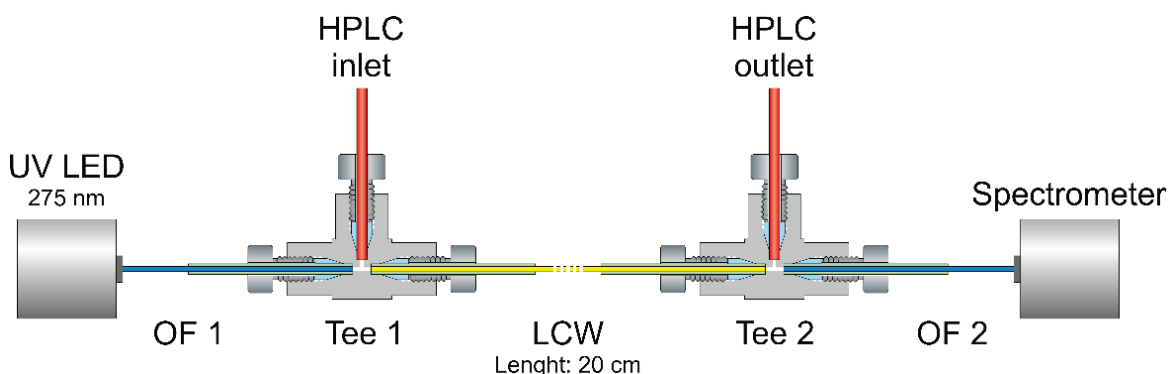
Figure 3. Assembly of the implemented liquid-core waveguide ultraviolet detection system consisting of a UV LED (absorption maximum: 275 nm), two optical fibers (OFs 1 and 2), a 20 cm liquid-core waveguide (LCW), two tee pieces and a charge-coupled device detector.

For detection, the light was collected by a second optical fiber connected to tee 2 and guided into a spectrometer (Kymera 328i B2 equipped with Newport diffraction grating

600 L/mm, blaze 300 nm, Oxford Instruments, Abingdon, UK), assembled with a charge-coupled device detector (CCD, iDus DV420A BU2, Oxford Instruments, Abingdon, UK). For spectra acquisition, the exposure time was set to 0.03 s, and the number of accumulations for each spectrum was set to 16, resulting in an acquisition rate of 2.08 Hz. The readout mode was adjusted to full vertical binning, the vertical pixel shift was 16.25 µs and the readout rate was 100 kHz.

2.6. Mathematical Description

The definition of absorbance is:

$$A = \log\left(\frac{I_0}{I}\right) = \varepsilon \times b \times c \tag{1}$$

A is the absorbance, I_0 is the incident intensity, I transmitted intensity, ε is the molar absorptivity, b is the path length and c is the molar concentration [39]. By increasing the light path b using a liquid-core waveguide, the absorbance A of pramipexole was increased, which was particularly important to be able to detect the low concentrations during dissolution testing.

Thus, in the first step, the LCW-UV setup was compared with an established method (mass spectrometry) for drug release of low-dosed filaments. To evaluate the similarity of the release curves measured by two different analytical methods, the mean dissolution time (MDT) and the similarity factor (f_2-value) were calculated [40,41].

$$\text{MDT} = \frac{ABC}{c_\infty} = \frac{\sum_{i=0}^{\infty}\left[(c_{i+1} - c_i) \times \frac{t_i + t_{i+1}}{2}\right]}{c_\infty} \tag{2}$$

ABC stands for the area between the curves and is calculated via the trapezoidal equation with c as the concentration of the API released over time t and c_∞ as the initial drug load of the filament.

$$f_2 = 50 \times \log\left\{\left[1 + \frac{1}{n}\sum_{t=1}^{n}(R_t - T_t)^2\right] \times 100\right\} \tag{3}$$

In this equation, R_t and T_t stand for the mean released amounts of the API in % at time point t of the reference (MS result) and the test method (LCW-UV result) and n for the number of time points. A f_2-value around 100 is desired, which indicates that the curves are identical. A value of 50 or more is accepted, which indicates that the values differ by a maximum of 10%. Values below 50 indicate that the curves can no longer be considered similar [34].

3. Results and Discussion

3.1. Spectroscopic Evaluation of LCW-UV Measurements

A small range of the rising slope of the UV LED was used for the absorbance measurement. The grating of the spectrometer was adjusted so that the CCD detector was in saturation from 268.5 nm upwards. The evaluation was performed between 262 and 268 nm. With these settings, the lowest LLOQ could be achieved. The raw spectrum of the blank (pure mobile phase) is displayed in Figure 4, where the detector depicts the highest signal, since the eluent shows hardly any absorbance at the evaluated wavelength range. As the concentration of pramipexole increases, the signal intensity decreases because the API is absorbing light originating from the UV-LED. The corresponding signals in the peak maximum of a concentration series of 5–100 ng are also shown Figure 4. To obtain a chromatogram from raw data of the measured intensity, spectra were integrated between 262 and 268 nm and evaluated with respect to the measurement time. The obtained peaks of pramipexole can be identified in the chromatogram obtained by LCW-UV measurement after 8.9 (method 1) and 19.3 min (method 2). These settings were consequently used for

spectroscopic evaluation of LCW-UV detection systems for calibration curves and for the quantification of pramipexole during drug release.
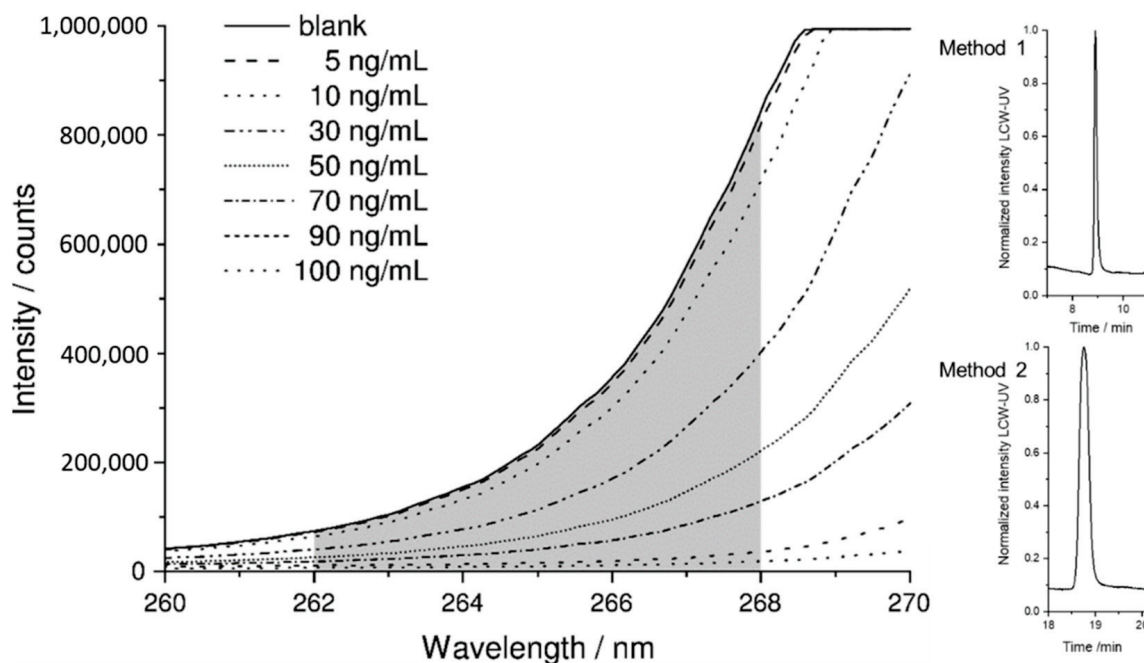
Figure 4. Measured intensity of a blank sample and of the peaks of various concentrations of pramipexole (5–100 ng/mL) with highlighted integration range between 262 and 268 nm (grey). Resulting pramipexole peaks (100 ng/mL) after integration for methods 1 and 2.

3.2. MS and LCW-UV Measurement in Comparison

For mass spectrometric measurements of pramipexole, an internal standard with a known concentration was used, which served to give a ratio of the signal intensity. Thus, the ratio of the areas of pramipexole and talipexole (area ratio P/T) was used for the calibration curve obtained by MS measurements. A linear range from 0.19 to 100 ng/mL (Figure 5B) was found; however, concentrations below 1 ng/mL were not relevant for the release study, since a higher concentration of pramipexole is already reached in the vessel after the first sample draw after 5 min. UV detection was able to quantify a concentration of 0.05 µg/mL (lower limit of quantification (LLOQ): 50 ng/mL with an S/N = 11) pramipexole, which for samples containing 88 µg pramipexole in 1000 mL release volume means that the release curve could only be described after a drug release of more than 56% (method 1). Thus, by using the LCW-UV detection system, the linear range of the UV investigation was extended, and a concentration of 2.5 ng/mL could be quantified (LLOQ: 2.5 ng/mL with S/N = 10). Applying the LCW-UV measurement, the detection limit was improved by a factor of 20, resulting in the ability to describe the drug release curve of low-dosed pramipexole preparations after a drug release of 2.5 ng/mL (2.8% API release). This enhancement of the detection limit only results from the extended light path evoked from the LCW, which is described by the Beer–Lambert law Equation (1). However, the measurements showed that the LCW has an upper limit of quantification at 100 ng/mL. Therefore, concentrations of pramipexole during drug release between 2.5 and 100 ng/mL (Figure 5A) can be determined by LCW-UV measurements, and concentrations above 100 ng/mL would need to be quantified by UV measurements. Since both methods have an overlapping linear range between 50 and 100 ng/mL, the evaluation of these concentrations of pramipexole could be depicted by both detection methods. After the calibration curve ranges of both methods were established, a drug release study was performed as described in Section 2.2. The dissolution profile of 0.5% (*w/w*) pramipexole filaments, which were

manufactured by HME (Section 2.1) and were collected in equilibrium condition for drug content [42], resulting from dissolution testing in 1000 mL of 0.1 N HCl, are shown in Figure 6.
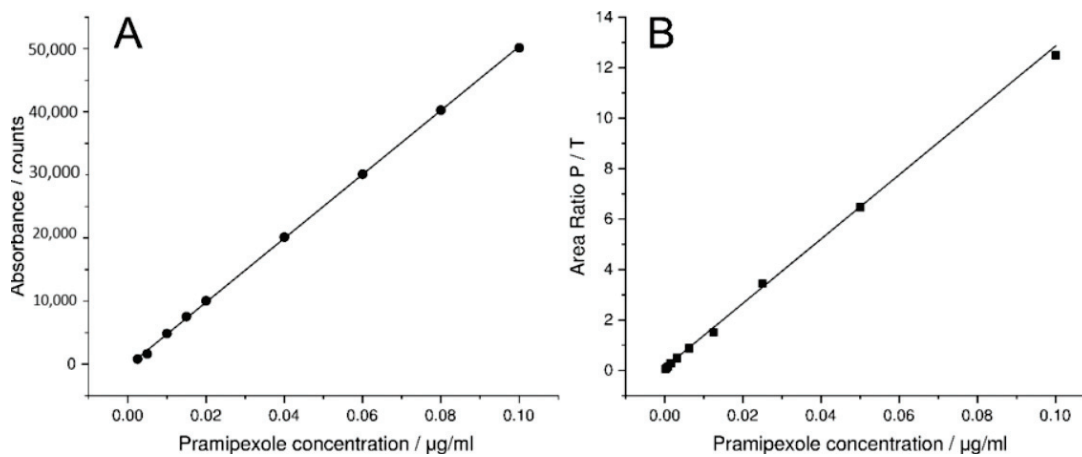
Figure 5. Calibration curve of LCW-UV detection system (**A**) of pramipexole (2.5–100 ng/mL) and calibration curve of MS analysis (**B**), where the ratio of the areas of pramipexole and talipexole (area ratio P/T) were plotted against the concentration of pramipexole (0.19–100 ng/mL).
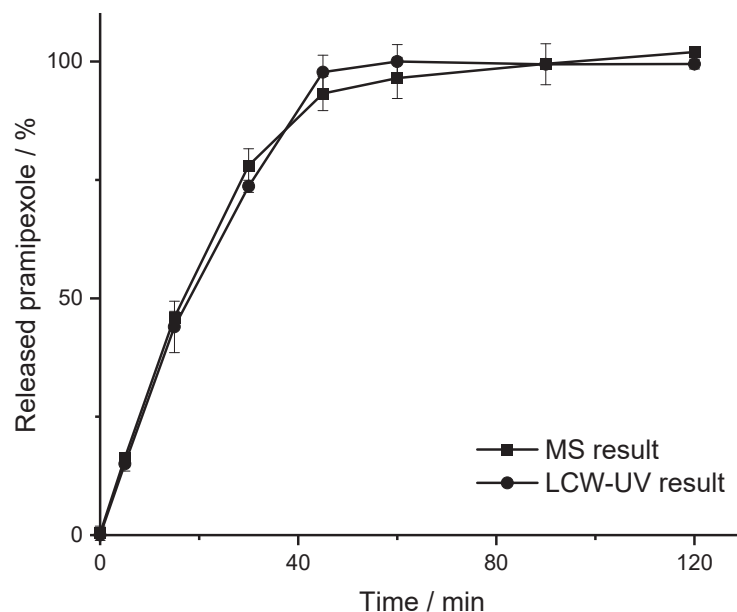
Figure 6. Release curve of 0.5% (*w/w*) pramipexole filaments ($\overline{m}$ = 17.61 mg) determined by MS and LCW-UV measurement (n = 3, $\overline{x} \pm$ SD).

The curves indicated that the results for MS and the LCW-UV result in a comparable dissolution profile. For MS results, the MDT is 20.38 min, and the MDT of the dissolution curve obtained by LCW-UV results is 19.73 min (Equation (2)). This results in a minimal discrepancy of the MDT in 33 s, which appears negligible. Since the calculated f_2-value corresponds to 92, it was assumed that the analysis with LCW-UV would show similar results to the investigation with an established method for low concentrations of pramipexole during release. With these results, it was shown that the drug release of pramipexole from the PVA matrix can be appropriately described by the LCW-UV. In the next step, a method was developed that can detect both the low pramipexole concentrations and

the higher concentrated APIs during drug release that would all be incorporated in a polymedication in an ongoing study. Following the approach of Wollmer and Klein, who quantified levodopa and benserazide with two other API, a new chromatographic method was developed [43].

3.3. Simultaneous Quantification of Levodopa, Benserazide and Pramipexole in Dissolution Testing

For the quantitative evaluation of the amounts of LD, BZ and P in dissolution studies, a new HPLC method was developed that enabled separation and quantification of all three APIs (method 2, described in Section 2.4). Levodopa eluted first at a retention time (R_t) of 7.1 min with a peak width of 0.5 min, followed by benserazide (R_t: 10.9 min) with a peak with of 1.5 min and pramipexole (R_t: 19.3 min) with a peak width of 0.4 min (Figure 7A).
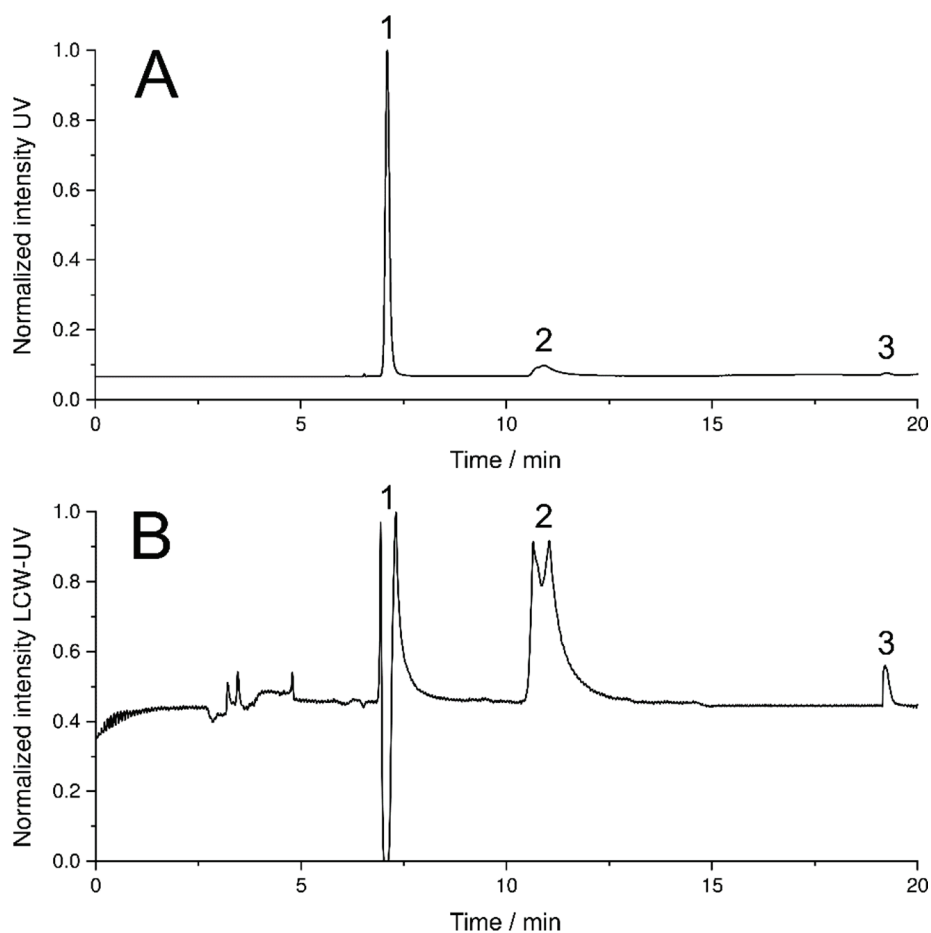
Figure 7. HPLC chromatogram using UV detection (**A**) and LCW-UV detection (**B**) of released levodopa (1), benserazide (2) and pramipexole (3) during dissolution study.

The extended flow line of the LCW-UV did not result in an additional measurable dead time (Figure 7B), but the peak widths increased greatly due to the long light path, particularly for levodopa and benserazide, which emphasizes the importance of the separation of both substances from pramipexole by more than 5 min. In the chromatogram of the HPLC run obtained by UV detection, the peak of levodopa shows a narrow peak width. In the chromatogram resulting from LCW-UV measurements, the elution of levodopa is shown as a peak splitting signal. The peak shown negatively in the chromatogram indicates that for a short time more light is detected, but this is caused by saturation of the signal between 262 and 268 nm. Quantitative evaluation of levodopa is not possible using the LCW-UV method but is performed using the UV detector integrated with the HPLC. For the quantita-

tive evaluation of benserazide, the UV detector is more suitable than the new implemented detector. The calculation of the LLOQ of pramipexole is involved the measurements of the UV and LCW-UV detector. By calculating the S/N, the LLOQ (S/N = 10) resulted in a concentration of 20 ng/mL (UV) and 1 ng/mL (LCW-UV). Compared to the first HPLC method, the LLOQ was subsequently lower for both LCW-UV and UV detection due to the focusing of pramipexole by the stepwise gradient of the second HPLC method. Again, an improvement of the quantification limit of the LCW-UV detection compared to UV detection after applying HPLC method 2 was achieved by a factor of 20. Calibration curves were also successfully established for LD (0.01–0.12 mg/mL) and BZ (0.005–0.03 mg/mL) by UV measurements. Figure 8 shows the resulting linear ranges of the three APIs.
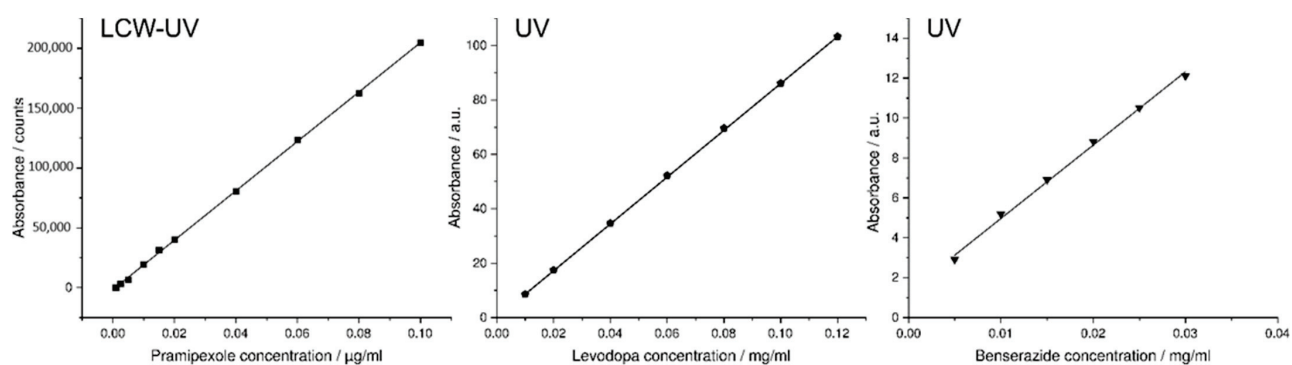
Figure 8. Calibration curve of pramipexole measured with the help of the LCW-UV detection system (1–100 ng/mL); calibration curves of benserazide (5–30 μg/mL), and levodopa (10–1200 μg/mL) both examined by UV detection.

After the identification of the calibration curves, a second drug release study was performed as described in Section 2.2. Attempts were again made to represent the real dose for pharmacotherapy of the respect API, so the filament amount was taken to examine 88 μg of pramipexole, 25 mg of benserazide and 100 mg of levodopa. Since the filament length of the EVA-LD-BZ filament exceeded the size of the basket, the filament was cut into four shorter pieces. Thus, five filaments (one PVA-P filament stick, four EVA-LD-BZ filament sticks) were placed in the baskets. The dissolution profile of 0.5% (*w/w*) pramipexole filaments and filaments containing 40% (*w/w*) levodopa and 10% (*w/w*) benserazide are shown in Figure 9. Both the drug release of pramipexole and benserazide can be described according to first order kinetics. Within 80 min, 100% of the pramipexole was released from the PVA matrix and could be categorized as unmodified drug release. For benserazide, 100% of the drug was released from the insoluble EVA matrix after 180 min. For the third API, levodopa, the drug release from the EVA matrix can be described by Higuchi (square root) kinetics since the diffusion distance to be passed by the API through the matrix does not remain constant but increases steadily. The authors assume that levodopa and benserazide are not homogeneously distributed in the matrix consisting of VA and EVA, leading to the different drug release behaviors of LD and BZ. It is further speculated that the pore former VA might be the reason that the affinity of the distribution differs for the two API. This assumption would lead to the conclusion, that benserazide would have a higher affinity for VA than for EVA. In addition, the slightly better water solubility of BZ may also lead to the faster release. Further dissolution studies and formulation development will be performed as part of an ongoing study to obtain the required release kinetics. However, this study showed that all three APIs can be detected during drug release.
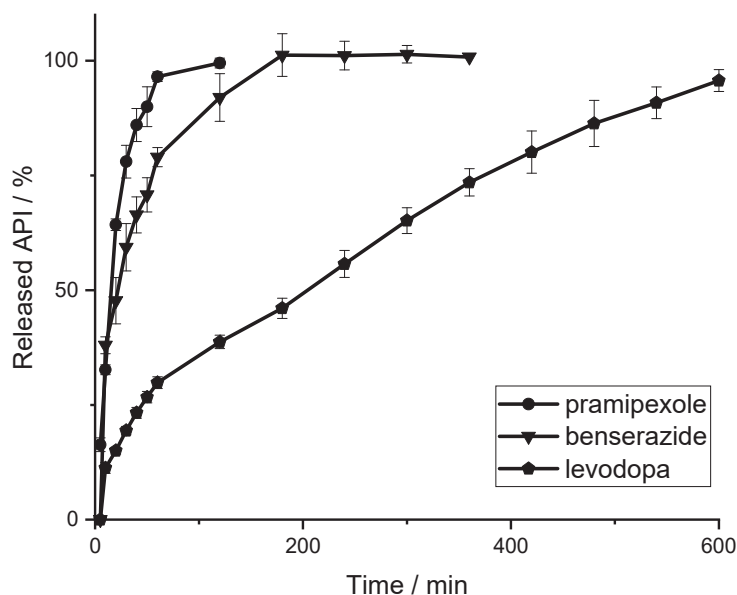
Figure 9. Release curve of 0.5% (*w/w*) pramipexole filaments ($\overline{m}$ = 17.51 mg) and levodopa/ benserazide (40/10% *(w/w))* filaments ($\overline{m}$ = 250.7 mg) determined with LCW-UV (P) and UV (LD, BZ) measurement (*n* = 6, $\overline{x}$ ± SD).

4. Conclusions

In this study, an LCW was applied as a flow cell to increase the light path using total internal reflection. For pramipexole, the LLOQ was improved by a factor of 20 with LCW-UV detection compared to conventional UV detection. With the help of this method, concentrations of 1–100 ng/mL, which occur during drug release of low-dosed pramipexole preparations, were detected simultaneously with two other released higher-dose APIs by UV detection. The calculated f_2-value for comparison of LCW-UV vs. LC-MS/MS was >90, indicating that similar results for both technologies were obtained. The MDT was comparable for both methods (20 ± 0.4 min). The new method offers a promising alternative to expensive and time-consuming analytical technologies and can be easily integrated into existing HPLC systems. Especially during the development phase of individualized drug preparations and drug products of levodopa, benserazide and pramipexole, this analytical method can provide fast results after dissolution studies. The integration of the LCW-UV detection system can be used for various formulated API–polymer combinations and also drug products, e.g., 3D printed tablets, where the API dosing differs substantially regarding therapeutic regimens.

Conflicts of Interest: The authors declare no conflict of interest. Merck KGaA and TER Chemicals had no role in the design of the study; in the collection, analyses or interpretation of data; in the writing of the manuscript or in the decision to publish the results.

Abbreviations

API	active pharmaceutical ingredient
BZ	benserazide
EVA	poly (ethylene-vinyl acetate)-copolymer
DAD	diode array detection
HME	hot melt extrusion
HPLC	high-performance liquid chromatography
LCW	liquid-core waveguide
LD	levodopa
LLOQ	lower limit of quantification
MDT	mean dissolution time
MS	mass spectrometry
P	pramipexole
PVA	polyvinyl alcohol
SD	standard deviation
S/N	signal-to-noise ratio
UV	ultraviolet
VA	poly (vinylpyrrolidone-vinyl acetate)-copolymer

References

1. Williams, B.; Mancia, G.; Spiering, W.; Agabiti Rosei, E.; Azizi, M.; Burnier, M.; Clement, D.L.; Coca, A.; de Simone, G.; Dominiczak, A.; et al. 2018 ESC/ESH Guidelines for the management of arterial hypertension. *Eur. Heart J.* **2018**, *39*, 3021–3104. [CrossRef]
2. Guglietta, A.; Guerrero, M. Issues to consider in the pharmaceutical development of a cardiovascular polypill. *Nat. Clin. Pract. Cardiovasc. Med.* **2009**, *6*, 112–119. [CrossRef] [PubMed]
3. Combination Products. Available online: https://www.fda.gov/combination-products/about-combination-products (accessed on 7 February 2022).
4. Vaz, V.M.; Kumar, L. 3D Printing as a Promising Tool in Personalized Medicine. *AAPS PharmSciTech* **2021**, *22*, 49. [CrossRef] [PubMed]
5. Goyanes, A.; Robles Martinez, P.; Buanz, A.; Basit, A.W.; Gaisford, S. Effect of geometry on drug release from 3D printed tablets. *Int. J. Pharm.* **2015**, *494*, 657–663. [CrossRef] [PubMed]
6. Khaled, S.A.; Burley, J.C.; Alexander, M.R.; Roberts, C.J. Desktop 3D printing of controlled release pharmaceutical bilayer tablets. *Int. J. Pharm.* **2014**, *461*, 105–111. [CrossRef]
7. Khaled, S.A.; Burley, J.C.; Alexander, M.R.; Yang, J.; Roberts, C.J. 3D printing of tablets containing multiple drugs with defined release profiles. *Int. J. Pharm.* **2015**, *494*, 643–650. [CrossRef]
8. Melocchi, A.; Uboldi, M.; Maroni, A.; Foppoli, A.; Palugan, L.; Zema, L.; Gazzaniga, A. 3D printing by fused deposition modeling of single-and multi-compartment hollow systems for oral delivery—A review. *Int. J. Pharm.* **2020**, *579*, 119155. [CrossRef]
9. Windolf, H.; Chamberlain, R.; Quodbach, J. Dose-independent Drug Release from 3D Printed Oral Medicines for Patient-specific Dosing to Improve Therapy Safety. *Int. J. Pharm.* **2022**, *616*, 121555. [CrossRef]
10. Scheubel, E.; Lindenberg, M.; Beyssac, E.; Cardot, J.M. Small volume dissolution testing as a powerful method during pharmaceutical development. *Pharmaceutics* **2010**, *2*, 351–363. [CrossRef]
11. Timed-Release Tablets and Capsules—In Vitro Test Procedure. In *National Formulary XIV*; The United States Pharmacopeial Convention, Inc.: Rockville, MD, USA, 1975.
12. Dissolution Methods for Drug Products Database, U.S. Department of Health and Human Services, Food and Drug Administration, Center for Drug Evaluation and Research (CDER). 2008. Available online: https://www.accessdata.fda.gov/scripts/cder/dissolution/dsp_SearchResults_Dissolutions.cfm?PrintAll=1 (accessed on 7 February 2022).
13. European Pharmacopoeia Commission 5.17.1. Recommendations on Dissolution Testing. In *European Pharmacopoeia*; EDQM: Strasbourg, France, 2020; Volume 10.2, pp. 801–807.
14. Pedersen, B.L.; Brøndsted, H.; Lennernäs, H.; Christensen, F.N.; Müllertz, A.; Kristensen, H.G. Dissolution of hydrocortisone in human and simulated intestinal fluids. *Pharm. Res.* **2000**, *17*, 183–189. [CrossRef]

15. Wang, B.; Armenante, P.M. Experimental and computational determination of the hydrodynamics of mini vessel dissolution testing systems. *Int. J. Pharm.* **2016**, *510*, 336–349. [CrossRef] [PubMed]

16. Klein, S. The Mini Paddle Apparatus—A Useful Tool in the Early Development Stage? Experiences with Immediate-Release Dosage Forms. *Dissolution Technol.* **2006**, *13*, 6–11. [CrossRef]

17. Gibaldi, M.; Feldman, S. Establishment of sink conditions in dissolution rate determinations. Theoretical considerations and application to nondisintegrating dosage forms. *J. Pharm. Sci.* **1967**, *56*, 1238–1242. [CrossRef] [PubMed]

18. Abdel-Hamid, M.E. Comparative LC–MS and HPLC analyses of selected antiepileptics and beta-blocking drugs. *Il Farm.* **2000**, *55*, 136–145. [CrossRef]

19. Neilson, A.P.; Green, R.J.; Wood, K.V.; Ferruzzi, M.G. High-throughput analysis of catechins and theaflavins by high performance liquid chromatography with diode array detection. *J. Chromatogr.* **2006**, *1132*, 132–140. [CrossRef]

20. Li, Q.; Morris, K.J.; Dasgupta, P.K.; Raimundo, I.M., Jr.; Temkin, H. Portable flow-injection analyzer with liquid-core waveguide based fluorescence, luminescence, and long path length absorbance detector. *Anal. Chim. Acta* **2003**, *479*, 151–165. [CrossRef]

21. Kottke, D.; Burckhardt, B.B.; Breitkreutz, J.; Fischer, B. Application and validation of a coaxial liquid core waveguide fluorescence detector for the permeation analysis of desmopressin acetate. *Talanta* **2021**, *226*, 122145. [CrossRef]

22. LeWitt, P.A. Levodopa therapy for Parkinson's disease: Pharmacokinetics and pharmacodynamics. *Mov. Disord.* **2015**, *30*, 64–72. [CrossRef]

23. Rinne, U.K.; Mölsä, P. Levodopa with benserazide or carbidopa in Parkinson disease. *Neurology* **1979**, *29*, 1584–1589. [CrossRef]

24. Bennett, J.P., Jr.; Piercey, M.F. Pramipexole—A new dopamine agonist for the treatment of Parkinson's disease. *J. Neurol. Sci.* **1999**, *163*, 25–31. [CrossRef]

25. Dasgupta, P.K.; Shelor, C.P.; Kadjo, A.F.; Kraiczek, K.G. Flow-Cell-Induced Dispersion in Flow-through Absorbance Detection Systems: True Column Effluent Peak Variance. *Anal. Chem.* **2018**, *90*, 2063–2069. [CrossRef] [PubMed]

26. Le, T.; Tao, S. Intrinsic UV absorption spectrometry observed with a liquid core waveguide as a sensor technique for monitoring ozone in water. *Analyst* **2011**, *136*, 3335–3342. [CrossRef]

27. Pan, J.-Z.; Yao, B.; Fang, Q. Hand-held Photometer Based on Liquid-Core Waveguide Absorption Detection for Nanoliter-scale Samples. *Anal. Chem.* **2010**, *82*, 3394–3398. [CrossRef] [PubMed]

28. Robles, T.; Paige, D.; Anastasio, C. Lens-coupled liquid core waveguide for ultraviolet-visible absorption spectroscopy. *Rev. Sci. Instrum.* **2006**, *77*, 073103. [CrossRef]

29. Li, J.; Dasgupta, P.K. Selective Measurement of Gaseous Hydrogen Peroxide with Light Emitting Diode-Based Liquid-Core Waveguide Absorbance Detector. *Anal. Sci.* **2003**, *19*, 517–523. [CrossRef]

30. Byrne, R.H.; Kaltenbacher, E. Use of liquid core waveguides for long pathlength absorbance spectroscopy: Principles and practice. *Limnol. Oceanogr.* **2001**, *46*, 740–742. [CrossRef]

31. D'Sa, E.J.; Steward, R.G.; Vodacek, A.; Blough, N.V.; Phinney, D. Determining optical absorption of colored dissolved organic matter in seawater with a liquid capillary waveguide. *Limnol. Oceanogr.* **1999**, *44*, 1142–1148. [CrossRef]

32. Fujiwara, K.; Ito, S. Application of waveguiding in solutions for absorption and fluorescence spectrometry. *Trends Anal. Chem.* **1991**, *10*, 184–190. [CrossRef]

33. Quodbach, J.; Bogdahn, M.; Breitkreutz, J.; Chamberlain, R.; Eggenreich, K.; Elia, A.G.; Gottschalk, N.; Gunkel-Grabole, G.; Hoffmann, L.; Kapote, D.; et al. Quality of FDM 3D Printed Medicines for Pediatrics: Considerations for Formulation Development, Filament Extrusion, Printing Process and Printer Design. *Ther. Innov. Regul. Sci.* **2021**, 1–19. [CrossRef]

34. European Pharmacopoeia Commission 2.9.3. Dissolution Test for Solid Dosage Forms. In *European Pharmacopoeia*; EDQM: Strasbourg, France, 2020; Volume 10.2, pp. 326–333.

35. Windolf, H.; Chamberlain, R.; Quodbach, J. Predicting Drug Release from 3D Printed Oral Medicines Based on the Surface Area to Volume Ratio of Tablet Geometry. *Pharmaceutics* **2021**, *13*, 1453. [CrossRef]

36. Tzankov, B.; Voycheva, C.; Yordanov, Y.; Aluani, D.; Spassova, I.; Kovacheva, D. Development and In Vitro safety evaluation of pramipexole-loaded Hollow Mesoporous Silica (HMS) particles. *Biotechnol. Equip.* **2019**, *33*, 1204–1215. [CrossRef]

37. Dinç, E.; Kaya, S.; Doganay, T.; Baleanu, D. Continuous wavelet and derivative transforms for the simultaneous quantitative analysis and dissolution test of levodopa–benserazide tablets. *J. Pharm. Biomed. Anal.* **2007**, *44*, 991–995. [CrossRef] [PubMed]

38. Krisai, K.; Charnvanich, D.; Chongcharoen, W. Increasing the solubility of levodopa and carbidopa using ionization approach. *Thai. J. Pharm. Sci.* **2020**, *44*, 251–255.

39. Wang, W.; He, Q.; Wang, T.; Fen, M.; Liao, Y.; Ran, G. Absorbance study of liquid-core optical fibers in spectrophotometry. *Anal. Chem.* **1992**, *64*, 22–25. [CrossRef]

40. Costa, P.; Lobo, J.M.S. Modeling and comparison of dissolution profiles. *Eur. J. Pharm. Sci.* **2001**, *13*, 123–133. [CrossRef]

41. U.S. Food and Drug Administration (FDA). *FDA Guidance for Industry—Dissolution Testing of Immediate Release Solid Oral Dosage Forms*; FDA Center for Drug Evaluation and Research: Silver Spring, MD, USA, 1997; Volume 1, pp. 1–17.

42. Chamberlain, R.; Windolf, H.; Geissler, S.; Quodbach, J.; Breitkreutz, J. Precise Dosing of Pramipexole for Low-Dosed Filament Production by Hot Melt Extrusion Applying Various Feeding Methods. *Pharmaceutics* **2022**, *14*, 216. [CrossRef]

43. Wollmer, E.; Klein, S. Development and validation of a robust and efficient HPLC method for the simultaneous quantification of levodopa, carbidopa, benserazide and entacapone in complex matrices. *Int. J. Pharm. Sci.* **2017**, *20*, 258–269. [CrossRef]

D.3 3D Printed Mini-Floating-Polypill for Parkinson's Disease: Combination of Levodopa, Benserazide, and Pramipexole in Various Dosing for Personalized Therapy

Hellen Windolf, Rebecca Chamberlain, Jörg Breitkreutz, Julian Quodbach

Pretext

Through the previous studies, the release profile could be changed by means of the SA/V ratio, but also a dose-independent release could be achieved by keeping the SA/V ratio constant despite variable volumes and thus a changed dose.

Since the realization of polypills by means of 3D printing is one of the major advantages of this process, the dose-independent release was transferred to just these. Since the therapy of Parkinson's disease (PD) consists of a combination of different active ingredients, some of them with very potent APIs, levodopa, benserazide and pramipexole were chosen as APIs for the polypill. The therapy of PD belongs to these, which must be individually tailored to the patient and are thus predisposed for personalized therapy. Vacuum compression molding (VCM) technology was used to develop the formulation. Due to the absorption of levodopa in the upper GIT, a low-density polymer was chosen to generate a floating dosage form that releases the APIs levodopa (LD) and benserazide (BZ) consistently over time. PDM, on the other hand, should be released immediately to act directly. Thus, this API was processed separately with another polymer and only combined with the other APIs in one geometry during 3D printing. By changing the geometry, various release profiles could be obtained, but also unchanged profiles, despite variable dosing (dose-independent release). Due to the swallowing difficulties that often occur in Parkinson's patients, a mini-polypill was also developed that can be variably combined with PDM.

Evaluation of authorship:

author	idea [%]	study design [%]	experimental [%]	evaluation [%]	manuscript [%]
Hellen Windolf	60	60	60	50	50
Rebecca Chamberlain	30	40	40	35	35
Jörg Breitkreutz	10	-	-	5	5
Julian Quodbach	-	-	-	10	10

Evaluation of Copyright permission:

The research paper was published under a Creative Commons license (Open Access) and is free to share and adapt (MDPI | Open Access Information; accessed on 09.10.2022).

3D Printed Mini-Floating-Polypill for Parkinson's Disease: Combination of Levodopa, Benserazide, and Pramipexole in Various Dosing for Personalized Therapy

Hellen Windolf, Rebecca Chamberlain, Jörg Breitkreutz, Julian Quodbach

Abstract

Therapy for Parkinson's disease is quite challenging. Numerous drugs are available for symptomatic treatment, and levodopa (LD), in combination with a dopa decarboxylase inhibitor (e.g., benserazide (BZ)), has been the drug of choice for years. As the disease progresses, therapy must be supplemented with a dopamine agonist (e.g., pramipexole (PDM)). Side effects increase, as do the required dose and dosing intervals. For these specific requirements of drug therapy, the 3D printing method fused deposition modeling (FDM) was applied in this study for personalized therapy. Hot melt extrusion was utilized to produce two different compositions into filaments: PDM and polyvinyl alcohol for rapid drug release and a fixed combination of LD/BZ (4:1) in an ethylene-vinyl acetate copolymer matrix for prolonged drug release. Since LD is absorbed in the upper gastrointestinal tract, a formulation that floats in gastric fluid was desired to prolong API absorption. Using the FDM 3D printing process, different polypill geometries were printed from both filaments, with variable dosages. Dosage forms with 15–180 mg LD could be printed, showing similar release rates ($f_2 > 50$). In addition, a mini drug delivery dosage form was printed that released 75% LD/BZ within 750 min and could be used as a gastric retentive drug delivery system due to the floating properties of the composition. The floating mini-polypill was designed to accommodate patients' swallowing difficulties and to allow for individualized dosing with an API release over a longer period of time.

Article

3D Printed Mini-Floating-Polypill for Parkinson's Disease: Combination of Levodopa, Benserazide, and Pramipexole in Various Dosing for Personalized Therapy

Hellen Windolf [1], Rebecca Chamberlain [1], Jörg Breitkreutz [1] and Julian Quodbach [1,2,*]

1   Institute of Pharmaceutics and Biopharmaceutics, Heinrich Heine University, Universitätsstr. 1, 40225 Düsseldorf, Germany; hellen.windolf@hhu.de (H.W.); rebecca.chamberlain@hhu.de (R.C.); joerg.breitkreutz@hhu.de (J.B.)
2   Department of Pharmaceutics, Utrecht Institute for Pharmaceutical Sciences, Utrecht University, Universiteitsweg 99, 3584 CG Utrecht, The Netherlands
*   Correspondence: j.h.j.quodbach@uu.nl

Abstract: Therapy for Parkinson's disease is quite challenging. Numerous drugs are available for symptomatic treatment, and levodopa (LD), in combination with a dopa decarboxylase inhibitor (e.g., benserazide (BZ)), has been the drug of choice for years. As the disease progresses, therapy must be supplemented with a dopamine agonist (e.g., pramipexole (PDM)). Side effects increase, as do the required dose and dosing intervals. For these specific requirements of drug therapy, the 3D printing method fused deposition modelling (FDM) was applied in this study for personalized therapy. Hot melt extrusion was utilized to produce two different compositions into filaments: PDM and polyvinyl alcohol for rapid drug release and a fixed combination of LD/BZ (4:1) in an ethylene-vinyl acetate copolymer matrix for prolonged drug release. Since LD is absorbed in the upper gastrointestinal tract, a formulation that floats in gastric fluid was desired to prolong API absorption. Using the FDM 3D printing process, different polypill geometries were printed from both filaments, with variable dosages. Dosage forms with 15–180 mg LD could be printed, showing similar release rates ($f_2 > 50$). In addition, a mini drug delivery dosage form was printed that released 75% LD/BZ within 750 min and could be used as a gastric retentive drug delivery system due to the floating properties of the composition. The floating mini-polypill was designed to accommodate patients' swallowing difficulties and to allow for individualized dosing with an API release over a longer period of time.

Keywords: FDM 3D printing; polypill; Morbus Parkinson; personalized medicine; additive manufacturing; gastro retentive drug delivery

1. Introduction

Worldwide, about 9% of the world's population is older than 65 years. Over the next few decades, the UN expects the proportion of older people to continue to rise significantly, so that by 2100 almost 23% of the population will be at least 65. In the EU, the aging process is already more advanced; in 2020, more than 20% of the EU population was 65 years and older [1–3]. Due to the increase in susceptibility to disease with age, approximately 50% of Rx-medications are prescribed to patients older than 65 years [4–8]. The average geriatric patient (≥65 years) takes 8.5 tablets per day at different times [3]. This can lead to complications between the different drugs with potential interactions, but also to a decrease in medication adherence, as certain dosing times and intervals are not adhered to or administration is forgotten [9,10]. To promote patient adherence, community pharmacies frequently offer to blister tablets in pouches or place them in medication boxes for daily use [7]. Also, pharmaceutical manufacturers are trying to produce tablets that contain multiple active pharmaceutical ingredients (APIs) in fixed dosages that are often prescribed together [11,12]. For example, several APIs are prescribed for high blood pressure or

cardiovascular diseases, and these are now in just one tablet for ingestion (e.g., Vocado®
HCT, Berlin-Chemie AG, with olmesartan, amlodipine and hydrochlorothiazide). Another
disease that requires the administration of multiple tablets is Parkinson's disease. So far,
the disease can only be treated symptomatically and must be tailored very precisely to the
patient, since here effect and side effect go hand in hand, as both too low and too high
dopamine levels can lead to symptoms [13–15]. Parkinson's disease is the second most
common neurodegenerative disease. On average, patients are diagnosed with Parkinson's
at around 60 years of age. However, the onset is probably preceded by decades of changes
in the body. The number of patients worldwide has increased from 2.5 million in 1990 to
6.1 million in 2016. The main cause is the increasing aging of the population. However, the
incidence of the disease has also increased by more than 20% within individual age groups
during this time [16,17]. Parkinson's disease is characterized by progressive degeneration
of dopaminergic neurons in the substantia nigra [18–22]. This results in an imbalance in the
transmitter system with disinhibition of cholinergic neurons and increased glutamatergic
activity (dopamine deficiency and excess of acetylcholine). This results in inhibition of
movement. Due to the lack of dopamine, akinesia and bradyphrenia develop, rigor and
tremor are consequences of the disinhibited cholinergic system. The disease advances in a
progressive manner, showing a stepwise course associated with various motor, behavioral,
and psychological disabilities. Therapy begins early with the diagnosis. Suitable APIs and
API-classes are: levodopa (LD) (always in combination with dopa decarboxylase inhibitors
(DDI, e.g., benserazide, carbidopa)), dopamine agonists (DA, e.g., pramipexole, ropinirole),
monoamine oxidase B (MAO-B) inhibitors (selegiline, rasagiline), cathechol-O-methyl
transferase (COMT, entacapone, tolcapone) inhibitors, N-methyl-D-aspartate (NMDA)
agonists (e.g., amantadine), and anticholinergics (biperidine). For patients <70 years of
age (biological age), DA are the drug of choice. In patients >70 years, LD combined with
DDI is the preferred therapy [23,24]. As the disease progresses, however, it becomes more
difficult to control symptoms by taking tablets alone [21,25–28]. The effect of the medication
then sets in increasingly later and does not last as long: The optimal range of action in
which a drug is available in the desired concentration in the body and has the intended
effect decreases. Phases with good mobility (ON phases) and with under-mobility (OFF
phases) thus become more and more prominent. Non-motor symptoms such as behavioral
changes or depression may also become more apparent [24,29,30]. That is why the therapy
of Parkinson's patients is constantly adapted and rarely remains a monotherapy. In the
later course, DA and LD are often combined. As patient suffering increases, pharmaceutical
manufacturers are trying to develop dosage forms that can alleviate suffering. Thus, there
are intestinal pumps (Duodopa®, Lecigon®, [31–33]), transdermal therapeutic systems
(TTS, Neupro®), orodispersible films and tablets (ODF, ODT [34,35]), tablets, capsules, and
floating dosage forms (Madopar® HBS [36,37]) for therapy on the market or in clinical
trials. Various research groups are also working on improved therapy [38]. Accordion
Pill® is one of the new innovative dosage forms [39]. It contains LD and carbidopa (DDI)
in a novel drug delivery system with combined immediate release (IR) and sustained
release (SR) kinetics. The design allows gastric retention and thus improved API uptake
for Parkinson's patients. In another approach, nanoparticles are being investigated as oral
and nasal dosage forms, as well as a LD powder inhaler [40–44]. Other research groups test
microspheres, liposome nanocapsules, and niosomes loaded with DA for the treatment of
Parkinson's disease. The lipophilic formulation is expected to improve transport through
the blood-brain barrier to achieve dose reduction, thereby reducing side effects [45–47].

As Fused Deposition Modelling (FDM) 3D printing is currently being investigated for
many drugs for personalized medicine [48–59], some research groups are also interested
in printing individual drug dosage forms for Parkinson's patients with tailored dosages
and release profiles [48,49,60–63]. The layered structure of the geometries from FDM 3D
printing and semi-solid 3D printing allows very precise dosage and adjustment of the dose.
This allows the required dose to be administered without triggering side effects, even for
APIs with a small therapeutic range [63,64]. FDM 3D printing, also called fused filament

fabrication, requires a filament, which is previously produced by hot-melt extrusion (HME) from a mixture of API and polymer as matrix. By simply changing the filament during printing, FDM 3D printing enables the use of multiple APIs and polymer matrices in one tablet during one manufacturing step. This offers the advantage of also being able to combine APIs that are incompatible with each other in a combined formulation, as well as being able to individually adjust the release properties of the APIs due to the polymer matrix and surface area to volume (SA/V) ratio [65,66]. For example, Khaled et al. developed a 3D printed polypill with five different drugs in various compartments and two different release profiles for cardiovascular therapy [67].

In our study, we aimed to develop a 3D printed polypill-dosage form containing three APIs with different release kinetics for the therapy of Parkinson's disease: pramipexole (PDM), levodopa (LD), and benserazide (BZ). In addition, the dosage form should be adapted to the requirements of Parkinson's patients and thus be easy to swallow, individually dosed, and have the longest possible gastric residence time (GRT) to saturate the transporters in the upper small intestine section with LD over a long period of time to reduce side effects and ON-OFF fluctuations. Levodopa is a precursor of dopamine and is used in the treatment of movement disorders in Parkinson's disease and restless legs syndrome. The initial dose is 100 mg LD once or twice daily combined with 25 mg BZ. A dose increase should be made every 3rd– 7th day, until a maximum daily dose of 800 mg LD is reached. LD and BZ are dosed in a 4:1 combination. PDM is a dopamine agonist. The initial dose is 0.26 mg pramipexole per day (corresponds to 0.375 mg PDM), the lowest dose of one tablet is 0.088 mg. The daily dose may be increased by 0.52 mg at weekly intervals, to a maximum dose of 3.15 mg per day (corresponds to 4.5 mg PDM) [23]. For individual dosage and adjusted release rate, the FDM 3D printing process was used. The DA PDM should have a fast release and the combination LD/BZ should display sustained release from the dosage form. Therefore, PDM was processed by HME in a polyvinyl alcohol (PVA)-filament and the combination LD/BZ in an ethylene-vinyl acetate-copolymer (EVA)-filament. The dosage form design should be adjusted for the release rate with respect to the absorption window in the upper jejunum via the SA/V ratio.

2. Materials and Methods

2.1. Materials

For formulation development, various sustained release (SR) polymers were first screened using the vacuum compression molding (VCM) method (Table 1).

Table 1. SR-polymers used for VCM-formulation development (MW, molecular weight; MFI, melt flow index).

	Polyvinyl Alcohol (PVA)	Hydroxypropyl Cellulose (HPC H)	Hydroxypropyl Cellulose (HPC SSL)	Ethylene Vinyl Acetate (EVA) (72:28)	Hydroxypropyl Methylcellulose Acetate Succinate (HPMC-AS)
Manufacturer	Parteck MXP®, 87–89% hydrolysis grade, MW: approx. 32,000 Da, Merck, Darmstadt, Germany	MW: 1,000,000 Da, Nisso Chemical Europe, Düsseldorf, Germany	MW: 40,000 Da, Nisso Chemical Europe, Düsseldorf, Germany	Escorene UL 02528®, MFI: 25 g/10 min, TER Chemicals, Hamburg, Germany	Aquasolve®, MW: 75,100 Da, Ashland, Wilmington, DE, USA

After formulation development, the polypill was printed with two different filaments, manufactured by hot-melt extrusion (HME). The composition of the filaments is shown in Table 2.

Table 2. Formulations used for the polypill.

Filament 1			
API and Excipients	**%**	**Function**	**Manufacturer/Source**
Pramipexole 2 HCl * H_2O (PDM)	5.0	API	99.5%, Chr. Olesen, Gentofte, Denmark
Mannitol	10.0	plasticizer	Parteck M®, Merck, Darmstadt, Germany
Polyvinyl alcohol (PVA)	84.0	polymer	Parteck MXP®, Merck, Darmstadt, Germany
Fumed silica	1.0	glidant	Aerosil® 200 VV Pharma, Evonik, Essen, Germany
Filament 2			
APIs and Excipients	**%**	**Function**	**Manufacturer/Source**
Levodopa (LD)	40.0	API	99.6%, Zhejiang Wild Wind Pharmaceutical, Dongyang, Zhejiang Prov., China
Benserazide (BZ)	10.0	API	99.8%, BioPharma Synergies, Barcelona, Spain
Vinylpyrrolidone-vinyl acetate copolymer 60:40 (PVP-VA)	15.0	polymer	Kollidon VA 64®, MW: 40,000 Da, BASF, Ludwigshafen, Germany
Ethylene-vinyl acetate copolymer 82:18 (EVA)	34.5	polymer	Escorene® FL01418, MFI: 14 g/10 min, TER Chemicals, Hamburg, Germany
Fumed silica	0.5	glidant	Aerosil® 200 VV Pharma, Evonik, Essen, Germany

LD, BZ and PDM exhibit good water solubility (c_s (LD) $\geq$ 12 mg/mL, c_s (BZ) $\geq$ 10 mg/mL, c_s (PDM) $\geq$ 200 mg/mL [68–70]) and thus belong to the biopharmaceutical classification system (BCS) class I. As HME and FDM 3D printing are heat intensive processes, care was also taken to ensure that the process temperatures were below the decomposition temperatures (260–330 °C) [62,71–74]. Due to the high water solubility of the drug substances, the dissolution is governed solely by the polymer properties and not by their solid-state properties.

2.2. Methods

2.2.1. Vacuum Compression Molding

To compare the release profiles of different sustained release (SR) polymers under the same conditions, molten platelets were prepared with vacuum compression molding (VCM, MeltPrep GmbH, Graz, Austria) technology [75]. The resulting platelets had the same surface area (SA) and volume (V), so that the SA/V ratio did not influence the release profile. For this purpose, powder mixtures of different SR polymers with 33% LD each were prepared so that there was 100 mg LD in each VCM-sample (300 mg). The physical mixture of SR polymer and LD was filled into the sample holder, which was connected to a vacuum source. A piston was pressed onto the sample, which was melted on the hot plate until the sample was homogeneously mixed. The process settings used are shown in Table 3. Afterwards, the VCM-platelet was cooled and removed from the holder. The dimensions of the resulting VCM-platelet were 20 mm in diameter and 1.5 mm in height (Figure 1).

Table 3. VCM-Process settings for different SR-polymers.

	PVA	HPC H	HPC SSL	EVA (72:28)	HPMC-AS
Heating temperature/°C	210	170	170	120	210
Heating time/min	7	7	8	7	7
Mass/mg (MV)	307	310	308	311	310
SA/V ratio/mm^{-1}	1.5	1.5	1.5	1.5	1.5

Figure 1. VCM platelets of different SR polymers.

2.2.2. Hot-Melt Extrusion for Filament Fabrication

All filaments were prepared by HME with a co-rotating twin-screw extruder (Pharmalab HME 16, Thermo Fisher Scientific, Rockford, IL, USA). A gravimetric feeder (K-SFS-24/6, Coperion K-Tron, Stuttgart, Germany) was used for all experiments. An in-house manufactured die with a diameter of 1.85 mm was used. The desired filament diameter was achieved using a belt haul-off unit of a winder (Model 846700, Brabender, Duisburg, Germany) with a belt speed of 0.8 m/min and the filament was transported through a roller system with four 360°—air flow ring nozzles (Super Air Wipe™, Exair®, Cincinnati, OH, USA). With the help of a laser-based diameter measurement module (Laser 2025 T, Sikora, Bremen, Germany), the filament diameter was detected and logged during the process with a readout rate of 1 Hz to ensure the production of filaments with low diameter fluctuations. For extrusions with EVA, the screw speed was set to 20 rpm and powder feed rate was set to 2 g/min. The screw configurations and the temperatures of the heating zones are summarized in Table 4 and also described in previous publications [60,61,76].

Table 4. Extrusion parameters with adjusted temperatures during extrusion and screw configuration of performed extrusions.

				Temperature Profile in Zone 2–10 [°C]					
	2	3	4	5	6	7	8	9	10
PDM-PVA filament	20	20	100	180	180	180	180	195	195
LD/BZ-EVA filament	20	20	100	100	100	100	100	100	100
Screw Configuration (Die-Gear)									
PVA/EVA filaments	die–10 CE 1 L/D–KZ 1: 5 × 60°–3 × 30°–5 CE 1 L/D–KZ 2: 4 × 90°–5 × 60°–3 × 30°–16 CE 1 L/D–2 CE 3/2 L/D–1 L/D adapter–gear CE = conveying element, KZ = kneading zone								

2.2.3. 3D Printing Process of the Polypill-Geometries

To achieve various dosages and release profiles, the geometries were designed with the computer-aided design (CAD) program Fusion360® (Autodesk, San Rafael, CA, USA) with focus on the volume and surface area to volume (SA/V) ratio. Afterwards, the generated stl-files were transferred to the slicing program PrusaSlicer® (Prusa research, Prague, Czech Republic). The individual parts of the geometries were assigned to the respective filament. The layer height and extrusion width were adjusted to generate the

desired height and width of the geometry. The G-code was sent to a Prusa 3D printer (Prusa i3 Mk3, Prusa research, Prague, Czech Republic), which printed the objects defined in the data file (Figure 2). The multi material unit (MMU) from Prusa® was used for printing the polypill. A cleaning tower was printed between filament changes so that the previous filament could be washed out of the nozzle and the following used filament was not contaminated. The best results were obtained with the following temperatures: PDM-PVA filament: 185 °C print temperature and 70 °C bed temperature, LD/BZ-EVA-filament: 220 °C print temperature and 70 °C bed temperature. Cooling during printing was turned off, otherwise the layers would not adhere to each other. The objects were printed one by one. The printing speed was set to 10 mm/s because the geometries had little contact area with the print bed due to their small size and quickly detached, interrupting the printing process.

Figure 2. Printed polypills in various designs.

2.2.4. Dissolution Tests of the Polypills

The dissolution tests for the polypill (n = 3) were performed according to European Pharmacopoeia monographs 2.9.3 and 5.17.1 [77,78]. A modified basket apparatus was used for the dissolution apparatus (DT 700, Erweka, Langen, Germany) [61,63]. Adapted baskets were 3D printed with water insoluble polylactide acid filament (PLA, Bavaria-Filaments, Freilassing, Germany) with a mesh size of 3 mm and the same outer dimensions as the regular baskets described in the European Pharmacopoeia. This adjustment was necessary because the 3D printed tablets clogged the small meshes of the original Erweka baskets (0.36–0.44 mm) with swollen polymer, affecting the hydrodynamics around the printed tablet. The use of the modified baskets prevented this blockage. In addition, a 3D printed PLA-plate with a mesh size of 3 mm was clipped into the basket above the floating dosage form so that it could not stick to the stirrer and thus distort the release profiles. As dissolution medium degassed 0.1 N hydrochloric acid (HCl) was used. The volume was 1000 mL, the stirring speed was set to 50 rpm and the temperature was set to 37 ± 0.5 °C. The dissolution tests were performed under sink conditions [63,76]. Samples were drawn using an autosampler (Vision® AutoFill™ + AutoPlus™, Teledyne Hanson Research, Chatsworth, CA, USA). At the set time point, 5 mL were withdrawn from the vessel, 3.5 mL were used to wash the tubes before sampling, and 1.5 mL were transferred directly to a HPLC vial. For polypill design (PP) 1-PP3, the first sample was drawn after 15 min, then after 30 min, and subsequently every 30 min until 180 min. Afterwards, a sample was taken every hour until 360 min, then every 2 h until 600 min. For PP3 additional samples were taken after 600 min every 5 h until 50 h. For the mini tablet designs *MiniTab* and *MiniHC*, the first sample was taken after 10 min, then every 10 min until 60 min, followed by every 30 min to 120 min, then after 1 h to 240 min, and every 2 h to 600 min. Subsequently, samples were taken every 5 h to 1500 min.

2.2.5. HPLC Method: Chromatographic Conditions for Simultaneous Quantification of Levodopa, Benserazide and Pramipexole

The following method is described in more detail in [76]. High performance liquid chromatography (HPLC) analysis was used to separate all three APIs (PDM, LD, BZ). The HPLC (Dionex, Sunnyvale, CA, USA) was equipped with a quaternary pump (P 580 A, Dionex, Sunnyvale, CA, USA) and an autosampler (ASI-100, Dionex, Sunnyvale, CA, USA).

For the HPLC method, a C18-column (Eurospher II 100-5, Knauer, Berlin, Germany) with integrated precolumn was used. The eluent consisted of methanol (mobile phase B) and ammonium acetate buffer (0.05 M, pH 4). The flow rate was set to 1 mL/min and the oven temperature for tempering the column to 40 °C. The gradient was as follows: mobile phase B was increased from 1 to 5% (v/v), within the first min, held at 5% (v/v) for 4 min, increased from 5 to 10% (v/v) within 1 min, held at 10% (v/v) for 4 min, increased again from 10 to 20% (v/v) within 1 min, held for 4 min at 20% (v/v), increased again from 20 to 99% (v/v) within 5 min, held for 2 min at 99% (v/v) and decreased to 1% (v/v) within 0.5 min, again until 22.5 min after sample injection. An equilibration time of 3.5 min per run was allowed to pass before the next sample was injected. An injection volume of 200 µL was chosen to analyze the APIs. Detection was achieved by measuring the UV absorption of the sample at 264 nm with the help of the HPLC UV-detector [77].

2.2.6. Density Measurements with Helium Pycnometer

To determine the true density of the filaments and printed tablets, measurements were made using a helium pycnometer (AccuPyk 1330, Model 133/00010/10, Micromeritics, Norcross, GA, USA). The analysis conditions were 10 cycles with a purging filling pressure of 134.55 kPa with Helium. 5 measurements per sample were performed in a 1 cm^3 chamber.

2.2.7. Comparison of Release Profiles
Mean Dissolution Time

The *Mean Dissolution Time (MDT)*, expressed in units of time, was used to compare the curves and to categorize them [61,79,80]. The **MDT** was calculated according to Equation (1).

$$MDT = \frac{ABC}{c_\infty} = \frac{\sum_{i=0}^{\infty}\left[(c_{i+1} - c_i) \times \frac{(t_i + t_{i+1})}{2}\right]}{c_\infty} \tag{1}$$

The quotient of the **ABC** (*area between the curves*) and c_∞, the initial drug load of the dosage form results in the **MDT**. Via the trapezoidal equation, **ABC** is calculated with c_i as the concentration of the API released over time **t**. Values up to 100% API release were used, since the **ABC** does not change afterwards.

Similarity Factor

In addition, the similarity factor was used to compare the release curves. Equation (2) was used to perform the calculation [61,79,81,82].

$$f_2 = 50 \times log\left\{\left[1 + \frac{1}{n}\sum_{t=1}^{n}(R_t - T_t)^2\right]^{-0.5} \times 100\right\} \tag{2}$$

R_t represents the API in % at time point **t** for the reference and T_t the API in % at time point **t** for the test product. The factor **n** summarizes the considered number of time points. Since the f_2 value is sensitive to the number of measurement points, the number of the considered values was constantly limited to 12 time points. An f_2 value of 100 results if the dissolution curve of the test product is completely identical to the reference curve. The measured values may deviate from the reference by a maximum of 10%, resulting in f_2 values between 50–100. If the achieved f_2 value is below 50, the dissolution profiles differ strongly, and they are not considered similar.

3. Results and Discussion
3.1. Polymer Selection for Levodopa

To increase Parkinson's patients' adherence to their therapy, the LD/BZ combination should be released slowly over 12–24 h so that dosing intervals increase, and ON-OFF fluctuations decrease. The PVA-formulation with PDM has already been developed for previous studies [60,61,63]. To find a suitable SR polymer for the LD/BZ combination,

VCM-platelets were prepared with a drug loading of 33% (*w/w*) LD and established SR polymers: PVA, HPC H, HPC SSL, EVA and HPMC-AS. All VCM-platelets had the same SA/V ratio and could thus be compared based on their dissolution properties (Figure 3).
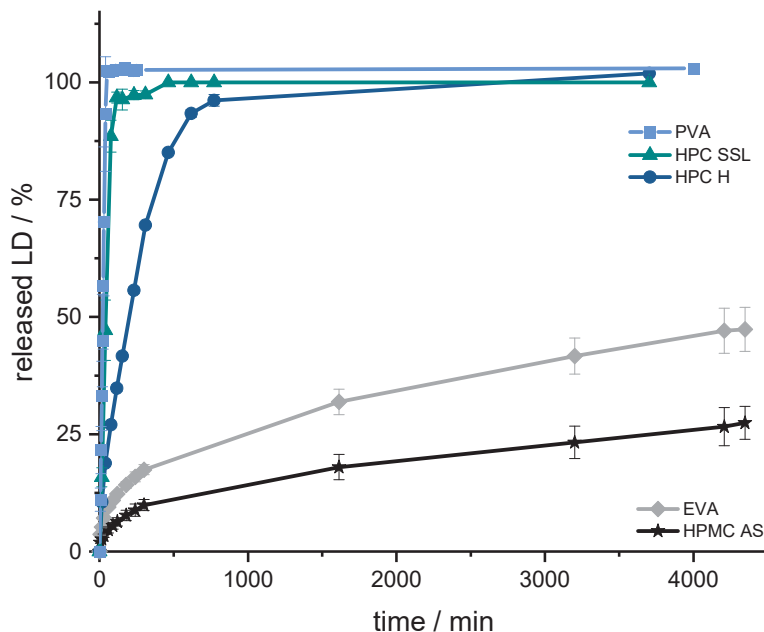
Figure 3. Dissolution profiles of LD from SR-polymer-VCM platelets (33% (*w/w*) LD-loading); modified basket apparatus, 1000 mL 0.1 N HCl, 50 rpm, 37.0 ± 0.5 °C. x $\pm$ s; *n* = 3.

The aim was to achieve prolonged release with a constant dissolution rate of the API. This target was set regarding the prolonged gastrointestinal passage in Parkinson's patients [83,84] and the resorption window of levodopa in the small intestinal tract via large neutral amino acid (LNAA) transport carrier [85,86]. To achieve continuous availability of LD/BZ in the body, the dosage form should release a constant amount of LD/BZ and saturate the transporters for as long as possible so the "wearing off" phenomenon at the end of dose interval is decreased [87–89]. To ensure a constant release, the tablet should release 75% within 12 h, so that a constant API exposition is realized within the desired time frame. Using the VCM-platelets, it was determined that PVA, HPC H and HPC SSL would not be considered because they released the API too fast (HPC SSL 75% LD in 25 min, PVA: 75% LD in 33 min, and HPC H 75% LD in 133 min) based on their high hydrophilicity, the formation of a hydrocolloid matrix, and swelling, as well as eroding properties of the matrix so that the API can be solubilized faster. The final formulation including BZ should have 50% drug-loading and thus become even more hydrophilic, so that the API release will be faster than the VCM-API release. The API release of HPMC-AS, on the other hand, was too slow (25% LD in 63 h), so the decision was made for the SR polymer EVA (50% API in 75 h). In addition, EVA has a lower density (0.95 g/cm^3) than water and 0.1 N HCl (gastric fluid), so this property can be exploited for a floating, gastro-retentive drug delivery dosage form [86].

3.2. Formulation Development with EVA

First, a formulation containing 40% LD and 60% EVA was extruded (F1, Table 5). However, the API release was too slow, even with a high SA/V ratio of 3 mm^{-1} (Figure 4), and the printing process of the filament was difficult, because of the high flexibility of the filament. Therefore, the formulation was changed. PVA was added in equal parts with EVA as hydrophilic polymer (F2). Nevertheless, the flexibility of EVA with a VA content of 28% was too high, so that the printability was poor, the printed objects were not reproducible, and the printing process repeatedly stopped because the filament clogged the nozzle. Drug

release was faster than in F1, but still not suitable. Therefore, the EVA polymer with a VA content of 28% was replaced by EVA with a VA content of 18% (F3). The same excipient combination with other quantification was now extruded and printed with EVA (18% VA). Drug release was much faster than with formulation F2, but the dosage form disintegrated within a few minutes, so no gastro-retentive drug delivery form can be developed with this composition. Therefore, the EVA content was increased, PVA was replaced by PVP-VA, and mannitol was added, as the filament otherwise became too brittle (F4).

Table 5. Formulation development of SR LD-EVA formulation.

	F1	F2	F3	F4
LD/%	40	10	10	10
EVA (72:28)/%	60	44.5	-	-
EVA (82:18)/%	-	-	25	39.5
PVA/%	-	44.5	64	-
Mannitol/%	-	-	-	10
PVP-VA/%	-	-	-	39.5
Fumed Silica/%	-	1	1	1
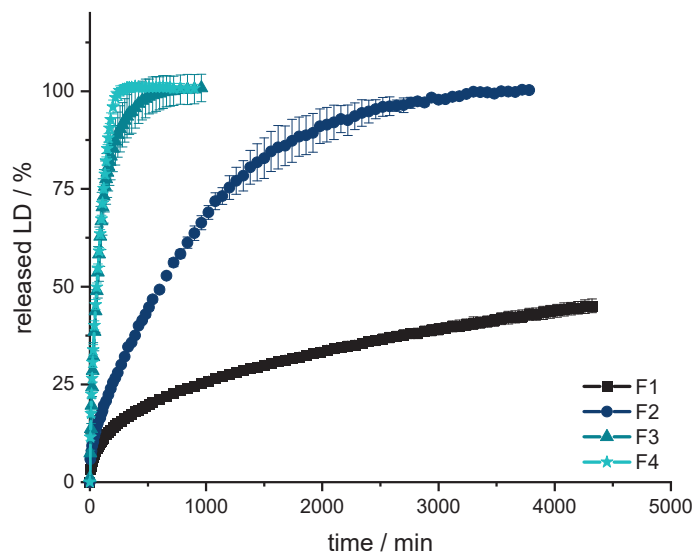
Figure 4. Dissolution of LD from F1, F2, F3 and F4; modified basket apparatus, 1000 mL 0.1 N HCl, 50 rpm, 37.0 ± 0.5 °C. x ± s; *n* = 3.

All formulations show a burst in the first few minutes. Subsequently, the API is released constantly over time until approximately 80% of LD has been released. Thereafter, the release of LD is slower and results in a plateau. The release profile can be described with Higuchi's square root-of-time kinetics [90–92]. First, the API, which is on the surface of the dosage form, is dissolved. The larger the surface, the more API goes directly into the solution. This results in what is known as a burst. The API is then released from the matrix. In the inert matrix, depending on the diffusion path, the amount of dissolved API remains constant over time. After a certain time, the diffusion paths for the API become longer and longer and less API is released over time until the plateau at 100% is reached.

The formulations F3 and F4 result in a fast release profile (50% released API in 60 min, 75% released API in 125 min), which may be advantageous when the dosage form is not gastro retentive, and the API must be fully released prior to small intestinal passage. However, since F3 dissolves and does not retain an inert matrix, F4 was used as orientation for the fixed-combination formulation. Formulations F1 and F2 released the API much more slowly (F1: 25% released API in 960 min; F2: 75% released API in 1200 min) and were thus not developed further.

From the obtained results, it could be concluded that the fixed-combination formulation should contain more than 25% EVA for the tablet to remain durable. In addition, PVP-VA was identified as a good pore former and stiffness enhancer for better printability. Since the desired release profile of the fixed combination should still be slower than displayed by F4, the amount of EVA could be increased.

3.3. Formulation Development for Fixed Combination LD/BZ

Based on the previously found formulation with 10% LD, different fixed combinations (FC) were now extruded. The EVA content was set above 30% to produce an inert, non-disintegrating matrix (Table 6). The API proportions were fixed, as they are dosed in a 4:1 ratio (LD:BZ). The maximum dose is 200 mg LD per tablet, which is equivalent to a 500 mg tablet at 40% content, which should be swallowable by patients and designable so that the dimensions of the dosage form are similar to those of tablets on the market. The PVP-VA content varied from 5–20%. The filaments with 20% PVP-VA (FC4) were too brittle and broke directly during cooling after HME, so that they could not be used for printing. The density measurements also reflect the EVA content. The higher the content of EVA in the filament, the lower the density.

Table 6. Formulation development of LD/BZ fixed combination (FC) formulation.

	FC1	FC2	FC3	FC4
LD/%	40	40	40	40
BZ/%	10	10	10	10
EVA (82:18)/%	44.5	39.5	34.5	29.5
PVP-VA/%	5	10	15	20
Fumed Silica/%	0.5	0.5	0.5	0.5
Density/g/cm^3	1.15	1.16	1.17	-

After extrusion, parts of the filaments were used for dissolution tests to assess which formulation was most likely to reproduce the desired release profile (SA/V: 2.3 mm^{-1}). Parallel quantification of LD and BZ is challenging, and the development of a suitable analytical method to quantify the APIs simultaneous in the presence of PDM is described in another publication [76]. As other publications have already shown, the release profiles of BZ and LD are comparable [93–97]. To simplify the analyses in the present study, the release profile of LD is also used as a surrogate for BZ release (Figure 5).
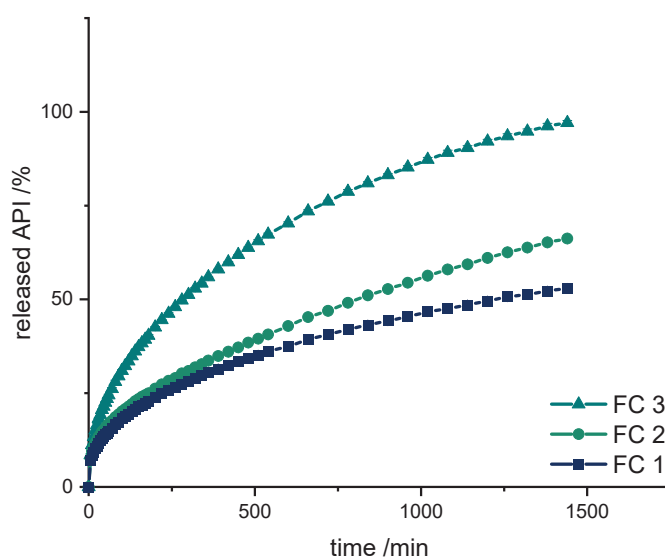
Figure 5. Dissolution of LD/BZ from FC1, FC2, and FC3; modified basket apparatus, 1000 mL 0.1 N HCl, 50 rpm, 37.0 ± 0.5 °C. x ± s; *n* = 3.

Also with these formulations, the release starts with a burst effect. Subsequently, the release of the APIs is more uniform. The diffusion paths within the filament strand are very short (Ø 1.75 mm), so that the decrease in the release rate towards the end is small.

The formulations FC 1+2 release the APIs too slow (FC 1: 50% API in 1260 min, FC 2: 50% API in 780 min), whereas FC 3 shows the fastest release course and displays the desired course (50% API in 290 min, 75% API in 720 min, 100% API in 1440 min).

3.4. Design and Dissolution of Polypill Tablet Variations

With the final LD-EVA filament formulation (FC3), and the beforehand developed PDM-PVA filament, different geometries with various PDM and LD/BZ contents were printed and released. The selected doses were adjusted to the dosages in available market preparations.

First, a simple polypill design was chosen (PP1) to observe the release behavior of the printed formulation (Figure 6 left). A cylinder with a diameter of 10 mm was selected as geometry, which should therefore also be easy to swallow (Figure 6 right). A LD/BZ dose of 50/12.5 mg was targeted, which corresponds to the lowest dose of tablets available on the market, as well as a PDM dose of 3.5 mg (Table 7). The release rate was calculated for the linear section of the profiles, after the burst until the end of the measurement (LD/BZ), or until the plateau was reached (PDM).
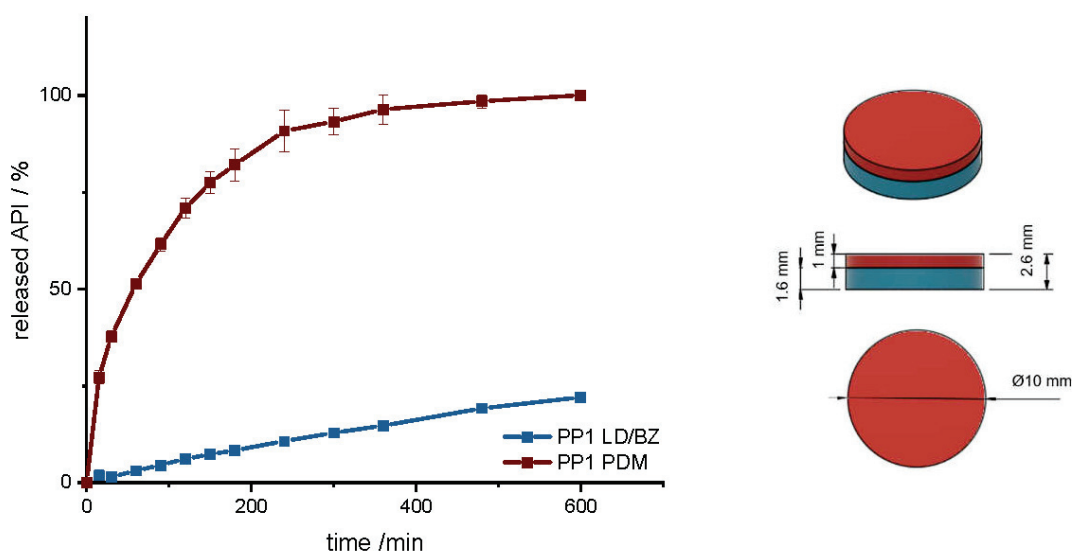
Figure 6. (**Left**): release profile of PP1; modified basket apparatus, 1000 mL 0.1 N HCl, 50 rpm, 37.0 ± 0.5 °C, x ± s; *n* = 3. (**Right**): Image of PP1: red: PDM-PVA, blue: LD/BZ-EVA.

Table 7. Structure and release properties of PP1.

	LD/BZ	PDM
SA/V total/mm^{-1}		1.2
SA/V/mm^{-1}	1.6	2.4
mg API/mg	50.0/12.5	3.5
% API in 600 min	22	100
$t_{75\%}$/min	n.d.	140
MDT/min	n.d.	97
release rate/%/min	0.03	0.33

The geometry has a total SA/V ratio of 1.17 mm^{-1}. As the PDM-PVA formulation dissolves over time, the SA of the insoluble LD/BZ formulation increases to 1.65 mm^{-1}. The release of PDM can be described by the Peppas Sahlin equation [61]. The formulation releases the API by diffusion and erosion due to the formation of a hydrocolloid matrix [98].

Due to the layered structure of the FDM printed geometry, the medium can easily penetrate the cylinder and release the API from the individual strands. The formulation begins to swell and dissolve over time. The API can release through the layers and dissolve directly due to its good solubility. After 140 min, 75% PDM was released, and thus the dissolution profile can be categorized as prolonged release. The combination of LD/BZ is released very slowly from the SR polymer. The matrix is inert, and the APIs can only enter solution by diffusion. After 600 min, just 22% LD/BZ is released. The density of the entire PP1 is 1.18 g/cm^3. Due to the low EVA density and most probably included pores, the buoyancy of the polypill is maintained (Figure 7). While the PDM-PVA layer (density 1.3 g/cm^3) dissolves over time, the remaining EVA-based part retains the floating property.
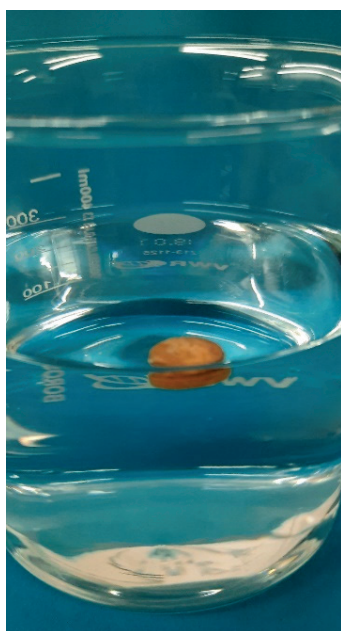
Figure 7. Floating properties of PP1 in 300 mL 0.1 N HCl, 37 $\pm$ 0.5 $^\circ$C.

To increase the dose, a hollow cylinder-geometry (PP2) was designed that is built up in three layers, with a total SA/V ratio of 0.9 mm^{-1} (Table 8). The SA/V ratio was kept similar to PP1 to see if it is possible to increase the dose without strongly affecting the overall release. This is of particular importance for personalized therapy [63]. The PDM filament was printed between two LD/BZ-EVA hollow cylinder layers, so that these two hollow cylinders can detach from each other after a while due to the solubility of PDM-PVA-compartment and further increase the SA of the geometry during release to a SA/V ratio of 1.3 mm^{-1} (Figure 8).

Table 8. Structure and release properties of PP2.

	LD/BZ	PDM
SA/V total/mm^{-1}	0.9	
SA/V/mm^{-1}	1.3	2.6
mg API/mg	83/20.75	3.5
SA/V/mm^{-1}	1.2	-
mg API/mg	97/24.25	-
%API in 600 min	21	100
t$_{75\%}$/min	n.d.	310
MDT/min	n.d.	187
release rate/%/min	0.02	0.20
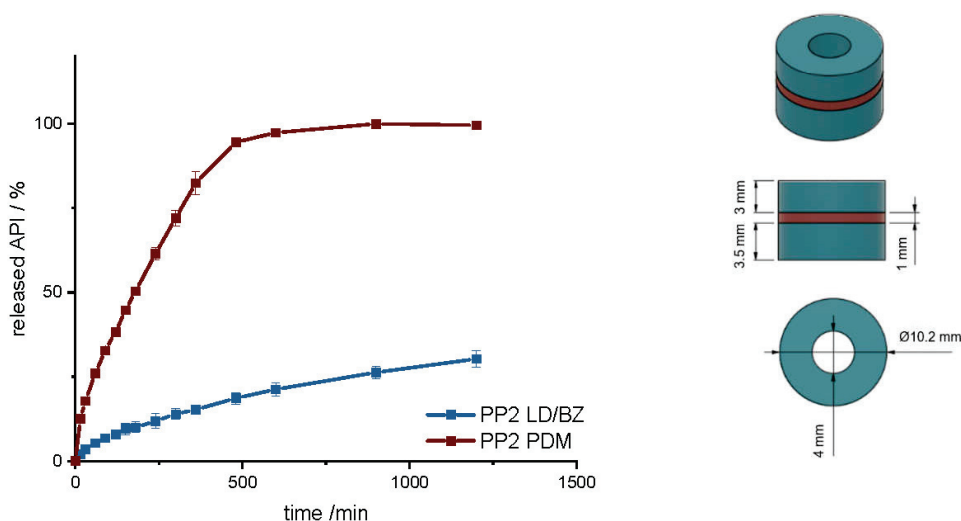
Figure 8. (**Left**): release profile of PP2; modified basket apparatus, 1000 mL 0.1 N HCl, 50 rpm, 37.0 ± 0.5 °C, x ± s; *n* = 3. (**Right**): Image of PP2: red: PDM-PVA, blue: LD/BZ-EVA.

Compared to PP1, PDM is released more slowly here. This is due to the enclosed SA of the two LD/BZ hollow cylinders. The LD/BZ release curve is very similar to PP1 (f_2: 87.5). Here, 21% API is also released in 600 min. Due to the small outer SA of the PVA formulation in contact with the medium (24% of the SA), the separation of the layers could not proceed as quickly as desired, so that the increase in SA due to the separation of the hollow cylinders occurred late and thus did not lead to a faster API dissolution. In addition, it was observed that during printing of the PVA layer, EVA residues were still present in the print head, which were rinsed out despite the intermediate cleaning step and thus contaminated the PVA layer with EVA. The total density of the PP2 is 1.1 g/cm^3. Despite the large shape, the dosage form floats on the medium, again most likely because of air entrapped in the structure (Figure 9). If the PDM-PVA layer between the LD/BZ-EVA-hollow cylinders dissolves, both parts (hollow cylinders with LD/BZ-EVA) float on the surface of the medium.

Figure 9. Floating properties of PP2 in 300 mL 0.1 N HCl, 37 ± 0.5 °C.

In another polypill design (PP3), the PDM dose was changed. The total SA/V ratio was kept similar to PP1 and PP2. PP3 design was a hollow cylinder, this time with a small cylinder as inlay printed with the PDM-PVA filament (Figure 10). PDM-PVA was low-dosed with 1.5 mg and LD/BZ-EVA had a content of 50/12.5 mg (Table 9).
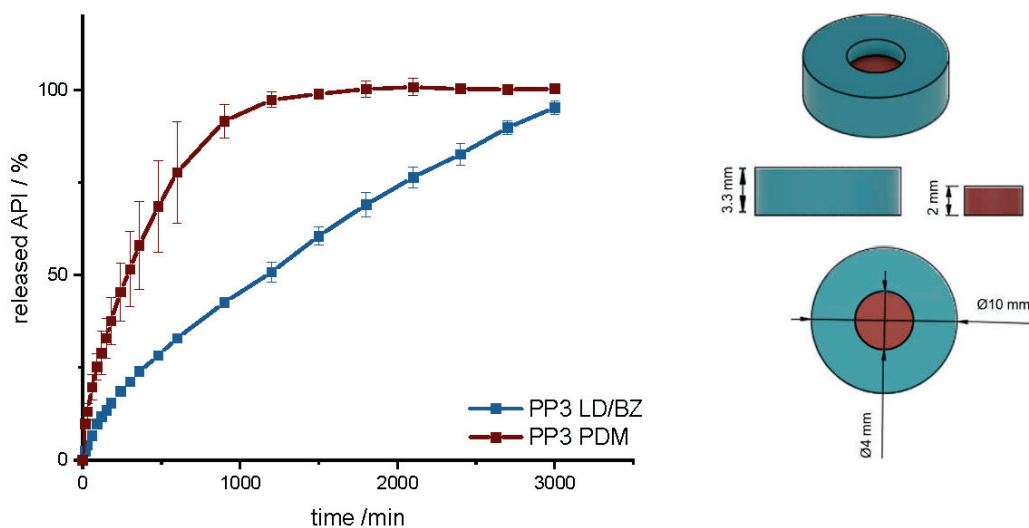
Figure 10. (**Left**): release profile of PP3; modified basket apparatus, 1000 mL 0.1 N HCl, 50 rpm, 37.0 ± 0.5 °C, x $\pm$ s; *n* = 3. (**Right**): Image of PP3: red: PDM-PVA, blue: LD/BZ-EVA.

Table 9. Structure and release properties of PP3.

	LD/BZ	PDM
SA/V total/mm^{-1}		1.1
SA/V/mm^{-1}	1.3	2.0
mg API/mg	50.0 / 12.5	1.5
% API in 600 min	33	75
t$_{75\%}$/min	2100	600
MDT/min	1130	360
release rate/%/min	0.03	0.11

To represent the complete release profile, the time of the dissolution test was extended to 3000 min. In this design, PDM was released very slowly. Despite a comparable SA/V ratio to PP1 and PP2, only 75% PDM was released within 600 min. The SA in contact with the medium was limited to 50%, so the SA in the complete design was reduced by the hollow cylinder from the EVA formulation. In addition, a filament change had to be performed for every single layer in this geometry, which again resulted in carryover of EVA into the PVA layers. For the LD/BZ-EVA formulation, a constant drug release after the burst could be realized with this design. With a release rate of 0.03% API/min, the release profile is comparable to PP1 and PP2, which was desired with the choice of SA/V ratio (f$_2$: 60.1). The total density of the PP3 is 1.1 g/cm^3. It also floats on the surface of the medium and maintains this property over the time of release.

With these geometries, it is possible to achieve a prolonged gastro-retentive API release for various dosages, which allows a larger time interval for drug absorption. In addition, due to the different geometric forms but comparable SA/V ratios, it is possible to vary the dosages from 50/12.5 mg–200/50 mg LD/BZ but keep the release profile similar (f$_2$ > 50). However, the release profile of the LD/BZ combination is very slow (75% LD/BZ in 2100 min). For patients who need to respond more specifically to LD/BZ spikes, a 24 h ingestion-interval is not an option. In addition, the selected tablet sizes are not advantageous for patients with swallowing difficulties. Therefore, the possibility of printing mini tablets was also investigated in this study.

3.5. Design and Dissolution of Polypill Mini Tablet Variations

With mini tablets, the dose can be finely adjusted by the patient himself by the selected number of mini tablets. Since the diameter is $\leq$5 mm, these dosage forms are easy to swallow [99,100].

First, a mini tablet (MiniTab) was printed with the dimensions of 4 mm in diameter and 3.6 mm in height (Figure 11 and Figure S1, Supplementary Material). The dose of LD/BZ was reduced to 15/3.75 mg per mini tablet, so the patient can adjust the desired LD/BZ dose in 15/3.75 mg steps by the number of tablets (Table 10). The dose of PDM was set to 0.375 mg, which represents the smallest dose in market preparations for SR. Therefore, the therapy can be adapted in small discreet steps.
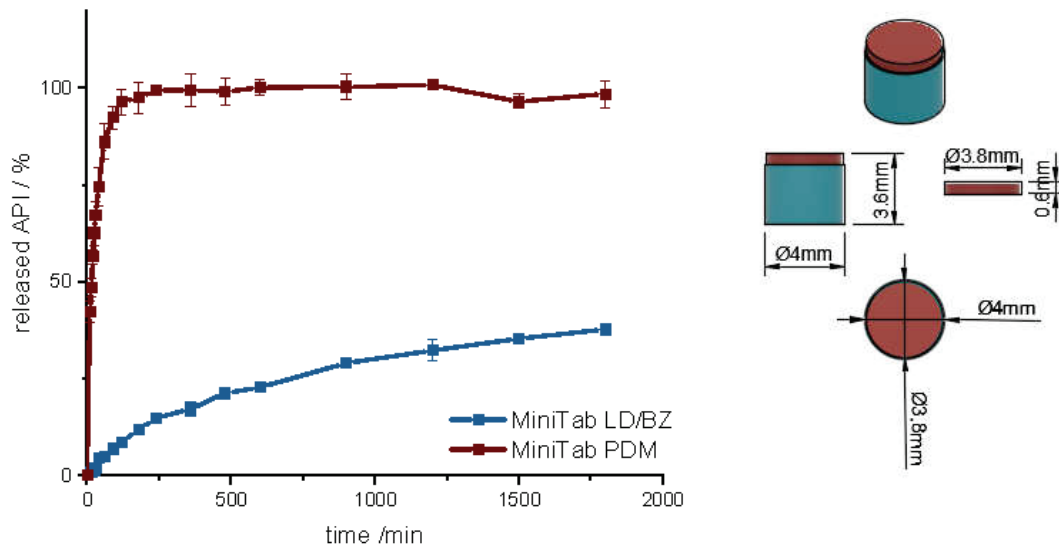
Figure 11. (**Left**): release profile of polypill design MiniTab; modified basket apparatus, 1000 mL 0.1 N HCl, 50 rpm, 37.0 ± 0.5 °C, $x \pm s$; $n = 3$. (**Right**): Image of MiniTab: red: PDM-PVA, blue: LD/BZ-EVA.

Table 10. Structure and release properties of MiniTab.

	LD/BZ	PDM
SA/V total/mm^{-1}		2.1
SA/V/mm^{-1}	1.6	4.4
mg API/mg	15/3.75	0.375
% API in 600 min	22.7	100
t$_{75\%}$/min	n.d.	40
MDT/min	n.d.	26
release rate/%/min	0.02	0.80

The release of PDM is fast (100% PDM in 60 min). The small cylinder can be well covered by the medium, so that the API is quickly released from the matrix and the PDM-PVA cylinder can be well dissolved. The release of LD/BZ is again comparable to PP1-PP3 (f$_2$: 80.3). 23% API was released in 600 min, and the release rate is 0.02% API/ min. With the MiniTab design, it would therefore be possible to reproduce the same release rate as with PP1-PP3, but the dose can be individually adjusted in small steps. In addition, PDM is released much faster with this form, so that any OFF phases of the patient can be treated quickly. Due to the low density (1.1 g/cm^3), as well as the low volume likely in combination with entrapped air, this dosage form also floats on the surface of the medium and can thus be used as a gastro-retentive dosage form.

To increase the release rate of the LD/BZ combination, a SA/V ratio of 4.7 mm^{-1} was targeted with the next design. Therefore, a mini-hollow cylinder (MiniHC) with a dose of 10 mg LD and the appropriate SA/V ratio was printed. The interior was filled with a cross of PDM-PVA (Figure 12, Figures S2 and S3). This design allows for maximum circulation of the medium around both formulations. In addition, the dose of PDM can be varied by the height of the cross, or with a different design, which can be inserted into the hollow

cylinder. The variation in height was tested with two different PDM-doses (Table 11). Figure 12 shows the release of MiniHC with cross with 0.4 mg PDM (MiniHCwC1, Top) and bottom shows the release of MiniHCwC2 with 1.5 mg PDM.
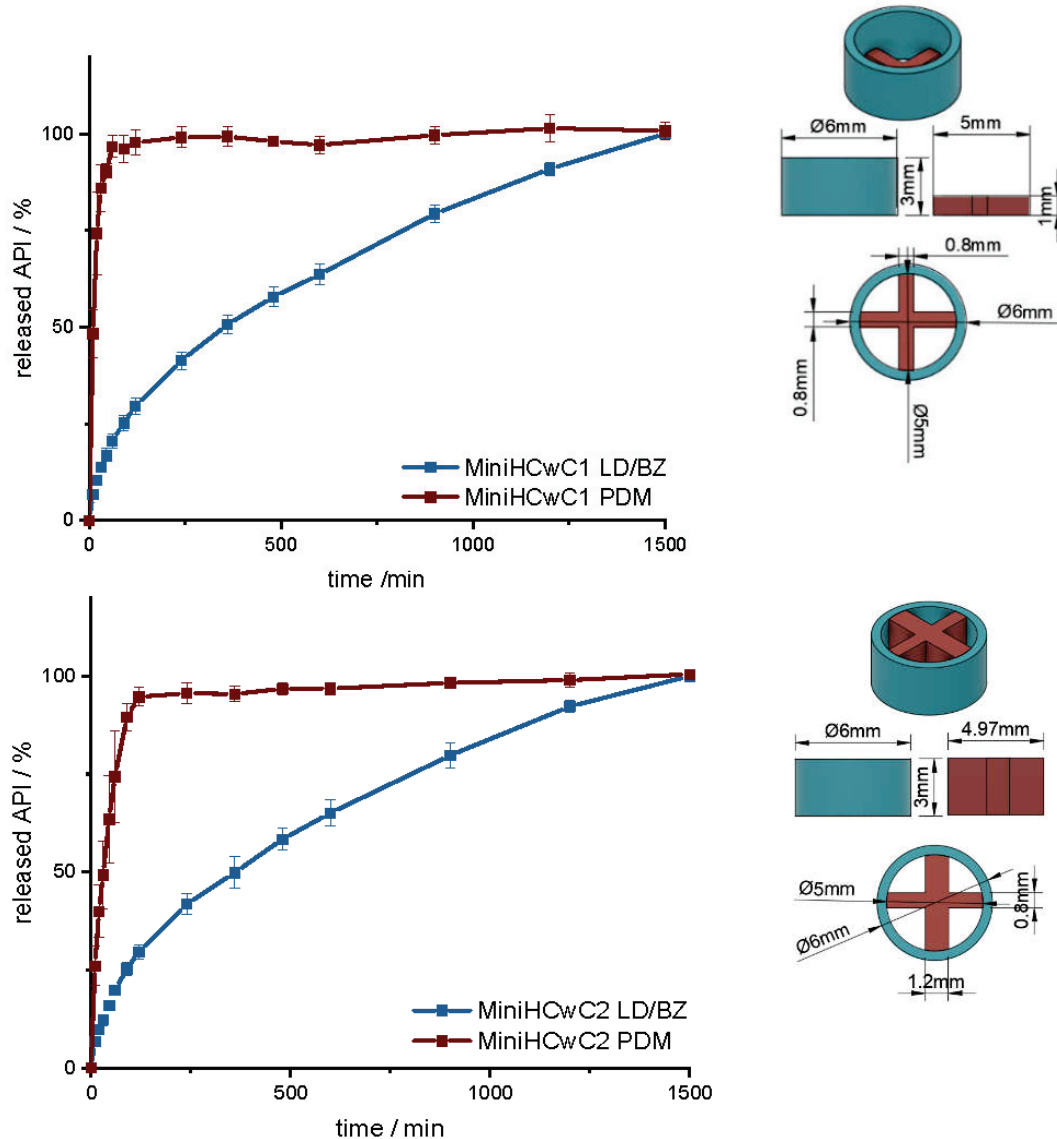
Figure 12. (**Left**): release profile of MiniHCwC 1 (**top**) and 2 (**bottom**); modified basket apparatus, 1000 mL 0.1 N HCl, 50 rpm, 37.0 ± 0.5 °C, x ± s; *n* = 3. (**Right**): Image of MiniHCwC1 + 2: red: PDM-PVA, blue: LD/BZ-EVA.

Table 11. Structure and release properties of MiniHC with a cross.

	LD/BZ 1 + 2	PDM 1	PDM 2
SA/V total/mm^{-1}	-	4.7 with LD/BZ	3.7 with LD/BZ
SA/V/mm^{-1}	4.7	4.6	2.9
mg API/mg	10/2.5	0.4	1.5
% API in 600 min	65	100	100
t$_{75\%}$/min	750	20	60
MDT/min	363	14	28
release rate/%/min	0.07	1.88	0.95

The LD/BZ release shows the same dissolution profile in both MiniHC versions. First, a burst is seen; then, the API is released continuously over time at a rate of 0.07% API/min. Due to the low wall thickness of the HC (1 mm) and the resulting short diffusion pathways for the APIs, the release profile remains constant over a long time and the release rate hardly decreases towards the end. With a released API fraction of 75% LD/BZ in 750 min, this release profile corresponds to the initially desired course. The PDM release is faster and differs in both variations. This was expected due to the various SA/V ratios. The printed cross with 0.4 mg PDM (PDM1, Table 11) has almost twice the SA/V ratio than the cross with 1.5 mg PDM (PDM2). Thus, the MDT is half as big, and the drug is released faster. This design makes it possible to insert various designs of other filaments, various SA/V ratios, and APIs, and to combine different release profiles. The inserted geometries can also be printed and inserted individually, independently of the outer hollow cylinder, so that there is no cross-contamination or mixing of the filaments. The floating property of the formulation allows prolongation of the GRT, a continuous release of the API and thus a saturation of the amino acid transporters in the upper small intestine section with LD (Figure 13). The small diameter and height, as well as the flexibility of the structure facilitate the swallowing of the 3D printed form for the Parkinson's patients. This allows the therapy to be individually adapted to the patient.
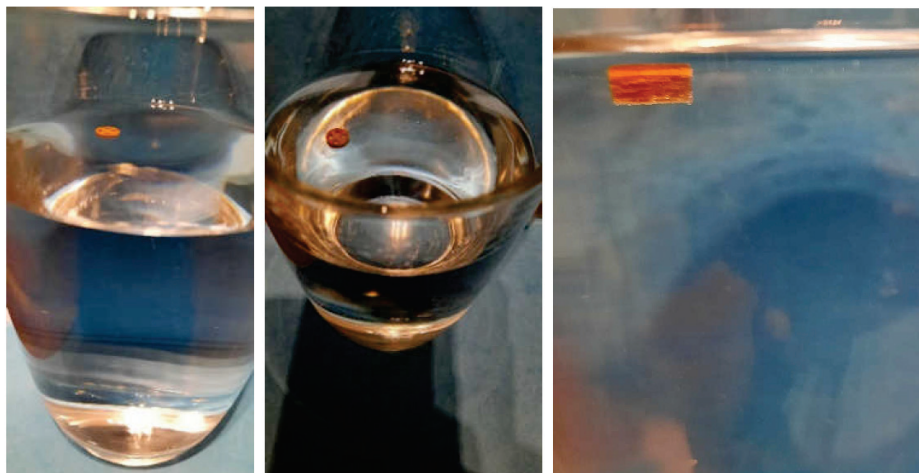
Figure 13. Floating properties of MiniHCwC in 300 mL 0.1 N HCl, 37 ± 0.5 °C.

4. Conclusions

In this study, the first printed oral dosage form with PDM/LD/BZ was developed. VCM was used as another new technology that is very useful to study the release properties of polymers without the influence of SA/V ratio. HME was used to prepare a fixed-combination of two drugs, and the FDM 3D printing process allowed the filament with the fixed-combination to be combined with another drug-loaded filament in variable dosages. In addition, the FDM 3D printing process enables variation of the SA/V ratio through the variety of possible geometries, as well as the incorporation of different layers and pores, all of which have an impact on the drug release process. Thus, not only the dose but also the onset and duration of the effect can be influenced. This approach makes it possible to address the individual needs of Parkinson's patients, titrating the dose and increasing or decreasing it in small steps as needed. In this study, it was possible to increase the LD/BZ dose from 15–180 mg LD (3.75–107 mg BZ) and achieve a similar release profile ($f_2 > 50$). In addition, mini tablets and mini hollow cylinders were printed, which might be easier for Parkinson's patients to swallow and can be varied in number for ingestion so that the dose can be adjusted to the situation and the daily dose, to respond to ON-OFF-phenomena. Furthermore, the formulation has a low density, resulting in a floating property, which was used to prolong GRT. For drugs that are absorbed in the upper part of the small intestine,

this increases the time of API absorption, and thus the medicine intake interval is increased. This improves patient adherence to their therapy.

The choice of polymer resulted in a very slow release; further studies may test whether the results can be achieved with other polymers. In addition, the polypill was prepared only with well water-soluble APIs. It would also be interesting to see how such a combination behaves with APIs of different BCS classes.

References

1. The World Bank. Population Ages 65 and above (% of Total Population). Available online: https://data.worldbank.org/indicator/SP.POP.65UP.TO.ZS (accessed on 6 February 2022).
2. BiB-Fakten. Anteil Junger Und Älterer Menschen an Der Bevölkerung, Welt (1950–2020). Available online: https://www.bib.bund.de/DE/Fakten/Fakt/W04-Junge-aeltere-Menschen-Welt-ab-1950.html (accessed on 6 February 2022).
3. Rochon, P.A.; Petrovic, M.; Cherubini, A.; Onder, G.; O'Mahony, D.; Sternberg, S.A.; Stall, N.M.; Gurwitz, J.H. Polypharmacy, Inappropriate Prescribing and Deprescribing in Older People: Through a Sex and Gender Lens. *Lancet Healthy Longev.* **2021**, *2*, e290–e300. [CrossRef]
4. Ludwig, W.-D.; Mühlbauer, B.; Seifert, R. *Arzneiverordnungs-Report 2021*; Springer: Berlin/Heidelberg, Germany, 2021; Volume 1, ISBN 978-3-662-63825-5.
5. Vrdoljak, D.; Borovac, J.A. Medication in the Elderly-Considerations and Therapy Prescription Guidelines. *Acta Med. Acad.* **2015**, *44*, 159–168. [CrossRef] [PubMed]
6. Milton, J.C.; Hill-Smith, I.; Jackson, S.H.D. Prescribing for Older People. *BMJ Br. Med. J.* **2008**, *336*, 606–609. [CrossRef] [PubMed]
7. Mehta, R.S.; Kochar, B.D.; Kennelty, K.; Ernst, M.E.; Chan, A.T. Emerging Approaches to Polypharmacy among Older Adults. *Nat. Aging* **2021**, *1*, 347–356. [CrossRef]
8. Drenth-van Maanen, A.C.; Wilting, I.; Jansen, P.A.F. Prescribing Medicines to Older People—How to Consider the Impact of Ageing on Human Organ and Body Functions. *Br. J. Clin. Pharmacol.* **2020**, *86*, 1921–1930. [CrossRef] [PubMed]
9. Barat, I.; Andreasen, F.; Damsgaard, E.M.S. Drug Therapy in the Elderly: What Doctors Believe and Patients Actually Do. *Br. J. Clin. Pharmacol.* **2001**, *51*, 615–622. [CrossRef]
10. Chang, T.I.; Park, H.; Kim, D.W.; Jeon, E.K.; Rhee, C.M.; Kalantar-Zadeh, K.; Kang, E.W.; Kang, S.W.; Han, S.H. Polypharmacy, Hospitalization, and Mortality Risk: A Nationwide Cohort Study. *Sci. Rep.* **2020**, *10*, 18964. [CrossRef]
11. Fuster, V.; Gambús, F.; Patriciello, A.; Hamrin, M.; Grobbee, D.E. The Polypill Approach-An Innovative Strategy to Improve Cardiovascular Health in Europe. *BMC Pharmacol. Toxicol.* **2017**, *18*, 10. [CrossRef]
12. Sleight, P.; Pouleur, H.; Zannad, F. Benefits, Challenges, and Registerability of the Polypill. *Eur. Heart J.* **2006**, *27*, 1651–1656. [CrossRef]

13. Obeso, J.A.; Stamelou, M.; Goetz, C.G.; Poewe, W.; Lang, A.E.; Weintraub, D.; Burn, D.; Halliday, G.M.; Bezard, E.; Przedborski, S.; et al. Past, Present, and Future of Parkinson's Disease: A Special Essay on the 200th Anniversary of the Shaking Palsy. *Mov. Disord.* **2017**, *32*, 1264–1310. [CrossRef]

14. Poewe, W.; Seppi, K.; Tanner, C.M.; Halliday, G.M.; Brundin, P.; Volkmann, J.; Schrag, A.E.; Lang, A.E. Parkinson Disease. *Nat. Rev. Dis. Primers* **2017**, *3*, 17013. [CrossRef]

15. Charvin, D.; Medori, R.; Hauser, R.A.; Rascol, O. Therapeutic Strategies for Parkinson Disease: Beyond Dopaminergic Drugs. *Nat. Rev. Drug Discov.* **2018**, *17*, 804–822. [CrossRef] [PubMed]

16. Heinzel, S.; Berg, D.; Binder, S.; Ebersbach, G.; Hickstein, L.; Herbst, H.; Lorrain, M.; Wellach, I.; Mätzler, W.; Petersen, G.; et al. Do We Need to Rethink the Epidemiology and Healthcare Utilization of Parkinson's Disease in Germany? *Front. Neurol.* **2018**, *9*, 500. [CrossRef] [PubMed]

17. Dorsey, E.R.; Elbaz, A.; Nichols, E.; Abd-Allah, F.; Abdelalim, A.; Adsuar, J.C.; Ansha, M.; Brayne, C.; Choi, J.-Y.; Collado-Mateo, D.; et al. Global, Regional, and National Burden of Parkinson's Disease, 1990–2016: A Systematic Analysis for the Global Burden of Disease Study 2016. *Lancet Neurol.* **2018**, *17*, 939–953. [CrossRef]

18. Hornykiewicz, O. The Discovery of Dopamine Deficiency in the Parkinsonian Brain. *J. Neural Transm. Suppl.* **2006**, *70*, 9–15. [CrossRef]

19. Jankovic, J. Parkinson's Disease: Clinical Features and Diagnosis. *J. Neurol. Neurosurg. Psychiatry* **2008**, *79*, 368–376. [CrossRef]

20. Dauer, W.; Przedborski, S. Parkinson's Disease: Mechanisms and Models. *Neuron* **2003**, *39*, 889–909. [CrossRef]

21. Lees, A.J.; Hardy, J.; Revesz, T. Parkinson's Disease. *Lancet* **2009**, *373*, 2055–2066. [CrossRef]

22. Parkinson, J. An Essay on the Shaking Palsy. 1817. *J. Neuropsychiatry Clin. Neurosci.* **2002**, *14*, 223–236. [CrossRef]

23. Deutsche Gesellschaft für Neurologie (DGN). S3 Leitlinie Idiopathisches Parkinson-Syndrom. *AWMF-Regist. Nr.* **2016**, *1*, 1–77.

24. Cotzias, G.C.; Papavasiliou, P.S.; Gellene, R. Modification of Parkinsonism—Chronic Treatment with L-Dopa. *N. Engl. J. Med.* **1969**, *280*, 337–345. [CrossRef]

25. Olanow, C.W.; Koller, W.C. An Algorithm (Decision Tree) for the Management of Parkinson's Disease: Treatment Guidelines. *Neurology* **1998**, *50* (Suppl. S3), S1–S88. [CrossRef] [PubMed]

26. Poewe, W. Should Treatment of Parkinson's Disease Be Started with a Dopamine Agonist? *Neurology* **1998**, *51*, S21–S24. [CrossRef] [PubMed]

27. Rascol, O.; Brooks, D.J.; Korczyn, A.D.; de Deyn, P.P.; Clarke, C.E.; Lang, A.E. A Five-Year Study of the Incidence of Dyskinesia in Patients with Early Parkinson's Disease Who Were Treated with Ropinirole or Levodopa. *N. Engl. J. Med.* **2000**, *342*, 1484–1491. [CrossRef] [PubMed]

28. Hauser, R.A. Levodopa: Past, Present, and Future. *Eur. Neurol.* **2009**, *62*, 1–8. [CrossRef] [PubMed]

29. Fahn, S. Levodopa-Induced Neurotoxicity: Does It Represent a Problem for the Treatment of Parkinson's Disease? *CNS Drugs* **1997**, *8*, 376–393. [CrossRef]

30. Ahlskog, J.E.; Muenter, M.D. Frequency of Levodopa-Related Dyskinesias and Motor Fluctuations as Estimated from the Cumulative Literature. *Mov. Disord.* **2001**, *16*, 448–458. [CrossRef]

31. Olanow, C.W.; Kieburtz, K.; Odin, P.; Espay, A.J.; Standaert, D.G.; Fernandez, H.H.; Vanagunas, A.; Othman, A.A.; Widnell, K.L.; Robieson, W.Z.; et al. Continuous Intrajejunal Infusion of Levodopa-Carbidopa Intestinal Gel for Patients with Advanced Parkinson's Disease: A Randomised, Controlled, Double-Blind, Double-Dummy Study. *Lancet Neurol.* **2014**, *13*, 141–149. [CrossRef]

32. Senek, M.; Nielsen, E.I.; Nyholm, D. Levodopa-Entacapone-Carbidopa Intestinal Gel in Parkinson's Disease: A Randomized Crossover Study. *Mov. Disord.* **2017**, *32*, 283–286. [CrossRef]

33. Pålhagen, S.E.; Sydow, O.; Johansson, A.; Nyholm, D.; Holmberg, B.; Widner, H.; Dizdar, N.; Linder, J.; Hauge, T.; Jansson, R.; et al. Levodopa-Carbidopa Intestinal Gel (LCIG) Treatment in Routine Care of Patients with Advanced Parkinson's Disease: An Open-Label Prospective Observational Study of Effectiveness, Tolerability and Healthcare Costs. *Parkinsonism Relat. Disord.* **2016**, *29*, 17–23. [CrossRef]

34. Rascol, O.; Azulay, J.P.; Blin, O.; Bonnet, A.-M.; Brefel-Courbon, C.; Césaro, P.; Damier, P.; Debilly, B.; Durif, F.; Galitzky, M.; et al. Orodispersible Sublingual Piribedil to Abort OFF Episodes: A Single Dose Placebo-Controlled, Randomized, Double-Blind, Cross-over Study. *Mov. Disord.* **2010**, *25*, 368–376. [CrossRef] [PubMed]

35. Lai, K.L.; Fang, Y.; Han, H.; Li, Q.; Zhang, S.; Li, H.Y.; Chow, S.F.; Lam, T.N.; Lee, W.Y.T. Orally-Dissolving Film for Sublingual and Buccal Delivery of Ropinirole. *Colloids Surf. B Biointerfaces* **2018**, *163*, 9–18. [CrossRef] [PubMed]

36. Arora, S.; Ali, J.; Ahuja, A.; Khar, R.K.; Baboota, S. Floating Drug Delivery Systems: A Review. *AAPS PharmSciTech* **2005**, *6*, E372–E390. [CrossRef] [PubMed]

37. Jansen, E.N.H.; Meerwaldt, J.D. Madopar HBS in Parkinson Patients with Nocturnal Akinesia. *Clin. Neurol. Neurosurg.* **1988**, *90*, 35–39. [CrossRef]

38. Schapira, A.H.V.; Bezard, E.; Brotchie, J.; Calon, F.; Collingridge, G.L.; Ferger, B.; Hengerer, B.; Hirsch, E.; Jenner, P.; Le Novère, N.; et al. Novel Pharmacological Targets for the Treatment of Parkinson's Disease. *Nat. Rev. Drug Discov.* **2006**, *5*, 845–854. [CrossRef]

39. LeWitt, P.A.; Giladi, N.; Navon, N. Pharmacokinetics and Efficacy of a Novel Formulation of Carbidopa-Levodopa (Accordion Pill®) in Parkinson's Disease. *Parkinsonism Relat. Disord.* **2019**, *65*, 131–138. [CrossRef]

40. Sharma, S.; Lohan, S.; Murthy, R.S.R. Formulation and Characterization of Intranasal Mucoadhesive Nanoparticulates and Thermo-Reversible Gel of Levodopa for Brain Delivery. *Drug Dev. Ind. Pharm.* **2014**, *40*, 869–878. [CrossRef]

41. Bartus, R.T.; Emerich, D.; Snodgrass-Belt, P.; Fu, K.; Salzberg-Brenhouse, H.; Lafreniere, D.; Novak, L.; Lo, E.S.; Cooper, T.; Basile, A.S. A Pulmonary Formulation of L-Dopa Enhances Its Effectiveness in a Rat Model of Parkinson's Disease. *J. Pharmacol. Exp. Ther.* **2004**, *310*, 828–835. [CrossRef]

42. Bahrainian, S.; Mirmoeini, M.S.; Gilani, Z.; Gilani, K. Engineering of Levodopa Inhalable Microparticles in Combination with Leucine and Dipalmitoylphosphatidylcholine by Spray Drying Technique. *Eur. J. Pharm. Sci.* **2021**, *167*, 106008. [CrossRef]

43. Shankar, J.K.M.G.; Wilson, B. Potential Applications of Nanomedicine for Treating Parkinson's Disease. *J. Drug Deliv. Sci. Technol.* **2021**, *66*, 102793. [CrossRef]

44. Ahmad, J.; Haider, N.; Khan, M.A.; Md, S.; Alhakamy, N.A.; Ghoneim, M.M.; Alshehri, S.; Imam, S.S.; Ahmad, M.Z.; Mishra, A. Novel Therapeutic Interventions for Combating Parkinson's Disease and Prospects of Nose-to-Brain Drug Delivery. *Biochem. Pharmacol.* **2022**, *195*, 114849. [CrossRef] [PubMed]

45. Kar, K.; Pal, R.N.; Bala, N.N.; Nandi, G. Evaluation of Stability of Ropinirole Hydrochloride and Pramipexole Dihydrochloride Microspheres at Accelerated Condition. *Int. J. Appl. Pharm.* **2018**, *10*, 82–86. [CrossRef]

46. Li, S.; Liu, J.; Zhang, X.; Li, G. Near-Infrared Light-Responsive, Pramipexole-Loaded Biodegradable PLGA Microspheres for Therapeutic Use in Parkinson's Disease. *Eur. J. Pharm. Biopharm.* **2019**, *141*, 1–11. [CrossRef] [PubMed]

47. Subbarao, K.; Suresh, G. Preparation and Evaluation of Floating Microspheres of Pramipexole HCL-Review Article. *Am. J. Pharm. Tech. Res.* **2018**, *8*, 44–58. [CrossRef]

48. Skowyra, J.; Pietrzak, K.; Alhnan, M.A. Fabrication of Extended-Release Patient-Tailored Prednisolone Tablets via Fused Deposition Modelling (FDM) 3D Printing. *Eur. J. Pharm. Sci.* **2015**, *68*, 11–17. [CrossRef] [PubMed]

49. Goyanes, A.; Robles Martinez, P.; Buanz, A.; Basit, A.W.; Gaisford, S. Effect of Geometry on Drug Release from 3D Printed Tablets. *Int. J. Pharm.* **2015**, *494*, 657–663. [CrossRef]

50. Sadia, M.; Arafat, B.; Ahmed, W.; Forbes, R.T.; Alhnan, M.A. Channelled Tablets: An Innovative Approach to Accelerating Drug Release from 3D Printed Tablets. *J. Control. Release* **2018**, *269*, 355–363. [CrossRef]

51. Sun, Y.; Soh, S. Printing Tablets with Fully Customizable Release Profiles for Personalized Medicine. *Adv. Mater.* **2015**, *27*, 7847–7853. [CrossRef]

52. Than, Y.M.; Titapiwatanakun, V. Tailoring Immediate Release FDM 3D Printed Tablets Using a Quality by Design (QbD) Approach. *Int. J. Pharm.* **2021**, *599*, 120402. [CrossRef]

53. Đuranović, M.; Obeid, S.; Madžarevic, M.; Cvijić, S.; Ibrić, S. Paracetamol Extended Release FDM 3D Printlets: Evaluation of Formulation Variables on Printability and Drug Release. *Int. J. Pharm.* **2021**, *592*, 120053. [CrossRef]

54. Okwuosa, T.C.; Pereira, B.C.; Arafat, B.; Cieszynska, M.; Isreb, A.; Alhnan, M.A. Fabricating a Shell-Core Delayed Release Tablet Using Dual FDM 3D Printing for Patient-Centred Therapy. *Pharm. Res.* **2017**, *34*, 427–437. [CrossRef] [PubMed]

55. Quodbach, J.; Bogdahn, M.; Breitkreutz, J.; Chamberlain, R.; Eggenreich, K.; Elia, A.G.; Gottschalk, N.; Gunkel-Grabole, G.; Hoffmann, L.; Kapote, D.; et al. Quality of FDM 3D Printed Medicines for Pediatrics: Considerations for Formulation Development, Filament Extrusion, Printing Process and Printer Design. *Ther. Innov. Regul. Sci.* **2021**, *1*, 1–19. [CrossRef] [PubMed]

56. Schneider, C.; Langer, R.; Loveday, D.; Hair, D. Applications of Ethylene Vinyl Acetate Copolymers (EVA) in Drug Delivery Systems. *J. Control. Release* **2017**, *262*, 284–295. [CrossRef] [PubMed]

57. Genina, N.; Holländer, J.; Jukarainen, H.; Mäkilä, E.; Salonen, J.; Sandler, N. Ethylene Vinyl Acetate (EVA) as a New Drug Carrier for 3D Printed Medical Drug Delivery Devices. *Eur. J. Pharm. Sci.* **2016**, *90*, 53–63. [CrossRef] [PubMed]

58. Goyanes, A.; Kobayashi, M.; Martínez-Pacheco, R.; Gaisford, S.; Basit, A.W. Fused-Filament 3D Printing of Drug Products: Microstructure Analysis and Drug Release Characteristics of PVA-Based Caplets. *Int. J. Pharm.* **2016**, *514*, 290–295. [CrossRef]

59. Ibrahim, M.; Barnes, M.; McMillin, R.; Cook, D.W.; Smith, S.; Halquist, M.; Wijesinghe, D.; Roper, T.D. 3D Printing of Metformin HCl PVA Tablets by Fused Deposition Modeling: Drug Loading, Tablet Design, and Dissolution Studies. *AAPS PharmSciTech* **2019**, *20*, 195. [CrossRef]

60. Chamberlain, R.; Windolf, H.; Geissler, S.; Quodbach, J.; Breitkreutz, J. Precise Dosing of Pramipexole for Low-Dosed Filament Production by Hot Melt Extrusion Applying Various Feeding Methods. *Pharmaceutics* **2022**, *14*, 216. [CrossRef]

61. Windolf, H.; Chamberlain, R.; Quodbach, J. Predicting Drug Release from 3D Printed Oral Medicines Based on the Surface Area to Volume Ratio of Tablet Geometry. *Pharmaceutics* **2021**, *13*, 1453. [CrossRef]

62. Gültekin, H.E.; Tort, S.; Acartürk, F. An Effective Technology for the Development of Immediate Release Solid Dosage Forms Containing Low-Dose Drug: Fused Deposition Modeling 3D Printing. *Pharm. Res.* **2019**, *36*, 128. [CrossRef]

63. Windolf, H.; Chamberlain, R.; Quodbach, J. Dose-Independent Drug Release from 3D Printed Oral Medicines for Patient-Specific Dosing to Improve Therapy Safety. *Int. J. Pharm.* **2022**, *616*, 121555. [CrossRef]

64. El Aita, I.; Rahman, J.; Breitkreutz, J.; Quodbach, J. 3D-Printing with Precise Layer-Wise Dose Adjustments for Paediatric Use via Pressure-Assisted Microsyringe Printing. *Eur. J. Pharm. Biopharm.* **2020**, *157*, 59–65. [CrossRef] [PubMed]

65. Goyanes, A.; Wang, J.; Buanz, A.; Martínez-Pacheco, R.; Telford, R.; Gaisford, S.; Basit, A.W. 3D Printing of Medicines: Engineering Novel Oral Devices with Unique Design and Drug Release Characteristics. *Mol. Pharm.* **2015**, *12*, 4077–4084. [CrossRef] [PubMed]

66. Gioumouxouzis, C.I.; Baklavaridis, A.; Katsamenis, O.L.; Markopoulou, C.K.; Bouropoulos, N.; Tzetzis, D.; Fatouros, D.G. A 3D Printed Bilayer Oral Solid Dosage Form Combining Metformin for Prolonged and Glimepiride for Immediate Drug Delivery. *Eur. J. Pharm. Sci.* **2018**, *120*, 40–52. [CrossRef] [PubMed]

67. Khaled, S.A.; Burley, J.C.; Alexander, M.R.; Yang, J.; Roberts, C.J. 3D Printing of Five-in-One Dose Combination Polypill with Defined Immediate and Sustained Release Profiles. *J. Control Release* **2015**, *217*, 308–314. [CrossRef] [PubMed]
68. Komal, C.; Dhara, B.; Sandeep, S.; Shantanu, D.; Priti, M.J. Dissolution-Controlled Salt of Pramipexole for Parenteral Administration: In Vitro Assessment and Mathematical Modeling. *Dissolution Technol.* **2019**, *26*, 28–36. [CrossRef]
69. Tzankov, B.; Voycheva, C.; Yordanov, Y.; Aluani, D.; Spassova, I.; Kovacheva, D. Development and Invitro Safety Evaluation of Pramipexole-Loaded Hollow Mesoporous Silica (HMS) Particles. *Biotechnol. Biotechnol. Equip.* **2019**, *33*, 1204–1215. [CrossRef]
70. Krisai, K.; Charnvanich, D.; Chongcharoen, W. Increasing the Solubility of Levodopa and Carbidopa Using Ionization Approach. *Thai J. Pharm. Sci.* **2020**, *44*, 251–255.
71. Łaszcz, M.; Trzcínska, K.; Kubiszewski, M.; Kosmacínska, B.; Glice, M. Stability Studies and Structural Characterization of Pramipexole. *J. Pharm. Biomed. Anal.* **2010**, *53*, 1033–1036. [CrossRef]
72. Pawar, S.M.; Khatal, L.D.; Gabhe, S.Y.; Dhaneshwar, S.R. Establishment of Inherent Stability of Pramipexole and Development of Validated Stability Indicating LC–UV and LC–MS Method. *J. Pharm. Anal.* **2013**, *3*, 109–117. [CrossRef]
73. Panditrao, V.M.; Sarkate, A.P.; Sangshetti, J.N.; Wakte, P.S.; Shinde, D.B. Stability-Indicating HPLC Determination of Pramipexole Dihydrochloride in Bulk Drug and Pharmaceutical Dosage Form. *J. Braz. Chem. Soc.* **2011**, *22*, 1253–1258. [CrossRef]
74. Ledeti, A.; Olariu, T.; Caunii, A.; Vlase, G.; Circioban, D.; Baul, B.; Ledeti, I.; Vlase, T.; Murariu, M. Evaluation of Thermal Stability and Kinetic of Degradation for Levodopa in Non-Isothermal Conditions. *J. Anal. Calorim.* **2017**, *131*, 1881–1888. [CrossRef]
75. Shadambikar, G.; Kipping, T.; Di-Gallo, N.; Elia, A.G.; Knüttel, A.N.; Treffer, D.; Repka, M.A. Vacuum Compression Molding as a Screening Tool to Investigate Carrier Suitability for Hot-Melt Extrusion Formulations. *Pharmaceutics* **2020**, *12*, 1019. [CrossRef]
76. Chamberlain, R.; Windolf, H.; Burckhardt, B.B.; Breitkreutz, J.; Fischer, B. Embedding a Sensitive Liquid-Core Waveguide UV Detector into an HPLC-UV System for Simultaneous Quantification of Differently Dosed Active Ingredients during Drug Release. *Pharmaceutics* **2022**, *14*, 639. [CrossRef]
77. European Pharmacopoeia Commission 2.9.3. Dissolution Test for Solid Dosage Forms. In *European Pharmacopoeia*; EDQM: Strasbourg, France, 2020; Volume 10.2, pp. 326–333.
78. European Pharmacopoeia Commission 5.17.1. Recommendations on Dissolution Testing. In *European Pharmacopoeia*; EDQM: Strasbourg, France, 2020; Volume 10.2, pp. 801–807.
79. Costa, P.; Sousa Lobo, J.M. Modeling and Comparison of Dissolution Profiles. *Eur. J. Pharm. Sci.* **2001**, *13*, 123–133. [CrossRef]
80. Tanigawara, Y.; Yamaoka, K.; Nakagawa, T.; Uno, T. New Method for the Evaluation of in Vitro Dissolution Time and Disintegration Time. *Chem. Pharm. Bull.* **1982**, *30*, 1088–1090. [CrossRef]
81. U.S. Department of Health and Human Services. FDA Guidance for Industry: Dissolution Testing of Immediate Release Solid Oral Dosage Forms. *Academy* **1997**, *1*, 15–22.
82. Shah, V.P.; Tsong, Y.; Sathe, P.; Liu, J.-P. In Vitro Dissolution Profile Comparison—Statistics and Analysis of the Similarity Factor, F2. *Pharm. Res.* **1998**, *15*, 889–896. [CrossRef]
83. Nyholm, D.; Lennernäs, H. Irregular Gastrointestinal Drug Absorption in Parkinson's Disease. *Expert Opin. Drug Metab. Toxicol.* **2008**, *4*, 193–203. [CrossRef]
84. Doi, H.; Sakakibara, R.; Sato, M.; Masaka, T.; Kishi, M.; Tateno, A.; Tateno, F.; Tsuyusaki, Y.; Takahashi, O. Plasma Levodopa Peak Delay and Impaired Gastric Emptying in Parkinson's Disease. *J. Neurol. Sci.* **2012**, *319*, 86–88. [CrossRef]
85. Gundert-Remy, U.; Hildebrandt, R.; Stiehl, A.; Weber, E.; Zürcher, G.; da Prada, M. Intestinal Absorption of Levodopa in Man. *Eur. J. Clin. Pharmacol.* **1983**, *25*, 69–72. [CrossRef]
86. Awasthi, R.; Kulkarni, G.T. Decades of Research in Drug Targeting to the Upper Gastrointestinal Tract Using Gastroretention Technologies: Where Do We Stand? *Drug Deliv.* **2014**, *23*, 378–394. [CrossRef] [PubMed]
87. Klausner, E.A.; Lavy, E.; Barta, M.; Cserepes, E.; Friedman, M.; Hoffman, A. Novel Gastroretentive Dosage Forms: Evaluation of Gastroretentivity and Its Effect on Levodopa Absorption in Humans. *Pharm. Res.* **2003**, *20*, 1466–1473. [CrossRef] [PubMed]
88. Hoffman, A. Pharmacodynamic Aspects of Sustained Release Preparations. *Adv. Drug Deliv. Rev.* **1998**, *33*, 185–199. [CrossRef]
89. Nutt, J.G.; Holford, N.H.G. The Response to Levodopa in Parkinson's Disease: Imposing Pharmacological Law and Order. *Ann. Neurol.* **1996**, *39*, 561–573. [CrossRef] [PubMed]
90. Siepmann, J.; Peppas, N.A. Higuchi Equation: Derivation, Applications, Use and Misuse. *Int. J. Pharm.* **2011**, *418*, 6–12. [CrossRef] [PubMed]
91. Petropoulos, J.H.; Papadokostaki, K.G.; Sanopoulou, M. Higuchi's Equation and beyond: Overview of the Formulation and Application of a Generalized Model of Drug Release from Polymeric Matrices. *Int. J. Pharm.* **2012**, *437*, 178–191. [CrossRef]
92. Higuchi, T. Mechanism of Sustained-action Medication. Theoretical Analysis of Rate of Release of Solid Drugs Dispersed in Solid Matrices. *J. Pharm. Sci.* **1963**, *52*, 1145–1149. [CrossRef]
93. Erni, W.; Held, K. The Hydrodynamically Balanced System: A Novel Principle of Controlled Drug Release: (With 2 Color Plates). *Eur. Neurol.* **1987**, *27*, 21–27. [CrossRef]
94. Schneider, F.; Hoppe, M.; Koziolek, M.; Weitschies, W. Influence of Postprandial Intragastric Pressures on Drug Release from Gastroretentive Dosage Forms. *AAPS PharmSciTech* **2018**, *19*, 2843–2850. [CrossRef]
95. Qu, Y.; Lai, W.L.; Xin, Y.R.; Zhu, F.Q.; Zhu, Y.; Wang, L.; Ding, Y.-P.; Xu, Y.; Liu, H.F. Development, Optimization, and Evaluation In Vitro/In Vivo of Oral Liquid System for Synchronized Sustained Release of Levodopa/Benserazide. *AAPS PharmSciTech* **2019**, *20*, 312. [CrossRef]

96. Dinç, E.; Kaya, S.; Doganay, T.; Baleanu, D. Continuous Wavelet and Derivative Transforms for the Simultaneous Quantitative Analysis and Dissolution Test of Levodopa-Benserazide Tablets. *J. Pharm. Biomed. Anal.* **2007**, *44*, 991–995. [CrossRef] [PubMed]

97. Iravani, M.; Ferraro, L.; Xie, C.-L. Levodopa/Benserazide PLGA Microsphere Prevents L-Dopa-Induced Dyskinesia via Lower β-Arrestin2 in 6-Hydroxydopamine Parkinson's Rats. *Front. Pharmacol.* **2019**, *10*, 660. [CrossRef]

98. Freichel, O.L. Hydrokolloidretardarzneiformen Mit Endbeschleunigter Freisetzung. Ph.D. Thesis, Heinrich-Heine-Universität, Düsseldorf, Germany, 2002.

99. Goole, J.; Vanderbist, F.; Amighi, K. Development and Evaluation of New Multiple-Unit Levodopa Sustained-Release Floating Dosage Forms. *Int. J. Pharm.* **2007**, *334*, 35–41. [CrossRef] [PubMed]

100. Keerthi, M.L.; Kiran, S.; Rao, U.M.; Sannapu, A.; Dutt, A.G.; Krishna, K.S. Pharmaceutical Mini-Tablets, Its Advantages, Formulation Possibilities and General Evaluation Aspects: A Review. *Int. J. Pharm. Sci. Rev. Res.* **2014**, *28*, 214–221.

Chapter E:

Traceability Concept

Blind-Watermarking—Proof-of-Concept of a Novel Approach to Ensure Batch Traceability for 3D Printed Tablets

Hellen Windolf, Rebecca Chamberlain, Arnaud Delmotte, Julian Quodbach

Pretext

In addition to the possibilities offered by 3D printing in terms of dosage and release behavior, attention should also be paid to the fact that due to the ease and affordability of purchasing commercial printers, counterfeit printed drugs can be easily produced. This study followed an approach developed by Delmotte et al. to place a blind-watermarking bit-code on FDM 3D printed objects and detect this code with a 2D paper scanner. This idea has now been tested for 3D printed oral dosage forms in a proof-of-concept study. For this purpose, various polymers, blends, APIs, and print and scan settings were tested. Different influencing properties could be determined, which enable or prevent the insertion as well as the detection of the bits.

Evaluation of authorship:

author	idea [%]	study design [%]	experimental [%]	evaluation [%]	manuscript [%]
Hellen Windolf	40	50	90	75	75
Rebecca Chamberlain	-	5	-	10	10
Arnaud Delmotte	-	5	10	5	5
Julian Quodbach	60	60	-	10	10

Evaluation of Copyright permission:

Blind-Watermarking – Proof-of-Concept of a Novel Approach to Ensure Batch Traceability for 3D Printed Tablets

Hellen Windolf, Rebecca Chamberlain, Arnaud Delmotte, Julian Quodbach

Abstract

Falsified medicines are a major issue and a threat around the world. Various approaches are currently investigated to mitigate the threat. In this study, a concept is tested that encodes binary digits (bits) on the surface of Fused Deposition Modeling (FDM) 3D printed geometries. All that is needed is a computer, a FDM 3D printer and a paper scanner for detection. For the experiments, eleven different formulations were tested, covering the most used polymers for 3D printing in pharma: Ethylene-vinyl acetate (EVA), polyvinyl alcohol (PVA), polylactic acid (PLA), Hypromellose (HPMC), ethyl cellulose (EC), basic butylated-methacrylate-copolymer (EPO), and ammonio-methacrylate-copolymer type A (ERL). In addition, the scanning process and printing process were evaluated. It was possible to print up to 32 bits per side on oblong shaped tablets corresponding to the dimensions of market preparations of oblong tablets and capsules. Not all polymers or polymer blends were suitable for this method. Only PVA, PLA, EC, EC+HPMC, and EPO allowed the detection of bits with the scanner. EVA and ERL had too much surface roughness, too low viscosity, and cooled down too slowly preventing the detection of bits. It was observed that the addition of a colorant or active pharmaceutical ingredient (API) could facilitate the detection process. Thus, the process could be transferred for 3D printed pharmaceuticals, but further improvement is necessary to increase robustness and allow use for more materials.

Article

Blind-Watermarking—Proof-of-Concept of a Novel Approach to Ensure Batch Traceability for 3D Printed Tablets

Hellen Windolf [1][ID], Rebecca Chamberlain [1][ID], Arnaud Delmotte [2] and Julian Quodbach [1,3,*][ID]

1   Institute of Pharmaceutics and Biopharmaceutics, Heinrich Heine University, Universitätsstr. 1, 40225 Düsseldorf, Germany; hellen.windolf@hhu.de (H.W.); rebecca.chamberlain@hhu.de (R.C.)
2   Optical Media Interface Laboratory, Nara Institute of Science and Technology, 8916-5 Takayama-cho, Nara 630-0192, Japan; delmotte_ar@yahoo.fr
3   Department of Pharmaceutical Sciences, Utrecht Institute for Pharmaceutical Sciences, Utrecht University, Universiteitsweg 99, 3584 CG Utrecht, The Netherlands
*   Correspondence: j.h.j.quodbach@uu.nl

Abstract: Falsified medicines are a major issue and a threat around the world. Various approaches are currently being investigated to mitigate the threat. In this study, a concept is tested that encodes binary digits (bits) on the surface of Fused Deposition Modelling (FDM) 3D printed geometries. All that is needed is a computer, a FDM 3D printer and a paper scanner for detection. For the experiments, eleven different formulations were tested, covering the most used polymers for 3D printing in pharma: Ethylene-vinyl acetate (EVA), polyvinyl alcohol (PVA), polylactic acid (PLA), Hypromellose (HPMC), ethyl cellulose (EC), basic butylated-methacrylate-copolymer (EPO), and ammonio-methacrylate-copolymer type A (ERL). In addition, the scanning process and printing process were evaluated. It was possible to print up to 32 bits per side on oblong shaped tablets corresponding to the dimensions of market preparations of oblong tablets and capsules. Not all polymers or polymer blends were suitable for this method. Only PVA, PLA, EC, EC+HPMC, and EPO allowed the detection of bits with the scanner. EVA and ERL had too much surface roughness, too low viscosity, and cooled down too slowly preventing the detection of bits. It was observed that the addition of a colorant or active pharmaceutical ingredient (API) could facilitate the detection process. Thus, the process could be transferred for 3D printed pharmaceuticals, but further improvement is necessary to increase robustness and allow use for more materials.

Keywords: FDM 3D printing; traceability; blind-watermarking; anti-counterfeiting; falsified medicine; personalized medicine

1. Introduction

A global threat to healthcare is falsified and substandard medicine. Worldwide, an estimated 10% of medicines on the market are falsified [1–8]. In developing countries, the percentage of falsified and substandard drugs is higher, at about 10–30% [3,9–16]. Particularly at risk of counterfeiting are those drugs that are expensive or promise high sales. In developing countries, these are often antibiotics, viral drugs, or malaria preparations [14–17]. In rich countries, falsified medicines of new and expensive so-called "lifestyle pharmaceuticals" are most common, for example, hormones, steroids, and antihistamines [18]. Falsified drugs usually contain no active pharmaceutical ingredient (API), the wrong API or the wrong amount of API, and thus lead to no effect in the best cases [19]. However, they can also cause allergies and other side effects or even death [17,20]. For example, falsified vaccines do not contain an effective component and cannot protect patients from disease [21]. Counterfeited and falsified pharmaceuticals and medical devices are also currently a major issue during the SARS-CoV-2 pandemic. Falsified COVID-19 vaccines, fake masks, hand sanitizers, and self-test kits are sold to private persons, hospitals, and community pharmacies [22–25]. To prevent and trace these crimes, various systems have been integrated and are further

developed [17,26–30]. Since February 2019, for EU Member States, pharmaceuticals must correspond to the requirements of the Commission Delegated Regulation 2016/161 [31] and Directive 2011/62/EU [32]. Pharmaceuticals marketed in the EU must be serialized and equipped with tamper-evident or tamper-resistant function (manipulation-safe sealing of packaging carton) [33]. This sealing contains a unique 2D barcode which includes the batch, serial and national identification number, expiry date, and product information [34]. In addition, it is sometimes possible to identify falsified medicines visually (e.g., packaging, labelling, dosage units, watermarks, holograms), physically (discoloration, microscopical investigations of the surface, evaluation of disintegration), or chemically (API assay via spectroscopic, spectrometric, or chromatographic measurements) [30,35].

However, a new traceability-system is needed for personalized medicine, which is not or will likely not be produced industrially on a large scale, but individually in compounding centers, community pharmacies, or hospitals in small or on-demand batches [36–41]. These tailored medicines would be produced in the absence of serialized/anti-counterfeit packaging. Therefore, it would be highly advantageous if the traceability system is directly included in or on the dosage form. For oral dispersible films (ODF), Edinger et al. investigated a QR Code traceability system, which is printed with an ink-jet printer on a previous manufactured ODF [42]. In another study, a laser-based technology was used to mark an individual QR code on the surface of a tablet [30]. Rui et al. ink-jet printed fingerprint characters on the surface of tablets, which are detectable by pictures with regular smartphones [43].

Currently, a lot of research is being done on 3D printed dosage forms, as they enable low-cost, personalized drug therapy, especially the fused deposition modelling (FDM) method [37,44–52]. With this technique, a drug-loaded filament is conveyed through a heated nozzle on a print bed and the previous designed object is built layer-by-layer. The required filament is previously manufactured via hot-melt extrusion (HME). This type of individual dosage form is particularly interesting for developing countries. Production is inexpensive and the dosage can be flexibly adjusted so that a larger part of the population can be supplied with medicine. This could counteract the circumvention of the health care system and the purchase of drugs on the black market. However, commercial FDM 3D printers are available for anyone to purchase, and the process is easy to learn, so counterfeiting can be expected with this innovative dosage form as well. That is why various research groups are currently working on different ways to avoid counterfeit. Trenfield et al. developed a track-and trace system for 3D printed oral dosage forms with a combined 2D printing technology for printed QR codes and data matrices on the surface of "printlets" [39]. It was possible to scan these codes with a smartphone device.

In this proof-of-concept study, the blind-watermarking concept developed by Delmotte et al. [53] was transferred to FDM 3D printed oral dosage forms. In this method, binary digits (bits) are inserted on the flat sides of the object via a variation of the layer thickness. The bits are inserted into the previously created G-Code using a self-programmed C++ script. The insertion of individual blind-watermarking bits is intended to implement a security system that will prevent falsifying the drug. The change of the layer thickness has no influence on printing time, appearance, weight, or API content of the dosage form. In addition, no other equipment is needed for the implementation, except for a FDM 3D printer. A simple paper scanner is used to detect the bits as well as a Python script. The concept was tested by the research group on large non-pharmaceutical objects printed with polylactic acid (PLA). This traceability approach could improve the safety of 3D printed tablets, as the process could be established in community pharmacies and hospitals, requiring no equipment other than a FDM 3D printer and a paper scanner. In our study, oblong shaped tablets were designed, and it was examined whether bits could also be inserted on these geometries. Various materials were tested that could be considered for FDM printed oral dosage forms, in some cases also containing API. Different dimensions, variable number of bits, scanning methods, and two layer heights were tested.

2. Materials and Methods

2.1. Materials

The transfer of the blind-watermarking concept of Delmotte et al. [53] was first tested with commercial polylactic acid filaments (PLA, Bavaria filaments, Freilassing, Germany). After the geometries and G-Codes were created with the desired number of bits, self-extruded pharmaceutical filament compositions were tested (Table 1). These filaments differed in appearance, in color, in roughness, and in their melt viscosity.

Table 1. Composition of the filaments used.

Filament	Materials	Concentration/%	Manufacturer/Source
PLA	Polylactic acid (PLA)	100	Bavaria filaments, Freilassing, Germany
PVA	Polyvinyl alcohol (PVA)	100	Parteck MXP®, Merck, Darmstadt, Germany
PVA + PZQ [37]	Polyvinyl alcohol (PVA)	95	Parteck MXP®, Merck, Darmstadt, Germany
	Praziquantel (PZQ)	5	Bayer AG, Leverkusen, Germany
PVA + PDM [37]	Polyvinyl alcohol (PVA)	84	Parteck MXP®, Merck, Darmstadt, Germany
	Mannitol	10	Parteck M®, Merck, Darmstadt, Germany
	Pramipexole 2 HCl*H$_2$O (PDM)	5	Chr. Olesen, Gentofte, Denmark
	Fumed silica	1	Aerosil® 200 VV Pharma, Evonik, Essen, Germany
PVA + Triam [54]	Triamcinolone acetonide (Triam)	5	Farmabios, Gropello Cairoli, Italy
	Polyethylene glycol 300	10	Polyglycol 300, Clariant, Pratteln, Switzerland
	Polyvinyl alcohol (PVA)	85	Parteck MXP®, Merck, Darmstadt, Germany
PVA + colorant	Polyvinyl alcohol (PVA)	84	Parteck MXP®, Merck, Darmstadt, Germany
	Mannitol	10	Parteck M®, Merck, Darmstadt, Germany
	Methylene blue	5	Spectrum Lab Products, Gardena, CA, US
	Fumed silica	1	Aerosil® 200 VV Pharma, Evonik, Essen, Germany
EPO + API	Basic butylated-methacrylate-copolymer (EPO)	80	Eudragit E PO®, Evonik, Essen, Germany
	Pramipexole 2 HCl*H$_2$O (PDM)	20	Chr. Olesen, Gentofte, Denmark
EC	Ethyl cellulose (EC)	100	Aqualon® N10, Ashland, KY, US
EC + HPMC [55]	Ethyl cellulose (EC)	72.93	Aqualon® N10, Ashland, KY, US
	Hypromellose (HPMC)	16.67	Metolose 60SH 50, Shin Etsu Chemical, Tokyo, Japan
	Triethyl citrate	10	Citrofol AI Extra, Jungbunzlauer, Basel, Switzerland
	Fumed silica	0.4	Aerosil® 200 VV Pharma, Evonik, Essen, Germany
EVA + PVA	Ethylene-vinyl acetate copolymer 82:18 (EVA)	25	Escorene® FL01418, TER Chemicals, Hamburg, Germany
	Polyvinyl alcohol (PVA)	65	Parteck MXP®, Merck, Darmstadt, Germany
	Mannitol	10	Parteck M®, Merck, Darmstadt, Germany
EVA + PVP-VA + API	Ethylene-vinyl acetate copolymer 82:18 (EVA)	35	Escorene® FL01418, TER Chemicals, Hamburg, Germany
	Vinylpyrrolidone-vinyl acetate copolymer 60:40 (PVP-VA)	15	Kollidon VA 64®, BASF, Ludwigshafen a. R., Germany
	Levodopa	40	Zhejiang Wild Wind Pharmaceutical, Dongyang, China
	Benserazide	10	BioPharma Synergies, Barcelona, Spain
ERL + API [56]	Anhydrous Theophylline	30	BASF, Ludwigshafen a. R., Germany
	Ammonio-methacrylate-copolymer type A (ERL)	62.6	Eudragit® RL PO, Evonik, Essen, Germany
	Stearic acid	7	Baerlocher, Lingen, Germany
	Fumed silica	0.4	Aerosil® 200 VV Pharma, Evonik, Essen, Germany

2.2. Methods

2.2.1. Hot Melt Extrusion

The self-extruded filaments were prepared by hot-melt extrusion (HME) [37,44,52,54,55]. A co-rotating twin-screw extruder (Pharmalab HME 16; Thermo Fisher Scientific, Waltham, MA, USA) was used with an in-house manufactured die (1.85 mm diameter) to produce filaments with a diameter of 1.75 mm. A haul-off unit of a winder (Model 846700, Brabender, Duisburg, Germany) was used to achieve the required filament diameter. This was controlled with a laser-based diameter measurement module (Laser 2025 T, Sikora, Bremen, Germany) with a readout rate of 1 Hz.

2.2.2. Creation of Geometries, G-Codes and Bits

Different oblong tablets were designed with various lengths and heights to investigate what sizes are necessary for a certain number of bits and how many bits can fit on a large oblong tablet. Since bits are generated only on straight, flat sides and can thus be scanned with a 2D scanner, the oblong design was selected. For the design, the computer-aided design (CAD) software Fusion360® (Autodesk, San Rafael, USA) was chosen. For generating the G-Code, PrusaSlicer® (2.2.0, Prusa Research, Prague, Czech Republic) was used. In the settings, the temperature, speed, and layer height were adjusted (Section 2.2.4). The extrusion width was set to 0.4 mm and the variable layer thickness option disabled, so the C++ script for bit-generation could insert the layer thickness changes to encode the bits. In addition, care was taken to ensure that each new layer starts at the same position and the resulting seam is not in the watermarked patch. In the C++ script for bit-insertion, the length of the flat tablet-side for the bits was set (Figure 1, green + red) as well as the number of bits per line, number of bits in height, and number of parity bits. Subsequently, a G-Code with the desired number of bits and parity-bits was created and inserted in the G-Code of the tablet geometry.

Figure 1. Detail from the watermark-embedding process. The side length (green + red) is recognized without the roundings and is encoded with bits.

2.2.3. Watermark Embedding

For the blind-watermarking method, the layer thickness is locally modified, which results in a pattern on the surface of the 3D printed object. Normally, the layer thickness of a FDM 3D print is constant with little noise. For embedding the watermark, a number of bits is selected, as well as the number of separating layers between the bits. The code is formed by the interaction of two layers, which in sum always have the same thickness. If the lower layer becomes thinner (1 − a) to encode a 0, the upper layer compensates this with 1 + a layer thickness. If the lower layer is thicker with 1 + a, to encode a 1, the upper layer balances this again with 1 − a layer thickness. Thus, despite the differences in thickness between the layers above and below, the result is an even layer so that the code is clearly recognizable (Figure 2). As a minimum distance between encoding bit layers, two separating layers were selected. It was avoided to insert the blind-watermark too close to the bottom or top of the tablet, because the tablets often stuck to the print bed or because the printing precision was insufficient in these layers. Therefore, the bits were only encoded at least four layers above the print bed and at least four layers below the top of the tablet.
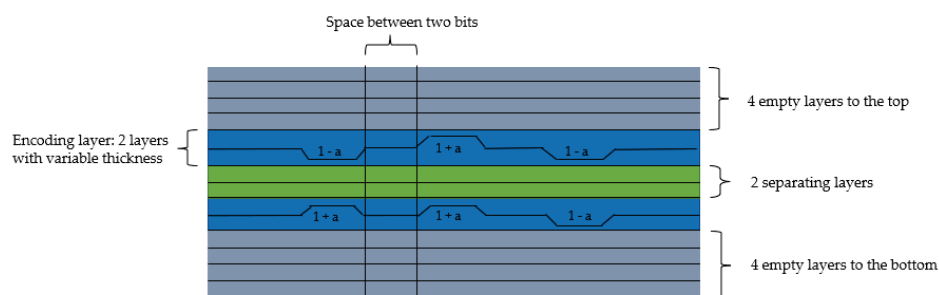
Figure 2. Scheme of the watermark embedding parameters and procedure. Adapted from the illustration in the original publication [53], IEEE, 2020.

2.2.4. 3D Printing Process

The oblong tablets were printed with a FDM 3D Printer Prusa i3MK3 (Prusa Research, Prague, Czech Republic). The settings of the printing process were adjusted for each filament (Table 2). Print settings were determined manually to enable the best possible print image. In most cases, the best results were achieved at the lowest possible temperatures. If the printing temperature was too low, the nozzle became clogged, and no molten filament flowed through it. If the temperature was too high, the surface of the tablet became uneven. For EVA and PVA/PVA + PZQ filaments, higher temperatures had to be used because the layers adhered poorly to each other. At higher temperatures, they were better bonded. EVA filaments were very flexible, and the conveying wheels in the print head could not be used fully to transport the filament through the nozzle, otherwise the filament would wrap around the conveying wheels after a few minutes. The necessary transport to the nozzle could only be ensured by a high printing temperature, as this caused the filament to melt faster and offer less resistance. For a fast cooling of the printed object, the fan was activated. The printing speed was set to 10 mm/s, which is very low for FDM 3D printing. However, for the materials used and following the recommendation of Delmotte et al. [53], a low printing speed should reduce artifacts.

Table 2. Settings of the 3D printing process.

Filament	Bed Temperature/°C	Nozzle Temperature/°C
PLA	60	215
PVA	90	190
PVA + PZQ	90	188
PVA + PDM/colorant	60	188
PVA + Triam	60	190
EPO + API	45	176
ERL + API	55	180
EC	60	180
EC + HPMC	63	180
EVA + PVA	50	220
EVA + PVP-VA + API	50	220

2.2.5. Scan and Detection

To detect the bits, the printed oblong tablets ($n = 3$) were placed with the flat side on a paper scanner (Epson Expression Premium XP-610, Suwa, Nagano Prefecture, Japan) and scanned with the parameters shown in Table 3. The resolution was set to 1200 dpi. Higher resolution settings did not result in better scans and detectability but increased the processing time of the analytical computer script. During scanning, the tablets were covered with a black box so that the process would not be disturbed by room light and the scanning light would not be reflected.

Table 3. Settings of the scanning process.

Filament	Brightness	Contrast
PLA	−19	31
PVA	−100	30
PVA + PZQ	−100	55
PVA + PDM	−19	70
PVA + colorant	−50	25
PVA + Triam	−100	50
EPO + API	−100	60
ERL + API	−100	40
EC	−45	40
EC + HPMC	−80	55
EVA + PVA	−70	40
EVA + PVP-VA + API	−70	40

Afterwards, the scanned files were analyzed with a self-programmed Python script for detection. A region of interest surrounding the watermark area is defined and the script runs an algorithm to extract the encoded bits by determination of layer thickness variations. A more detailed description of the algorithm can be found in Delmotte et al. [53]. Afterwards the result is displayed (Figure 3).
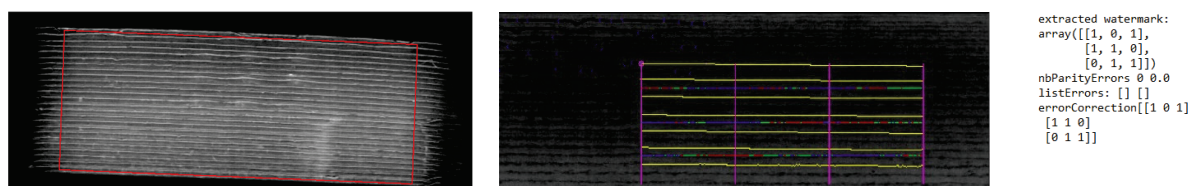
Figure 3. Example of the detection process (EC + HPMC); form left to right: scanned 3D printed oblong tablet with region of interest, detected watermark-patch and result of the bit detection.

2.2.6. Melt Viscosity Measurements

To be able to describe the print behavior of the polymers and blends used, the rheological properties were investigated ($n = 1$). The viscosity was measured with a Modular Advanced Rheometer System (HAAKE MARS 60, Thermo Fisher Scientific, Waltham, MA, USA). Samples of 500 mg each were weighed in. The gap was adjusted to 1 mm and an angular speed of 6.3 rad/s was set. A temperature range was scanned to be able to follow the viscosity curve of the polymers. This range covered the print temperature used. The data was recorded with HAAKE RheoWin (4.87.0006, Thermo Fisher, Waltham, MA, USA) with a frequency of 1 Hz. For the measurements, the API was replaced with mannitol to reduce the toxicity profile of the mixtures.

3. Results and Discussion

3.1. Minimum and Maximum Size of Oblong Shaped Tablets

The blind-watermarking system can, in its current version, only modify straight and flat surfaces. No bits can be implemented on rounded surfaces. Additionally, the long side must have a certain length so that the script can recognize the side and insert a desired number of bits. As a security measure, parity bits are inserted to recognize errors in the detected bits. The minimum bit count is four bits per site (2×2) with four parity bits (Table 4). In the original publication [53], a layer height of 0.2 mm was recommended. With this most simple setup, 16 different combinations are possible (2^4) for information deposit, and the required length was calculated to be 12 mm (Figure 4).

Table 4. Minimum bit insertion per side (parity bits marked in grey).

0	1	1
1	1	0
1	0	1
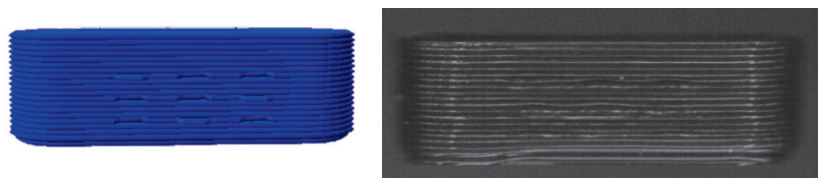
Figure 4. Pictured G-Code (**left**) and scanning image of 3D printed oblong tablet with 4 bits + 5 parity bits per side (**right**). Oblong tablet size: 12 mm length, 4 mm height, 4 mm width.

Subsequently, it was determined how many bits fit on an oblong shaped tablet of maximum size, which will still meet the criteria for swallowability. For this purpose, market preparations with large oblong tablets or capsules were examined regarding their size and the dimensions were adopted [57]. The largest oblong tablets have a length of 23 mm, a height of 6 mm and a width of 8 mm (e.g., Amoxicillin Sandoz 1000 mg: 23 mm × 8 mm × 6 mm; Furobeta® 500 betapharm Arzneimittel GmbH: 23 × 8 × 6 mm; Rosuvastatin/Amlodipin-ratiopharm® capsules 23 × 8.1 mm). A dosage form of such dimensions was designed (Figure 5). The number of bits was increased until the patch became too large so that the required distance between bits was no longer possible. The maximum number of bits per line was nine bits (including one parity bit per row) and five bits in height, again with one parity bit per column (Table 5).
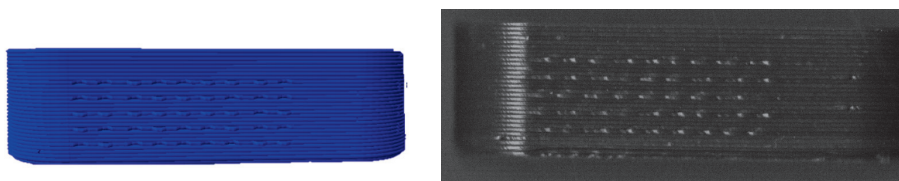
Figure 5. Pictured G-Code (**left**) and scanning image of 3D printed oblong tablet with 32 bits + 13 parity bits per side. Oblong tablet size: 23 mm length, 6 mm height, 8 mm width.

Table 5. Maximum bit code: 9 bits per line, 5 bits in height. 8 × 4 bits with 13 parity bits (grey marked).

0	0	1	0	0	1	1	1	0
0	0	0	1	1	1	0	0	1
1	1	1	1	1	1	1	0	1
1	0	0	1	0	0	1	0	1
0	1	0	1	0	1	1	1	1

This number of bits generates a wide spectrum of possible combinations (2^{32}). Thus, this method allows variable information content from the smallest bit set of 4 bits to 32 bits per side. Depending on the size of the tablet, the number of bits can be adjusted for the necessary information content.

3.2. Variation in Layer Height

To further increase the number of bits per tablet side, it was tested whether it is possible to reduce the layer height from 0.2 mm as recommended by Delmotte et al. [53] to 0.1 mm, thus doubling the number of bits per side. The smallest tablet size (12 × 4 × 4 mm)

was chosen for this purpose, as it is particularly interesting to be able to increase the bit number for smaller dimensions (Figure 6). The filament used was PVA + colorant.
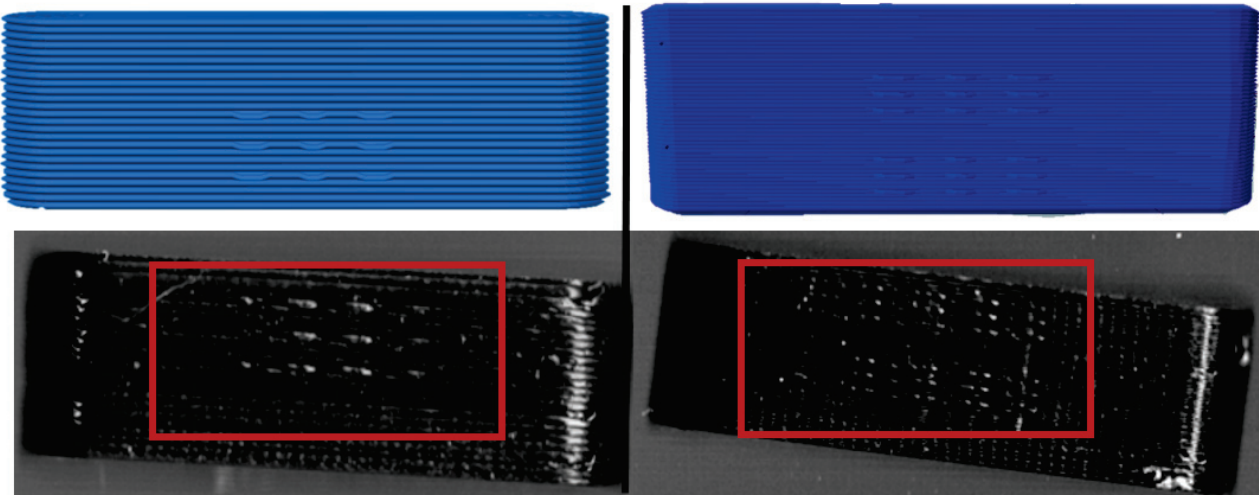
Figure 6. G-Codes (**top**) and scanning images of 3D printed oblong tablets (**bottom**). Left: 0.2 mm layer height (9 bits), right: 0.1 mm layer height (18 bits).

With the smaller layer height, in theory up to 18 bits can be encoded in the given geometry. The detection for the reference tablet with 0.2 mm layer height worked without problems, and the correct code could be detected directly (Figure 7 top). For the tablet with 0.1 mm layer height, both patches could be detected, but the correct code was not generated immediately. The correct code was determined by the error correction function shown in Figure 7 (bottom) using the parity bits. The lower distance between encoding layers made detection of the bits difficult. It is possible to decrease the layer height and thus increase the number of bits per tablet. Yet, a layer height of 0.1 mm should be considered to be too low. Proper detection using the parity bits is feasible, but considering that the reduction of the layer height from 0.2 mm to 0.1 mm also doubles the printing time per tablet, the drawbacks become prohibitive.

Figure 7. Top: results of the detection process of printed tablet with 0.2 mm layer height (9 bits). **Bottom**: Results of the detection process of printed tablet with 0.1 mm layer height (18 bits).

3.3. Optimization of the Scanning Process

During the scanning process it was observed that there is a difference in the visibility of bits, depending on the orientation of the tablet to the scan light.

When the samples were oriented perpendicular to the moving scan light, individual bits reflected the light, and the bits were better visible on the image than in a parallel orientation to the scan light. In parallel orientation, hardly any contrast was visible between the bit and the encoding layer. Yet, the layer structure itself was better visible (Figure 8, used bit code Table 6).
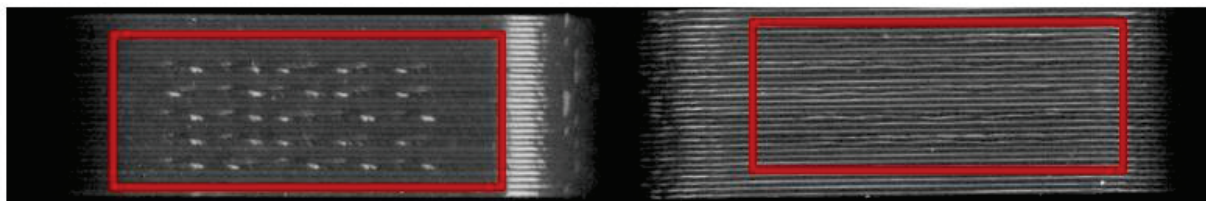
Figure 8. Influence of the orientation of the tablet with bits to the scan light. **Left**: perpendicular to the scan light, **right**: parallel to the scan light. Tablet: PLA with 25 bits.

Table 6. Bit code: 5 bits per line, 5 bits in height. 4×4 bits with 9 parity bits (grey marked).

1	1	0	0	0
0	1	1	0	0
1	1	0	1	1
1	1	0	0	0
1	0	1	1	1

For an automatized detection, the parallel orientation to the direction of the scanning light is more suitable, as the layer structure can be seen more clearly and the differences in layer thickness can be detected more easily. The script is oriented on the layer pattern that results from the 0.2 mm layer heights. The bit variations due to $(1 - a)$ and $(1 + a)$ layer thicknesses are recognized by the script due to the deviation from the normal 0.2 mm layer pattern. This is better detectable with the parallel scan. For the eye, on the other hand, the blind watermarking code is better detectable with the perpendicular alignment, since the reflections of the bits clearly show the intended unevenness. Here, however, the layer structure is not clearly visible.

3.4. Variations of the Material

To test the applicability of blind-watermarking for 3D printed tablets, various materials were evaluated. Common polymers that are often used for FDM 3D printing of drugs were utilized: PLA, PVA, EPO, EVA, EC, HPMC, PVP-VA, and ERL [37,47,52,55,58–63]. These polymers were in some cases mixed with APIs, but also with colorants to observe any influence. The same bit code was used as shown in Table 4 and Figure 4, as well as the associated G-codes with the appropriate print temperatures for each filament. $13 \times 5 \times 5$ mm tablets of each formulation were printed and scanned and the detection was evaluated. Only formulations where the bits were identified directly in all cases were considered suitable (Table 7). A layer height of 0.2 mm was used to keep the error level low and to be able to draw more accurate conclusions about the materials. The tablets were scanned in both parallel and perpendicular orientations to obtain optimal images suitable for the script. In the end, it was always the images in parallel orientation that had the most suitable structure for the script.

Table 7. Material variations: images, scans and detection result.
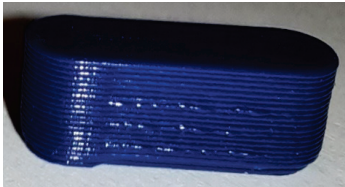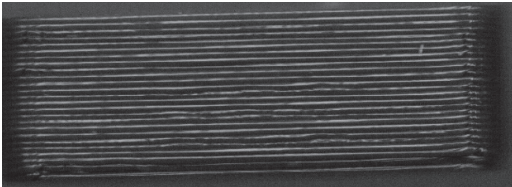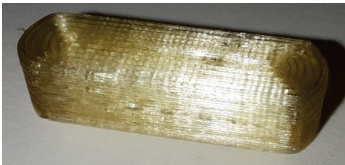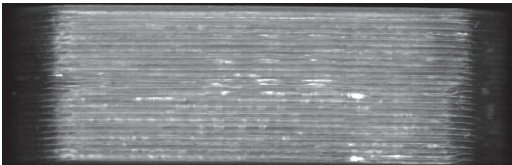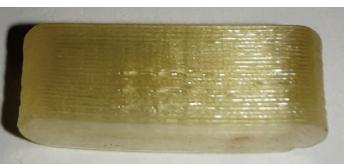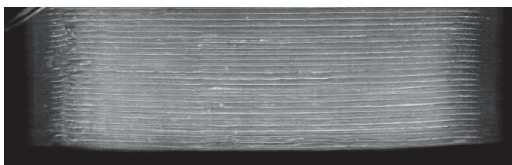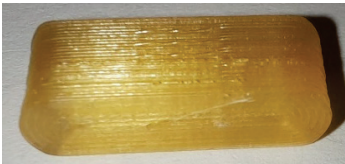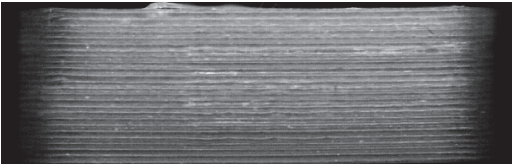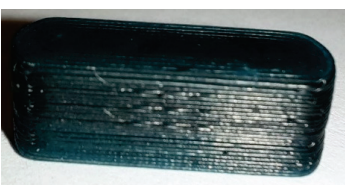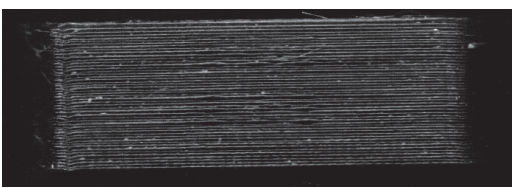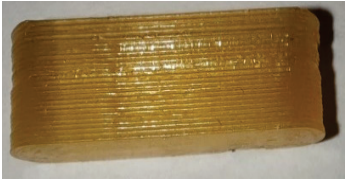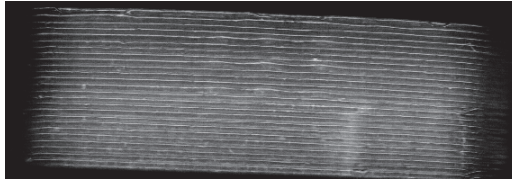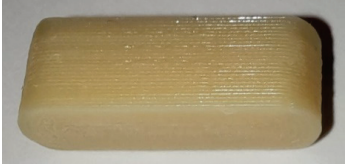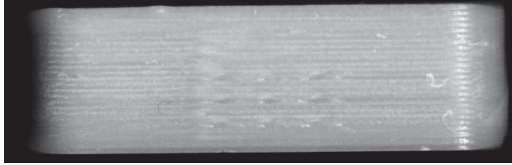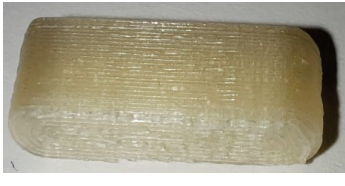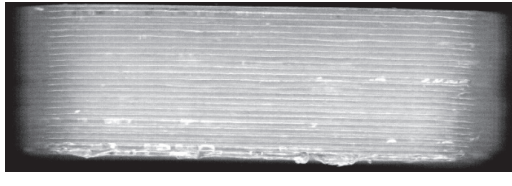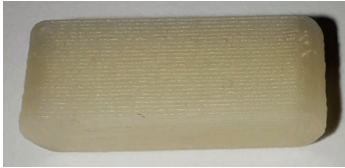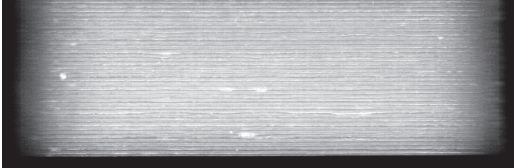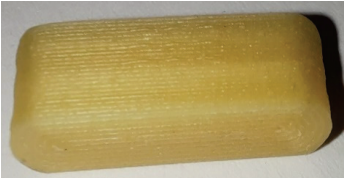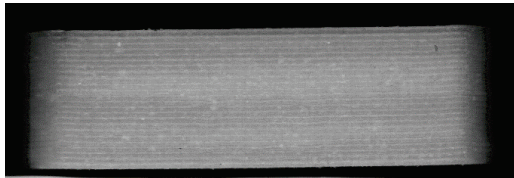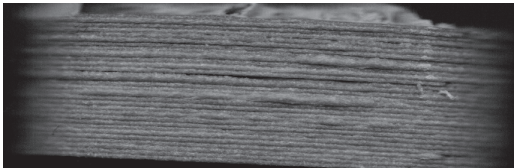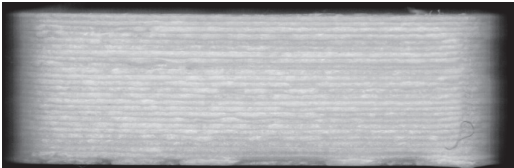
Filament	Image	Scan (Parallel Orientation)	Detection	
PLA			Yes 3/3	(a)
PVA			No 0/3	(b)
PVA + PZQ			No 1/3	(c)
PVA + PDM			No 0/3	(d)
PVA + colorant			Yes 3/3	(e)
PVA + Triam			Yes 3/3	(f)
EPO + API			Yes 3/3	(g)
EC			Yes 3/3	(h)

Table 7. *Cont.*

Filament	Image	Scan (Parallel Orientation)	Detection	
EC + HPMC			Yes 3/3	(i)
EVA + PVA			No 0/3	(j)
EVA + PVP -VA + API			No 0/3	(k)
ERL + API			No 0/3	(l)

During printing and scanning, it became apparent that not every material is suitable for a blind-watermarking approach. The printed tablets made of PLA (Table 7 (a)) could be printed and scanned well. The bits were recognized by the written Python script without any problems. Delmotte et al. [53] already investigated different colors of commercial PLA filaments. By adjusting the brightness and contrasts during the scanning process, different colors could be used for blind-watermarking. In some printed tablets (Table 7 (b–d)), despite adjusting the brightness and contrast of the scanner, the visibility of the bits could not be ensured because the dosage forms were too transparent and reflective (PVA, PVA + PZQ, PVA + PDM) and the scan light was reflected by the object. For the eye, the bits were visible, but not detectable with the scanning light. Using a different imaging technique might be able to solve this issue. In our study, we examined if this issue can be solved by mixing a colorant into the filament so that it was more opaque (PVA + Methylene blue, Table 7 (e)) with less reflection. The reflection-problem should also be solved by adding an API or excipient that did not completely dissolve in the polymer or melted during HME and 3D printing, so that the filament looked slightly milky. As a result, the scanning light was not reflected as strongly, and the bits could be detected (PVA + Triam, Table 7 (f)). The printed tablets with EPO, EC and EC + HPMC (Table 7 (g–i)) were able to visualize the bits, so that the bits could be presented well during the scanning process and the detection script could read out the code. The tablets had a cloudy appearance and neither color nor transparency had a negative impact.

EVA filaments did not result in visible bits imprinted into the tablets (Table 7 (j + k)). It was assumed that the formulations with EVA had a too low melt viscosity. In this case the polymer would only flow out of the nozzle and not retain the bit structure. This could not be remedied by lowering the print temperature from 220 °C to 210 °C, because the nozzle would clog, and the flexible filament would begin to wrap around the conveyor

wheels in the print head. During printing it was observed that the printed filament is also likely to take longer to cool and solidify so that the movement of the print head and the following layers destroy the fine bit structure.

The detection of tablets printed from filaments with a rough surface after HME, which is also apparent after printing (EVA + PVP-VA + API; ERL + API, Figure 7 (k + l)) was not possible. A rough surface can result from immiscible excipients and APIs in HME, high polymer blend viscosity, as well as from a high proportion of unmelted, suspended components [64,65]. This noise of the rough surface makes it impossible to recognize the inserted bits.

During the printing process, it was also observed that setting the correct print temperature had a major impact on the appearance of blind-watermarking patches. In addition to lowering the melt viscosity, increased temperature can also lead to the formation of gas bubbles. In the case of PVA + PZQ and EPO+API filaments, even a small difference in printing temperature (2–9 °C) resulted in significant changes in the printed material (Figure 9). If the temperature was slightly too high, gas bubbles were formed in the printed filament, which made the surface of the tablet appear inhomogeneous and did not allow bits to be detected. This may be due to thermal degradation of the API or polymer, moisture in the filament, or due to the release of water. Since PVA is a very hydrophilic polymer, it may absorb water from the environment after a short storage time, which evaporates during printing and leaves gas bubbles. The API PDM contains hydrate water, which is degraded at high temperature [52]. These processes can be controlled by adjusting the print temperature and optimizing the storage conditions. Since lowering the printing temperature increases the melt viscosity, this can cause the nozzle of the 3D printer to clog, and the filament cannot be printed. This must be considered when selecting the polymer composition.
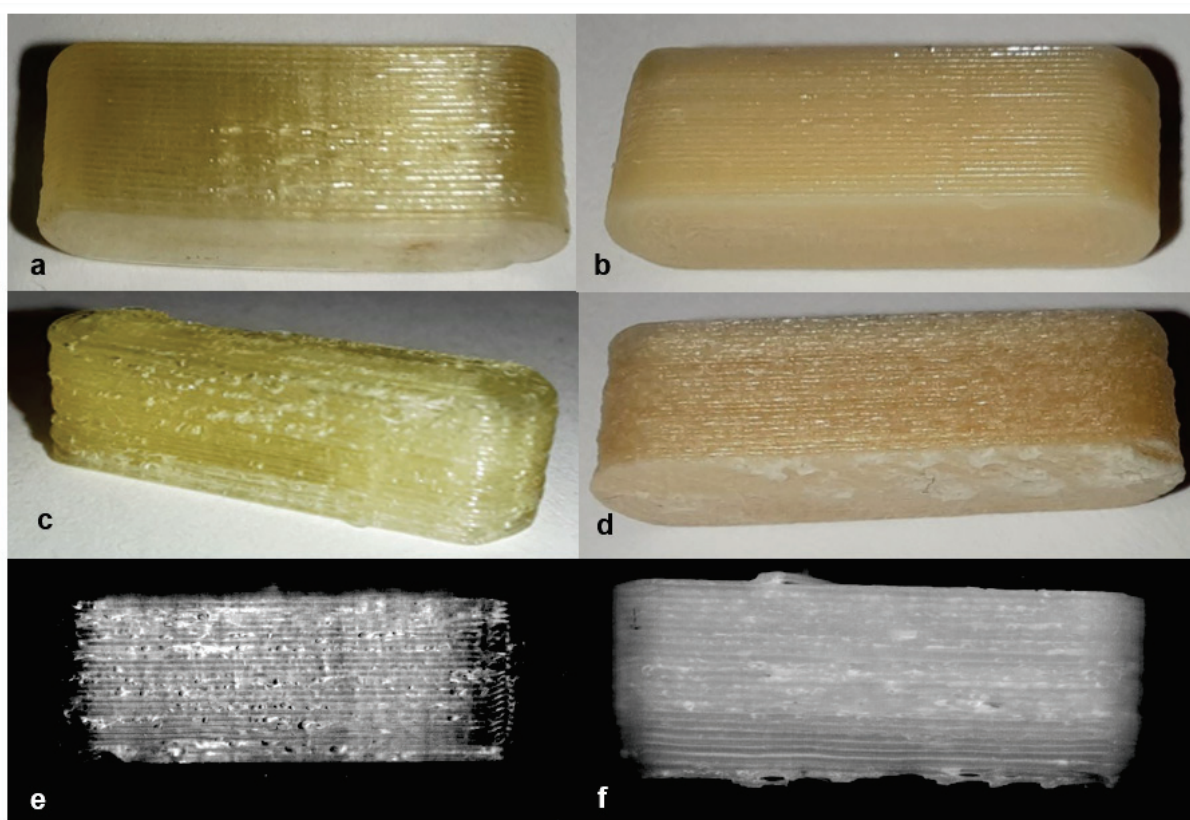
Figure 9. Filament PVA + PZQ printed at 188 °C (**a**) and 190 °C (**c**). Filament EPO + API printed at 176 °C (**b**) and 185 °C (**d**). Scanning image (**e**) present the scan of printed tablet shown in (**c**), and scanning image (**f**) present the scan of printed tablet shown in image (**d**).

Since it was assumed that the melt viscosity seems to have a major influence on the printing result, rheological measurements of the formulations without API were conducted to find a possible quantifiable parameter to exclude or include filaments in advance for this process (Table 8). The filament blends containing ERL were omitted, as it was the roughness that led to the poor detection and not the melt viscosity.

Table 8. Melt viscosity of the used materials at their specific print temperatures.

Filament	Nozzle Temperature/°C	Melt Viscosity/kPa*s
PVA	190	7.251
PVA + PZQ/PDM/colorant	188	6.407
PVA + Triam	190	4.321
EPO + API	176	0.169
EC	180	24.200
EC + HPMC	180	15.920
EVA + PVA	220	0.251
EVA + PVP-VA + API	220	0.135

The results of the viscosity measurement confirm that the melt viscosity has a major influence on the blind-watermark method. The filaments suitable for the blind-watermarking process have a melt viscosity between 4–24 kPa*s (PVA mixtures and EC mixtures). The filaments made of EVA have a very low viscosity of only 0.25 kPa*s, which was already suspected due to the non-existing bit structure in the printed EVA-tablets. The EVA + PVP-VA blend has the lowest viscosity, which is due to the high EVA content. Additionally, other excipients can reduce the viscosity, for example APIs or in this case mannitol. However, the EPO mixture also has a very low viscosity (0.169 kPa*s), although it was possible to detect the blind-watermarking patches made with these filaments. It seems that the property to solidify quickly after the polymer is melted has also a major influence on the blind-watermarking process and can compensate for the melt viscosity. Unfortunately, it was not possible to measure the solidification behavior over time. Therefore, this hypothesis cannot be confirmed here. An overview of the results of the blind-watermarking proof-of-concept is shown in Table 9.

Concluding, various influences can determine whether a material or mixture is suitable for the blind-watermarking process. Since the scanning process is very susceptible to light reflections, materials that are transparent or reflect light too strongly are not suitable, an issue that might be solved with another imaging technique. In addition, the quality of the blind-watermark code depends on the melting and solidification properties of the materials, so that only materials that have a high melt viscosity or very rapid solidification behavior can be considered. It must also be ensured that the filaments have a surface as homogeneous and smooth as possible, so that the inherent structure of the filaments does not interfere with the structure of the bit code. However, these influences can also be modified by adding a colorant or API that makes the filament appear less transparent and by changing the filament composition with components that increase melt viscosity and decrease solidification time.

Table 9. Overview of detection influences and results.

Filament	Transparent/ Reflective	Surface Roughness	Visible to the Eye	Detectable	Likely Reason
PLA	no	no	yes	yes	Good solidification behavior, no roughness, no reflection.
PVA	yes	no	yes	no	Transparent, reflection of the scan-light. High melt viscosity.
PVA + API	Dissolved API: yes Susp. API: no	no	yes	Dissolved API: no Susp. API: yes	Transparent, dissolved API does not decrease the reflection of the scan-light, suspended API or excipient forms slight milky filaments. High melt viscosity.
PVA + colorant	no	no	yes	yes	The colorant decreases the transparency of PVA. High melt viscosity.
EPO + API	no	no	yes	yes	Good solidification behaviour, low melt viscosity, no roughness, no reflection.
ERL + API	no	yes	no	no	Too rough, no bits recognizable.
EC	no	no	yes	yes	Good solidification behaviour, high melt viscosity, no roughness, no reflection.
EC + HPMC	no	no	yes	yes	Good solidification behaviour, high melt viscosity, no roughness, no reflection.
EVA + PVA	no	no	no	no	Solidification of the printed object occurs too slowly + low melt viscosity, the bits and layers deform.
EVA + PVP-VA + API	no	yes	no	no	Solidification of the printed object occurs too slowly + low melt viscosity, the bits and layers deform.

4. Conclusions

In this study, a simple but powerful concept was tested to improve therapeutic safety and traceability of FDM 3D printed tablets for personalized medicine. It was shown that the blind-watermarking process can be used for oblong shaped tablets, as the bit-insertion and scanning process is currently only possible for straight, flat sides. Additionally, not every material is suitable for this approach. The color, roughness, and transparency of the filaments and printed objects have an impact on the detectability of the bits. However, when the filament used has a cloudy appearance or an added colorant, the detection process is feasible, and the bits are easy to detect. In addition, it is important to identify the correct print temperature of the used formulation since the formation of gas bubbles complicates the detection of the bits. For the formation of the bits, the melt viscosity and the solidification time of the printed filament seems to have a major impact. Unfortunately, a precise quantitative assessment of whether a filament is suitable for this process could not be made.

In comparison to other methods [39,42], this approach can be easily adapted in hospitals or community pharmacies with a cheap paper scanner and FDM 3D printer, as the dosage form and the blind-watermark codes are produced in one step without additional equipment. The method of Edinger et al. [42] requires a printer or film casting bench for the dosage form and an inkjet printer for the codes. Additionally, the traceability method of Trenfield et al. [39] needs more equipment for their track-and-trace process: a 2D and a 3D printer, for manufacturing the dosage form and printing the QR-code. Comparing the amount of information that can be put on a dosage form using these methods, more information can be covered in a QR code than in bits encoded in the tablet. Especially if the

dosage form is very small, the information content per tablet is quite low. An attempt could be made to modify the bit encoding script, so that both sides of the tablet contain different information, thus doubling the bits per tablet. Nevertheless, 2^{32} variations can be encoded on a large tablet, resulting in almost 4.3 billion possible combinations. While this is not sufficient to replace a QR code, the simplicity of the approach allows the implementation of an additional layer of security without investments in further equipment.

In addition, other processes that build up the dosage form layer by layer and are controlled by G-Code could also be investigated (e.g., semi-solid 3D printing). Furthermore, it would be interesting to test other scan methods. It would be easier to use the camera of a smartphone with an application for detection. As most of the bits were easier to detect by eye than with the scanning procedure, it could extend the range of suitable materials and possibly the range of geometries, as round surfaces could be scanned.

References

1. Substandard and Falsified Medical Products. Available online: https://www.who.int/health-topics/substandard-and-falsified-medical-products#tab=tab_1 (accessed on 30 December 2021).
2. McManus, D.; Naughton, B.D. A Systematic Review of Substandard, Falsified, Unlicensed and Unregistered Medicine Sampling Studies: A Focus on Context, Prevalence, and Quality. *BMJ Glob. Health* **2020**, *5*, e002393. [CrossRef] [PubMed]
3. Fernandez, F.M.; Hostetler, D.; Powell, K.; Kaur, H.; Green, M.D.; Mildenhall, D.C.; Newton, P.N. Poor Quality Drugs: Grand Challenges in High Throughput Detection, Countrywide Sampling, and Forensics in Developing Countries. *Analyst* **2011**, *136*, 3073–3082. [CrossRef] [PubMed]
4. Feldschreiber, P. Public Health Issues with Counterfeit Medicines. *Clin. Med. J. R. Coll. Physicians Lond.* **2009**, *9*, 63–64. [CrossRef] [PubMed]
5. Clark, F. Rise in Online Pharmacies Sees Counterfeit Drugs Go Global. *Lancet* **2015**, *386*, 1327–1328. [CrossRef]
6. Fantasia, H.C.; Vooys, K.M. Public Health Implications of Counterfeit Medications. *Nurs. Women's Health* **2018**, *22*, 264–268. [CrossRef] [PubMed]
7. Hamilton, W.L.; Doyle, C.; Halliwell-Ewen, M.; Lambert, G. Public Health Interventions to Protect against Falsified Medicines: A Systematic Review of International, National and Local Policies. *Health Policy Plan.* **2016**, *31*, 1448–1466. [CrossRef] [PubMed]
8. Sweileh, W.M. Substandard and Falsified Medical Products: Bibliometric Analysis and Mapping of Scientific Research. *Glob. Health* **2021**, *17*, 114. [CrossRef]
9. Vorrath, J.; Voss, M. The Hidden Dangers of Falsified and Substandard Medicines. Developing Countries Are Most Affected by the Illegal Trade. *Stift. Wiss. Politik Ger. Inst. Int. Secur. Aff.* **2019**, *C25*, 1–4. [CrossRef]
10. Newton, P.N.; Dondorp, A.; Green, M.; Mayxay, M.; White, N.J. Counterfeit Artesunate Antimalarials in Southeast Asia. *Lancet* **2003**, *362*, 169. [CrossRef]
11. Newton, P.N.; Caillet, C.; Guerin, P.J. A Link between Poor Quality Antimalarials and Malaria Drug Resistance? *Expert Rev. Anti-Infect. Ther.* **2016**, *14*, 531–533. [CrossRef]
12. Bolla, A.S.; Patel, A.R.; Priefer, R. The Silent Development of Counterfeit Medications in Developing Countries—A Systematic Review of Detection Technologies. *Int. J. Pharm.* **2020**, *587*, 119702. [CrossRef] [PubMed]

13. Rozendaal, J. Fake Antimalaria Drugs in Cambodia. *Lancet* **2001**, *357*, 890. [CrossRef]

14. Chaccour, C.; Kaur, H.; del Pozo, J.L. Falsified Antimalarials: A Minireview. *Expert Rev. Anti-Infect. Ther.* **2015**, *13*, 505–509. [CrossRef] [PubMed]

15. Arora, T.; Sharma, S. Global Scenario of Counterfeit Antimalarials: A Potential Threat. *J. Vector Borne Dis.* **2019**, *56*, 288–294. [CrossRef]

16. Suthar, A.B.; Coggin, W.; Raizes, E. Antimicrobial Resistance and Substandard and Falsified Medicines: The Case of HIV/AIDS. *J. Infect. Dis.* **2019**, *219*, 672–673. [CrossRef] [PubMed]

17. *World Health Organization WHO Global Surveillance and Monitoring System for Substandard and Falsified Medical Products*; World Health Organization: Geneva, Switzerland, 2017.

18. Substandard and Falsified Medical Products. Available online: https://www.who.int/en/news-room/fact-sheets/detail/substandard-and-falsified-medical-products (accessed on 30 December 2021).

19. Uddin, M. Blockchain Medledger: Hyperledger Fabric Enabled Drug Traceability System for Counterfeit Drugs in Pharmaceutical Industry. *Int. J. Pharm.* **2021**, *597*, 120235. [CrossRef]

20. Han, S.; Bae, H.J.; Kim, J.; Shin, S.; Kwon, S.; Park, W. Drug Authentication Using High Capacity and Error-Correctable Encoded Microtaggants. In Proceedings of the 16th International Conference on Miniaturized Systems for Chemistry and Life Sciences, MicroTAS 2012, Okinawa, Japan, 28 October–1 November 2012; pp. 1429–1431.

21. Falsified Medicines: Overview | European Medicines Agency. Available online: https://www.ema.europa.eu/en/human-regulatory/overview/public-health-threats/falsified-medicines-overview (accessed on 30 December 2021).

22. *Europol Information How COVID-19-Related Crime Infected Europe during 2020*; European Union Agency for Law Enforcement Cooperation: Haag, The Netherlands, 2020.

23. *Europol Information Pandemic Profiteering—How Criminals Exploit the COVID-19 Crisis*; European Union Agency for Law Enforcement Cooperation: Haag, The Netherlands, 2020.

24. Layach, O.B. International and National Obligations to Protect from the Risks of Pharmaceutical Crime: The Crime of Counterfeit Pharmaceutical Products in the COVID-19 Crisis. *Syst. Rev. Pharm.* **2020**, *11*, 648–657. [CrossRef]

25. Borse, N.N.; Cha, J.; Chase, C.G.; Gaur, R.; Koduri, C.K.; Kokai-Kun, J.F.; Kwan, D.C.; Lee, R.; Moore, J.C.; Raghavendran, V.; et al. *Responding to the Surge of Substandard and Falsified Health Products Triggered by the Covid-19 Pandemic*; USP: North Bethesda, MD, USA, 2021.

26. Seibert, H.H.; Maddox, R.R.; Flynn, E.A.; Williams, C.K. Effect of Barcode Technology with Electronic Medication Administration Record on Medication Accuracy Rates. *Am. J. Health-Syst. Pharm.* **2014**, *71*, 209–218. [CrossRef]

27. Klein, K.; Stolk, P. Challenges and Opportunities for the Traceability of (Biological) Medicinal Products. *Drug Saf.* **2018**, *41*, 911–918. [CrossRef]

28. Alam, N.; Hasan Tanvir, M.R.; Shanto, S.A.; Israt, F.; Rahman, A.; Momotaj, S. Blockchain Based Counterfeit Medicine Authentication System. In Proceedings of the ISCAIE 2021—IEEE 11th Symposium on Computer Applications & Industrial Electronics, Penang, Malaysia, 3–4 April 2021; pp. 214–217. [CrossRef]

29. Nawale, S.D.; Konapure, R.R. Blockchain IoT Based Drugs Traceability for Pharma Industry. In Proceedings of the 2021 IEEE International Conference on Engineering, Technology and Innovation (ICE/ITMC), Cardiff, UK, 21–23 June 2021; pp. 1–4. [CrossRef]

30. Ludasi, K.; Jójárt-Laczkovich, O.; Sovány, T.; Hopp, B.; Smausz, T.; Andrásik, A.; Gera, T.; Kovács, Z.; Regdon, G. Anti-Counterfeiting Protection, Personalized Medicines − Development of 2D Identification Methods Using Laser Technology. *Int. J. Pharm.* **2021**, *605*, 120793. [CrossRef]

31. European Commission Commission Delegated Regulation (EU) 2016/ 161. Official Journal of the European Union 2015. Available online: https://eur-lex.europa.eu/legal-content/EN/TXT/?uri=CELEX:32016R0161 (accessed on 30 December 2021).

32. European Commission Directive 2011/62/EU Of The European Parliament And Of The Council of 8 June 2011 Amending Directive 2001/83/EC on the Community Code Relating to Medicinal Products for Human Use, as Regards the Prevention of the Entry into the Legal Supply Chain of Falsified Medicinal Products (Text with EEA Relevance). Official Journal of the European Union 2011. Available online: https://eur-lex.europa.eu/legal-content/EN/TXT/?uri=CELEX%3A32011L0062 (accessed on 30 December 2021).

33. Sträter, B. Arzneimittelfälschungen: Maßnahmen Der Gesetzgeber in Der Europäischen Union Und in Deutschland. *Bundesgesundheitsblatt—Gesundheitsforschung—Gesundheitsschutz* **2017**, *60*, 1188–1195. [CrossRef] [PubMed]

34. Szücs, C. 2D-Barcode Auf Der Verpackung—Ein System Zur Authentifizierung Verschreibungspflichtiger Arzneimitteln. *Jusletter IT* **2020**, 599–606. [CrossRef]

35. Roth, L.; Biggs, K.B.; Bempong, D.K. Substandard and Falsified Medicine Screening Technologies. *AAPS Open* **2019**, *5*, 1–12. [CrossRef]

36. Hamburg, M.A.; Collins, F.S. The Path to Personalized Medicine. *New Engl. J. Med.* **2010**, *363*, 301–304. [CrossRef] [PubMed]

37. Windolf, H.; Chamberlain, R.; Quodbach, J. Predicting Drug Release from 3D Printed Oral Medicines Based on the Surface Area to Volume Ratio of Tablet Geometry. *Pharmaceutics* **2021**, *13*, 1453. [CrossRef] [PubMed]

38. Nørfeldt, L.; Bøtker, J.; Edinger, M.; Genina, N.; Rantanen, J. Cryptopharmaceuticals: Increasing the Safety of Medication by a Blockchain of Pharmaceutical Products. *J. Pharm. Sci.* **2019**, *108*, 2838–2841. [CrossRef]

39. Trenfield, S.J.; Xian Tan, H.; Awad, A.; Buanz, A.; Gaisford, S.; Basit, A.W.; Goyanes, A. Track-and-Trace: Novel Anti-Counterfeit Measures for 3D Printed Personalized Drug Products Using Smart Material Inks. *Int. J. Pharm.* **2019**, *567*, 118443. [CrossRef]

40. Hodson, R. Precision Medicine. *Nature* **2016**, *537*, S49. [CrossRef]

41. Ashley, E.A. Towards Precision Medicine. *Nat. Rev. Genet.* **2016**, *17*, 507–522. [CrossRef]

42. Edinger, M.; Bar-Shalom, D.; Sandler, N.; Rantanen, J.; Genina, N. QR Encoded Smart Oral Dosage Forms by Inkjet Printing. *Int. J. Pharm.* **2018**, *536*, 138–145. [CrossRef]

43. Ishiyama, R.; Takahashi, T.; Makino, K.; Kudo, Y.; Kooper, M.; Abbink, D. Medicine Tablet Authentication Using Fingerprints of Ink-Jet Printed Characters. In Proceedings of the 2019 IEEE International Conference on Industrial Technology (ICIT), Melbourne, Australia, 13–15 February 2019; pp. 871–876. [CrossRef]

44. Korte, C. 3D-Drug-Printing: Extrusion of Printable Drug-Loaded Filaments and Development of Novel Solid Dosage Forms. Ph.D. Thesis, Heinrich-Heine-Universität, Düsseldorf, Germany, 2018.

45. Sadia, M.; Arafat, B.; Ahmed, W.; Forbes, R.T.; Alhnan, M.A. Channelled Tablets: An Innovative Approach to Accelerating Drug Release from 3D Printed Tablets. *J. Control. Release* **2018**, *269*, 355–363. [CrossRef] [PubMed]

46. Goyanes, A.; Fina, F.; Martorana, A.; Sedough, D.; Gaisford, S.; Basit, A.W. Development of Modified Release 3D Printed Tablets (Printlets) with Pharmaceutical Excipients Using Additive Manufacturing. *Int. J. Pharm.* **2017**, *527*, 21–30. [CrossRef] [PubMed]

47. Obeid, S.; Madžarević, M.; Ibrić, S. Tailoring Amlodipine Release from 3D Printed Tablets: Influence of Infill Patterns and Wall Thickness. *Int. J. Pharm.* **2021**, *610*, 121261. [CrossRef] [PubMed]

48. Đuranović, M.; Madžarević, M.; Ivković, B.; Ibrić, S.; Cvijić, S. The Evaluation of the Effect of Different Superdisintegrants on the Drug Release from FDM 3D Printed Tablets through Different Applied Strategies: In Vitro-in Silico Assessment. *Int. J. Pharm.* **2021**, *610*, 121194. [CrossRef] [PubMed]

49. Buyukgoz, G.G.; Kossor, C.G.; Davé, R.N. Enhanced Supersaturation via Fusion-Assisted Amorphization during Fdm 3d Printing of Crystalline Poorly Soluble Drug Loaded Filaments. *Pharmaceutics* **2021**, *13*, 1857. [CrossRef] [PubMed]

50. Quodbach, J.; Bogdahn, M.; Breitkreutz, J.; Chamberlain, R.; Eggenreich, K.; Elia, A.G.; Gottschalk, N.; Gunkel-Grabole, G.; Hoffmann, L.; Kapote, D.; et al. Quality of FDM 3D Printed Medicines for Pediatrics: Considerations for Formulation Development, Filament Extrusion, Printing Process and Printer Design. *Ther. Innov. Regul. Sci.* **2021**, *1*, 1–19. [CrossRef]

51. Cailleaux, S.; Sanchez-Ballester, N.M.; Gueche, Y.A.; Bataille, B.; Soulairol, I. Fused Deposition Modeling (FDM), the New Asset for the Production of Tailored Medicines. *J. Control. Release* **2021**, *330*, 821–841. [CrossRef]

52. Chamberlain, R.; Windolf, H.; Geissler, S.; Quodbach, J.; Breitkreutz, J. Precise Dosing of Pramipexole for Low-Dosed Filament Production by Hot Melt Extrusion Applying Various Feeding Methods. *Pharmaceutics* **2022**, *14*, 216. [CrossRef]

53. Delmotte, A.; Tanaka, K.; Kubo, H.; Funatomi, T.; Mukaigawa, Y. Blind Watermarking for 3-D Printed Objects by Locally Modifying Layer Thickness. *IEEE Trans. Multimed.* **2020**, *22*, 2780–2791. [CrossRef]

54. Karagianni, A. Development of Printable Drug-Loaded Filaments (Rheological and Solid-State Characterization). Master Thesis, Heinrich-Heine-Universität, Düsseldorf, Germany, 2019.

55. Ponsar, H.; Wiedey, R.; Quodbach, J. Hot-Melt Extrusion Process Fluctuations and Their Impact on Critical Quality Attributes of Filaments and 3D-Printed Dosage Forms. *Pharmaceutics* **2020**, *12*, 511. [CrossRef]

56. Korte, C.; Quodbach, J. 3D-Printed Network Structures as Controlled-Release Drug Delivery Systems: Dose Adjustment, API Release Analysis and Prediction. *AAPS PharmSciTech* **2018**, *19*, 3333–3342. [CrossRef] [PubMed]

57. Gelbe Liste Identa I Gelbe Liste. Available online: https://www.gelbe-liste.de/identa/results (accessed on 16 September 2021).

58. Korte, C.; Quodbach, J. Formulation Development and Process Analysis of Drug-Loaded Filaments Manufactured via Hot-Melt Extrusion for 3D-Printing of Medicines. *Pharm. Dev. Technol.* **2018**, *23*, 1117–1127. [CrossRef] [PubMed]

59. Genina, N.; Holländer, J.; Jukarainen, H.; Mäkilä, E.; Salonen, J.; Sandler, N. Ethylene Vinyl Acetate (EVA) as a New Drug Carrier for 3D Printed Medical Drug Delivery Devices. *Eur. J. Pharm. Sci.* **2016**, *90*, 53–63. [CrossRef] [PubMed]

60. Henry, S.; de Wever, L.; Vanhoorne, V.; de Beer, T.; Vervaet, C. Influence of Print Settings on the Critical Quality Attributes of Extrusion-Based 3D-Printed Caplets: A Quality-by-Design Approach. *Pharmaceutics* **2021**, *13*, 2068. [CrossRef] [PubMed]

61. Crișan, A.G.; Porfire, A.; Ambrus, R.; Katona, G.; Rus, L.M.; Porav, A.S.; Ilyés, K.; Tomuță, I. Polyvinyl Alcohol-Based 3d Printed Tablets: Novel Insight into the Influence of Polymer Particle Size on Filament Preparation and Drug Release Performance. *Pharmaceuticals* **2021**, *14*, 418. [CrossRef]

62. Nober, C.; Manini, G.; Carlier, E.; Raquez, J.M.; Benali, S.; Dubois, P.; Amighi, K.; Goole, J. Feasibility Study into the Potential Use of Fused-Deposition Modeling to Manufacture 3D-Printed Enteric Capsules in Compounding Pharmacies. *Int. J. Pharm.* **2019**, *569*, 118581. [CrossRef]

63. Gottschalk, N.; Bogdahn, M.; Harms, M.; Quodbach, J. Brittle Polymers in Fused Deposition Modeling: An Improved Feeding Approach to Enable the Printing of Highly Drug Loaded Filament. *Int. J. Pharm.* **2021**, *597*, 120216. [CrossRef]

64. Bandari, S.; Nyavanandi, D.; Dumpa, N.; Repka, M.A. Coupling Hot Melt Extrusion and Fused Deposition Modeling: Critical Properties for Successful Performance. *Adv. Drug Deliv. Rev.* **2021**, *172*, 52–63. [CrossRef]

65. Zhang, J.; Xu, P.; Vo, A.Q.; Bandari, S.; Yang, F.; Durig, T.; Repka, M.A. Development and Evaluation of Pharmaceutical 3D Printability for Hot Melt Extruded Cellulose-Based Filaments. *J. Drug Deliv. Sci. Technol.* **2019**, *52*, 292–302. [CrossRef]

Summary and Outlook

The aim of this work was to use the advantages offered by the FDM 3D printing process for the development of oral DDF for personalized therapy. For this purpose, different APIs (levodopa, benserazide, pramipexole, and praziquantel) as well as different polymers (e.g., PVA, EVA) were used. First, PVA filaments with 5% pramipexole were prepared via HME, printed via FDM 3DP, and used for the first dissolution experiments. Different geometries with various dosages and SA/V ratios were designed with a CAD program, printed, and the API release analysed. The influence of the swelling behavior of the PVA hydrocolloid matrix on the release of the drug from the matrix was investigated, and a description of similar curves to each other with the f_2 value and the MDT was found. During these experiments, a correlation between the MDT and the SA/V ratio was identified, expanded with further experiments, and used for predictions. The release profiles with PVA could be described with the Peppas Sahlin equation due to the diffusion and erosion properties of the matrix. These experiments were transferred to an inert polymer (EVA) with 10% drug loading (levodopa, BCS I) and PVA with 5% praziquantel (BCS II). For the dissolution profile of the BCS II compound, the Weibull equation was used to describe the release. Also, for these formulations, the predictions to the given SA/V ratio worked to predict the resulting release course. This approach can be used in the future as part of the workflow from prescription to 3D printed dosage form. Based on the correlation, the release profile for a printed tablet can be predicted for the desired formulation but also the SA/V ratio needed to release the API in the required time. Further studies could confirm whether these predictions also apply to in-vivo profiles. Due to the different characteristics of the APIs (BCS I+II), the influence on the resulting blood plasma concentration could be different and cancel the correlation. To avoid unnecessary animal testing, in-silico experiments could be performed and thus predictions of possible in-vivo courses could be made. In addition, it should be investigated whether the correlation can also apply to other polymers and APIs whose release profiles follow different release kinetics. Furthermore, other 3D printing technologies could be used to test this concept so that the portfolio of possible DDFs and formulations can be expanded.

To incorporate newer technologies, various ANN architectures were built with the collected release data (~200 geometries; ~1000 release curves) to make predictions on possible geometries based on release profile and dosage. With a standard net (classification architecture), a training accuracy of 68.5% could be achieved, but in the test runs only an accuracy

of 44.4% could be reached. However, to predict the exact dimensions of the geometry, the underlying geometry/class must first be predicted. Nevertheless, this is not possible based on the dissolution curve since the profile is determined not by the geometry but by the SA/V ratio. Thus, an attempt was made to predict the underlying SA/V ratio from the given release data and dosages to calculate the required SA and to design the corresponding geometry with the known V and SA. This scalar prediction architecture was able to make more reliable predictions with a mean square error loss of 0.05. Since the PVA-polymer tends to swell and pores can clog during this process, deviations between the calculated and real SA can occur, so a minimum distance or minimum pore size must be specified for the respective polymer in order for the desired SA to not be reduced over time. The prediction of the SA/V ratio via ANN worked, but not for the prediction of the exact geometry, which could be used for the prescription process of 3DP DDF. Accordingly, further network designs would have to be investigated (e.g., Random Forest Classification or Random Forest Regression), or one would have to work with a large data network in future, so that the pharmacist would not need additional time to design the appropriate geometry first and thus represent a possible risk factor.

With the help of these data, a concept for dose-independent drug release could be developed: the hollow cylinder-based Geometry Model (HCb). This model allows to cover a broad range of doses with a certain SA/V ratio for different formulations. Thus, for patients, the dose can be customized without changing the API's release pattern. This works for the 5% PDM-PVA formulation for a range of 4 to 32 mg API, for LD-EVA from 8.8 to 48.2 mg, and for PZQ-PVA from 4.8 to 36 mg. Thereby, a factor of 7 on average can be varied in doses without significantly altering the release profile. Due to the additively layered structure of the FDM 3DP DDF, the dose can be varied in 0.13 mg increments, for a formulation with 5% drug-load. The developed dose-independent release model was then applied to a fixed combination of levodopa-benserazide in EVA. For Parkinson's patients, only symptomatic therapy is available so far, which involves many different drugs and narrow therapeutic ranges, since here effect and side effect go hand in hand. Another filament with the third API, pramipexole, in PVA was added to the fixed-combination filament and printed to form a polypill with three APIs and two polymers. Immediate release was achieved with PDM+PVA, and constant release over 12 h was achieved with the LD+BZ+EVA combination. With the help of different geometries and layer combinations of the two formulations, the advantages of FDM 3D printing could be fully exploited and

thus dosages of 2 to 200 mg LD/BZ and 0.4 to 3.5 mg PDM could be printed in different polypill variations. The dissolution profiles could be maintained over this dosing range, but also varied with the help of the SA/V ratio. To map the releases of the three APIs precisely and accurately from low (0.4 mg PDM) to high dose (200 mg LD), a new analytical technique had to be developed. While LD+BZ could be detected by HPLC-UV, the dosage of PDM in the first minutes of release was too low to be above the limit of quantification (LoQ). Therefore, a fibre-technique was connected between the six-way valve and the detector of the HPLC machine and a new measurement mode for PDM was run in parallel to HPLC-UV. This allowed the LoQ for PDM to be lowered and the three APIs to be analysed in parallel. Further investigations could be undertaken regarding the transfer of DDF models from in-vitro to in-vivo models, or in-silico modulations. Of course, the patient's acceptance of the unconventional forms must also be present in order for the therapy adherence to persist. In addition, it would have to be tested whether these geometries can also be realized for other polymers that exhibit stronger swelling behavior or can only be printed with a lower print precision (due to viscosity and solidification properties) or other 3DP technique.

Since FDM 3D printers can now be purchased very cheaply on the market, a technique must also be developed for the case of counterfeiting. Since filaments of various polymers and colors are available for buying, it must be expected that 3D printed drugs can be easily falsified in the future. To circumvent this crime, a concept of blind-watermarking for 3D printed oral dosage forms was tested. The concept was demonstrated in 2019 by Delmotte et al. for 3D printed objects without pharmaceutical applications in mind [297]. These scripts were adapted for oblong tablets, allowing a minimum of 9 bits per tablet side up to 32 bits per tablet side to be inserted onto the printed form. It was found that the melt viscosity as well as the color, transparency, and solidification behavior of the formulations have an influence on the printability and detectability of the bits. However, there are often easy solutions to convert the formulation to a usable one for the blind watermarking system, so that in the future this technology can be used, for example, to support an additional QR code on the dosage form, since only a simple paper scanner is required for detection in addition to the FDM 3D printer. However, the method alone is not sufficient to make a DDF completely counterfeit-proof and cannot be used for every polymer. But it can be used as supporting tool, since blind-watermarking bits can be incorporated directly into the G-Code and therewith do not involve any additional effort.

The experiments presented in this work were able to exploit the advantages of FDM 3DP for personalized medicine of oral dosage forms, but also highlighted the limits and challenges of the process. The polymers and blends used have different properties that influence both the FDM 3DP and its precision, but also influence the release properties (swelling behavior) and the incorporation of blind-watermarking bits. Both API and polymer properties have an impact on the prediction models and also the dose-independent release model. It cannot be generalized that these approaches will work for all formulations, and it would take a great deal of effort to test through all possible combinations. Furthermore, it cannot be generalized that the predictions as well as DDF models will behave the same in-vivo as in-vitro. For this, further investigations or in-silico modulations have to be performed in any case. For a future prescription process for personalized 3DP oral dosage forms, a large database containing any APIs, polymers, and mixtures with different geometries and release profiles could be used so that the pharmacist could determine the required SA/V ratio, mg of API, and controlled release profile from it and print the given geometry directly without requiring any manual changes. In summary, the advantages offered by FDM 3D printing can be used for personalized medicine, designing swallowable, patient-tailored oral dosage forms with controlled release profiles. Due to the digital design of DDF, the release profiles for the respective dosages can be predicted in advance, due to known SA and V. By combining different traceability techniques, the previously existing safety gap can be closed. However, the limitations offered by the printing time and the lack of clarity regarding regulatory processes remain and require further work, as well as the establishment of GMP-capable 3D printers.

Acknowledgements / Danksagung

Eidesstattliche Erklärung

Ich versichere an Eides Statt, dass die Dissertation von mir selbständig und ohne unzulässige fremde Hilfe unter Beachtung der „Grundsätze zur Sicherung guter wissenschaftlicher Praxis an der Heinrich-Heine-Universität Düsseldorf" erstellt worden ist.

_____

Hellen Mazur